

Heavy Meson Semileptonic Form Factors from Lattice Quantum Chromodynamics

Euan McLean

Supervised by Prof. Christine Davies

*Submitted in fulfillment of the requirements for the degree of
Doctor of Philosophy*

April 2019



*The University of Glasgow
College of Science and Engineering*

Declaration of originality

This thesis is my own work, except where explicit attribution to others is made. In particular chapter 6 is based on the now published [not out yet!], and chapter 7 is based on [not out yet!].

All results and figures presented in these chapters are my own, except for figures 2.3 and 2.8 which are courtesy of the Particle Data Group [1], fig. 2.3 from the HFLAV collaboration [2], fig. 3.7 was produced by McNeile et. al [3] .

'Part of being a winner is knowing when enough is enough. Sometimes you have to give up the fight and walk away, and move on to something that's more productive.'

- Donald Trump

TODO:

Conclusion

tadpole improvement?

Chiral symmetry section - say why $B_s \rightarrow D_s$ and $B \rightarrow D$ are approx. equal.
acknowledge NRQCD has no continuum limit in lattice NRQCD section...

Luke's theorem bit needs to be tighter, specifically why you get specific h_{A_1}, h_+
expressions.

READING LIST:

Lenz, Flavour physics lectures. 1812.11211, 1703.08170

'The B-physics program' :<https://www.ncbi.nlm.nih.gov/pmc/articles/PMC4737432/#andp2015002sec-0020title>

Chiral Anomalies and rooted staggered fermions - Creutz
Conjugate Gradient without the excruciating pain

Acknowledgments

I claim sole credit for everything in this thesis.

Contents

1	Introduction	1
2	Motivation & Tools from the Continuum	3
2.1	Testing the Standard Model	3
2.2	Flavour-Changing Charged Currents	5
2.2.1	The CKM Matrix	7
2.2.2	Weak Decays	10
2.2.3	$b \rightarrow c$ Transitions and $ V_{cb} $	14
2.2.4	Flavour Anomalies & Lepton Flavour Violation	16
2.3	Strong Interaction Physics	19
2.3.1	Quantum Chromodynamics	19
2.3.2	Chiral Symmetry	21
2.4	Heavy Quark Physics	23
2.4.1	HQET	23
2.4.2	NRQCD	27
3	Lattice Quantum Chromodynamics	29
3.1	Lattice Gauge Fields	30
3.1.1	The Gauge Action	33
3.1.2	Symmanzik Improvements of the Gauge Action	34
3.2	Lattice Fermions	36
3.2.1	The Naive Fermion Action & The Doubling Problem	37
3.2.2	Staggered Quarks	38
3.2.3	Highly Improved Staggered Quarks	41
3.3	Heavy Quarks on the Lattice	42
3.3.1	Heavy HISQ	43
3.3.2	Lattice NRQCD	44
4	Lattice Calculations	47
4.1	Evaluating Lattice Correlation Functions	47
4.1.1	Generation of Gauge Ensembles	48
4.1.2	Dirac Operator Inversion	52
4.1.3	Staggered Correlation Functions	54

4.2	Analysis of Correlation Functions	57
4.2.1	Fitting Correlation Functions	58
4.2.2	Signal Degredation	60
4.3	Renormalization of Currents	61
5	<i>b</i>-Physics from Lattice NRQCD	63
5.1	NRQCD-HISQ currents	63
5.2	Relativistic Normalisation of the $b \rightarrow c$ temporal axial current	65
5.3	$B_{(s)} \rightarrow D_{(s)} l \nu$ form factors	68
5.3.1	Calculation Details	69
5.3.2	Correlator Fits	71
5.3.3	Form Factors	71
5.3.4	Results	73
5.3.5	Form factors from V_0 and S in $B_{(s)} \rightarrow D_{(s)}$	76
5.4	Non-Perturbative Renormalization using $B_c \rightarrow \eta_c$ Data	78
5.4.1	Z_S	79
5.4.2	Z_{V_0}	81
5.4.3	Z_{V_k}	82
5.5	Conclusion of NRQCD work	83
6	$B_s \rightarrow D_s^* l \nu$ Axial Form Factor at Zero Recoil from Heavy-HISQ	85
6.1	Motivation	86
6.2	Calculation Details	87
6.2.1	Lattice Setup	87
6.2.2	Correlator Fits	90
6.2.3	Normalization of Axial Current	93
6.2.4	Extrapolation to Physical Point	97
6.3	Results and Discussion	101
6.3.1	$h_{A_1}^s(1)$	101
6.3.2	Extrapolation Stability	104
6.3.3	Hints about $B \rightarrow D^*$	107
6.3.4	HQET Low Energy Constants	108
6.3.5	Extrapolation of $h_{A_1}^s(1)/(f_{H_c} \sqrt{M_{H_c}})$ and f_{H_c}	109
6.4	Conclusions	110

7 $B_s \rightarrow D_s l \nu$ Form Factor at All Physical q^2 from Heavy-HISQ	113
7.1 Motivation	114
7.2 Calculation Details	116
7.2.1 Lattice Setup	116
7.2.2 Analysis of Correlation Functions	120
7.2.3 Vector Current Renormalization	123
7.2.4 Extrapolation to the Physical Point	125
7.3 Results and Discussion	130
7.3.1 Ratio Method	130
7.3.2 Direct Method	133
7.3.3 Unitarity Test	135
7.3.4 R_{D_s}	137
7.4 Reconstructing Form Factors	137
7.5 $h_+^s(1)$ and HQET low energy constants	138
7.6 Conclusions	140
7.7 Numerical Values for Lattice Results	141

CHAPTER 1

Introduction

As the LHC continuously refuses to supply new resonances, the high energy physics community places their hope in the intensity frontier to finally break the standard model. Subtle differences between experimental measurements and standard model predictions are the new rock and roll. As collider experiments collect more data and measurements become more precise, theorists must keep up the pace and improve our predictions. What else but Lattice QCD could answer the call of providing first-principle calculations of non-perturbative quantities?

This thesis focuses on the study of calculating form factors for semileptonic $b \rightarrow c$ transitions. These transitions occur between hadrons, bound together by QCD. At the confinement scale ($\sim 1\text{GeV}$), perturbation theory breaks down due to asymptotic freedom, and the only sensible option is to compute the path integral directly, i.e., via lattice calculations.

The b quark is difficult to deal with on the lattice, due to its mass being beyond the momentum cutoff imposed by computationally feasible lattice spacings. I calculate $b \rightarrow c$ form factors using two approaches to dealing with the heavy b , one employing a non-relativistic action for the b (*NRQCD*), and the other relying on heavy quark effective theory to extrapolate upwards to the b mass (*Heavy-HISQ*). The main take-home from this thesis is the following: **when it comes to semileptonic form factors; NRQCD is on shaky ground, and Heavy-HISQ is an excellent way to live.**

Using NRQCD, I attempted to compute form factors for the $B_{(s)} \rightarrow D_{(s)} l \nu$ decays. The depletion of the signal/noise ratio in correlation functions featuring high spacial momentum means lattice data for this decay was limited to the high q^2 region.

In NRQCD, flavour-changing current operators are made of an infinite series of terms in powers of the b -quark velocity v , each requiring their own normalisation via perturbative matching to continuum QCD. It was discovered during this work that subleading terms in this series, that were originally thought to be negligible, in fact may be an important contribution. Since the perturbative matching calculations for these terms have not been performed, this caused a somewhat insurmountable obstacle for the NRQCD approach to calculating $b \rightarrow c$ form factors.

The NRQCD approach could in principle be saved by finding non-perturbative normalizations of these large subleading terms in the current. We investigated a way of achieving this by comparing NRQCD lattice data to pre-existing and more reliable Heavy-HISQ lattice data, with limited success.

To sidestep the problems with NRQCD, We focused instead on the Heavy-HISQ approach. With this, we successfully calculated the $B_s \rightarrow D_s^* l \nu$ axial form factor at zero recoil. This demonstrated the power of heavy-HISQ and layed the groundwork for a study of both $B_s \rightarrow D_s^* l \nu$ and $B_s \rightarrow D_s l \nu$ form factors away from zero recoil, which is now underway. We also calculated $B_s \rightarrow D_s l \nu$ form factors throughout the full physical range of momentum transfer. These studies, when combined with future experimental data of the $B_s \rightarrow D_s l \nu$ and $B_s \rightarrow D_s^* l \nu$ decays, will supply new tests of the standard model, and new channels to determining the CKM parameter $|V_{cb}|$.

All work reported in this thesis was performed using gluon ensembles courtesy of the MILC collaboration, accounting for dynamical up, down, strange and charm HISQ quarks in the sea. We computed correlation functions using a combination of the MILC code, and HPQCD's NRQCD code.

CHAPTER 2

Motivation & Tools from the Continuum

In this chapter, we lay out the physics context of this work and some theoretical machinery that was useful in our studies. This section consists of a definition and empirical status of the standard model. Then, we will expand on the details of the specific sector we are interested in - the flavour sector and the CKM matrix.

We will then move onto some lay down some physics machinery used in our work, namely QCD and chiral symmetry, and effective field theories for heavy quarks.

2.1 Testing the Standard Model

The Standard Model of Particle Physics (SM) is, so far, the most successful theory for describing fundamental particles and their interactions. It is an effective Yang-Mills quantum field theory. It is most succinctly defined by listing its symmetries, field content, and the irreducible representations (irreps) of the symmetries that those fields transform under.

The symmetries are the following. The Lorentz group $SO(3, 1)$, the group of coordinate transformations that leave the Minkowski metric invariant, which can be decomposed into $SU(2)_l \times SU(2)_r$ (*left-handed* and *right-handed*). We denote an irrep as (a, b) where a is the σ^z eigenvalue under $SU(2)_l$ transforms, and b is that of $SU(2)_r$. Then there are internal local gauge symmetries:

$$SU(3)_C \times SU(2)_L \times U(1)_Y, \quad (2.1)$$

irreps of which we denote with (x, y, z) , where x, y are the $SU(3)_C$ and $SU(2)_W$ irreps and z is the charge under $U(1)_Y$.

The field content is: gauge bosons for each generator of the above gauge symmetries, each transforming in the adjoint of their corresponding symmetry and in the $(1/2, 1/2)$ irrep of the Lorentz group, denoted B_μ , W_μ , G_μ respectively. There are

6 $SU(2)_L$ doublets in the $(1/2, 0)$ Lorentz irrep;

$$Q_{1,2,3} = \begin{pmatrix} u_L \\ d_L \end{pmatrix}, \begin{pmatrix} c_L \\ s_L \end{pmatrix}, \begin{pmatrix} t_L \\ b_L \end{pmatrix} , \quad (\mathbf{3}, \mathbf{2}, 1/6) \quad (2.2)$$

$$L_{1,2,3} = \begin{pmatrix} \nu_{e,L} \\ e_L \end{pmatrix}, \begin{pmatrix} \nu_{\mu,L} \\ \mu_L \end{pmatrix}, \begin{pmatrix} \nu_{\tau,L} \\ \tau_L \end{pmatrix} , \quad (\mathbf{1}, \mathbf{2}, -1) \quad (2.3)$$

and 9 $SU(2)_L$ singlets in the $(0, 1/2)$ Lorentz irrep;

$$u_{1,2,3}^R = u_R, c_R, t_R , \quad (\bar{\mathbf{3}}, \mathbf{1}, 2/3) \quad (2.4)$$

$$d_{1,2,3}^R = d_R, s_R, b_R , \quad (\bar{\mathbf{3}}, \mathbf{1}, -1/3) \quad (2.5)$$

$$e_{1,2,3}^R = e_R, \mu_R, \tau_R , \quad (\mathbf{1}, \mathbf{1}, -1). \quad (2.6)$$

We have also listed the SM gauge irreps next to each definition. There is also in principle a further set of right-handed $SU(2)_L$ singlets, $\nu_{1,2,3}^R = (\nu_{e,R}, \nu_{\mu,R}, \nu_{\tau,R})$, but these are singlets of the entire SM gauge group so in a phenomenological sense very much 'not there'. There is also a Lorentz scalar $SU(2)_L$ doublet, the Higgs H , with in gauge irrep $(\mathbf{1}, \mathbf{2}, 1/2)$ that obtains a vacuum expectation value under $\sim 200\text{GeV}$ and causes a breaking of the above gauge group to $SU(3)_C \times U(1)_E$, where $U(1)_E$ is the electroweak gauge group mediated by the photon.

There is at present no confirmed evidence of physics beyond the SM (or *new physics* (NP)), besides the presence of neutrino (ν) masses. However, there are a number of problems with the SM that heavily imply that there must be new physics. Among the most famous sources of concern are:

- **Dark Matter & Dark Energy** - an estimated 96% of the content of the universe is dark matter and dark energy, that does not interact with the SM gauge group (only via gravity), so cannot be explained by the SM.
- **Matter/Antimatter Asymmetry** - the SM requires there to be an equal amount of matter and antimatter in the universe, however, we observe a massive dominance of matter over antimatter.
- **Neutrino Oscillations** - different species of neutrinos oscillate into each other over time, there is no SM mechanism to explain this.
- **The Hierarchy Problem** - the SM is 'finely tuned', the chances of the Higgs choosing its current vacuum expectation value is estimated to be one in $\sim 10^{45}$.

The central goal of particle physics is currently to pin down evidence against the standard model. Only once we have detailed knowledge of how it breaks down will theorists be able to uniquely determine a new theory of fundamental physics.

There are many promising approaches to achieve this. They are traditionally separated into

- **The Energy Frontier** - explore the highest possible energies reachable with accelerators, directly looking for new physics via the production and identification of new states of matter.
- **The Cosmic Frontier** - use the universe as an experimental laboratory and observatory, taking advantage of naturally occurring events to observe indications of new interactions.
- **The Intensity Frontier** - use intense sources of particles from accelerators, reactors, the sun and the atmosphere to make ultra-precise measurements and find subtle deviations from SM predictions.

The work in this thesis contributes to the third approach. There is a rising tide of more and more SM observables being measured and predicted more and more precisely. It is only a matter of time until one of these observables yields a statistically significant deviation from the SM.

2.2 Flavour-Changing Charged Currents

The SM tests relevant to this work are on quark flavour-changing interactions. Here we will detail the parts of the SM relevant to these interactions.

The $SU(2)_L$ gauge symmetry of the SM is mediated by the vector boson $W = W^1\tau_1 + W^2\tau_2 + W^3\tau_3$, where τ_i are the three $SU(2)$ generators acting on the $SU(2)_L$ doublets defined in the last section. It is convenient to redefine the fields $W = W^+(\tau_0 + i\tau_1) + W^-(\tau_0 - i\tau_1) + W^3\tau_3$. W^\pm, W^3 are the stationary states at low energies due to electroweak symmetry breaking.

The part of the SM Lagrangian that describes the coupling of W^\pm to fermions is given by

$$\mathcal{L}_{\text{FCCC}} = \frac{e}{\sqrt{2} \sin \theta_W} \left(\bar{u}_L^i W^+ d_L^i + \bar{d}_L^i W^- u_L^i + \bar{\nu}_L^i \bar{W}^+ e_L^i + \bar{e}_L^i W^- \nu_L^i \right), \quad (2.7)$$

where e is the electron charge, θ_W is the Weinberg angle (a parameter of the SM), and $\not{V} = \gamma^\mu V_\mu$ where γ^μ are members of the Clifford algebra acting on fermion

spin components. To understand the interactions these terms cause we must also consider the mass terms for the fermions:

$$\mathcal{L}_{\text{mass}} = y_{ij}^u \left(\frac{v}{\sqrt{2}} \right) u_L^i u_R^j + y_{ij}^d \left(\frac{v}{\sqrt{2}} \right) d_L^i d_R^j + y_{ij}^e \left(\frac{v}{\sqrt{2}} \right) e_L^i e_R^j. \quad (2.8)$$

These terms come from the coupling of the fermions to the Higgs field, where the Higgs has taken a vacuum expectation value v at low energies. $y_{ij}^{u,d,e}$ are the Yukawa matrices, parameterising the coupling of the fermions to the Higgs, consisting of free SM parameters. The absence of right-handed neutrinos forbids an analogous term for neutrinos.

Due to these nondiagonal mass terms, the fundamental fermion fields are not stationary states. To obtain a more useful representation, one rotates the fields to diagonalise these terms

$$\psi_i^L \rightarrow L_{ij}^\psi \psi_j^L, \psi_R^i \rightarrow R_{ij}^\psi \psi_R^j, \quad (2.9)$$

where $\psi = u, d$ or e , and we fix L_{ij}^ψ, R_{ij}^ψ according to

$$y^\psi \left(\frac{v}{\sqrt{2}} \right) = L^\psi M^\psi R^\psi \quad (2.10)$$

where M^ψ is diagonal. This results in diagonal mass terms, but also has an effect on $\mathcal{L}_{\text{FCCC}}$:

$$\mathcal{L}_{\text{FCCC}} = \frac{e}{\sqrt{2} \sin \theta_W} \left(V_{ij} \bar{u}_L^i W^+ d_L^j + V_{ij}^* \bar{d}_L^i W^- u_L^j + \bar{\nu}_L^i W^+ e_L^i + \bar{e}_L^i W^- \nu_L^i \right). \quad (2.11)$$

$V = L^{u\dagger} L^u$ is by construction a unitary matrix ($V^\dagger V = (L^{d\dagger} L^d)(L^{u\dagger} L^u) = L^d L^{d\dagger} = 1$). V is the famous Cabibbo–Kobayashi–Maskawa (CKM) matrix, consisting of parameters that must be fixed by experiment.

There is no non-diagonal flavour structure in the last two terms because we have redefined the neutrino fields: $\nu_L \rightarrow L^{e\dagger} \nu_L$, absorbing the rotation of the e_L fields. This can be done with impunity due to the lack of neutrino mass terms. While the SM does not include neutrino mass terms, it has in fact been experimentally confirmed that neutrinos have mass. It is however known that these masses are extremely small in comparison to the scales of the SM ($m_\nu \lesssim 0.05 \text{ eV}$). Any lepton flavour-changing effect this could in principle have would be much smaller than the current sensitivity of any experiment, for example, $\mathcal{B}(\mu \rightarrow \tau \gamma) \simeq 10^{-34}$.

Another useful redefinition is to collect the left-handed and right-handed fermion fields into Dirac spinors ψ :

$$\psi = \psi_L + \psi_R, \psi_L = \frac{1}{2} (1 - \gamma^5) \psi, \psi_R = \frac{1}{2} (1 + \gamma^5) \psi \quad (2.12)$$

In terms of Dirac spinors, $\mathcal{L}_{\text{FCCC}}$ can be written as

$$\mathcal{L}_{\text{FCCC}} = \frac{e}{\sqrt{2} \sin \theta_W} \left(V_{ij} J_\mu^{ij} W^{+\mu} + V_{ij}^* J_\mu^{ij\dagger} W^{-\mu} + L_\mu^{ii} W^{+\mu} + L_\mu^{ii\dagger} W^{-\mu} \right), \quad (2.13)$$

$$L_\mu^{ij} = \frac{1}{2} (\bar{\nu}^i \gamma_\mu e^j - \bar{\nu}^j \gamma_5 \gamma_\mu e^i), \quad (2.14)$$

$$J_\mu^{ij} = \frac{1}{2} (\bar{u}^i \gamma_\mu d^j - \bar{u}^j \gamma_5 \gamma_\mu d^i) \equiv V_\mu^{ij} - A_\mu^{ij}. \quad (2.15)$$

J_μ^{ij} is known as the Flavour-Changing Charged Current (FCCC). It is often broken up into the *vector* and *axial-vector* components, V_μ and A_μ respectively, since these two components can be categorised according to their transformations under the Lorentz group. V_μ is labelled 1^+ , where the 1 represents its total spin, and the + represents its positive parity $P : V_\mu \rightarrow V_\mu$. A_μ is instead labelled 1^- , due to its negative parity $P : A_\mu \rightarrow -A_\mu$.

We can now turn to the physical consequences of $\mathcal{L}_{\text{FCCC}}$. The interactions given in this part of the Lagrangian describe a quark changing flavour while emitting a W^\pm boson. The propensity for flavour i to decay into another flavour j is governed in part by energy constraints and in part by the associated CKM element V_{ij} . These interactions at the quark level mediate meson decays, namely leptonic and semileptonic decays, described in section 2.2.2.

The deviation of V_{ij} from a unit matrix breaks some of the symmetries of the SM. $\mathcal{L}_{\text{SM}} - \mathcal{L}_{\text{FCCC}}$ has the property that one can independently rephase each of the quark fields, $q_i \rightarrow e^{i\theta_i} q_i$, a global $U(1)$ symmetry for each quark flavour. This implies, via Noether's theorem, that the number of quarks of each flavour, N_i , is conserved. However, $\mathcal{L}_{\text{FCCC}}$ breaks this symmetry $U(1)^6 \rightarrow U(1)$, where there is only a remnant symmetry of transforming all flavours by the same phase. Individual quark flavour number is no longer conserved, but overall quark number is.

Since there is no off-diagonal flavour structure for the Leptons, the equivalent global $U(1)^6$ symmetry for the leptons survives in the SM, and individual lepton flavour number is conserved. This property of the SM is referred to as lepton flavour universality.

2.2.1 The CKM Matrix

The exact values of the CKM matrix elements are of interest in the search for new physics. The CKM matrix is unitary by construction, however, if we were to discover that the values we measure experimentally do not combine to produce a unitary matrix, this would be evidence that the elements we are measuring, in fact,

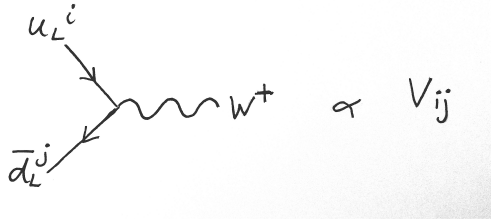


Figure 2.1: The flavour-changing charged current vertex.

compose a submatrix of a unitary matrix larger than 3×3 . This would imply the presence of further, heavier quark generations.

The CKM contains 3 real parameters and 1 complex phase. There is only one complex phase since we can freely redefine the phases of the quark fields in order to absorb the majority of the phases in the CKM. A common parameterisation is

$$V = \begin{pmatrix} 1 & 0 & 0 \\ 0 & \cos \theta_{23} & \sin \theta_{23} \\ 0 & -\sin \theta_{23} & \cos \theta_{23} \end{pmatrix} \begin{pmatrix} 1 & 0 & \sin \theta_{12} e^{i\delta} \\ 0 & 1 & 0 \\ -\sin \theta_{13} e^{i\delta} & 0 & \cos \theta_{13} \end{pmatrix} \begin{pmatrix} \cos \theta_{12} & \sin \theta_{12} & 0 \\ -\sin \theta_{12} & \cos \theta_{12} & 0 \\ 0 & 0 & 1 \end{pmatrix}. \quad (2.16)$$

A useful parameterisation for understanding the relative sizes of the CKM elements is due to Wolfenstein. Define the Wolfenstein parameter $\lambda = \sin \theta_{12}$, which is known experimentally to be around $\lambda \simeq 0.22$. Then $\cos \theta_{12} = \sqrt{1 - \sin^2 \theta_{12}} = \sqrt{1 - \theta^2} \simeq 1 - \lambda^2/2$. Observing then that $\sin \theta_{23} \sim 0.04 \simeq \lambda^2$ and $\sin \theta_{13} \sim 0.004 \simeq \lambda^3/3$, we can write the matrix as

$$V \simeq \begin{pmatrix} 1 - \frac{1}{2}\lambda^2 & \lambda & \frac{1}{3}\lambda^3 e^{i\delta} \\ -\lambda & 1 - \frac{1}{2}\lambda^2 & \lambda^2 \\ \lambda^3(1 - \frac{1}{3}e^{i\delta}) & -\lambda^2 & 1 \end{pmatrix} = \begin{pmatrix} \mathcal{O}(1) & \mathcal{O}(\lambda) & \mathcal{O}(\lambda^3) \\ \mathcal{O}(\lambda) & \mathcal{O}(1) & \mathcal{O}(\lambda^2) \\ \mathcal{O}(\lambda^3) & \mathcal{O}(\lambda^2) & \mathcal{O}(1) \end{pmatrix} \quad (2.17)$$

There is a clear hierarchy between the values - the CKM matrix is close to the unit matrix. Inter-generational mixing is dominant, dropping from second to first generation is suppressed by λ , dropping from third to second by λ^2 , and dropping from third to first by λ^3 . The SM supplies no compelling explanation of why this hierarchy exists, it is expected that new physics beyond the SM will supply some natural explanation.

The assumption of unitarity in V ,

$$V_{ji}^* V_{jk} = \delta_{ik}, \quad (2.18)$$

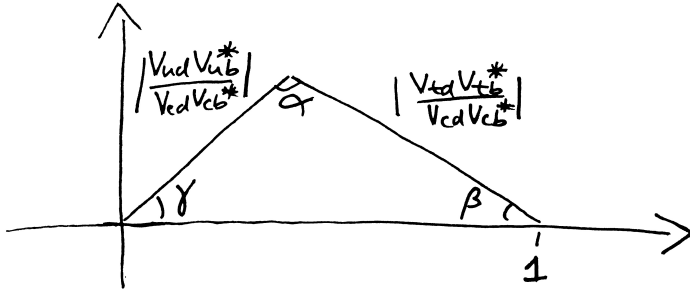


Figure 2.2: A sketch of the unitarity triangle.

imposes 9 constraints on the CKM elements. Each of these constraints gives a test of the SM, if one of these constraints is found to be violated, this represents evidence of new physics. The most studied constraint is given by taking $i = 3, k = 1$;

$$\frac{V_{ud} V_{ub}^*}{V_{cd} V_{cb}^*} + \frac{V_{td} V_{tb}^*}{V_{cd} V_{cb}^*} + 1 = 0. \quad (2.19)$$

This can be visualized as a triangle (known as the *unitarity triangle*) on the complex plane, as shown in figure 2.2.

For unitarity, the triangle must close, in other words, $\alpha + \beta + \gamma = \pi/2$. Hence to test the CKM unitarity experimentalists measure these angles

$$\alpha = \arg\left(-\frac{V_{td} V_{tb}^*}{V_{ud} V_{ub}^*}\right), \beta = \arg\left(-\frac{V_{cd} V_{cb}^*}{V_{td} V_{tb}^*}\right), \gamma = \arg\left(-\frac{V_{ud} V_{ub}^*}{V_{cd} V_{cb}^*}\right). \quad (2.20)$$

The unitarity triangle also contains information about CP-violation from flavour-changing charged currents. The so-called Jarlskog invariant, $J = \sin \theta_{12} \sin \theta_{23} \sin \theta_{31} \cos \theta_{12} \cos \theta_{23} \cos \theta_{31}^2 \sin \delta$, a measure of CP-violation, is proportional to the area enclosed by the triangle.

The most recent PDG update [1] reports the following averages for the measurements of CKM elements;

$$|V| = \begin{pmatrix} 0.97446 \pm 0.00010 & 0.22452 \pm 0.00044 & 0.00365 \pm 0.00012 \\ 0.22438 \pm 0.00044 & 0.97359^{+0.00010}_{-0.00011} & 0.04214 \pm 0.00076 \\ 0.00896^{+0.00024}_{-0.00023} & 0.04133 \pm 0.00074 & 0.999105 \pm 0.000032 \end{pmatrix}. \quad (2.21)$$

The averages given here are consistent with unitarity in all available tests. The angles of the unitarity triangle currently satisfy $\alpha + \beta + \gamma = (180 \pm 7)^\circ$. Increasing the precision of CKM determinations are necessary to provide more stringent tests of CKM unitarity.

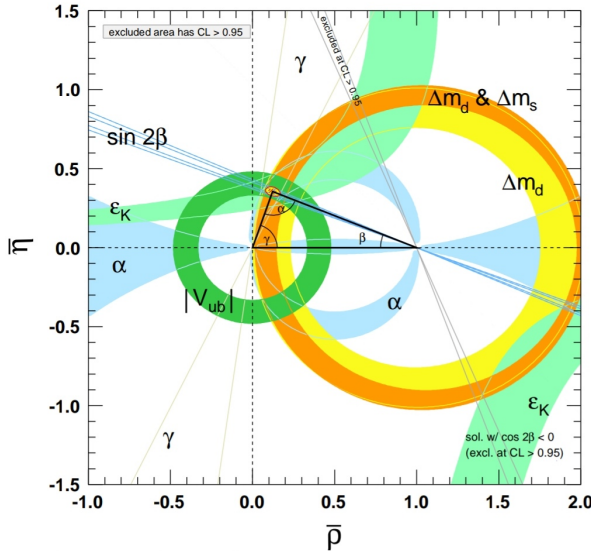


Figure 2.3: Exclusion regions for the vertices of the CKM triangle from various measurements, courtesy of the most recent PDG update [1].

2.2.2 Weak Decays

We now move on to the methods of determining CKM elements. At the confinement scale ($\sim 1\text{GeV}$ and below), quarks are confined by QCD in hadrons. At these energies, the dynamics of quarks are only experimentally accessible by probing the dynamics of hadrons. CKM matrix elements are determined by studying hadron decays.

First a word on hadrons. Hadrons are broadly categorized into mesons (charged with one valence quark and one valence antiquark) and baryons (three valence quarks). The entirety of this thesis is concerned with mesons. Mesons are categorized in terms of the flavours they are charged under and their representations under the Lorentz group. We use the same notation as for the quantum numbers of the weak currents; L^\pm where L denotes spin and \pm denotes parity. In this thesis, we are concerned mostly with pseudoscalar (0^-) and vector (1^-) mesons.

Weak decays of mesons are categorized according to the final products:

- **Leptonic:** $\text{meson} \rightarrow \text{leptons}$.
- **Semileptonic:** $\text{meson} \rightarrow \text{meson} + \text{leptons}$.
- **Hadronic:** $\text{meson} \rightarrow \text{mesons}$.
- **Oscillation:** $\text{meson} \rightarrow \text{meson}$.

All of these types of decay are dependent on CKM elements so can in principle

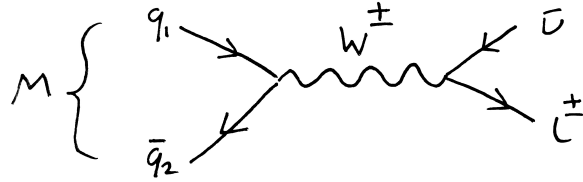


Figure 2.4: Leptonic decay of meson M at tree level in the electroweak coupling.

to be used for studying them. We are most interested in the first two, leptonic and semileptonic, so will give detail of such decays here.

Fig. 2.4 shows a generic leptonic decay at tree level (in electroweak coupling, virtual quark and gluon lines are implicit). The corresponding amplitude is given by

$$\mathcal{M} = \left(\frac{ie}{\sqrt{2} \sin \theta_W} \right) V_{q_1 q_2} \langle l \bar{\nu} | L_\mu^l D_W^{\mu\nu} J_\nu^{q_1 q_2} | M \rangle, \quad (2.22)$$

where D_W is a free W^{+-} propagator, $|M\rangle$ is the ground state of the meson M , and $|l \bar{\nu}\rangle$ is a lepton-antineutrino state. We are using the notation $L_\mu^l = L_\mu^{kk}$, where l indexes the k th charged lepton. If the momentum of the meson, p^2 , is much smaller than the W mass squared, one can integrate out the dynamics of the W to move into the Fermi effective theory [4];

$$\begin{aligned} \left(\frac{ie}{\sqrt{2} \sin \theta_W} \right)^2 D_W^{\mu\nu}(p^2) &= \left(\frac{ie}{\sqrt{2} \sin \theta_W} \right)^2 \left(\frac{-ig^{\mu\nu}}{p^2 - M_W^2} \right) \\ &= \underbrace{\frac{i}{M_W^2} \left(\frac{ie}{\sqrt{2} \sin \theta_W} \right)^2 g^{\mu\nu}}_{\equiv -2\sqrt{2}G_F} + \mathcal{O}\left(\frac{p^2}{M_W^4}\right). \end{aligned} \quad (2.23)$$

Then \mathcal{M} can be factorised;

$$\mathcal{M} \simeq -2\sqrt{2}V_{q_1 q_2} \langle l \bar{\nu} | L_\mu^l | \Omega \rangle \langle \Omega | J_\mu^{q_1 q_2} | M \rangle. \quad (2.24)$$

$\langle \Omega | J_\mu^{q_1 q_2} | M \rangle$ is a non-perturbative quantity, since it concerns the transitions of a strongly coupled bound state (QCD at the confinement scale). We know that it has a lorentz index μ , and the only Lorentz vector in the system is the meson's 4-momentum p_μ . So we define

$$\langle \Omega | J_{q_1 q_2}^\mu | M \rangle = p^\mu f_M, \quad (2.25)$$

where f_M is a Lorentz invariant known as the *decay constant* of the meson M , and encodes all non-perturbative information in the amplitude.

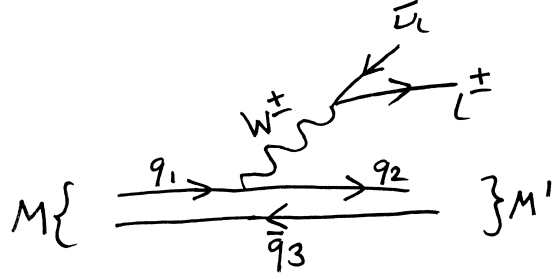


Figure 2.5: Semileptonic decay, $M \rightarrow M' l \bar{\nu}$, at tree level in electroweak coupling.

By taking the modulus squared of \mathcal{M} , and integrating over all allowed momenta of the final state, one finds the decay rate of the process;

$$\Gamma(M \rightarrow l \bar{\nu}) = \frac{G_F^2}{8\pi} f_M^2 m_l^2 M_M \left(1 - \frac{m_l}{M_M^2}\right)^2 |V_{q_1 q_2}|^2, \quad (2.26)$$

In order to find $|V_{q_1 q_2}|$, one requires both a measurement of $\Gamma(M \rightarrow l \bar{\nu})$, and a value for f_M . f_M can be computed in a Lattice QCD calculation.

A similar story accompanies semileptonic decays. At tree level in the electroweak coupling, a typical semileptonic decay is depicted in fig. ???. The amplitude is given by

$$\begin{aligned} \mathcal{M} &= \left(\frac{ie}{\sqrt{2} \sin \theta_W} \right) V_{q_1 q_2} \langle M', l \bar{\nu} | J_\mu^{q_1 q_2} D_W^{\mu\nu} L_\nu^l | M \rangle \\ &\simeq -2\sqrt{2} G_F V_{q_1 q_2} \langle M', l \bar{\nu} | J_\mu^{q_1 q_2} L^l{}^\mu | M \rangle \\ &\simeq -2\sqrt{2} G_F V_{q_1 q_2} \langle l \bar{\nu} | L^l{}^\mu | \Omega \rangle \langle M' | J_\mu^{q_1 q_2} | M \rangle, \end{aligned} \quad (2.27)$$

where on the second line we have integrated out the W propagator in using the same expansion as in the leptonic case, and on the third line we have factorised the QCD part from the electroweak part. The matrix element $\langle M' | J_\mu^{q_1 q_2} | M \rangle$ is a non-perturbative quantity. Unlike in the previous case, there are a number of ways one can choose to parameterise this matrix element, and appropriate choices vary depending on the quantum numbers of M and M' . Of interest to us are the cases where M is a pseudoscalar meson 0^- , and M' is either pseudoscalar or vector 1^- .

In the **pseudoscalar**→**pseudoscalar** case, only the vector component of the current survives in the matrix element, $\langle M' | J_\mu^{q_1 q_2} | M \rangle = \langle M' | V_\mu^{q_1 q_2} | M \rangle$. $\langle M' | A_\mu^{q_1 q_2} | M \rangle$ vanishes since this does not respect the parity invariance of QCD. The most popular parameterisation of $\langle M' | V_\mu^{q_1 q_2} | M \rangle$ is

$$\langle M' | V_\mu^{q_1 q_2} | M \rangle = f_+(q^2) \left[P_\mu + p_\mu - \frac{M^2 - m^2}{q^2} q_\mu \right] + f_0(q^2) \frac{M^2 - m^2}{q^2} q_\mu. \quad (2.28)$$

M, P_μ are the M -meson mass and momentum, m, p_μ are the M' -meson mass and momentum. $f_0(q^2)$ and $f_+(q^2)$, known as the scalar and vector form factors, encoding all non-perturbative information. We now have non-perturbative functions of q^2 rather than a single number. $q^2 = (P - p)^2$, the momentum carried away from the meson by the W , has an allowed range of values if the final states are on-shell;

$$m_l^2 \leq q^2 \leq (M - m)^2. \quad (2.29)$$

By integrating $|\mathcal{M}|^2$ over all final lepton and neutrino momenta, one finds a differential decay rate,

$$\begin{aligned} \frac{d\Gamma}{dq^2}(M \rightarrow M' l \bar{\nu}) = & \eta_{\text{EW}} \frac{G_F^2 |V_{q_1 q_2}|^2}{24\pi^3 M^2} \left(1 - \frac{m_l^2}{q^2}\right)^2 |\mathbf{p}| \times \\ & \left[\left(1 + \frac{m_l^2}{2q^2}\right) M^2 |\mathbf{p}|^2 f_+^2(q^2) + \frac{3m_l^2}{8q^2} (M^2 - m^2)^2 f_0^2(q^2) \right]. \end{aligned} \quad (2.30)$$

η_{EW} accounts for electroweak corrections due to diagrams where photons or Z s are exchanged in addition to a W^- , as well as the Coulomb attraction of the final-state charged particles [5–7]. \mathbf{p} is the final meson state (M') spacial momentum. Once again, to deduce $|V_{q_1 q_2}|$, one requires both the decay rates $d\Gamma/dq^2$, and the form factors $f_0(q^2), f_+(q^2)$. To precisely determine the form factors requires a Lattice QCD calculation.

In the **pseudoscalar→vector** case, both the vector and axial-vector components of the current survive in the matrix element. A common choice of parameterisation is

$$\langle M'(\epsilon) | V_{q_1 q_2}^\mu | M \rangle = i\sqrt{Mm} h_V^s(w) \epsilon_{\mu\nu\alpha\beta} \epsilon^{*\nu} v'^\alpha v^\beta, \quad (2.31)$$

$$\langle M'(\epsilon) | A_{q_1 q_2}^\mu | M \rangle = \sqrt{Mm} [h_{A_1}^s(w)(w+1)\epsilon_\mu^* -$$

$$h_{A_2}^s(w) \epsilon^* \cdot v v_\mu - h_{A_3}^s(w) \epsilon^* \cdot v v'^\mu].$$

$v = P/M$ and $v' = p/m$ are the 4-velocities of M and M' respectively. ϵ is the polarization of the vector meson M' . $w = v \cdot v'$ is known as the recoil parameter, this is an alternative to q^2 often used in heavy quark effective theory. $h_V(w), h_{A_0}(w), h_{A_1}(w)$, and $h_{A_2}(w)$ are the form factors accounting for the non-perturbative physics. The decay rate is given by

$$\frac{d\Gamma}{dw}(M \rightarrow M' l \bar{\nu}) = \frac{G_F^2 m^3 |\eta_{\text{EW}} V_{q_1 q_2}|^2}{4\pi^3} (M - m)^2 \sqrt{w^2 - 1} \chi(w) |\mathcal{F}(w)|^2, \quad (2.33)$$

where $\mathcal{F}(w)$ is a linear combination of the form factors and $\chi(w)$ is a known function of w (both given in e.g. appendix G of [8]).

At the zero recoil point, where q^2 is maximized at $q_{\max}^2 = (M - m)^2$, (corresponding to $w = 1$), a single form factor contributes

$$\mathcal{F}(1) = h_{A_1}(1). \quad (2.34)$$

However the differential decay rate vanishes at $w = 1$. A common approach to determine $|V_{q_1 q_2}|$, for example used to find $|V_{cb}|$ via the $B \rightarrow D^* l \bar{\nu}$ decay, is to find $|\mathcal{F}(1)V_{cb}|^2$ at zero recoil by extrapolating from experimental data at non-zero recoil, and combining this with a lattice QCD determination of $h_{A_1}(1)$.

2.2.3 $b \rightarrow c$ Transitions and $|V_{cb}|$

The family of weak decays that have attracted the most attention are decays of B mesons (pseudoscalar mesons containing a valence b and u, d, s or c quark). B mesons decay into a rich variety of decay products. It is the heaviest quark flavour that can be found in hadrons (the only heavier quark, the top quark, has a mass far above the confinement scale, so does not feature as a valence quark in hadrons).

The b can decay into either a c or a u quark via the flavour changing charged current. In this thesis we are interested in the $b \rightarrow c$ transition, with an amplitude proportional to the CKM element $|V_{cb}|$. In this section, we give a brief overview of how this is calculated and the value's current status.

B meson decays can be measured in a number of experiments. There are two so-called b -factories, the Belle (II) experiment at the KEKB collider in Japan, and the BaBar experiment at the PEP-II collider at SLAC laboratory in the US. These are $e^+ e^-$ colliders, that collide with an energy tuned to the mass of the $\Upsilon(4s)$, an excited state of the Υ meson (a 1^- state with $\bar{b}b$ valence quarks). The $\Upsilon(4s)$ has a large branching fraction into a $B\bar{B}$ pair, the decays of these can be measured with large statistics. B decays can also be measured in proton colliders, like at the LHCb experiment at CERN. Measurements from LHCb have poorer statistics but cover a larger range of the phase space of final states, due to the variance of momenta in the initial state protons.

So far 3 approaches to determining $|V_{cb}|$ have been carried out:

- $B \rightarrow D^* l \bar{\nu}$ decay rate measurements are extrapolated to zero recoil to determine $|V_{cb} h_{A_1}(1)|$. Then dividing out $h_{A_1}(1)$ from a Lattice calculation, one finds $|V_{cb}|$.
- $B \rightarrow D l \bar{\nu}$ decay rates are measured throughout q^2 , and combined with $f_0(q^2)$ and $f_+(q^2)$ from lattice calculations.

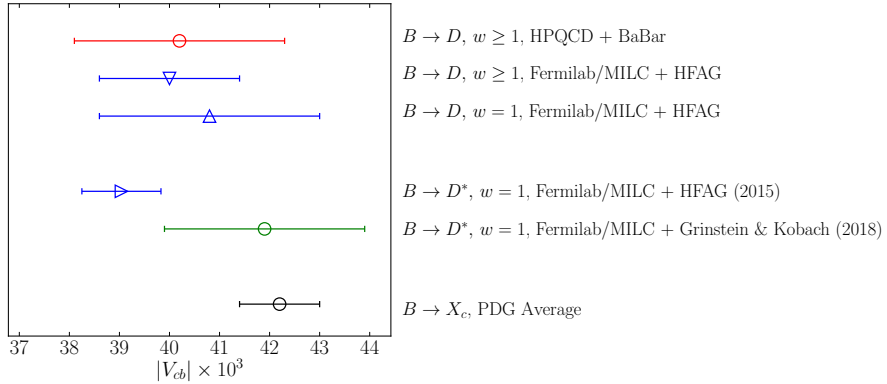


Figure 2.6: Different determinations of $|V_{cb}|$. Points labelled $w = 1$ are determinations from extrapolating measurements of decay rates to the zero recoil point, and combining them with a lattice determination of the form factor at zero recoil. Points labelled $w \geq 1$ are results from using a combination of both branching fractions and lattice form factors through some range of w . The first name mentioned in the labels give the source of the lattice form factors, and the second gives the source of the experimental data (e.g. the HPQCD+BaBar point used form factors from the HPQCD collaboration and data from the BaBar experiment). The highest point is from [11], the second and third highest from [12], fourth from [13], fifth from [14]. The bottom point is from the PDG [1], using data from the ALPEPH [15], Belle [16], BaBar [17, 18], and CLEO [19] experiments.

- $B \rightarrow X_c l \bar{\nu}$ decay rates are measured (where X_c is all possible charmed final state mesons), this is used to constrain elements in the operator product expansion, a method first devised in [9, 10].

The first two are referred to as *exclusive* and the third *inclusive*. A selection of the most accurate examples of each method of determination is given in figure 2.6.

This figure tells a story of the recent history of $|V_{cb}|$. Determinations from $B \rightarrow D l \bar{\nu}$ have been consistent but not as precise as via the other two methods. Until recently, there was a 3σ tension between determinations from the $B \rightarrow D^* l \bar{\nu}$ decay and inclusive decays. This was on its way to being resolved when concern was raised about the method of extrapolating experimental data for $B \rightarrow D^* l \bar{\nu}$ decay rates to the zero recoil point ($w = 1$).

The Heavy Flavour Averaging Group HFAG (Now HFLAV) determination of $|V_{cb} h_{A_1}(1)|$ in 2015 parameterised the form factors in the extrapolation using the CLN parameterisation (defined in section ?). It has become clear that the con-

straints the CLN parameterisation imposes on the form factors are not justified. In [14, 20], the results of an extrapolation using the CLN parameterisation were compared to results from a more general, model-independent parameterisation, the BGL parameterisation. It was found that they differed by 3.5σ . Since the BGL makes fewer assumptions, one may consider this the more reliable result.

The $|V_{cb}|$ result using BGL to extrapolate the decay rates is given in the green point on fig. 2.6. Hence, if this work is to be trusted, the long-standing $|V_{cb}|$ tension has been resolved.

There are however a number of other reasons to be interested in studying $|V_{cb}|$, namely improving its precision. It is currently the least precisely determined element of the CKM matrix. It constrains one side of the unitarity triangle via the ratio $|V_{ub}|/|V_{cb}|$, so it is the bottleneck for precise tests of CKM unitarity. It is also a dominant uncertainty in the determination of the CP -violation parameter ϵ_K (that is currently at tension between the SM and experiment, see for example [21] where a 4σ tension is reported).

2.2.4 Flavour Anomalies & Lepton Flavour Violation

The SM can be tested by studying semileptonic decays more directly, without any consideration of CKM elements. CKM-independent observables can be constructed by taking ratios of branching fractions for decays with common CKM dependence. Then, form factors from lattice QCD can be used to form pure SM predictions of these ratios, and compared to purely experimental measurements. Such comparisons have uncovered a number of tensions between the SM and experiment.

The ratios are defined by

$$R_{X_q} = \frac{\Gamma(B_q \rightarrow X_q \tau \nu_\tau)}{\frac{1}{2} [\Gamma(B_q \rightarrow X_q e \nu_e) + \Gamma(B_q \rightarrow X_q \mu \nu_\mu)]}, \quad (2.35)$$

where X_q is any meson with valence quark content $x\bar{q}$. The numerator and denominator will have the same power of $|V_{bx}|$, so cancel in the ratio.

There is currently tension between SM and experiment in R_D and R_{D^*} .

$$R_{D^*}|_{\text{exp}} = 0.306(13)_{\text{stat}}(07)_{\text{sys}} , \quad R_{D^*}|_{\text{SM}} = 0.252(3) \quad (2.36)$$

$$R_D|_{\text{exp}} = 0.407(39)_{\text{stat}}(24)_{\text{sys}} , \quad R_D|_{\text{SM}} = 0.300(8). \quad (2.37)$$

The experimental values are the HFLAV averages, from BaBar [22,23], Belle [24–27], and LHCb [28–30] data. The $R_{D^*}|_{\text{SM}}$ number is from [31]. $R_D|_{\text{SM}}$ is an average of Lattice results from the HPQCD [11] and FNAL/MILC collaborations [12].

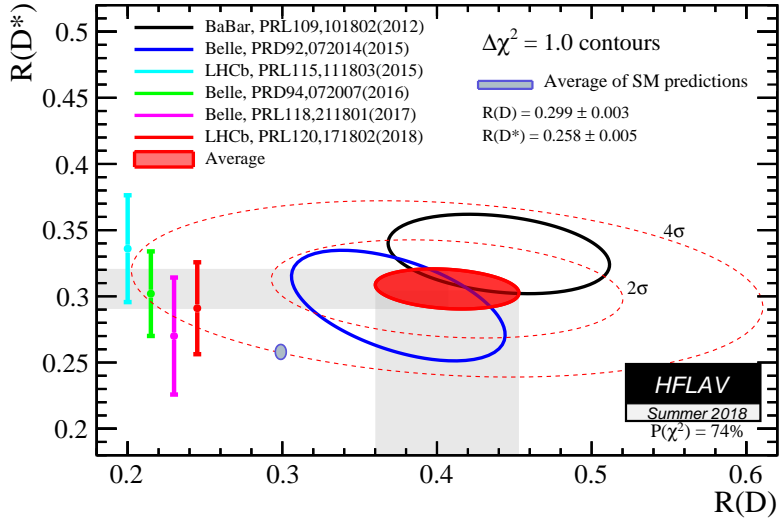


Figure 2.7: $R(D^{(*)})$ determinations from SM and measurement [2]

A joint analysis of R_D and R_{D^*} by HFLAV shows the combined tension to have a significance of 4.0σ (see fig. 2.7). Clearly more precise experimental results are necessary to either confirm or dismiss this anomaly. While the SM values are currently much more precise than the experimental ones, further work on the theoretical results is necessary. More independent calculations are required to make the SM numbers more robust, so that, if this tension ever hits 5σ , we can be confident that it is due to new physics.

There are also tensions in the quantities [32]

$$R_{K^{(*)}} = \frac{\Gamma(B \rightarrow K^{(*)}\mu^+\mu^-)}{\Gamma(B \rightarrow K^{(*)}e^+e^-)}. \quad (2.38)$$

LHCb measured R_K between 1 and 6 GeV, and found a disagreement with the SM value [33,34] of 2.6σ [35]. LHCb also measured R_{K^*} in 2 bins ($0.045 < q^2 < 1.1 \text{ GeV}^2$ and $1.1 < q^2 < 1.6 \text{ GeV}^2$), and reported disagreement with the SM prediction [36–43] of $2.1\text{--}2.3\sigma$ and $2.4\text{--}2.5\sigma$ respectively [44].

Each of these anomalies points to one potential new physics scenario: lepton flavour violation (LFV), a breakdown of the lepton flavour universality in the SM discussed in Sec. 2.2. A consequence of LFV would be that the different leptons generations would no longer have the same coupling to gauge fields. For example, imagine couplings like $U_{ij}\bar{e}_L^i W^+ \nu_L^j$, where U_{ij} is unitary but non-diagonal, then the different lepton generations would have different couplings to W . This can lead to a

modification of the $B \rightarrow D^{(*)}l\nu$ and $B \rightarrow K^{(*)}\bar{l}l$ decays rates by different amounts depending on the lepton flavours in the final state, resulting in the ratios $R_{D^{(*)}}$, $R_{K^{(*)}}$ deviating from the SM prediction.

There are broadly speaking two ways one can explain LFV. The first is to posit that there are in fact right-handed neutrinos, ν_R , and neutrinos have Dirac mass terms $m\bar{\nu}_L\nu_R$, from their coupling with the Higgs, just like the charged leptons and quarks. Then, the argument preventing the presence of non-trivial lepton flavour structure in $\mathcal{L}_{\text{FCCC}}$ breaks down, we obtain an equivalent of the CKM matrix for leptons (the Pontecorvo-Maki-Nakagawa-Sakata (PMNS) matrix), and lepton flavour violation is mediated by the W . Neutrinos have in fact already been shown to have mass, the PMNS matrix exists, and its elements have been measured. However, as mentioned already, these effects would be extremely small due to the extreme lightness of the neutrinos. Experiments have looked for evidence of W -mediated LFV processes, $\tau \rightarrow \mu\gamma$ and $\mu \rightarrow e\gamma$, and they found upper bounds for their branching fractions of 4.2×10^{-13} [45] and 3.1×10^{-7} [46] respectively.

Besides there being no evidence for W -mediated LFV, this picture of neutrino masses is not very aesthetically satisfying. It requires unnaturally small Yukawa couplings between the Higgs and the neutrinos. The second, and much more popular approach, to explaining both LFV and neutrino masses, is the presence of new physics.

In the face of evidence against the SM, the most general way to parameterise the space of possible new physics models is to study the Standard Model Effective Theory (SMEFT). In this approach, one introduces a higher dimension, non-renormalisable operators to the standard model (the SM has only renormalisable dimension 4 operators), and impose a hard momentum cutoff Λ . Then, the SMEFT is

$$\mathcal{L}_{\text{SMEFT}} = \mathcal{L}_{\text{SM}} + \sum_i \frac{c_i^{(5)}}{\Lambda} \mathcal{O}_i^{(5)} + \sum_i \frac{c_i^{(6)}}{\Lambda^2} \mathcal{O}_i^{(6)} + \dots \quad (2.39)$$

where $\mathcal{O}_i^{(d)}$ is the set of dimension- d operators that satisfy the symmetries of the SM, and $c_i^{(d)}$ are coefficients to be measured, known as Wilson coefficients. Wilson coefficients differing from the SM expectation can be evidence that the SM must be augmented with new fields at energies above Λ , and the quantum numbers of the associated operators gives information about the quantum numbers of the new fields.

One can fit the available $B \rightarrow D^{(*)}l\bar{\nu}$ and $B \rightarrow K^{(*)}\bar{l}l$ data to predictions from

SMEFT, in order to infer the Wilson coefficients necessary to explain the anomalies. In [47] it was found that $R_{D(*)}$ can be explained with the $d = 6$ operators

$$\begin{aligned} (\bar{c}\gamma_\mu P_L b)(\bar{\tau}\gamma^\mu P_L \nu_\tau), \quad (\bar{c}\sigma^{\mu\nu} P_L b)(\bar{\tau}\sigma_{\mu\nu} P_L \nu_\tau), \quad (\bar{\tau}P_L c^c)(\bar{b}^c P_L \nu_\tau), \\ (\bar{\tau}\gamma_\mu P_R b)(\bar{c}\gamma^\mu P_L \nu_\tau), \quad (\bar{\tau}\gamma_\mu P_L b)(\bar{c}\gamma^\mu P_L \nu_\tau), \quad (\bar{\tau}P_R c^c)(\bar{b}^c \gamma^\mu P_L \nu), \end{aligned} \quad (2.40)$$

where $P_{L/R} = (1 \pm \gamma_5)/2$, $\psi^c = -i(\bar{\psi}\gamma^0\gamma^2)^T$ and $\bar{\psi}^c = -i(\gamma^0\gamma^2\psi)^T$. In [32], a similar process found the operators necessary to explain $R_{K(*)}$:

$$\begin{aligned} (\bar{s}\gamma_\mu P_L b)(\bar{e}\gamma^\mu e), \quad (\bar{s}\gamma_\mu P_L b)(\bar{\mu}\gamma^\mu \mu) \\ (\bar{s}\gamma_\mu P_L b)(\bar{e}\gamma^\mu \gamma_5 e), \quad (\bar{s}\gamma_\mu P_L b)(\bar{\mu}\gamma^\mu \gamma_5 \mu) \end{aligned} \quad (2.41)$$

This information, along with constraints from other measurements, strongly reduces the space of possible new physics models that could produce these anomalies. Hot topics include Leptoquarks, Z' models, and partial compositeness [32, 47–49].

2.3 Strong Interaction Physics

The work of this thesis is essentially quantifying the effect the strong interaction has on branching fractions for semileptonic decays. The strong interaction and the observed pattern of hadrons can be explained with Quantum Chromodynamics (QCD). In this section we review the fundamental theory, and the force's physical features.

2.3.1 Quantum Chromodynamics

QCD is an $SU(3)$ Yang-Mills gauge theory. The Lagrangian is derived by requiring:

- N_f fermion fields transforming in the fundamental representation of the $SU(3)_C$ gauge group.
- Invariance under that gauge group.
- Renormalizability of all interactions.

From these we find [50]

$$\mathcal{L}_{\text{QCD}} = \sum_i \bar{q}_i (iD^\mu - m_i) q_i - \frac{1}{4} \text{Tr} G_{\mu\nu} G^{\mu\nu} - g \frac{\bar{\theta}}{64\pi^2} \epsilon^{\mu\nu\rho\sigma} \text{Tr} G_{\mu\nu} G_{\rho\sigma} \quad (2.42)$$

$$D_\mu = \partial_\mu - igG_\mu, \quad G_{\mu\nu} = [D_\mu, D_\nu].$$

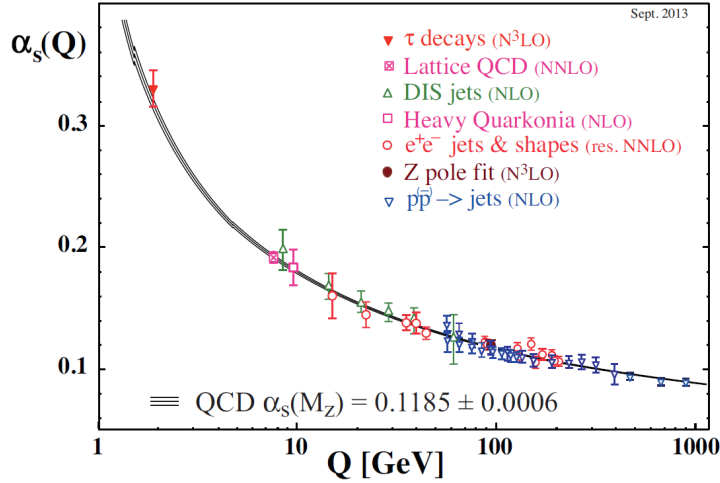


Figure 2.8: The relationship between scale Q and the strong coupling constant α_s , from the PDG [1].

$q_i = (q_{i,r}, q_{i,b}, q_{i,g})$ are the N_f fermions, vectors in *color space*, transforming under

$$q_i(x) \rightarrow \Lambda(x)q_i(x), \bar{q}_i(x) \rightarrow \bar{q}_i(x)\Lambda^\dagger(x), \quad (2.43)$$

where $\Lambda(x)$ is an $SU(3)$ matrix acting on color the color space. G_μ are the $\mathfrak{su}(3)$ -valued gluon fields, transforming under the Gauge group like

$$G_\mu(x) \rightarrow \Lambda(x)G_\mu(x)\Lambda^\dagger(x) - \frac{i}{g}[\partial_\mu\Lambda(x)]\Lambda^\dagger(x). \quad (2.44)$$

g is the coupling constant of the theory, often expressed instead as $\alpha_s = (g/4\pi)^2$. $\bar{\theta}$ has strong experimental bounds on it's size, to the extent that for our purposes it can be neglected [51].

The most notable feature of QCD is due to the running of the QCD coupling α_s [52]. In contrast with the electroweak force, the coupling of the strong force diverges at low energies. This is referred to as *asymptotic freedom*. At energies around or below $\Lambda_{\text{QCD}} \sim 0.5\text{GeV}$, α_s becomes too large to be a good expansion parameter, and perturbation theory becomes unreliable for making predictions.

At large α_s , quarks and gluons become strongly interacting, this is believed to be the source of confinement, the mechanism that bounds quarks together into hadrons.

Broadly speaking there are two approaches to QCD at low energies:

1. Chiral Perturbation theory - an effective theory of hadrons with the same symmetry properties as QCD.

2. Lattice simulations - solve the path integral by brute force, eliminating the need for an expansion in α_s . This is covered in chapters 3 and 4, since it is the method used in the work presented in this thesis.

2.3.2 Chiral Symmetry

In the limit of $m_i \rightarrow 0 \forall i$, QCD develops two new global symmetries between the flavours;

$$q_i \rightarrow \exp(i\theta_a \lambda_a^{ij}) q_j \quad (2.45)$$

$$q_i \rightarrow \exp(i\gamma_5 \theta_a \lambda_a^{ij}) q_j \quad (2.46)$$

where λ_a are $U(N_f)$ matrices. They are labelled $U(N_f)_V$ and $U(N_f)_A$ respectively, standing for vector and axial-vector.

Via Noether's theorem, these symmetries imply currents that are conserved in the massless limit [53];

$$V_\mu^a = \bar{q} \gamma_\mu \lambda_a q \quad , \quad A_\mu^a = \bar{q} \gamma_\mu \gamma_5 \lambda_a q \quad (2.47)$$

The way in which the chiral symmetry is realised in quantum mechanics is captured by the *Ward identities*. There is an infinite number of possible Ward identities, but for the purpose of our work, we only need to consider the most simple of them.

Consider the partition function for QCD:

$$\mathcal{Z} = \int [d\psi d\bar{\psi} dA] e^{iS[\psi, \bar{\psi}, A]}, \quad (2.48)$$

where $[d\psi d\bar{\psi} dA]$ represents the functional integral over quark, antiquark and gauge fields. Consider performing a shift of the integration variables of the form (2.45), and allow the parameters θ_a to be local, $\theta_a = \theta_a(x)$. The partition function becomes

$$\mathcal{Z} = \int \mathcal{J}[d\psi d\bar{\psi} dA] (1 + i\delta S) e^{iS[\psi, \bar{\psi}, A]} \quad (2.49)$$

\mathcal{J} is the Jacobian of the measure $[d\psi d\bar{\psi} dA]$ under the coordinate transform (2.45). In many cases, \mathcal{J} will be non-trivial, due to either regularization schemes that don't respect the symmetry or quantum anomalies. The symmetries we are concerned with here are anomaly free, so $\mathcal{J} = 1$.

The effect of the local version of (2.45) on the action is

$$\delta S = \int d^4x \theta_a(x) [\partial_\mu V_a^\mu(x) - i\bar{q}(x)[\lambda_a, M]q(x)], \quad (2.50)$$

where $M = \text{diag}(m_u, m_d, m_s, \dots)$ acts on flavour. Setting the arbitrary parameters $\theta_a(x)$ to 1 and removing \mathcal{Z} from each side of (2.49), and removing the spacetime integral $\int d^4x$ results in

$$\partial_\mu \langle V_a^\mu \rangle = i \langle \bar{q}[\lambda_a, M]q \rangle, \quad (2.51)$$

where $\langle \rangle$ represents a quantum expectation value, the state the expectation value is taken need not be specified since the above derivation does not assume any particular state. Repeating the above steps with the vector chiral transform replaced with the axial-vector chiral transform, one finds

$$\partial_\mu \langle A_a^\mu \rangle = i \langle \bar{q}\{\lambda_a, M\}q \rangle. \quad (2.52)$$

(2.51) and (2.52) are examples of Ward identities, they describe the non-conservation of the chiral currents.

A useful theorem [54] is that partially conserved currents (currents that become conserved when some parameter in the theory vanishes, like V_a^μ and A_a^μ) require no renormalisation under any regularisation scheme. The conserved or partially conserved current J_a^μ has a corresponding charge $Q_a(t) = \int d^3x J^0(\underline{x}, t)$ that is the generator of it's corresponding symmetry transform on Hilbert space. In this case, these charges are members of the Lie algebra of the symmetry group;

$$[Q_a(t), Q_b(t)] = if_{abc}Q_c(t), \quad (2.53)$$

where f_{abc} are the structure constants of the algebra. Under some regularisation, change in regularisation scheme, or running of scale, each operator in the theory may require multiplicative renormalisations; $Q_a \rightarrow Z_Q Q_a$. Equation (2.53) demands that $Z_Q = 1$, so J^0 obtains no renormalisation, and if the regularization is lorentz invariant, this carries on to J^μ .

Since one can transform any flavour into any other flavour via the chiral $U(N_f)$ generators, one can build currents charged with any combination of flavours from linear combinations of V_a^μ and A_a^μ ;

$$V_{ij}^\mu = \bar{q}_i \gamma^\mu q_j, \quad \partial_\mu \langle V_{ij}^\mu \rangle = i(m_i - m_j) \langle S_{ij} \rangle \quad (2.54)$$

$$A_{ij}^\mu = \bar{q}_i \gamma^\mu \gamma^5 q_j, \quad \partial_\mu \langle A_{ij}^\mu \rangle = i(m_i + m_j) \langle P_{ij} \rangle \quad (2.55)$$

where we have defined $S_{ij} = \bar{q}_i q_j$ and $P_{ij} = \bar{q}_i \gamma^5 q_j$, the scalar and pseudoscalar densities. The non-renormalisation of V_a^μ and A_a^μ carry on to V_{ij}^μ and A_{ij}^μ , and onto the operators $(m_i - m_j)S_{ij}$, $(m_i + m_j)P_{ij}$ via the Ward identities.

The partially conserved currents V_μ^{ij} and A_μ^{ij} are the same currents that feature in the matrix element of leptonic and semileptonic decays in Sec. 2.2, and their expectation values appear in amplitudes for leptonic and semileptonic decays. Hence, the fact that these can be related to alternative expectation values via ward identities, and that they obtain no renormalisation, is very useful in the calculation of these amplitudes.

2.4 Heavy Quark Physics

Quarks with mass $m_Q \gg \Lambda_{\text{QCD}}$ are referred to as heavy quarks. Charm and bottom quarks are considered heavy: $\Lambda_{\text{QCD}}/m_c \sim 1/4$, $\Lambda_{\text{QCD}}/m_b \sim 1/14$. This separation of scales can come in very useful. They mean one can integrate out the degrees of freedom at m_Q , and still have a good description of the dynamics at Λ_{QCD} . This philosophy gives rise to Heavy Quark Effective Theory (HQET). We will summarise the aspects of this theory most relevant to our work.

2.4.1 HQET

HQET is an effective field theory with the cutoff at the heavy quark mass m_Q , and terms organized in a series in Λ_{QCD}/m_Q . Since at the b (and c) mass QCD is perturbative ($\alpha_s(m_Q) \ll 1$), one can match HQET to perturbative QCD at m_Q , then run the couplings of HQET down to produce useful predictions at the confinement scale.

HQET Lagrangian

We will derive HQET for a single heavy quark interacting with gluons, the generalization to many flavours is straightforward. The fermion part of the Lagrangian is

$$\mathcal{L}_{\text{QCD}} = \bar{Q}(iD - m_Q)Q, \quad (2.56)$$

where Q is the heavy quark field. Define the heavy quark velocity v according to $v = p_Q/m_Q$. Split Q into ‘‘heavy’’ and ‘‘light’’ components:

$$Q = h + H \quad : \quad h = \frac{1}{2}e^{-im_Q v \cdot x}(1 + \not{v})Q \quad (2.57)$$

$$H = \frac{1}{2}e^{-im_Q v \cdot x}(1 - \not{v})Q \quad (2.58)$$

with the important property

$$\not{p}h = h \quad \not{p}H = -H. \quad (2.59)$$

In terms of these new fields the Lagrangian becomes

$$\mathcal{L}_{\text{QCD}} = i\bar{h}(v \cdot D)h - \bar{H}(i(v \cdot D) - 2m_Q)H + i\bar{h}\not{D}^\perp H + i\bar{H}\not{D}^\perp h. \quad (2.60)$$

where $v_\mu(v \cdot D)$ is the covariant derivative projected along the direction of v , and $D^\perp = D - v_\mu(v \cdot D)$ are the components perpendicular to v . A physical interpretation of the definition of h in (2.57) can be seen by acting a spacial derivative on the definition of h , and by recognising $\partial Q = -ip_Q$, $\partial h = -ip_h$, we find that

$$p_Q = m_Q v + p_h. \quad (2.61)$$

Since $p_h \ll p_Q$, we see that the quark's momentum is dominated by it's mass (the quark is close to on-shell), and the h field represents perturbations around on-shell due to interactions with the lighter degrees of freedom at Λ_{QCD} .

From (2.60), we see that h is a massless field and H has a mass of $2m_Q$. From this Lagrangian we can derive an equation of motion for H :

$$(i(v \cdot D) + 2m_Q)H = i\not{D}^\perp h, \quad (2.62)$$

with the solution

$$H = \frac{1}{i(v \cdot D) + 2m_Q}i\not{D}^\perp h = \frac{1}{2m_Q} \sum_{n=0}^{\infty} \frac{(-i(v \cdot D))^n}{2m_Q} \not{D}^\perp h. \quad (2.63)$$

By substituting this into the Lagrangian we arrive at

$$\mathcal{L}_{\text{HQET}} = i\bar{h}(v \cdot D)h - \bar{h}\not{D}^\perp \frac{1}{2m_Q} \sum_{n=0}^{\infty} \frac{(-i(v \cdot D))^n}{2m_Q} \not{D}^\perp h. \quad (2.64)$$

Since we expect $v \cdot D \sim \Lambda_{\text{QCD}}$, we can interpret the infinite sum as a series in Λ_{QCD}/m_Q , and truncate it at some order.

Leading order HQET exhibits new symmetries not present in full QCD, known as the heavy quark symmetries. Since m_Q is not present in the leading order Lagrangian, there is a flavour symmetry - a set of N heavy quarks with the same v can be mixed via an $SU(N)$ symmetry. Similarly, due to the absence of spin-mixing matrices, a heavy quark has an $SU(2)$ spin symmetry. This builds up a physical picture of a heavy quark in a meson being a static colour charge, the dynamics at Λ_{QCD} are not effected by its mass or spin.

We will now use HQET to derive a useful theorem used in our work.

Luke's Theorem

Luke's theorem, which can be derived from the Ademollo-Gatto (AG) theorem, tells us the leading order heavy quark mass dependence of form factors. First we will derive the AG theorem. We will follow the proof given in [55].

Consider the transition amplitude

$$\langle \alpha | Q_a | \beta \rangle, \quad (2.65)$$

where Q_a is a conserved charge associated with some global symmetry \mathcal{G} , and $|\alpha\rangle$ and $|\beta\rangle$ belong to an irrep of \mathcal{G} . Imagine explicitly breaking the symmetry with a term like $\mathcal{L}_{\text{break}} = \lambda \mathcal{O}_{\text{break}}$. The states in the broken theory can be expressed as

$$|\beta\rangle = c_{\beta\beta} |\beta'\rangle + \sum_m c_{\beta m} |m'\rangle \quad (2.66)$$

$$\langle \alpha | = c_{\alpha\alpha}^* \langle \alpha' | + \sum_n c_{\alpha n}^* \langle n' |. \quad (2.67)$$

where primed states are the new basis of states belonging to irreps of \mathcal{G} , after the breaking. Here $|m'\rangle$ can only be states that can be mixed with $|\beta\rangle$ by $\mathcal{O}_{\text{break}}$, i.e., via the broken dynamics of the theory. Similarly for $\langle n' |$ and $\langle \alpha |$. The transition amplitude becomes

$$\begin{aligned} \langle \alpha | Q_a | \beta \rangle &= c_{\alpha\alpha}^* c_{\beta\beta} \langle \alpha' | Q_a | \beta' \rangle \\ &+ \sum_m c_{\alpha\alpha}^* c_{\beta m} \langle \alpha' | Q_a | m' \rangle \\ &+ \sum_n c_{\alpha n}^* c_{\beta\beta} \langle n' | Q_a | \beta \rangle \\ &+ \sum_m \sum_n c_{\alpha n}^* c_{\beta m} \langle n' | Q_a | m' \rangle. \end{aligned} \quad (2.68)$$

The theorem applies to the situation where $|n'\rangle$ and $|m'\rangle$ live in different \mathcal{G} irreps to $|\alpha\rangle$ and $|\beta\rangle$ (we assume $|\alpha\rangle$ and $|\beta\rangle$ to be in the same irrep otherwise the transition amplitude would vanish). In this case the amplitudes in the second and third terms vanish. Now consider the order of the coefficients c_{nm} . We can assume that $c_{nm} = \mathcal{O}(\lambda)$ for arbitrary $n, m \neq \alpha, \beta$, since switching off the symmetry breaking by setting $\lambda = 0$ should cause $|\alpha\rangle$ and $|\alpha'\rangle$ to coincide. Then, using the normalization of the states $\sum_n |c_{\alpha n}|^2 = 1$, we find $c_{\alpha\alpha} = \sqrt{1 - \mathcal{O}(\lambda)^2} = 1 + \mathcal{O}(\lambda^2)$, and similarly for $c_{\beta\beta}$. Applying this to the two surviving terms in (2.68), we end up with

$$\langle \alpha | Q_a | \beta \rangle = 1 + \mathcal{O}(\lambda^2) \quad (2.69)$$

This is the AG theorem: if the current Q_a and the symmetry breaking term $\mathcal{O}_{\text{break}}$ act orthogonally on the states, the transition amplitude can have at most a second order correction in the symmetry breaking parameter.

Now we will apply this to HQET to produce Luke's theorem. Consider a transition including two heavy quarks (b and c). Then, the heavy quark symmetry is a spin symmetry for each flavour and a flavour symmetry between them. The leading order spin symmetry breaking terms can be found from (2.64) to be

$$\frac{1}{4m_Q} \bar{h} \gamma^\mu \gamma^\nu F_{\mu\nu} h. \quad (2.70)$$

for both $h = b$ and $h = c$. The leading order flavour breaking term is

$$\left(\frac{1}{2m_b} - \frac{1}{2m_c} \right) \frac{1}{2} \bar{h} \sigma_z \not{D}^{\perp 2} h, \quad (2.71)$$

where now $h = (b, c)$ and the σ_z is the third pauli matrix acting on flavour. These terms cause states, for example $|B\rangle$ to mix with states $|n'\rangle$, each being of the order of at least one of the following: $1/2m_b, 1/2m_c$, and $(1/2m_b - 1/2m_c)$. It can be shown [55] that the leading order symmetry breaking terms can only mix pseudoscalar and vector mesons with other irreps of the heavy quark symmetries. Hence, for example, in the $B \rightarrow D^*$ transition we can write

$$\langle D | \bar{c} \gamma_\mu b | B \rangle = \xi + \mathcal{O} \left(\left(\frac{1}{2m_b} - \frac{1}{2m_c} \right)^2 \right), \quad (2.72)$$

$$\langle D | \bar{c} \gamma_\mu \gamma_5 b | B \rangle = \xi + \mathcal{O} \left(\left(\frac{1}{2m_b} - \frac{1}{2m_c} \right)^2 \right). \quad (2.73)$$

where ξ is some b - and c -mass independent number.

This carries onto the pseudoscalar-vector and pseudoscalar-pseudoscalar form factors at zero recoil

$$h_{A_1}(1) = \eta_A \left(1 + \frac{l_V}{(2m_c)^2} + \frac{l_A}{m_b m_c} - \frac{l_P}{(2m_b)^2} \right), \quad (2.74)$$

$$h_+(1) = \eta_V \left(1 - l_P \left(\frac{1}{(2m_b)^2} - \frac{1}{(2m_c)^2} \right) \right), \quad (2.75)$$

where here h_+ comes from an HQET-inspired parameterisation of pseudoscalar-pseudoscalar transition amplitudes alternative to (2.28):

$$\frac{\langle M' | V_\mu^{q_1 q^2} | M \rangle}{\sqrt{Mm}} = h_+(w)(v + v')_\mu + h_-(w)(v - v')_\mu. \quad (2.76)$$

The factors $\eta_{A,V}$ in (2.74) and (2.75) are matching factors between QCD and HQET, and can contain logarithms of heavy masses. The factors $l_{V,A,P}$ are free non-perturbative parameters that must be fixed by some non-perturbative calculation e.g. a lattice QCD calculation.

2.4.2 NRQCD

An effective field theory closely related to HQET is Non-Relativistic QCD (NRQCD). This differs from HQET only by the power counting; instead of organizing terms in the Lagrangian according to their order in Λ_{QCD}/m , the terms are organized in terms of powers of the heavy quark's spacial velocity $v \sim |\mathbf{p}|/m$. NRQCD is derived with the following process:

- Separate the quark and antiquark components of the heavy quark. Since a non-relativistic fermion is decoupled from its antiparticle, our action only requires to describe the top two components of a Dirac spinor. Define the antiquark-free 2-component spinor h via the Foldy-Wouthuysen transformation $\psi \rightarrow h = e^{\gamma \cdot \mathbf{D}/2m}\psi$ [56]. This acts to remove the $\gamma \cdot \mathbf{D}$ term from the Dirac part of the Lagrangian, which is the only part that couples the fermion to the anti-fermion.
- Define power-counting by considering the expected expectation values of operators for heavy mesons [57]. The three relevant scales concerning the heavy meson are $M, p \sim Mv$ and $E_K \sim Mv^2$, where M is the meson mass, p the spacial momentum and E_K the kinetic energy. By relating operators to these three scales, we deduce their order in v . Start with the normalization of a scalar current:

$$\langle M | \int d^3x h^\dagger(x) h(x) | M \rangle \sim 1, \quad (2.77)$$

where $|M\rangle$ is some heavy meson state. Since we expect the meson state to be localized in a region of size $1/p$, we can assert that

$$\int d^3x \sim \frac{1}{p^3}. \quad (2.78)$$

From this and (2.77), we find $h \sim p^{3/2} \sim v^{3/2}$. The order of the derivative operator can be deduced from

$$E_K = \langle M | \int d^3x h^\dagger(x) \frac{D^2}{2M} h(x) | M \rangle \quad (2.79)$$

to be $D \sim v$. Following such a chain of arguments, we can deduce the order in v of any operator.

- The Lagrangian to $\mathcal{O}(v^n)$ is then simply all of the operators satisfying the symmetries of QCD of orders below v^n , with some Wilson coefficients [57]. To $\mathcal{O}(v^6)$:

$$\begin{aligned} \mathcal{L}_{\text{NRQCD}} = & h^\dagger \left(iD_0 + \frac{\mathbf{D}^2}{2m} + c_1 \frac{\mathbf{D}^4}{m^3} + c_2 g \frac{\mathbf{D} \cdot \mathbf{E} - \mathbf{E} \cdot \mathbf{D}}{m^2} \right. \\ & + c_3 ig \frac{\sigma \cdot (\mathbf{D} \times \mathbf{E} - \mathbf{E} \times \mathbf{D})}{m^2} + c_4 g \frac{\sigma \cdot \mathbf{B}}{m} \\ & + f_1 g \frac{\{\mathbf{D}^2, \sigma \cdot \mathbf{B}\}}{m^3} + f_2 ig \frac{\{\mathbf{D}^2, \sigma \cdot (\mathbf{D} \times \mathbf{E} - \mathbf{E} \times \mathbf{D})\}}{m^4} + f_3 ig^2 \frac{\sigma \cdot \mathbf{E} \times \mathbf{E}}{m^3} \Big) h \\ & + d_1 \frac{(h^\dagger H)(H^\dagger h)}{m^2} + d_2 \frac{(h^\dagger \sigma H) \cdot (H^\dagger \sigma h)}{m^2} \\ & + d_3 \sum_a \frac{(h^\dagger T^a H)(H^\dagger T^a h)}{m^2} + d_4 \sum_a \frac{(h^\dagger T^a \sigma H) \cdot (H^\dagger T^a \sigma h)}{m^2} \end{aligned} \quad (2.80)$$

\mathbf{E} and \mathbf{B} are the chromoelectric and chromomagnetic fields, T^a are fundamental representation of the $SU(3)$ color generators, and H is the antiquark components of the heavy quark. $c_{1,2,3,4}, f_{1,2,3}, d_{1,2,3,4}$ are Wilson coefficients, that can be fixed by perturbative matching to full QCD at the cutoff (the heavy quark mass, where QCD is perturbative).

CHAPTER 3

Lattice Quantum Chromodynamics

As discussed in Sec. 2.3.1, at low energies QCD becomes non-perturbative. In other words, the coupling α_s becomes $\mathcal{O}(1)$, and an expansion in α_s (as in perturbation theory) will not be dominated by the leading orders. In order to calculate observables of low energy QCD (like hadronic form factors), we require an alternative to perturbation theory.

The expectation value of an observable \mathcal{O} in a Yang-Mills theory can be expressed as a path integral;

$$\langle \mathcal{O} \rangle = \frac{1}{Z} \int [dG d\psi d\bar{\psi}] \mathcal{O} e^{iS[G, \psi, \bar{\psi}]}, \quad (3.1)$$

where G is the gauge field, $\psi(\bar{\psi})$ are the (anti)fermion fields, S is the classical action, and $[dG d\psi d\bar{\psi}]$ denotes integration over all configurations of the gauge and fermion fields. Z is the partition function. In the perturbative approach, we would expand $\exp(-\text{interacting part of } S)$ resulting in a power series in the gauge coupling populated by Feynman diagrams.

We must instead carry out the integral directly, by numerical brute force. Since it is not numerically feasible to carry out an infinite number of integrals, one must approximate spacetime as a discrete 4-dimensional lattice with spacing “ a ” between lattice sites, finite spacial volume L_x^3 and finite temporal extent L_t . The functional integral becomes

$$\int [dG d\psi d\bar{\psi}] = \prod_n \int dU(x_n) d\psi(x_n) d\bar{\psi}(x_n), \quad (3.2)$$

where n is a 4-vector with integer components labelling the sites, and $x_n^\mu = an^\mu$. This has a second benefit which is to naturally regularize the theory with a momentum cutoff $\Lambda \sim 1/a$. The gauge field has been replaced with the *gauge link* U , to be defined in the following section.

We require the lattice also to be finite in size, in this thesis we use only lattices that have the same number (N_x) of sites in each spatial direction. We use lattices that have periodic boundary conditions in the temporal direction, i.e $\psi(x + aN_t \hat{t}) = \psi(x)$ etc.

To avoid having to integrate over imaginary numbers (equivalently to avoid the scourge of the *sign problem* [58]), one also performs a *Wick rotation*. This is the redefinition $t \rightarrow it$, which changes the metric from Minkowski to Euclidean, and changes the weight $\exp(iS) \rightarrow \exp(-S)$. This has the advantage that it turns the quantum path integral into simply an average in statistical mechanics, this means we can apply all of the machinery of statistical mechanics to computing expectation values.

To obtain the 'real world' result for some expectation value, where real world means $a = 0$, one must perform the path integral at a number of different a values, and then extrapolate the results to $a = 0$.

One must choose a discretized version of the QCD action, one that becomes continuum QCD in the continuum ($a \rightarrow 0$) limit. This is a far from trivial step. There is an infinite number of choices of lattice actions that become QCD in the continuum limit. There therefore is a huge literature of different choices of discrete lattice actions. Different collaborations use different actions, and there is never-ending argument about the merits and pitfalls of each.

The rest of this chapter is dedicated to motivating and detailing the choices of discretisation used in the work of this thesis.

3.1 Lattice Gauge Fields

Often the best way to introduce some sophisticated method or technique is to first show how the naive approach breaks down. Imagine attempting a naive discretisation of the QCD action. Derivatives can be replaced with something like

$$\partial_\mu f(x) \rightarrow \frac{1}{2a} (f(x + a\hat{\mu}) - f(x - a\hat{\mu})) \quad (3.3)$$

where $\hat{\mu}$ is the unit vector in the μ direction. The quark kinetic part of the QCD action, $\bar{q}\not{D}q$, becomes

$$\frac{1}{2a} \bar{q}(x)\gamma^\mu q(x + a\hat{\mu}) - \frac{1}{2a} \bar{q}(x)\gamma^\mu q(x - a\hat{\mu}) - ig\bar{q}(x)G_\mu(x)\gamma^\mu q(x). \quad (3.4)$$

This is no longer invariant under the gauge trasforms (2.43), for example the first term becomes $\bar{q}(x)\Lambda(x)^\dagger\Lambda(x+a\hat{\mu})q(x+a\hat{\mu})$. The finite distance between lattice sites

force us to think more carefully about the interpretation of gauge symmetry on a lattice.

Formally speaking, a gauge field is a connection on a fibre bundle. So what does that all mean?

At each point x , there is a space of possible vectors that a quark field $q(x)$ could be, call it V_x . In this case, this is the colour space, the space of colour vectors (this refers to a single flavour, we suppress the flavour index here for brevity). V_x is a *fibre*. Spacetime, in our case \mathbb{E}^4 , is called the *base space* in this context.

The problem with our non-gauge-invariant terms above is that we are trying to compare vectors in different fibres. To compare colour vectors at two different spacetime points, i.e. two different fibres, one must *parallel transport* the vector from one point to another, according to some rule of how it changes, the so-called *connection*. In our case the parallel transport is a Wilson line:

$$\begin{aligned} W(x, y) : V_y &\rightarrow V_x, \\ W(x, y) &= Pe^{ig \int dc \cdot G}. \end{aligned} \quad (3.5)$$

where c is some curve between x and y , and P orders the operation of the gauge field G on the fibres, i.e. it operates at x first and y last. A wilson line transforms under the gauge group like $W(x, y) \rightarrow \Lambda(x)W(x, y)\Lambda^\dagger(y)$, so operators like $\bar{q}(x)W(x, y)q(y)$ are gauge-invariant, reflecting the fact that the color vector $q(y)$ has been parallel transported into the same fibre as $\bar{q}(x)$.

From this we see that, on a lattice, the natural degrees of freedom are no longer the elements of the Lie algebra, G_μ , but Wilson lines connecting adjacent lattice sites, also known as *links*:

$$U_\mu(x) \in SU(N_c) : V_x \rightarrow V_{x+a\hat{\mu}}, \quad (3.6)$$

that Gauge transform like

$$U_\mu(x) \rightarrow \Lambda(x)U_\mu(x)\Lambda^\dagger(x + a\hat{\mu}). \quad (3.7)$$

Then, a bilinear of colour vectors at any two points can be made to be gauge invariant by including a path between them made of links. For example;

$$\begin{aligned} \bar{q}(x)U_\mu(x)q(x + a\hat{\mu}) &\rightarrow [\bar{q}(x)\Lambda^\dagger(x)](\Lambda(x)U_\mu(x)\Lambda^\dagger(x + a\hat{\mu}))[\Lambda(x + a\hat{\mu})q(x + a\hat{\mu})] \\ &= \bar{q}(x)U_\mu(x)q(x + a\hat{\mu}). \end{aligned} \quad (3.8)$$

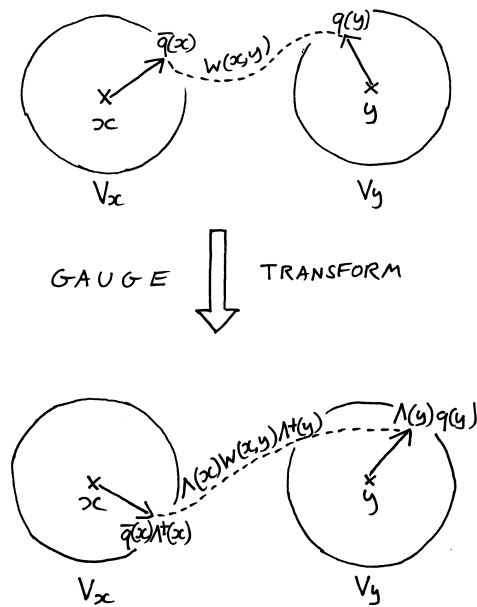


Figure 3.1: Depiction of colour spaces (fibres) at two points in spactime (base space) with the value of the quark field q represented at each point as a colour vector, and the connection $W(x,y)$ needed to compare the two colour vectors. A gauge transform changes the two vectors in different ways, for the comparison to be gauge independent, the connection must also transform appropriately.

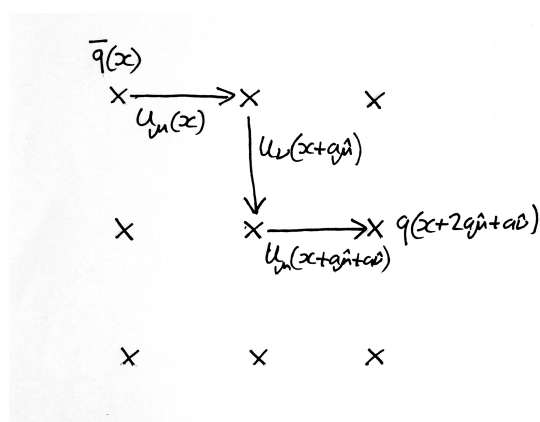


Figure 3.2: Depiction of a gauge invariant quark bilinear, connected by a Wilson line made of gauge links.

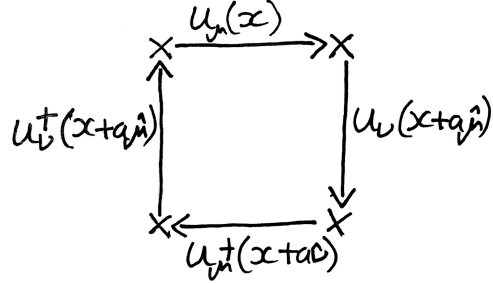


Figure 3.3: Elementary Plaquette.

The $\bar{q}Dq$ term in the QCD Lagrangian can then be represented on the lattice in a Gauge invariant way by

$$\frac{1}{2a} \bar{q}(x) \gamma_\mu (U_\mu(x) q(x + a\hat{\mu}) + U_\mu^\dagger(x - a\hat{\mu}) q(x - a\hat{\mu})). \quad (3.9)$$

If one defines the links in terms of the continuum gauge fields G_μ via

$$U_\mu(x) = \exp \left(ig a G_\mu \left(x + \frac{a\hat{\mu}}{2} \right) \right), \quad (3.10)$$

then (3.9) takes the correct form in the continuum limit, i.e. it becomes $\bar{q}Dq + \mathcal{O}(a^2)$.

3.1.1 The Gauge Action

We must design a pure gauge part of the action in terms of link variables. It is clear that the only gauge-invariant operator that depends only on the link variables are closed loops of links, as in fig. 3.3.

This brings us basically all the way to the correct answer. The simplest lattice discretisation of the Yang-Mills action is the real part of the smallest possible closed loop of gauge links;

$$S_G = -\frac{1}{g^2} \sum_x \sum_{\mu \neq \nu} \text{Re} \text{Tr} (1 - \square_{\mu\nu}(x)), \quad (3.11)$$

$$\square_{\mu\nu} = U_\mu(x) U_\nu(x + a\hat{\mu}) U_\mu^\dagger(x + a\hat{\nu}) U_\nu^\dagger(x). \quad (3.12)$$

$\square_{\mu\nu}$ is called the *elementary plaquette*. In the continuum limit this action reduces to

$$S_G = \frac{1}{4} \int d^4x \text{Tr} G_{\mu\nu} G^{\mu\nu} + \mathcal{O}(a^2), \quad (3.13)$$

as required.

This lattice action has a sensible interpretation in terms of the geometrical interpretation of gauge theory. The gauge force is due to *curvature* in the gauge field, a path-dependence in parallel transport. The gauge force is due to the presence of curvature, and the simplest local measure of the curvature is the plaquette.

In fact, any closed loop reduces to the Yang-Mills action in the continuum. This can be seen intuitively, taking the continuum limit means shrinking any closed loop into an infinitesimally small point. We then have a choice of gauge action on the lattice.

3.1.2 Symmanzik Improvements of the Gauge Action

Any lattice action is admissible for a calculation as long as it reduces to the appropriate QCD action in the continuum. This gives us a lot of freedom in how we chose our lattice action.

This freedom can be exploited in order to push expectation values of observables on the lattice closer to their continuum values (reduce the 'discretisation effects').

This program is known as *Symmanzik improvement*.

In general, a sensible lattice action looks like

$$S = \sum_i c_i(g) \mathcal{O}_{\text{lat}}^i = z_0(\{c_i\}) S_{\text{cont}} + a^2 \sum_{n=1} z_n(\{c_i\}) S_n \quad (3.14)$$

where S_{cont} is the continuum action. We are free to choose any $\{c_i\}$ such that $z_0(\{c_i\}) = 1$. In every example we are concerned with, $\mathcal{O}(a)$ terms are absent, but the argument carries straightforwardly to situations with $\mathcal{O}(a)$ corrections. A fundamental postulate of the Symmanzik approach is that improvement (removal of discretisation effects) of one observable results in improvement of all other observables. With this in mind, a reasonable approach is:

- Choose some set of lattice operators $\{\mathcal{O}_{\text{lat}}^i\}$. The number of operators required can be deduced by looking at the number of allowed irrelevant operators in the continuum theory at the mass dimension of the order of a you want to remove, i.e. the number of S_n operators in (3.14).
- Inspect the continuum limit of lattice action to find $z_0(\{c_i\})$, enforce $z_0(\{c_i\}) = 1$.
- Choose some observable \mathcal{O} that can be calculated in both the lattice and continuum theory. Use the remaining freedom in $\{c_i\}$ to remove the leading a

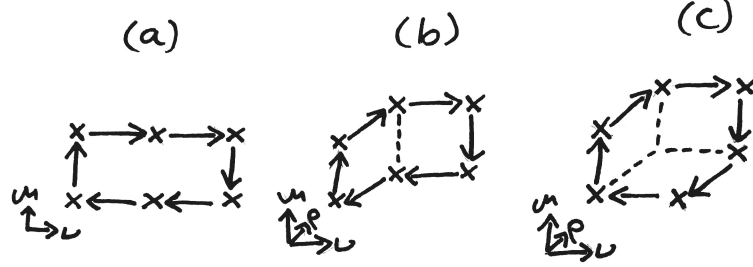


Figure 3.4: Terms additional to the elementary plaquette in the improved pure QCD action.

dependence in $\langle \mathcal{O} \rangle$ order by order in perturbation theory. i.e., if we write the expectation value as

$$\langle \mathcal{O} \rangle = \sum_{n,m} a^{2n} g^{2m} \langle \mathcal{O}_{n,m}(\{c_i\}) \rangle, \quad (3.15)$$

then this amounts to demanding that $\langle \mathcal{O}_{1,m}(\{c_i\}) \rangle = 0$, for as many m 's as possible.

Applying this to pure QCD, this procedure results in the Lüscher-Weitz action [59]. First consider the number of operators required. In continuum pure QCD, the only dimension 4 operator is $\text{Tr}G_{\mu\nu}G^{\mu\nu}$. There are no dimension 5 operators, hence there can be no $\mathcal{O}(a)$ contribution to the continuum limit of a lattice action. There are three independent dimension 6 operators:

$$\begin{aligned} & \text{Tr}J_{\mu\nu\rho}J_{\mu\nu\rho}, \quad \text{Tr}J_{\mu\mu\rho}J_{\nu\nu\rho}, \quad \text{Tr}J_{\mu\mu\nu}J_{\mu\mu\nu}, \\ & J_{\mu\nu\rho} = [D_\mu, G_{\nu\rho}] \end{aligned} \quad (3.16)$$

Hence we require 3 extra operators in the lattice action to be tuned in order to remove the three contributions from the a^2 terms in (3.14). The simplest choice is to take the plaquette action (3.12), and add all possible Wilson loops containing 6 links. This set consists of three families related by hypercubic invariance, *rectangles* (a), *parallelograms* (b) and *chairs* (c), depicted in fig. 3.4.

So the new lattice action is

$$S_G = -\frac{1}{g^2} \sum_x \sum_{\mu \neq \nu} (-c_0 \text{Re} \text{Tr}(1 - \square_{\mu\nu}(x)) + c_1 \text{Re} \text{Tr}(1 - \square_{\mu\nu}^a(x))) \quad (3.17)$$

$$+ \sum_{\rho \neq \mu, \nu} (c_2 \text{Re} \text{Tr}(1 - \square_{\mu\nu\rho}^b(x)) + c_3 \text{Re} \text{Tr}(1 - \square_{\mu\nu\rho}^c(x))) \quad (3.18)$$

where $\square_{\mu\nu(\rho)}^{a,b,c}$ are the Wilson loops in fig. 3.4. Expanding this in small a , one finds the function $z_0(\{c_i\})$, setting this to one we find the condition [60];

$$c_0 + 8(c_1 + c_2) + 16c_3 = 1. \quad (3.19)$$

The rest of the freedom must be fixed by comparing observables in the lattice and continuum theories. In [61] for example, by matching the gluon propagator between the two theories, one constrains the coefficients further (at tree level)

$$c_1 = -\frac{1}{12} , \quad c_0 - 8c_3 = \frac{5}{3} \quad (3.20)$$

These are classical relations, so will only prevent lattice artifacts up to $\mathcal{O}(\alpha_s)$. For better improvement, one must compare observables that are sensitive to loop corrections. A popular choice of observable is the so-called static quark potential $V(L)$, this is the potential energy between two static colour charges, as a function of separation aL between them.

This procedure is effected by the presence of fermions, so it has been performed a number of times to accommodate different fermion discretisations. In this thesis we report results using the Lüscher-Weitz action for gauge fields and HISQ fermions (see sec. 3.2). The coefficients $\{c_i\}$ were fixed at one-loop in [62] to be

$$c_0 = \frac{5}{3} + (0.237088(46) - 0.1008(34)N_f)\alpha_s + \mathcal{O}(\alpha_s^2) \quad (3.21)$$

$$c_1 = -\frac{1}{12} + (-0.025218(4) + 0.0110(3)N_f)\alpha_s + \mathcal{O}(\alpha_s^2) \quad (3.22)$$

$$c_2 = 0 + (-0.025218(4) + 0.0110(3)N_f)\alpha_s + \mathcal{O}(\alpha_s^2) \quad (3.23)$$

$$c_3 = 0 \quad (3.24)$$

since these have been tuned to remove a^2 effects up to α_s , lattice artifacts in observables computed using this action will be of size $\mathcal{O}(a^2\alpha_s^2)$, so we say this action is $\mathcal{O}(a^2\alpha_s)$ -improved.

3.2 Lattice Fermions

Putting fermions on the lattice supply a much larger host of complications than gauge fields do. There exist a diverse array of approaches to dealing with fermions on the lattice adopted by different collaborations. Different actions are suited to different types of applications, and intense debates have taken place over the years about the theoretical grounding of various actions. The plethora of fermion actions is due mostly to the famous doubling problem, which we will describe below.

In this chapter we will focus only on the fermion actions used in this work; namely the Highly Improved Staggered Quark (HISQ) action, and the Non-Relativistic QCD (NRQCD) action.

Before beginning the discussion of fermion discretisations, we will define some common notation used for gamma matrices in this context. The Euclidian gamma matrices are defined to obey

$$\{\gamma_\mu, \gamma_\nu\} = 2\delta_{\mu\nu}. \quad (3.25)$$

These have the useful property $\gamma_\mu^2 = 1$. The full set of spin-mixing matrices can be labelled according to

$$\gamma_n = \prod_\mu (\gamma_\mu)^{n_\mu}, \quad n_\mu = \mathbb{Z}_2. \quad (3.26)$$

There are 16 such matrices representing corners of the hypercube. One can also use a general site vector x_μ to label the matrix, then $\gamma_x = \gamma_n$ where $n_\mu = x_\mu/a \bmod 2$. It is straightforward to show that for any n ; $\gamma_n^\dagger \gamma_n = 1$. We also define $\gamma_{5\mu} = i\gamma_5 \gamma_\mu$, and $\gamma_{5n} = \prod_\mu (\gamma_{5\mu})^{n_\mu}$.

3.2.1 The Naive Fermion Action & The Doubling Problem

The interacting Dirac action is most naively discretised with

$$S_F = \sum_{x,\mu} \bar{\psi}(x) \gamma_\mu \nabla_\mu \psi(x) + m \sum_x \bar{\psi}(x) \psi(x), \quad (3.27)$$

where ∇_μ is the gauge covariant finite difference operator,

$$\nabla_\mu \psi(x) = \frac{1}{2a} \left(U_\mu(x) \psi(x + a\hat{\mu}) - U_\mu^\dagger(x - a\hat{\mu}) \psi(x - a\hat{\mu}) \right). \quad (3.28)$$

S_F is invariant under a so-called *doubling symmetry*, which is generated by

$$\psi(x) \rightarrow \mathcal{B}_\mu \psi(x) \equiv (-1)^{x_\mu/a} \gamma_{5\mu} \psi(x), \quad (3.29)$$

$$\bar{\psi}(x) \rightarrow \bar{\psi}(x) \mathcal{B}_\mu^\dagger \equiv (-1)^{x_\mu/a} \bar{\psi}(x) \gamma_{5\mu}^\dagger. \quad (3.30)$$

The product space of these form a group of 16 elements $\{\mathcal{B}_\zeta\}$, labeled by vectors ζ with $\zeta_\mu \in \mathbb{Z}_2$ (e.g. the element $\mathcal{B}_0 \mathcal{B}_1$ is labeled by $\zeta = (1, 1, 0, 0)$).

The physical significance of this symmetry can be seen when we study its effect on the action. First, notice that

$$\mathcal{B}_\mu \psi(x) = \gamma_{5\mu} \sum_k \tilde{\psi}(k) e^{i(k + \frac{\pi}{a}\hat{\mu}) \cdot x} \quad (3.31)$$

$$= \gamma_{5\mu} \sum_k \tilde{\psi}(k - \frac{\pi}{a}\hat{\mu}) e^{ik \cdot x}, \quad (3.32)$$

where $\{k\}$ is a discrete set of 4-momenta, with k_μ values spaced by π/aN_μ (N_μ = number of sites in direction μ) and truncated at π/a , due to finite size and finite lattice spacing. The action in momentum space can be written as

$$S = \sum_k \bar{\psi}(k) M(k) \tilde{\psi}(k). \quad (3.33)$$

After the operation of \mathcal{B}_μ it becomes

$$S \rightarrow \sum_k \bar{\psi}(k) \gamma_{5\mu} M(k + \frac{\pi}{a} \hat{\mu}) \gamma_{5\mu} \tilde{\psi}(k). \quad (3.34)$$

Since we know S is invariant under this transformation, it must be true that $\gamma_{5\mu} M(k + \frac{\pi}{a} \hat{\mu}) \gamma_{5\mu} = M(k)$, and therefore

$$M^{-1}(k + \frac{\pi}{a} \hat{\mu}) = \gamma_{5\mu} M^{-1}(k) \gamma_{5\mu}. \quad (3.35)$$

This is the doubling problem. M^{-1} is the momentum space propagator for the fermion field, so (3.35) shows that the spectrum of the fermion is periodic, with a period of π/a . We expect a pole in $M^{-1}(k)$ where $k \sim m$, m is the pole mass of the fermion. But due to (3.35) there will now be a second pole at $m + \pi/a$.

Generalizing this argument to all elements of the doubling symmetry, we see that

$$M^{-1}(k + \frac{\pi}{a} \zeta) = \gamma_{5\zeta} M^{-1}(k) \gamma_{5\zeta}. \quad (3.36)$$

This leads to 16 poles in the fermion spectrum, one for each ζ choice, therefore 16 distinct excitations (called *tastes*).

One can isolate a single taste by a block-scaling procedure;

$$\psi^{(\zeta)}(x_B) = \frac{1}{16} \sum_{\delta x_\mu \in \mathbb{Z}_2} \mathcal{B}_\zeta(x_B + \delta x) \psi(x_B + \delta x). \quad (3.37)$$

For example, for $\zeta = 0$, it would only contain the original non-doubler taste, since all other poles at $|k| \sim \pi/a$ have been integrated out. For $\zeta \neq 0$, the \mathcal{B}_ζ operator pushes the ζ doubler to where the $\zeta = 0$ taste originally was in k space, then the blocking procedure integrates out the rest.

3.2.2 Staggered Quarks

There are a number of solutions to this problem. The most straightforward is to modify the action to push the mass of the unwanted tastes above the momentum cutoff, preventing it from influencing the dynamics, these are called *Wilson-type fermions* [63]. However, actions of this type explicitly break Chiral symmetry.

Among other issues, this causes additive renormalization of the fermion mass, immensely complicating renormalization procedures.

Another approach, known as *staggered fermions* [64], partially resolves the doubling issue while retaining a remnant chiral symmetry. The work presented in this thesis makes extensive use of the staggered formalism.

Staggered fermions are defined via the following. Redefine the fields according to

$$\psi(x) = \gamma_x \chi(x). \quad (3.38)$$

In terms of the new spinor variables $\chi(x)$, the naive action (3.27) becomes

$$S_F = \sum_{x,\mu} \bar{\chi}(x)(\alpha_\mu(x)\nabla_\mu + m)\chi(x) \quad (3.39)$$

where $\alpha_\mu(x) = (-1)^{\sum_{\nu < \mu} x^\mu/a}$. The action is now diagonal in spin, leading to 4 decoupled grassman variables with identical actions and identical coupling to the gauge field. As a result, χ propagators (on fixed gauge backgrounds) are spin diagonal:

$$M_\chi^{-1}(x, y) = g(x, y) \mathbf{1}_{\text{spin}}, \quad (3.40)$$

where $g(x, y)$ is a singlet under spin. One need only to include a single component of χ in a simulation (i.e. fix $\chi = (\chi_1, 0, 0, 0)$). Then they can compute $M_\chi^{-1}(x, y)[U]$ to obtain $g(x, y)$. Then, using the inverse of (3.38), $g(x, y)$ can be transformed to a propagator of the original spinors:

$$M_\psi^{-1}(x, y) = g(x, y) \gamma_x \gamma_y^\dagger. \quad (3.41)$$

This is clearly computationally beneficial. But also, by shaving off the other spinor components, one reduces the number propagating degrees of freedom by a factor of 4, cutting the number of tastes from 16 down to 4.

We can show more explicitly how this happens. To do this, consider rewriting an isolated taste (3.37) in the staggered formalism, i.e., in terms of χ ;

$$\psi^{(\zeta)}(x_B) = \frac{1}{16} \sum_{\delta x_\mu \in \mathbb{Z}_2} \gamma_{\delta x} \mathcal{B}_\zeta(0) \chi(x + \delta x). \quad (3.42)$$

Recall we set $\chi(x) = (\chi_1(x), 0, 0, 0)$. The product $\gamma_{\delta x} \mathcal{B}_\zeta(0)$ is simply a product of gamma matrices, so can only serve to “scramble” the elements of χ . Then, in the staggered formalism, all 16 tastes $\psi^{(\zeta)}$ amount to only 4 distinguishable fermions: $(\chi_1, 0, 0, 0)$, $(0, \chi_1, 0, 0)$, $(0, 0, \chi_1, 0)$, $(0, 0, 0, \chi_1)$ (with factors of (-1) and i).

To obtain a useful new notation for staggered quarks, we can rewrite (3.42) as

$$\psi^{\alpha a}(x_B) = \frac{1}{8} \sum_{\eta} \gamma_{\eta}^{\alpha a} \chi(x_B + a\eta), \quad (3.43)$$

where $\eta_{\mu} \in \mathbb{Z}_2 \forall \mu$. $\psi^{\alpha a}$ has spin α and taste a . Define the *spin-taste* notation for operators on $\psi^{\alpha a}$ as $(\gamma_n \otimes \gamma_m)$, where γ_n acts on the spin component α and γ_m acts on the taste component a .

One can see that the first operator in the spin-taste notation corresponds to regular spin in the continuum by writing the (free) action in terms of $\psi^{\alpha a}$:

$$\begin{aligned} S &= \sum_{x_B, \mu} \bar{\psi}(x_B) \left[(\gamma_{\mu} \otimes 1) \nabla_{\mu} + a(\gamma_5 \otimes \gamma_{\mu} \gamma_5^*) \nabla_{\mu}^{(2)} + \frac{m}{4} (1 \otimes 1) \right] \psi(x_B), \\ \nabla_{\mu} \psi(x_B) &= \frac{1}{a} (\psi(x_B + 2a) - \psi(x_B - 2a)), \\ \nabla_{\mu}^{(2)} \psi(x_B) &= \frac{1}{4a^2} (\psi(x_B + 2a) - 2\psi(x_B) + \psi(x_B - 2a)). \end{aligned} \quad (3.44)$$

One can see that if we interpret the first operator as the continuum spin, we obtain the continuum Dirac action in the $a \rightarrow 0$ limit. Including interactions make the $\mathcal{O}(a)$ term more complicated, but the argument is unchanged.

Hence, to reproduce some current $\bar{\psi} \gamma_n \psi$ in the continuum, one can use $\bar{\psi}(\gamma_n \otimes \gamma_m)\psi$ on the lattice, where we have the freedom to choose any γ_m . In terms of χ fields these look like

$$\bar{\psi}(x_B)(\gamma_n \otimes \gamma_m)\psi(x_B) = \sum_{\eta, \eta'} \text{Tr}(\gamma_{\eta} \gamma_n \gamma_{\eta'} \gamma_m) \chi^{\dagger}(x_B + a\eta) \chi(x_B + a\eta'). \quad (3.45)$$

The $n = m$ case results in local operators in terms of χ , since the trace will vanish unless $\eta = \eta'$. To build the case with $n \neq m$, one must use 'point-split' operators, i.e. $\chi^{\dagger}(x)\chi(x + \delta x)$.

In practice in lattice calculations, the multiplicity of tastes is tackled in 3 steps:

1. Ensure only one taste is created and destroyed in the propagator.
2. Minimize the interaction between tastes by a modification of the action.
3. Remove contributions of extra tastes in the fermion sea by taking $\det M \rightarrow \sqrt[4]{\det M}$ (the context required to understand this step is elucidated in chapter 4).

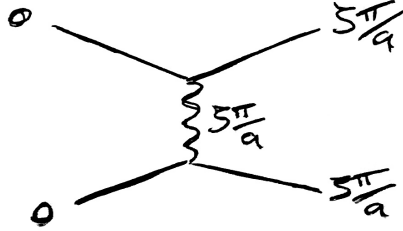


Figure 3.5: Taste mixing at tree level.

3.2.3 Highly Improved Staggered Quarks

Step 2 above is the guiding principle for the action we use in much of this work, the Highly Improved Staggered Quark (HISQ) action [65].

Interaction between different tastes (“taste mixing”) is dominated by the process in fig. 3.5, the exchange of single gluons carrying momenta close to $\zeta\pi/a$. In HISQ, this is suppressed by modifying the gauge fields in such a way as to minimize the coupling between a gluon with momentum $\zeta\pi/a$ and the fermions, in other words, minimize the vertices in fig. 3.5.

To this end, one can change the action so that fermions only couple to *smeared* gauge links, in which high-frequency excitations have been removed. Define the first and second covariant derivative operators;

$$\begin{aligned} \delta_\rho U_\mu(x) &\equiv \frac{1}{a}(U_\rho(x)U_\mu(x+a\hat{\rho})U_\rho^\dagger(x+a\hat{\mu}) \\ &\quad - U_\rho^\dagger(x-a\hat{\rho})U_\mu(x-a\hat{\rho})U_\rho(x-a\hat{\rho}+a\hat{\mu})), \end{aligned} \quad (3.46)$$

$$\begin{aligned} \delta_\rho^{(2)} U_\mu(x) &\equiv \frac{1}{a^2}(U_\rho(x+a\hat{\rho})U_\rho^\dagger(x+a\hat{\mu}) \\ &\quad - 2U_\mu(x) \\ &\quad + U_\rho^\dagger(x-a\hat{\rho})U_\mu(x-a\hat{\rho})U_\rho(x-a\hat{\rho}+a\hat{\mu})). \end{aligned} \quad (3.47)$$

With this we can define the smearing operator;

$$\mathcal{F}_\mu = \prod_{\rho \neq \mu} \left(1 + \frac{a^2 \delta_\rho^{(2)}}{4} \right). \quad (3.48)$$

HISQ uses two different smeared gauge fields defined by

$$X_\mu(x) \equiv \mathcal{U} \mathcal{F}_\mu U_\mu(x), \quad (3.49)$$

$$W_\mu(x) \equiv \left(\mathcal{F}_\mu - \sum_{\rho \neq \mu} \frac{a^2 (\delta_\rho)^2}{2} \right) \mathcal{U} \mathcal{F}_\mu U_\mu(x). \quad (3.50)$$

where \mathcal{U} is a re-unitarization operator, that acts on a matrix A like $\mathcal{U}A = A/\sqrt{A^\dagger A}$. The HISQ action can then be written as:

$$S_{\text{HISQ}} = \sum_x \bar{\psi}(x) \left(\gamma_\mu \left(\nabla_\mu(W) - \frac{a^2}{6} (1 + \epsilon_{\text{Naik}}) \nabla_\mu^3(X) \right) + m \right) \psi(x) \quad (3.51)$$

Where $\nabla_\mu(Z)$ is the covariant derivative (3.28) with gauge links replaced with Z . This action in fact not only removes tree level interactions like fig. 3.5, but also all taste mixing interactions at 1-loop.

The ∇_μ^3 term is a Symanzik improvement, it reduces the size of discretisation effects of observables computed using this action. The value of ϵ_{Naik} is fixed according to the constraint

$$\lim_{\underline{p} \rightarrow 0} \frac{E^2(\underline{p}) - m^2}{\underline{p}^2} = 1. \quad (3.52)$$

where $E(\underline{p})$ obeys the tree-level dispersion relation from the HISQ action. Tuning ϵ_{Naik} according to this constraint gives us the expression

$$\begin{aligned} \epsilon_{\text{Naik}} &= \frac{4 - \sqrt{4 + 12 \frac{m_{\text{tree}}}{\cosh(m_{\text{tree}}) \sinh(m_{\text{tree}})}}}{\sinh^2(m_{\text{tree}}) - 1}, \\ m_{\text{tree}} &= m \left(1 - \frac{3}{80} m^4 + \frac{23}{2240} m^6 + \frac{1783}{537600} m^8 \right. \\ &\quad \left. - \frac{76943}{23654400} m^{10} \right) + \mathcal{O}(m^{12}). \end{aligned} \quad (3.53)$$

3.3 Heavy Quarks on the Lattice

The range of different quark masses in nature present a number of further complications to lattice calculations. u and d quarks cause huge problems due to how light they are, this will be addressed in Sec. 4.1.2. s quarks are easy.

As quarks get heavier, we begin to encounter another problem. Discretisation effects will generally grow like the largest scale in the theory. If the observable being computed on the lattice is sensitive to the dynamics of a heavy quark of mass m_h , this will contain discretisation effects of size $(am_h)^n$ (where n depends on how improved the action is). This is essentially due to the de Broglie wavelength of the heavy quark excitations being close to the lattice spacing, the excitations 'hide' in-between lattice sites.

How heavy we can go is limited to two factors: the improvement of the lattice action and the lattice spacing. How fine we can get the lattice spacing is limited by

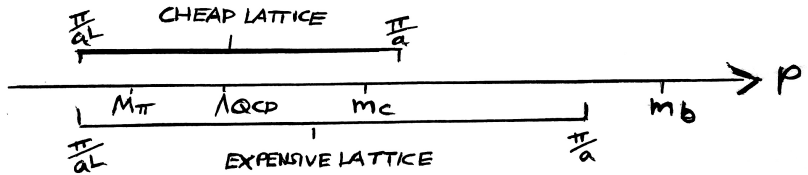


Figure 3.6: Different scales relevant to non-perturbative physics, and brackets showing the range of scales that typical lattices can resolve. The larger the range of scales resolved, the more computationally expensive the calculation.

computational cost. The physical size of the lattice must always be at least large enough to fit the lightest degrees of freedom in the system, namely it must be larger than the wavelength of pions. This means to get smaller lattice spacing requires increasing the number of sites on the lattice, hence increasing the computational costs (details in chapter 4).

In the past, c quarks resulted in uncontrollable discretisation effects, but now armed with highly improved actions like HISQ, and very fine lattices, c physics has been conquered on the lattice [66–72].

The mass of the b is still somewhat out of reach. Even with the HISQ action and the finest lattices available with current computational constraints, physical b quarks will create uncontrollable discretisation effects.

The work in this thesis concerns the decays of mesons containing b quarks. We approach the issue of the heavy b in two different ways, the *heavy-HISQ* approach, and the *Lattice NRQCD* action. Since the main results of this thesis result from our heavy-HISQ studies, we will not go into too much detail in describing lattice NRQCD.

3.3.1 Heavy HISQ

The heavy-HISQ approach is essentially to model the b with the HISQ action, but to perform the calculation at a number of unphysically light b masses (that we refer to generically as heavy h quarks), and extrapolate the results to the physical b mass. Typically the h masses span most of the region between the c mass and the b mass.

Luckily there exists an effective field theory for understanding how to perform such an extrapolation - HQET. HQET gives a framework to describe how observables depend on masses of heavy quarks, so one can use HQET to derive fit forms of such an extrapolation.

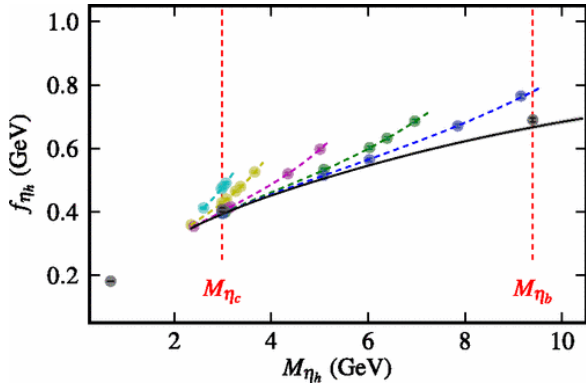


Figure 3.7: An extrapolation to $m_h = m_b$ of the η_h decay constant (where η_h is a pseudoscalar $\bar{h}h$ meson [3]. The colourful points are measurements of f_{η_h} on the lattice, the colour denotes lattice spacing. The x axis, M_{η_h} , is a proxy for the h -quark mass.

The heavy-HISQ approach is a reasonably new program. It has so far been used for computing b decay constants and masses [3], and a number of heavy-HISQ calculations of semileptonic form factors are currently underway. The work presented in chapters 6 and 7 adopt the heavy-HISQ approach for computing $B_s \rightarrow D_s^* l \nu$ and $B_s \rightarrow D_s l \nu$ form factors. Besides these, there are also currently ongoing calculations of form factors for the $B_c \rightarrow \eta_c l \nu$, $B_c \rightarrow J/\psi l \nu$ [73], $B_c \rightarrow B_s l \nu$, $B_s \rightarrow \eta_s l \nu$, and $B \rightarrow D^* l \nu$ decays.

3.3.2 Lattice NRQCD

The root of the problem of heavy quarks on the lattice is in the rest mass of the quark. Consider the expansion in momentum \mathbf{p}^2 of the continuum relativistic dispersion relation:

$$\omega = \sqrt{\mathbf{p}^2 + m^2} \simeq m + \frac{\mathbf{p}^2}{2m} - \frac{\mathbf{p}^4}{4m^3} + \dots \quad (3.54)$$

the first term (rest mass) is the source of the issue, when $m > 1/a$ the first term pushes the frequency of excitations ω close to or over π/a .

Another solution to heavy quarks is to replace the relativistic fermion action e.g. HISQ, with a lattice version of NRQCD [57]. In NRQCD the b has no rest mass.

Another benefit of NRQCD is that it does not suffer from a doubling problem, since the doubling problem is a purely relativistic issue (the doubling symmetry requires 4 component spinors for γ matrices to act on).

The lattice calculations we perform require us to compute propagators for b quarks on fixed gauge backgrounds. The form of the action allows propagators $M^{-1}[U]$ to be computed using a simple recursion relation

$$M_b^{-1}(\mathbf{x}, t+1)[U] = e^{-aH}[U]M_b^{-1}(\mathbf{x}, t)[U], \quad (3.55)$$

which is numerically very fast. H is the NRQCD Hamiltonian. In the interest of numerical stability, the time evolution operator is re-cast as

$$e^{-aH} = \left(1 - \frac{a\delta H}{2}\right) \left(1 - \frac{aH_0}{2n}\right)^n U_0^\dagger(\mathbf{x}, t) \left(1 - \frac{aH_0}{2n}\right)^n \left(1 - \frac{a\delta H}{2}\right), \quad (3.56)$$

where n is an arbitrary integer (chosen in our studies to be $n = 4$), and the Hamiltonian has been broken up into a leading part H_0 and correction δH . We use the $\mathcal{O}(\alpha_s v^4)$ corrected NRQCD Hamiltonian:

$$aH_0 = -\frac{\nabla^{(2)}}{2am_b}, \quad (3.57)$$

$$\begin{aligned} a\delta H = & -c_1 \frac{(\nabla^{(2)})^2}{8(am_b)^3} + c_2 \frac{i}{8(am_b)^2} (\nabla \cdot \tilde{\mathbf{E}} - \tilde{\mathbf{E}} \cdot \nabla) \\ & - c_3 \frac{1}{8(am_b)^2} \sigma \cdot (\nabla \times \tilde{\mathbf{E}} - \tilde{\mathbf{E}} \times \nabla) \\ & - c_4 \frac{1}{2am_b} \sigma \cdot \tilde{\mathbf{B}} + c_5 \frac{\nabla^{(4)}}{24am_b} \\ & - c_6 \frac{(\nabla^{(2)})^2}{16n(am_b)^2} \end{aligned} \quad (3.58)$$

where $\nabla^{(2,4)}$ are the second and fourth lattice derivative, $\tilde{\mathbf{E}}$ and $\tilde{\mathbf{B}}$ are the (Symmanzik improved) chromoelectric and chromomagnetic fields. The form of $\nabla^{(2,4)}, \tilde{\mathbf{E}}, \tilde{\mathbf{B}}$ are defined in sec. 4.2 of [57], and were improved upon in [74].

The coefficients $\{c_i\}$ have been fixed via various calculations adopting a number of methods. The coefficients of the kinetic terms, $c_{1,5,6}$, were most recently fixed by comparing the lattice NRQCD dispersion relation to that of the continuum in perturbation theory [75]. c_2 is a spin-independent term which can effect radial and orbital excitation energies, this is not expected to have as large an effect as the kinetic terms, so is set to its tree-level value of 1. The result of varying c_2 on relevant observables was investigated in Sec. IIIC of [76], and the effects were very small. c_3 and c_4 are spin-dependent terms, which would have a small effect on spin-averaged observables (i.e. all observables computed in this work). c_3 is set to 1, and c_4 is tuned non-perturbatively, by matching predictions of the fine structure of the Υ spectrum from lattice NRQCD to experiment [76].

Once the propagator for the 2-component non-relativistic b quark has been found, it must be transformed back into a 4-component spinor. This is done by an inverse Fouldy-Wouthuysen transformation [56]

$$\psi(x) = e^{-\frac{\gamma \cdot \mathbf{D}}{2m_b}} \begin{pmatrix} \psi_+(x) \\ 0 \end{pmatrix}. \quad (3.59)$$

CHAPTER 4

Lattice Calculations

The last chapter focused on how to discretize QCD on a lattice. This chapter is focused on the practical side of lattice QCD - given a lattice action, how does one perform the functional integral to determine expectation values of operators.

4.1 Evaluating Lattice Correlation Functions

All physics of a quantum field theory can be extracted from correlation functions. So a typical lattice calculation involves computing a correlation function (or just *correlator*) on the lattice, then extracting physical quantities from it. A typical correlator that is computed on the lattice is a 2-point meson correlator, i.e. when $\mathcal{O} = \Phi(x)\Phi^\dagger(y)$ and Φ is a meson creation operator. This is a good working example for showing the steps in a lattice calculation, the generalization to N -point correlators is reasonably natural.

A creation operator for a meson in this context can be any operator containing the same quantum numbers as the meson one studying. For example, the neutral B meson is a pseudoscalar charged with a d and \bar{b} quark, so a suitable operator is $\Phi(x) = \bar{b}(x)\gamma_5 d(x)$. The corresponding functional can then be written as

$$C(x, y) = \langle \Phi(x)\Phi^\dagger(y) \rangle = \int [d\psi d\bar{\psi} dU] (\bar{b}(x)\gamma_5 d(x)\bar{d}(y)\gamma_5 b(y)) \times \exp \left(-S_G[U] - \sum_{w,z,i} \bar{q}_i(w) M_{q_i}(w, z)[U] q_i(z) \right), \quad (4.1)$$

where we have broken the action up into a gauge part $S_G[U]$, and a fermion part. $M_{q_i}(x, y)[U]$ is the Dirac operator for flavour i , and can be seen as a matrix in lattice site, color and spin.

The integral over fermions can be performed analytically since the fermion fields

are Grassman valued. In our example, the result is [77];

$$\begin{aligned} C(x, y) = & \int [dU] \text{Tr} \left(M_b^{-1}(y, x)[U] \gamma_5 M_d^{-1}(x, y)[U] \gamma_5 \right) \\ & \times e^{-S_G[U]} \prod_i \det(M_{q_i}[U]). \end{aligned} \quad (4.2)$$

The quantities $M_{q_i}^{-1}(x, y)[U]$ are propagators of a quark of flavour q on a fixed gauge background U . Here U denotes a configuration of angles comprising an $SU(3)$ matrix for each element of the set of all links on the lattice $\{U_\mu(x) | \forall \mu, x\}$. The trace is over color and spin. The integration over gauge fields is generally carried out by an importance sampling method. A finite *ensemble* of gauge configurations $\{U_n\}$ is generated by a Monte Carlo Markov Chain (MCMC), where the probability of a gauge configuration U_n being added to the ensemble is proportional to

$$p(U_n) = e^{-S_G[U_n]} \prod_i \det(M_{q_i}[U_n]). \quad (4.3)$$

Once the ensemble is created, the path integral can be approximated by simply

$$C(x, y) \simeq \frac{1}{N} \sum_n \text{Tr} \left[M_b^{-1}(y, x)[U_n] \gamma_5 M_d^{-1}(x, y)[U_n] \gamma_5 \right] \quad (4.4)$$

where N is the size of the ensemble. The calculation of the correlation function then is split into 3 steps:

1. Generate an ensemble of Gauge configurations $\{U_i\}$ by MCMC (sec. 4.1.1).
2. Compute $M_{q_i}^{-1}(x, y)[U]$ by inverting the Dirac operator on each Gauge configuration (sec. 4.1.2).
3. Construct trace as in (4.4), and average over the ensemble. This step is dealt with in the context of staggered quarks in 4.1.3.

4.1.1 Generation of Gauge Ensembles

The calculation requires a number of samples of gauge configurations $\{U_n\}$ sampled from the distribution $p(U)$ defined in (4.3).

The physical interpretation of the determinant in (4.3) is that it accounts for virtual quark loops in the Dirac sea. In the early days of lattice calculations, this determinant was approximated to 1, since its presence caused an insurmountable computational cost, and it was expected that sea quarks had small effects on observables (this is known as the *quenched approximation*). These days, our computational

ability has improved and sophisticated approaches to the determinant have been developed, so we can include it in our calculations.

We will roughly follow the history of gauge ensemble generation, by first ignoring the determinant, and then showing how it is eventually included in the process.

Quenched MCMC

Gauge ensembles are generated via an MCMC, inspired by statistical mechanics. The distribution $\exp(-S_G[U])$ is suggestive of something like a Boltzmann distribution for a gas of particles, each with some state U_i , in thermal equilibrium. The ergodic hypothesis states that a single particle in this gas will jump between possible states over time such that, at any given time, its probability of being in state U_i is given by $\exp(-S_G[U_i])$. In MCMC, one starts with some random state U_0 , then repeatedly updates the state according to some update 'hopping rate' $p(U_i \rightarrow U_j)$. This results in a list of states that appear sampled from the distribution $\exp(-S_G[U])$.

The hopping rate must be designed to bring the chain into thermal equilibrium with the correct distribution. A sufficient condition for thermal equilibrium is so-called *detailed balance*, where the probability of jumps between any pair of states i and j is equal:

$$p(U_i)p(U_i \rightarrow U_j) = p(U_j)p(U_j \rightarrow U_i). \quad (4.5)$$

Hence $p(U_i \rightarrow U_j)$ must be designed according to the rule

$$\frac{p(U_i \rightarrow U_j)}{p(U_j \rightarrow U_i)} = \exp(-(S_G[U_i] - S_G[U_j])). \quad (4.6)$$

There are a number of possible choices of how to design $p(U_i \rightarrow U_j)$. One approach, known as **molecular dynamics** [78, 79] is to model the chain as the trajectory $U(\tau)$ of a system with hamiltonian

$$H(\pi, U) = \frac{\pi^2}{2} + S_G[U], \quad (4.7)$$

where π is a fictitious momentum conjugate to U . It can be demonstrated that such a trajectory obeys (4.6). The trajectory is computed via Runge-Kutta methods. To deal with the possibility of fixed points, limit cycles etc. in the dynamics (which would prevent ergodicity), one can introduce a periodic **refreshing** step, where π assigned a new value from normally distributed noise [80, 81].

Another problem that can occur in molecular dynamics is when errors in Runge-Kutta iterations accumulate over time. Diversion from the dynamics enforced by $H(\pi, U)$ can ruin the ergodicity of the trajectory. To fix this, one can add a **Metropolis** step at regular intervals $\delta\tau$ throughout the evolution [82]. In this step, one either accepts (continues onto the next stage of molecular dynamics) or rejects (refreshes π and re-calculates the last stage of molecular dynamics), according to the criterion

- If $S_G[U(\tau + \delta\tau)] < S_G[U(\tau)]$, always accept
- Otherwise, accept if $\exp(S_G[U(\tau + \delta\tau)] - S_G[U(\tau)]) > \lambda$, where λ is randomly chosen from the interval $[0, 1]$.

The metropolis step ensures (4.6) is satisfied even in the presence of Runge-Kutta errors.

The combination of molecular dynamics, refreshing steps and Metropolis steps is referred to as **Hybrid Monte Carlo** [83], and is the basic structure of how the ensembles we use in this thesis were generated. We now address how the determinant $\det M$ is included.

Unquenched MCMC

Simply evaluating $\det M[U]$ directly, given a configuration U , is prohibitively expensive due to the non-local nature of the determinant (recall $M[U]$ is a matrix in spin, colour, and lattice site, in modern calculations this will have a dimension of order 10^8 .) A solution to this is to use the Φ -algorithm [84].

First, we replace $\det M$ with $\det M^\dagger M$. If we were only including u and d quarks in the sea, this would be fine since we can approximate u and d to be two degenerate flavours, then $\prod_q \det M_q = \det M \det M = \det M^\dagger M$. In the case of an arbitrary set of flavours, this requires a correction that will be addressed later. This involves introducing new scalar fields $\Phi(x)$ and $\Phi^\dagger(x)$ via

$$\det M^\dagger M = \int [d\Phi^\dagger d\Phi] \exp(-\Phi^\dagger (M^\dagger M)^{-1} \Phi). \quad (4.8)$$

then one can add $-\Phi^\dagger (M^\dagger M)^{-1} \Phi$ to S_G in the Hybrid Monte Carlo algorithm. The extra functional integral over Φ, Φ^\dagger is easily evaluated, by sampling a vector η from a normal distribution $\exp(-\eta^\dagger \eta)$, then transforming it to $\Phi = M^\dagger \eta$.

The Dreaded Rooting Procedure

We will now address how to correct for the fact that we have replaced $\det M$ with $\det M^\dagger M$ in the presence of arbitrary non-degenerate flavours. We have explicitly doubled the fermions to two degenerate flavours per physical flavour. In the case of staggered quarks, this is not a huge deal since we already have four degenerate tastes which we have to deal with anyway. As mentioned in Sec. 3.2.2, in order to cut down the number of tastes in the sea, the solution is to take the fourth-root of $\det M$. When using the Φ -algorithm, this becomes the 8-th root of $\det M^\dagger M$.

$$\begin{aligned} (\det M^\dagger M)^{1/8} &= \left(\prod_i \lambda_i^2\right)^{1/8} = \left(\prod_i \lambda_i\right)^{1/4} \\ &\stackrel{?}{=} \left(\prod_i \lambda'_i{}^4\right)^{1/4} = \prod_i \lambda'_i \quad (a \rightarrow 0). \end{aligned} \tag{4.9}$$

where λ_i are eigenvalues of M . On the second line, we have assumed that the matrix M can be decomposed into four matrices for each of the four tastes, with eigenvalues λ'_i which are degenerate in the continuum limit.

This assumption is not rigorously justified in field theory, so the fourth-root trick is a source of much controversy, and is the main objection to staggered quarks [85–87]. There has so far emerged no evidence that this is harmful, since all observables ever computed from the staggered quark formalism have agreed with experiment, analytical approaches, and other lattice discretisations. The empiricists among us would say this is evidence for the validity of the fourth-root trick.

Introducing the 1/2 or 1/8th root to the determinant requires a modification of the Φ algorithm, we can no longer simply sample Φ using $\Phi = M^\dagger \eta$. The effective action is now $S_G + \Phi^\dagger (M^\dagger M)^{-1/8} \Phi$. The root is dealt with by replacing it with a partial fraction representation [88]:

$$(M^\dagger M)^{-1/8} \simeq a_0 + \sum_{n=1}^N \frac{a_n}{M^\dagger M + b_n}. \tag{4.10}$$

This can only be evaluated by some variation of a conjugate gradient algorithm (specifically a so-called multishift solver [89, 90]), conjugate gradient will be described in sec. 4.1.2. This approach is called the **Rational Hybrid Monte Carlo** (RHMC) algorithm.

The $N_f = 2 + 1 + 1$ MILC Ensembles

In this work we use ensembles of gauge configurations generated by the MILC collaboration [91, 92]. The ingredients of these configurations are

set	handle	a/fm	$N_x^3 \times N_t$	am_{l0}	am_{s0}	am_{c0}
0	very coarse	0.1543(8)	$16^3 \times 48$	0.013	0.067	0.838
1	coarse	0.1241(7)	$24^3 \times 64$	0.0102	0.0509	0.635
2	fine	0.0884(6)	$32^3 \times 96$	0.0074	0.037	0.440
3	fine-physical	0.0873(5)	$64^3 \times 96$	0.0012	0.0363	0.432
4	superfine	0.05922(12)	$48^3 \times 144$	0.0048	0.024	0.286
5	ultrafine	0.04406(23)	$64^3 \times 192$	0.00316	0.0158	0.188

Table 4.1: Parameters for gluon ensembles [91,92]. a values for sets 0-3 were deduced in [93], set 4 from [94]. We thank C. McNeile for computing the a value on set 5. These a values are determined by measuring the Wilson flow parameter w_0/a on the lattice, then using the known value for w_0 to isolate a . Columns 5-7 give the masses used in the action for light, strange and charm quarks in the sea.

- Gauge fields obeying the one-loop Symanzik improved Lüscher-Weitz action described in Sec. 3.1.2.
- Four flavours of quark in the sea, u,d,s and c (with $m_u = m_d \equiv m_l$), hence the notation $N_f = 2 + 1 + 1$, obeying the HISQ action, described in sec. 3.2.3.
- Ensemble generated using the RHMC Algorithm as described earlier in this section.

Table 7.1 gives the details of the MILC ensembles that were used in this work. One may notice that for the majority of ensembles here, the light quarks are obscenely heavier than in reality. The necessity for this is explained in the next section.

4.1.2 Dirac Operator Inversion

Once the ensemble $\{U_i\}$ has been generated, to compute the 2-point correlator (4.4) one must compute $M^{-1}[U_i]$ for each U_i . We have already seen how this can be done in the case of the flavour in question being governed by the NRQCD action, one can use the recursion relation (3.55). In the case of relativistic actions like HISQ, there is no equivalent recursion relation.

M is large but sparse, it technically has $\mathcal{O}(\text{Vol}^2)$ elements, but for suitably local actions (like HISQ) it has only $\mathcal{O}(\text{Vol})$ non-zero elements. This means it is well-

suites to the **conjugate gradient** (CG) algorithm [95] (and it's variants), which has become the most successful approach to computing M^{-1} . However, CG requires the matrix being inverted to be hermitian and positive definite, which is not necessarily the case for M . We instead invert $M^\dagger M$, which is hermitian and positive definite, then we can recover M^{-1} by acting M^\dagger on $(M^\dagger M)^{-1}$.

The design of CG requires a bunch of explanation which we will not go into here. We will instead briefly describe the philosophy behind it, and state the algorithm. The goal is, given some vector b and matrix A , to find x where

$$Ax = b. \quad (4.11)$$

In our case $A = M^\dagger M$ and b is a suitably chosen 'source' for the propagator (see sec. 4.1.3). This is equivalent to finding the $x = x^*$ that minimizes

$$f(x) = b^T Ax - b^T b. \quad (4.12)$$

A reasonable solution to this problem is something like a *steepest descent* approach, where one starts at a random x_0 , then moves some distance α_0 in the direction $r_0 = x^* - x_0 = b - Ax_0$ to $x_1 = x_0 - \alpha_0 r_0$, where α_0 is chosen to minimize $r_1 = x^* - x_1$. And then repeat. This approach has the property that each new step $\alpha_n r_n$ is orthogonal to every other step, this means the algorithm takes a sub-optimal zig-zag path towards the solution.

CG is designed to take a more direct path, by imposing the condition that the direction of each step $d_n = (x_n - x_{n-1})/\alpha_n$ is orthogonal with respect to the metric A , i.e. $d_n^T A d_m = 0$ for $n \neq m$. The CG algorithm is

$$\begin{aligned} x_{n+1} &= x_n + \alpha_n d_n, \text{ where} \\ \alpha_n &= \frac{r_n^T r_n}{d_n^T A d_n}, \\ d_n &= \begin{cases} r_0, & n = 0 \\ r_n + \beta_n d_{n-1}, & n > 0, \end{cases} \\ r_n &= b - Ax_n, \\ \beta_n &= \frac{r_n^T r_n}{r_{n-1}^T r_{n-1}}. \end{aligned} \quad (4.13)$$

One terminates the algorithm when some stopping condition is achieved, namely when $r_n < \epsilon$ where ϵ is some small number referred to as the error tolerance, or when some maximum number of iterations has been reached.

The complexity of the CG algorithm is $\mathcal{O}(c)$ where $c = \lambda_{\max}/\lambda_{\min}$ is the condition number of the matrix A ($\lambda_{\max/\min}$ are the largest and smallest eigenvalues of A). The condition number quantifies the size of rounding errors that accumulate in iterative processes like CG. In our case where $A = M^\dagger M \sim (-iD + m)(iD + m)$, the condition number is proportional to m^{-2} . Hence, propagators for lighter quarks are quadratically more expensive to compute than heavier ones. This not only effects the computation of correlation functions between light quarks via M^{-1} , but any unquenched calculation with rooting since in that case we must also invert (4.10).

For this reason, lattice calculations are often computed with unphysically heavy u/d quarks. When computing observables that are sensitive to the light quark masses, modern lattice calculations have measured the observable for a number of light quark masses and extrapolated downwards to the physical light mass, using chiral perturbation theory as a guide. In the MILC ensembles we use in this work, summarized in table 7.1, all but one have a light mass at around $m_l/m_s \simeq 1/5$, while set 3 has roughly physical light quarks at $m_l/m_s \simeq 1/30$.

4.1.3 Staggered Correlation Functions

We now turn to how to evaluate traces of quark propagators like in (4.2), specifically in the staggered formalism.

Recall ψ -propagators M^{-1} are related to χ -propagators g by

$$M^{-1}(x, y) = \gamma_x \gamma_y^\dagger g(x, y). \quad (4.14)$$

Throughout this section we will keep the U -dependence of M^{-1} and g implicit. By conjugating both sides and using the property of the naive propagator $(M^{-1})^\dagger(x, y) = \gamma_5 M^{-1}(y, x) \gamma_5$ (known as γ_5 -hermiticity) one can show that M^{-1} can also be written as

$$M^{-1}(x, y) = \phi_5(x) \phi_5(y) \gamma_x \gamma_y g^\dagger(y, x), \quad (4.15)$$

where $\phi_5(x) = (-1)^{\sum_\mu x_\mu}$.

2-point correlation functions

Consider the generic 2-point correlator:

$$\begin{aligned} C(x, y) &= \langle \Phi_X^\dagger(x) \Phi_Y(y) \rangle_{\psi, U} , \quad \Phi_X(x) = \frac{1}{4} \bar{\psi}_a(x) \gamma_X \psi_b(x) \\ &= \frac{1}{16} \langle \text{Tr}_{c,s} \gamma_X M_a^{-1}(x, y) \gamma_Y M_b^{-1}(y, x) \rangle_U \\ &= \frac{1}{16} \text{Tr}_s \left(\gamma_x^\dagger \gamma_X \gamma_x \gamma_y^\dagger \gamma_Y \gamma_y \right) \langle \text{Tr}_c (M_a^{-1}(x, y) M_b^{-1}(y, x)) \rangle_U \end{aligned} \quad (4.16)$$

Tr_s is a trace over spin and Tr_c is over colour. To deal with the spin trace, define the family of phases $\{\phi_X(x)\}$ according to

$$\gamma_x^\dagger \gamma_X \gamma_x = \phi_X(x) \gamma_X. \quad (4.17)$$

for example, if $X = 5$, then $\gamma_x^\dagger \gamma_5 \gamma_x = (-1)^{\sum_\mu x_\mu} \gamma_x^\dagger \gamma_x \gamma_5 = \phi_5(x) \gamma_5$. The map from X to ϕ_X is structure preserving, i.e. if $\gamma_X = \gamma_A \gamma_B$, then $\phi_X(x) = \phi_A(x) \phi_B(x)$. The spin trace becomes $\phi_X(x) \phi_Y(y) \text{Tr}_s(\gamma_X \gamma_Y)$. The remaining trace will vanish unless $Y = X$, and is 4 otherwise. We end up with

$$C(x, y) = \frac{1}{4} \phi_{5X}(x) \phi_{5X}(y) \langle \text{Tr}_c g_a(x, y) g_b^\dagger(x, y) \rangle_U, \quad (4.18)$$

where we have applied (4.15) to M_b^{-1} and $\phi_{5X}(x) = \phi_5(x) \phi_X(x)$. To obtain the correlation function of a meson in a momentum eigenstate with spacial momentum \mathbf{p} , the above must be replaced with

$$\begin{aligned} C_{\mathbf{p}}(t_0, t) &= \frac{1}{N_x^3} \sum_{\mathbf{x}, \mathbf{y}} e^{i\mathbf{p} \cdot (\mathbf{x} - \mathbf{y})} C(\mathbf{x}, t_0; \mathbf{y}, t) \\ &= \frac{1}{4N_x^3} \sum_{\mathbf{x}, \mathbf{y}} e^{i\mathbf{p} \cdot (\mathbf{x} - \mathbf{y})} \phi_{5X}(x) \phi_{5X}(y) \langle \text{Tr}_c g_a(x, y) g_b^\dagger(x, y) \rangle_U, \end{aligned} \quad (4.19)$$

where it is understood that $x_0 = t_0$ and $y_0 = t$. In order to evaluate this function, the simulation must perform inversions to create $g_{a/b}(x, y)$ for each x and y , so $2 \cdot \text{Vol}^2$ operations. This is prohibitively expensive. The number of inversions can be reduced using *random wall sources*. Define

$$P_{a, \mathbf{p}, X}^{t_0}(y) \equiv \frac{1}{\sqrt{N_x^3}} \sum_{\mathbf{x}} e^{i\mathbf{p} \cdot (\mathbf{x} - \mathbf{y})} \phi_{5X}(\mathbf{x}, t_0) \xi(\mathbf{x}) g_a(\mathbf{x}, t_0; y), \quad (4.20)$$

where $\xi(\mathbf{x})$ is a random field of colour vectors, varying configuration-by-configuration. This has the property

$$\langle f(\mathbf{x}, \mathbf{x}') \xi^*(\mathbf{x}') \xi(\mathbf{x}) \rangle_U = \delta_{\mathbf{x}, \mathbf{x}'} \langle f(\mathbf{x}, \mathbf{x}') \rangle_U. \quad (4.21)$$

Using this property the correlator can be built instead according to

$$C(t_0, t) = \frac{1}{4} \sum_{\mathbf{y}} \phi_{5X}(y) \langle \text{Tr}_c P_{a,\mathbf{p},X}^{t_0}(\mathbf{y}, t) P_{b,0,1}^{t_0}(\mathbf{y}, t) \rangle_U. \quad (4.22)$$

Now all one has to compute is $P_{a/b}^{t_0}(y)$ for general y , so 2·Vol operations, a reduction by a factor of Vol.

3-point correlation functions

The above discussion can be generalized to 3-(or N -)point correlation functions using *extended sources*. Consider a 3-point correlation function, for example encoding an $X \rightarrow Y$ semileptonic decay via a current $J(y)$;

$$\begin{aligned} C(x, y, z) &= \langle \Phi_X^\dagger(x) J(y) \Phi_Z(z) \rangle_{\psi, U} , \quad \Phi_X(x) &= \frac{1}{4} \bar{\psi}_b(x) \gamma_X \psi_s(x) \\ J(y) &= \bar{\psi}_b(y) \gamma_J \psi_a(y) \\ \Phi_Z(z) &= \frac{1}{4} \bar{\psi}_a(z) \gamma_Z \psi_s(z). \end{aligned} \quad (4.23)$$

We can reduce this in the same way as before

$$C(x, y, z) = \frac{1}{16} \text{Tr}_s \left(\gamma_x^\dagger \gamma_X \gamma_x \gamma_y^\dagger \gamma_J \gamma_y \gamma_z^\dagger \gamma_Z \gamma_z \right) \langle \text{Tr}_c g_b(x, y) g_a(y, z) g_s(x, z) \rangle_U \quad (4.24)$$

$$= \frac{1}{4} \phi_{5X}(x) \phi_J(y) \phi_{5Z}(z) \langle \text{Tr}_c g_b(x, y) g_a(y, z) g_s^\dagger(x, z) \rangle_U. \quad (4.25)$$

We have assumed that $\text{Tr}_s \gamma_X \gamma_J \gamma_Z = 4$, requiring that each gamma matrix in this combination has a partner and therefore cancels.

Putting X into an eigenstate of zero momentum, and Y into an eigenstate of momentum \mathbf{p} , we get

$$\begin{aligned} C_{\mathbf{p}}(t_0, t, T) &= \frac{1}{4N_x^3} \sum_{\mathbf{x}, \mathbf{y}, \mathbf{z}} e^{i\mathbf{p} \cdot (\mathbf{y} - \mathbf{z})} \phi_{5X}(x) \phi_J(y) \phi_{5Z}(z) \\ &\times \langle \text{Tr}_c g_b(\mathbf{x}, t_0; \mathbf{y}, t) g_a(\mathbf{y}, t, \mathbf{z}, T) g_s^\dagger(\mathbf{x}, t_0; \mathbf{z}, T) \rangle_U. \end{aligned} \quad (4.26)$$

This can be built by first creating propagators for the b and s quarks - $P_{b,0,X}^{t_0}(y), P_{s,0,1}^{t_0}(z)$. Then, build the a propagator using an extended source, i.e.:

$$P_{a,\mathbf{p},ext}^T(y) = \sum_{\mathbf{z}} P_{s,0,1}^{t_0}(\mathbf{z}, T) \phi_{5Z}(\mathbf{z}, T) g_a(\mathbf{z}, T; y). \quad (4.27)$$

Then, $P_{b,0,X}^{t_0}(y)$ and $P_{a,\mathbf{p},ext}^T(y)$ can be used to construct (4.22), giving a result for the 3-point correlation function.

We will briefly connect the above discussion to the spin-taste notation introduced in Sec. 3.2.2. In the above we have not performed any point-splitting of any of the operators (Ψ_X, J, \dots). Hence, we denote these operators in spin-taste notation as $(\gamma_n \otimes \gamma_n)$, where γ_n is the continuum spin structure we are aiming for. In the work in this thesis, we will not use any point-split operators, so the above discussion is sufficient for understanding our work.

Momentum Twist

The momentum space 2-point correlation function for an operator \mathcal{O} with external momentum \mathbf{p} is given by

$$C_{\mathbf{p}}(0, t) = \sum_{\mathbf{x}} e^{i\mathbf{p} \cdot \mathbf{x}} \langle \mathcal{O}^\dagger(\mathbf{x}, t) \mathcal{O}(\mathbf{0}, 0) \rangle. \quad (4.28)$$

To extend the method for computing zero momentum correlators to non-zero, one needs to add an appropriate phase to the operators;

$$\mathcal{O}(\mathbf{x}, t) \rightarrow \mathcal{O}(\mathbf{x}, t) e^{-i\mathbf{p} \cdot \mathbf{x}} \quad (4.29)$$

$$\implies C(\mathbf{0}, t) \rightarrow C(\mathbf{p}, t). \quad (4.30)$$

This generalised straightforwardly to n -point functions. One can assign the rephasing to any factor in \mathcal{O} , for example a fermion operator

$$\psi(\mathbf{x}, t) \rightarrow \psi(\mathbf{x}, t) e^{-i\mathbf{p} \cdot \mathbf{x}}. \quad (4.31)$$

Rephasing ψ is equivalent to introducing the so-called *momentum twist* to the gauge links [96]. The action of (4.29) on any gauge invariant quantity is equivalent to

$$U_i \rightarrow U_i e^{ip_i} \quad (\text{no sum}). \quad (4.32)$$

For example consider the effect this has on the following operator

$$\begin{aligned} & \psi^\dagger(x) U_\mu(x) U_\nu(x + a\hat{\mu}) \psi(x + a\hat{\mu} + a\hat{\nu}) \\ & \rightarrow \psi^\dagger(x) (e^{ip_\mu} U_\mu(x)) (e^{ip_\nu} U_\nu(x + a\hat{\mu})) \psi(x + a\hat{\mu} + a\hat{\nu}) \\ & \rightarrow \psi^\dagger(x) e^{-\mathbf{p} \cdot \mathbf{x}} U_\mu(x) U_\nu(x + a\hat{\mu}) e^{-\mathbf{p} \cdot (\mathbf{x} + a\hat{\mu} + a\hat{\nu})} \psi(x + a\hat{\mu} + a\hat{\nu}). \end{aligned} \quad (4.33)$$

(4.32) is how external momenta is simulated in the calculations in this thesis.

4.2 Analysis of Correlation Functions

Once correlation functions like $C_{\mathbf{p}}(t_0, t)$ and $C_{\mathbf{p}}(t_0, t, T)$ have been computed on the lattice (typically one computes these quantities for all possible t), how can we extract physics from them?

4.2.1 Fitting Correlation Functions

Typically 2-point correlators are used to find masses and decay constants of the propagating meson. One performs a χ^2 -fit of the correlator to a theoretically motivated function of t . To derive such a function, we use a complete set of momentum \mathbf{p} states -

$$1 = \sum_{n=0} \frac{1}{2E_n} |\lambda_n\rangle\langle\lambda_n|, \quad (4.34)$$

where E_n are the energies of each state. Inserting this into the correlation function, and moving from the Heisenberg to Schrödinger picture;

$$\begin{aligned} C_{\mathbf{p}}(t) &= \sum_{n=0} \frac{1}{2E_n} \langle \Omega | \left(e^{Ht} + e^{H(T_{\text{lat}}-t)} \right) \Phi(\mathbf{p}, 0) \left(e^{-Ht} + e^{-H(T_{\text{lat}}-t)} \right) | \lambda_n \rangle \\ &\quad \times \langle \lambda_n | \Phi^\dagger(\mathbf{p}, 0) | \Omega \rangle \\ &= \sum_{n=0} \left(\frac{\langle \Omega | \Phi(\mathbf{p}, 0) | \lambda_n \rangle}{\sqrt{2E_n}} \right) \left(\frac{\langle \lambda_n | \Phi^\dagger(\mathbf{p}, 0) | \Omega \rangle}{\sqrt{2E_n}} \right) \left(e^{-\bar{E}_n t} + e^{-\bar{E}_n (T_{\text{lat}}-t)} \right) \\ &\equiv \sum_{n=0} |a_n|^2 f(\bar{E}_n, t) \quad , \quad f(E, t) = \left(e^{-Et} + e^{-E(T_{\text{lat}}-t)} \right), \end{aligned} \quad (4.35)$$

where $T_{\text{lat}} = aN_t$ is the temporal extent of the lattice. We have here set $t_0 = 0$ for clarity. The fit results in a determination of the parameters a_n , and \bar{E}_n . In all of our calculations we use $n \in [0, 5]$. The sum over n will be populated only by states $|\lambda_n\rangle$ with the same quantum numbers as Φ , since $\langle \Omega | \Phi | \lambda_n \rangle$ would vanish otherwise. We can then interpret $|\lambda_0\rangle$ to be the ground state of the meson we are studying. The exponential decays mean the fit function is dominated by the ground state at large t , and subsequent excited states become less important as n increases. Hence by only including $C_{\mathbf{p}}(t)$ at suitably large t values, we can afford to truncate the sum in n . In our fits we use $n \in [0, 5]$.

We maintain a distinction between \bar{E}_n and E_n , since for example in calculations involving NRQCD quarks these differ - \bar{E}_n is not the relativistic energy but rather goes like $\mathbf{p}^2/2m$.

If this is not an issue, as is the case with HISQ, one can compute the correlation function at zero momentum $C_0(t)$, then fit it to find the parameter \bar{E}_0 , which will equal the meson's mass M . a_n can be related to the meson's decay constant. For example for a pseudoscalar meson; via the definition of a meson decay constant (2.25) and the Ward identity in (2.55), we find

$$f_M = (m_a - m_b) \sqrt{\frac{2}{M^3}} \left(\frac{a_0}{a^{3/2}} \right). \quad (4.36)$$

The above discussion can be straightforwardly generalized to 3-point correlation functions, from which we are able to extract quantities like the hadronic transition amplitudes $\langle M'|J_\mu|M\rangle$, from which we can determine semileptonic form factors.

The generalization of the above for 3-point correlators is

$$\begin{aligned} C_3(t, T) &= \sum_{n,m} \left(\frac{\langle 0|\Phi_{M'}|\lambda_n\rangle}{\sqrt{2E_{M,n}}} \right) \left(\frac{\langle \lambda_n|V_\mu|\lambda_m\rangle}{2\sqrt{E_{M,n}E_{M',m}}} \right) \left(\frac{\langle \lambda_m|\Phi_M^\dagger|0\rangle}{\sqrt{2E_{M,n}}} \right) \\ &\quad \times f(\bar{E}_{M',m}, T-t)f(\bar{E}_{M,n}, t) \\ &\equiv \sum_{n,m} a_{M',n} J_{nm} a_{M,m}^* f(\bar{E}_{M',m}, T-t)f(\bar{E}_{M,n}, t). \end{aligned} \quad (4.37)$$

$a_{M,n}$ will vanish for states $|\lambda_n\rangle$ which have different quantum numbers to Φ_M , and similarly for $a_{M',m}$ and $\Phi_{M'}$. Non-zero $a_{M,n}$'s will match the analogous parameters extracted from fitting a 2-point function $\langle \Phi_M^\dagger \Phi_M \rangle$, similarly for $a_{M',m}$'s and $\Phi_{M'}$. This carries on to the energies, $\{\bar{E}_{M,n}\}$ is the spectrum for the M' meson, and $\{\bar{E}_{M',m}\}$ is the spectrum for the M . Therefore, we compute and fit the appropriate 2-point functions to deduce the parameters $\{a_{M',n}\}, \{\bar{E}_{M',n}\}$. Then, fitting $C_p(t, T)$ results in an accurate determination of the remaining free parameters, J_{nm} . This set contains the transition amplitude one is interested in $\langle M'|J_\mu|M\rangle$, recognising that

$$J_{00} = \frac{\langle M'|J_\mu|M\rangle}{2\sqrt{E^M E^{M'}}}. \quad (4.38)$$

Oscillating States

In the case of staggered quarks, these fit functions must be modified to contain the effects of the so-called *oscillating states*. The oscillating states are the $\zeta = (1, 0, 0, 0)$ taste. No other tastes contribute, since Φ_p has a 3-momentum fixed at p , which we always take to be small relative to π/a , hence does not couple to the states at $k \sim (0, \pi/a, 0, 0)$, $k \sim (0, 0, \pi/a, 0)$ etc. However, Φ_p can couple to arbitrarily high energy states, so the $k \sim (\pi/a, 0, 0, 0)$ doubler contributes. The contribution of this extra taste to $\Phi_M = \bar{\psi}' \gamma_M \psi$ can be found by shifting it down to energies around p via the doubling transform $\psi \rightarrow (i\gamma_5 \gamma_0)(-1)^{t/a} \psi$. So for example if M is a pseudoscalar the extra taste is $\Phi_M \rightarrow i(-1)^{t/a} \bar{\psi} \gamma_0 \psi$, a scalar meson with a phase $(-1)^{t/a}$.

There is a special case where oscillating states do not contribute. If the two quarks in Φ_M are degenerate (have the same flavour, momentum etc.) then the doubling symmetry acts on both ψ and ψ' . If M is a pseudoscalar, $\gamma_M = \gamma_5$, then

the effect of the doubling symmetry cancels, and no oscillating states contribute.

$$\bar{\psi} \gamma_5 \psi \rightarrow -(-1)^{2 \times t/a} \bar{\psi} (i \gamma_5 \gamma_0) \gamma_5 (i \gamma_5 \gamma_0) \psi = \bar{\psi} \gamma_5 \psi. \quad (4.39)$$

Accounting for oscillating states modifies the fit functions to

$$C_{\mathbf{p}}(t)|_{\text{fit}} = \sum_{j=0}^{N_{\text{exp}}} |a_j|^2 f(\bar{E}_j, t) + (-1)^{t/a} |a_{j,o}|^2 f(\bar{E}_{j,o}, t) \quad (4.40)$$

$$\begin{aligned} C_3(t, T)|_{\text{fit}} = & \sum_{j,k=0}^{N_{\text{exp}}, N_{\text{exp}}} \left(a_j^M J_{jk}^{nn} a_k^{M'} f(\bar{E}^{H_s}, t) f(\bar{E}_n^{M'}, T-t) \right. \\ & + a_j^{M,o} J_{jk}^{on} a_k^{M'} (-1)^t f(\bar{E}_n^{M,o}, t) f(\bar{E}^{M'}, T-t) \\ & + a_j^M J_{jk}^{no} a_k^{M',o} (-1)^{T-t} f(\bar{E}^M, t) f(\bar{E}_n^{M'*}, T-t) \\ & \left. + a_j^{M,o} J_{jk}^{oo} a_k^{M',o} (-1)^T f(\bar{E}_n^{M,o}, t) f(\bar{E}^{M',o}, T-t) \right). \end{aligned} \quad (4.41)$$

We use the `CorrFitter` package [97] for performing Bayesian least-squares fitting to the correlation functions. The package employs the trust region method of least-squares fitting. The Bayesian approach, including the formalism used to set priors for the fits, was introduced in [98].

The fitter uses the trust region algorithm for non-linear multivariate fits. Given a fit function $f_\rho(x)$ with parameters $\{\rho_\alpha\}$, a set of indices $\{x_i\}$, and a set of corresponding observations $\{y_i\}$, with a covariance matrix σ_{ij}^y , the fitter minimizes

$$\chi^2 = \sum_{ij} (f_\rho(x_i) - y_i) \sigma_{ij}^{-2} (f_\rho(x_j) - y_j). \quad (4.43)$$

In our case, x_i is the set of times t , y_i are the correlators $C_{\mathbf{p}}(t)$, and ρ_α are a_n, E_n, J_{nm} . Using this χ^2 means we take into account all correlations between different timeslices t , and between different correlators.

A common problem for large fits such as those performed here is that the data's covariance matrix $\sigma_{C_i(t), C_j(t')}$ can be somewhat singular if there are strong correlations in the data. This makes it difficult to find $\sigma_{C_i(t), C_j(t')}^{-2}$ for use in the χ^2 . To address this we impose an *svd cut* c_{svd} , which replaces any element of the covariance matrix smaller than $c_{\text{svd}} x$ with $c_{\text{svd}} x$, where x is the largest element in the matrix. This makes the matrix less singular, and can be considered a conservative move since the only possible effect on the error of the final results is to inflate them.

4.2.2 Signal Degradation

A large obstacle in the analysis of correlation functions is the *signal degradation* of correlation functions computed on the lattice.

A random variable x has a mean and standard deviation

$$\hat{x} = \langle x \rangle, \quad \sigma^2 = \frac{1}{N}(\langle x^2 \rangle - \langle x \rangle^2), \quad (4.44)$$

where N is the size of the sample. So the (square of) the signal/noise ratio is

$$\frac{\hat{x}^2}{\sigma^2} = N \left(\frac{\langle x^2 \rangle}{\langle x \rangle^2} - 1 \right)^{-1}. \quad (4.45)$$

Consider 2 point correlators where $x = \Phi^\dagger(t)\Phi(0)$, where Φ is some meson operator.

$\langle x^2 \rangle$ and $\langle x \rangle$ can be written as

$$\langle x \rangle = \sum_n \frac{1}{2E_n} \langle 0 | \Phi^\dagger(t) | \lambda_n \rangle \langle \lambda_n | \Phi(0) | 0 \rangle e^{-E_n t} \xrightarrow{t \rightarrow \infty} e^{-E_0 t}, \quad (4.46)$$

$$\langle x^2 \rangle = \sum_n \frac{1}{2E_n} \langle 0 | \Phi^{\dagger 2}(t) | \lambda_n \rangle \langle \lambda_n | \Phi^2(0) | 0 \rangle e^{-E_n t} \xrightarrow{t \rightarrow \infty} e^{-E'_0 t}. \quad (4.47)$$

where we have assumed the ratio of matrix elements and energies are $\mathcal{O}(1)$. The two ground state energies E_0 and E'_0 need not be the same, since the lowest states for which $\langle \lambda_n | \Phi(0) | 0 \rangle \neq 0$ and $\langle \lambda_n | \Phi^2(0) | 0 \rangle \neq 0$ may differ.

The operator Φ^2 will contain two quark and two antiquark operators, connected by some matrices in spin space. Φ^2 can create a combination of all possible 2 meson states where the mesons are made of the available quark species, and quantum numbers. For example, for 2-point D -meson correlators ($c\bar{d}$ pseudoscalars), $E'_0 = (M_\pi + M_{\eta_c})$. Plugging $E_0 = M_{D_s}$ and this E'_0 expression into (4.46),(4.47) and (4.45), we see that D meson correlators have a signal/noise ratio that degrades like

$$\frac{\hat{x}^2}{\sigma^2} \propto e^{-(M_D - (M_\pi + M_{\eta_c})/2)t}. \quad (4.48)$$

In general, a meson with two valence quarks of very different masses will suffer from this problem. B -mesons suffer more than D -mesons. Adding spacial momentum to one of the quarks in the meson would have the effect of replacing M_D in the above equation with some higher energy E_D , thus exacerbating the problem further.

4.3 Renormalization of Currents

Once one has computed an observable on the lattice, like f_M or $\langle M' | J_\mu | M \rangle$, it needs to be translated into a continuum regularization scheme. Suppose we have some bare operator \mathcal{O}_0 , we expect this to be related to the renormalized operator in \overline{MS} at scale μ , $\mathcal{O}^{\overline{MS}}(\mu)$, via

$$\mathcal{O}^{\overline{MS}}(\mu) = Z^{\overline{MS}}(\mu) \mathcal{O}_0. \quad (4.49)$$

Similarly, in a lattice regularization,

$$\mathcal{O}^{\text{lat}}(1/a) = Z^{\text{lat}}(1/a)\mathcal{O}_0. \quad (4.50)$$

Hence we expect a multiplicative factor between the lattice matrix elements, and the continuum \overline{MS} ones:

$$\langle \mathcal{O} \rangle^{\overline{MS}} = \mathcal{Z}(\mu, 1/a) \langle \mathcal{O} \rangle^{\text{lat}} \quad (4.51)$$

where $\mathcal{Z}(\mu, 1/a) = Z^{\overline{MS}}(\mu)/Z^{\text{lat}}(1/a)$. These “matching factors” \mathcal{Z} can be deduced by equating observables calculated in both lattice QCD and continuum (appropriately regularized) QCD, producing equations which can be solved for \mathcal{Z} . The lattice side of the calculation can be done either through lattice perturbation theory (*perturbative matching*), or through a lattice calculation (*non-perturbative matching*).

The result that conserved (or partially conserved) currents (and densities connected to those currents via Ward identities) do not receive any renormalization in any scheme, i.e. $Z^{\text{any}} = 1$. They are said to be *absolutely normalized*.

In principle this is of great help, since the currents that mediate semileptonic decays, e.g. the weak vector and axial currents, are partially conserved, so we are not required to include any matching factors. However, in practice, this is complicated by the fact that the conserved current in the lattice theory is often computationally difficult or impossible to compute. For example, in NRQCD, the partially conserved current corresponding to $SU(N)_V$ is an infinite sum in $1/m_b$ where m_b is the bottom mass. The corresponding current in HISQ is also the sum of a large number of operators. This can be interpreted as a mixing in the renormalization:

$$\langle \mathcal{O}_i \rangle^{\overline{MS}} = \mathcal{Z}_{i,j} \langle \mathcal{O}_j \rangle^{\text{lat}} \quad (4.52)$$

Lattice calculations often use only the dominant operators that contribute to the conserved current. Since these will be “close” to the conserved current, one can expect the matching factor to only be a small deviation from unity, and the more sub-dominant operators you add, the overall matching factor should tend towards unity.

CHAPTER 5

b-Physics from Lattice NRQCD

This chapter gives some detail about a number of project attempted using the NRQCD formalism for the b quark. Much of the discussion in this chapter will concern the NRQCD-HISQ representation of the vector and axial $b \rightarrow c$ currents, i.e, the current if one of the quarks obeys NRQCD and the other obeys HISQ. We give a number of attempts to improve the normalization of these currents (sections 5.2 and 5.4) and an attempt at a calculation of the $B \rightarrow Dl\nu$ and $B_s \rightarrow D_s l\nu$ form factors (Sec. 5.3).

None of the work in this chapter reached a particularly satisfying conclusion. The takehome is that using NRQCD for $b \rightarrow c$ currents is riddled with issues. If it can be computationally afforded, an alternative approach like heavy-HISQ is a far simpler and has a stronger grounding.

5.1 NRQCD-HISQ currents

Much of this chapter concerns the nature of the NRQCD-HISQ current, a current with one NRQCD quark and one HISQ quark. To construct such a current, both the HISQ c and NRQCD b must be transformed into 4-component spinors such that they can be contracted with one-another in the current. The staggered c -quark χ_c is simply related to the naive spinor ψ_c by $\psi_c(x) = \gamma_x \chi_c(x)$. The NRQCD b , $\Psi_b = (\Psi_+, 0)$, is a 2-component spinor related to the 4-component spinor ψ_b via an inverse Fouldy-Wouthuysen transform $\psi_b = \exp(-\gamma \cdot \nabla / 2m_b) \Psi_b$.

Due to the Fouldy-Wouthuysen transform, a current $\bar{\psi}_c \Gamma \psi_b$ (where Γ is some product of gamma matrices) will be made of an infinite sum of lattice currents in terms of Ψ_b , $\bar{\psi}_c \Gamma \psi_b \sim \sum_j (1/m_b^j) \sum_k \bar{\psi}_c \mathcal{O}^{j,k} \Psi_b$. However, this is only half the story - as additionally to the contribution at tree-level from the Fouldy-Wouthuysen expansion, matching the lattice NRQCD theory to continuum QCD gives radiative corrections to this series. Relating continuum QCD currents to lattice NRQCD-HISQ currents causes a 'mixing' of operators as described in Sec. 4.3.

So a continuum current J_μ is constructed from a series of the form

$$J_\mu = \sum_{j,k} c_j(\alpha_s, am_b) \frac{1}{(2m_b)^j} \bar{\psi}_c \mathcal{O}^{j,k} \Psi_b. \quad (5.1)$$

where j sums over powers of inverse b -mass and k sums over all operators of dimension j . The coefficients $c_j(\alpha_s, am_b)$ are fixed by matching appropriate transition amplitudes in 1-loop continuum QCD and the lattice NRQCD/HISQ theory. The vector and axial vector currents take the general form [99];

$$\begin{aligned} J_\mu &= (1 + z_0^{J_\mu} \alpha_s) J_{\mu,\text{lat}}^{(0)} + (1 + z_1^{J_\mu} \alpha_s) J_{\mu,\text{lat}}^{(1)} \\ &\quad + \alpha_s \sum_{n=2}^4 z_n^{J_\mu} J_{\mu,\text{lat}}^{(n)} + \mathcal{O}(\alpha_s^2, (\Lambda_{\text{QCD}}/m_b)^2, (p/m_b)^2), \\ J_{\mu,\text{lat}}^{(0)} &= \bar{\psi}_c \Gamma_\mu \Psi_b, \quad J_{\mu,\text{lat}}^{(1)} = -\frac{1}{2am_b} \bar{\psi}_c \Gamma_\mu \gamma \cdot \nabla \Psi_b, \\ J_{\mu,\text{lat}}^{(2)} &= -\frac{1}{2am_b} \bar{\psi}_c \gamma \cdot \overset{\leftarrow}{\nabla} \Gamma_\mu \Psi_b, \quad J_{\mu,\text{lat}}^{(3)} = -\frac{1}{2am_b} \bar{\psi}_c \Gamma_0 \nabla_\mu \Psi_b, \\ J_{\mu,\text{lat}}^{(4)} &= \frac{1}{2am_b} \bar{\psi}_c \overset{\leftarrow}{\nabla}_\mu \Gamma_0 \Psi_b. \end{aligned} \quad (5.2)$$

where Γ_μ is the continuum spin structure (e.g. for A_μ ; $\Gamma_\mu = \gamma_5 \gamma_\mu$) and p is the spacial momentum of the c quark in the current. The last two currents $J_{\mu,\text{lat}}^{(3)}$ and $J_{\mu,\text{lat}}^{(4)}$ do not appear in the temporal current J_0 , $z_{3,4}^{J_0} = 0$.

A subset of the matching factors $\{z^{J_\mu}\}$ have been calculated for V_μ and A_μ in [100] via a perturbative matching calculation. In the case where the 'light' quark has a negligible mass (e.g. if we replaced the charm with an s , u or d), results for $z_{0,1,2}^{J_\mu}$ are available for both V_μ and A_μ . However, in the $b \rightarrow c$ case the c mass must be taken into account which complicates the calculation. In this case, only $z_0^{J_\mu}$ is available. To sidestep this, in studies using these currents an extra truncation in $\alpha_s p/m_b$ is added resulting in

$$\begin{aligned} J_\mu &= (1 + z_0^{J_\mu} \alpha_s) (J_{\mu,\text{lat}}^{(0)} + J_{\mu,\text{lat}}^{(1)}) \\ &\quad + \mathcal{O}(\alpha_s \Lambda_{\text{QCD}}/m_b, \alpha_s p/m_b, \alpha_s^2, (\Lambda_{\text{QCD}}/m_b)^2, (p/m_b)^2). \end{aligned} \quad (5.3)$$

One will often then also compute $\langle J_{\mu,\text{lat}}^{(2,3,4)} \rangle$ in the lattice calculation to check that their magnitude is suitably small such that they can be ignored.

5.2 Relativistic Normalisation of the $b \rightarrow c$ temporal axial current

In this small project we tested to see if a B_c meson containing a HISQ c quark and a (relativistically corrected) NRQCD b quark obeys a relativistic dispersion relation. The goal of this was to

- Provide a consistency check for the NRQCD-HISQ current truncation and normalizations (described in the last section) for the temporal axial current A_0 .
- Determine $z_{1,2}^{A_0}$ for the $b \rightarrow c$ case by demanding the relativistic dispersion relation is obeyed.

To test this process we originally computed B_c (pseudoscalar with b and c valence quarks) 2-point correlation functions on the fine ensemble (set 2 on table 7.1). The interpolating operators for creating/annihilating the (momentum space) B_c meson take the form

$$\tilde{\Phi}_n^\alpha(\mathbf{p}, t) = \sum_{\mathbf{x}, \mathbf{x}'} e^{-i\mathbf{p}\cdot\mathbf{x}} \bar{\psi}_c(\mathbf{x}, t) \phi^\alpha(\mathbf{x} - \mathbf{x}') \mathcal{O}_n \Psi_b(\mathbf{x}', t). \quad (5.4)$$

We choose \mathcal{O}_n to produce the current operators in eq. (5.2): $\mathcal{O}_0 = \gamma_0 \gamma_5$, $\mathcal{O}_1 = -\gamma_0 \gamma_5 \gamma \cdot \nabla / 2m_b$, $\mathcal{O}_2 = -\gamma \cdot \overleftarrow{\nabla} \gamma_0 \gamma_5 / 2m_b$. These have the same quantum numbers as the B_c meson so serve as suitable interpolating operators, but also probe the individual pieces of the NRQCD-HISQ $b \rightarrow c$ axial current.

In the interest of better statistics, we also here use a family of spacial *smearing* functions $\phi^\alpha(\mathbf{x} - \mathbf{x}')$:

$$\phi^0(\mathbf{y}) = \delta_{\mathbf{y}}, \quad \phi^{n>0}(\mathbf{y}) = e^{-|\mathbf{y}|/a_{\text{sm}}^n}. \quad (5.5)$$

where $a_{\text{sm}}^1 = 3a$ and $a_{\text{sm}}^2 = 6a$. The $n > 0$ smearing functions represent a stationary b quark with a wavefunction for the c that exponentially decays with the radius from the b . Using these increase the overlap with the B_c meson state $\langle \Omega | \tilde{\Phi}_n^\alpha | B_c \rangle$, which decreases the overlap with excited states therefore decreasing the contribution of excited states to the correlation functions. One can then afford to use timeslices closer to the source, increasing statistics.

The NRQCD-HISQ correlation functions are then generated using

$$C_{nm}^{\alpha\beta}(\mathbf{p}, t) = \left\langle \sum_{\mathbf{x}, \mathbf{x}'} \phi^\beta(\mathbf{x} - \mathbf{x}') \text{Tr}_c \left[P_{c,\mathbf{p}}^{\alpha,n}(\mathbf{x}', t) \text{Tr}_s \left(\gamma_x^\dagger \mathcal{O}_m P_{b,0}^{\alpha,n}(\mathbf{x}, t) \right) \right] \right\rangle. \quad (5.6)$$

$P_{b,0}^n$ is a propagator of the form (4.20), made from a random wall source at $t = t_0$ with momentum 0, operator \mathcal{O}_n and an NRQCD b propagator generated using (3.55). $P_{c,\mathbf{p}}^\alpha$ is a propagator built from a random source with momentum \mathbf{p} , smearing function ϕ^α , and a HISQ c propagator. Tr_s is a trace over spin and Tr_c is over color.

We generated these correlators on 500 configurations and 16 evenly spaced choices for t_0 . We obtained correlators at 3 different spacial momenta, $\mathbf{p} = 0, 3\pi/32(1, 1, 1), 5\pi/32(1, 1, 1)$, using momentum twists $\theta = 0, 3, 5$ in each direction.

These are then fitted to the fit functions

$$C_{nm}^{\alpha\beta}(t)|_{\text{fit}} = \sum_{j=0}^{N_{\text{exp}}} \left(a_j^{\alpha,n} a_j^{\beta,m} f(\bar{E}_j, t) + (-1)^{t/a} a_{j,o}^{\alpha,n} a_{j,o}^{\beta,m} f(\bar{E}_{j,o}, t) \right). \quad (5.7)$$

See sec. 4.2.1 for definitions of f and \bar{E} . One can recognise that

$$a_0^{\alpha,n} = \frac{\langle \Omega | \tilde{\Phi}_n^\alpha | B_c \rangle}{\sqrt{2E_{B_c}}}. \quad (5.8)$$

In the $\alpha = 0$ case, the matrix elements become $\langle \Omega | \bar{\psi}_c \mathcal{O}_n \Psi_b | B_c \rangle$, by correctly combining these like in eq (5.2), this should produce $\langle \Omega | A_0 | B_c \rangle$. We will show how these quantities are used to test the A_0 normalisation after this breif detour.

Kinetic Mass

In order to perform the test, we require a determination of the B_c mass. If we were using a fully relativistic action, one could simply consider \bar{E}_0 (with $\mathbf{p} = 0$) to be the mass. However, in our case one would expect NRQCD to cause a shift in energy E_s due to the effective removal of the first term in eq. (3.54), so

$$\bar{E}_0(\mathbf{p}) = E_s + \sqrt{\mathbf{p}^2 + M_{B_c}^2}. \quad (5.9)$$

We can deduce M_{B_c} in this case by taking the difference of energies at different momenta $\delta\bar{E}_0(\mathbf{p}) \equiv \bar{E}_0(\mathbf{p}) - \bar{E}_0(0)$, leading to

$$aM_{\text{kin}} = \frac{\mathbf{p}^2 - \delta\bar{E}_0^2(\mathbf{p})}{2\delta\bar{E}_0(\mathbf{p})}, \quad (5.10)$$

which one would expect to be invariant of \mathbf{p} . In fig. 2, the mass is deduced from different $\delta\bar{E}_0(\mathbf{p})$. M_{kin} is referred to as the *kinetic mass* of the B_c meson.

Using \bar{E}_0 results from the fit, we find $aM_{\text{kin}}^{\theta=3} = 2.8394(60)$, from the $\theta = 3$ point, and $aM_{\text{kin}}^{\theta=5} = 2.858(11)$ from the $\theta = 5$ point. Taking the mean of these we find

$$aM_{\text{kin}} = 2.8488(66). \quad (5.11)$$

Decay Amplitude Ratios

At leading order in $1/m_b$ and α_s , the temporal axial current is recreated using simply $a_0^{0,0} = \langle \Omega | A_0 | B_c \rangle / \sqrt{2M_{B_c}}$. Recalling the definition of the decay constant for a pseudoscalar meson: $\langle \Omega | A_\mu | M \rangle = p_\mu f_M$, we see that

$$a_0^{0,0} = f_{B_c} \sqrt{\frac{E_{B_c}}{2}}. \quad (5.12)$$

Assuming a relativistic dispersion relation $E^2 = \mathbf{p}^2 + M^2$, taking the ratio of $a_0^{0,0}$ at non-zero and zero momenta results in

$$\frac{a_0^{0,0}(\mathbf{p})}{a_0^{0,0}(0)} = \sqrt{\frac{E_{B_c}(\mathbf{p})}{M_{B_c}}} = 1 + \frac{\mathbf{p}^2}{4M_{B_c}^2} + \mathcal{O}\left(\frac{\mathbf{p}^4}{M_{B_c}^4}\right). \quad (5.13)$$

This is our probe of the dispersion relation of the B_c meson, we take the ratio of fit parameters on the left hand side, and compare to the expected dependence of \mathbf{p}^2 on the right hand side. This comparison is shown between the blue line and the grey dotted line in Fig. 5.1. We have used the kinetic mass (5.11) for the M_{B_c} mass here.

One can add $\mathcal{O}(1/m_b)$ corrections to this ratio by replacing $a_0^{0,0}$ with

$$\begin{aligned} a_0^{(0)}(\mathbf{p})\sqrt{2E_{B_c}(\mathbf{p})} &= \langle \Omega | A_{0,\text{lat}}^{(0)} | B_c(\mathbf{p}) \rangle \\ a_0^{(1)}(\mathbf{p})\sqrt{2E_{B_c}(\mathbf{p})} &= \langle \Omega | (1 + z_0^{A_0} \alpha_s) [A_{0,\text{lat}}^{(0)} + A_{0,\text{lat}}^{(1)}] | B_c(\mathbf{p}) \rangle \\ a_0^{(2)}(\mathbf{p})\sqrt{2E_{B_c}(\mathbf{p})} &= \langle \Omega | [(1 + z_0^{A_0} \alpha_s) A_{0,\text{lat}}^{(0)} + (1 + z_1^{A_0} \alpha_s) A_{0,\text{lat}}^{(1)} \\ &\quad + z_2^{A_0} \alpha_s A_{0,\text{lat}}^{(2)}] | B_c(\mathbf{p}) \rangle. \end{aligned} \quad (5.14)$$

we have here set the $\alpha = 0, n$ superscripts implicit to make room for the new superscripts. The lattice currents $A_{0,\text{lat}}^{(n)}$ are those defined in 5.2 for the temporal axial vector case. $a_0^{(0)}$ recreates the A_0 current to leading order in α_s and $1/m_b$, $a_0^{(1)}$ recreates A_0 up to $\mathcal{O}(\alpha_s \Lambda_{\text{QCD}}/m_b, \alpha_s p/m_b, \alpha_s^2, (\Lambda_{\text{QCD}}/m_b)^2, (p/m_b)^2)$, and $a_0^{(2)}$ is up to $\mathcal{O}(\alpha_s^2, (\Lambda_{\text{QCD}}/m_b)^2, (p/m_b)^2)$.

Since the $z_0^{A_0}$ value is immediately available from [100], we can show the result of taking the ratio $a_0^{(1)}(\mathbf{p})/a_0^{(0)}$ as the red line in Fig. 5.1. As can be seen, this pushes the ratio in the wrong direction, away from the relativistic dispersion relation line.

We can determine values for $z_1^{A_0} - z_0^{A_0}$ and $z_2^{A_0} - z_0^{A_0}$ by demanding that $a_0^{(2)}(\mathbf{p})/a_0^{(0)}(0) = 1 + \mathbf{p}^2/4M_{\text{kin}}^2$. Then, using the known $z_0^{A_0}$ values from perturbative matching we find

$$z_1^{A_0} = -3.746267(95), \quad z_2^{A_0} = -0.0002429(95). \quad (5.15)$$

$z_1^{A_0}$ here is required to be unnaturally large to overcome the suppression of α_s and drag the ratio downwards.

The above analysis shows that the truncation of NRQCD-HISQ temporal-axial current used in current calculations is not sufficient to create a meson obeying a relativistic dispersion relation. This is indicative that further orders in the expansion are in fact important and should be included in lattice calculations.

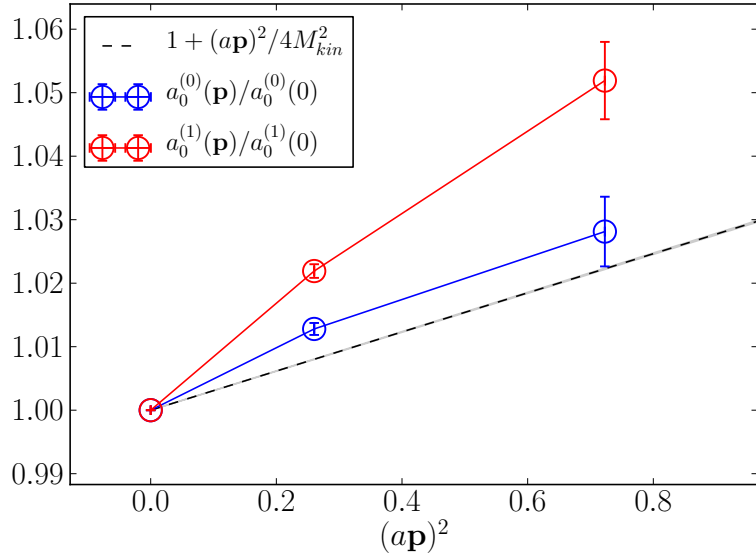


Figure 5.1: Decay amplitude ratios (colourful points) against the expected relativistic behaviour (grey dotted line and band). Adding the $A_{0,\text{lat}}^{(1)}$ piece of the current does not improve the relativistic behaviour of the ratio.

5.3 $B_{(s)} \rightarrow D_{(s)} l \nu$ form factors

We attempted a calculation of the $B \rightarrow D l \nu$ and $B_s \rightarrow D_s l \nu$ form factors, $f_{0,+}(q^2)$ and $f_{0,+}^s(q^2)$, using the 2+1+1 MILC ensembles, HISQ l,s and c valence quarks, and an NRQCD valence b quark. This study was similar to previous studies of $B \rightarrow D l \nu$ form factors [11] and $B_s \rightarrow D_s l \nu$ form factors [101]. The main difference between this study and the previous studies was that they used older MILC ensembles not taking the charm into account in the sea.

This study was not completed on account of two seemingly insurmountable problems:

- The subleading terms in the vector NRQCD-HISQ current that we must ignore due to the lack of perturbative normalizations, $V_k^{(3,4)}$, turned out to be significant in magnitude.
- On one ensemble in the $B_s \rightarrow D_s l \nu$ case, there was an anomalous result for the vector current matrix element extracted from the correlator fits.

We give an outline of the calculation here for completeness, but the crucial findings of this section are these two issues.

5.3.1 Calculation Details

Set	handle	am_{s0}	am_{c0}	am_{b0}	u_0	$c_{1,6}$	c_5	c_4	$\{T\}$	a_{sm}/a
0	very coarse	0.0705	0.826	3.297	0.8195	1.36	1.21	1.22	8, 11, 14	0, 2.0, 4.0
1	coarse	0.0541	0.645	2.66	0.8340	1.31	1.16	1.20	9, 12, 15	0, 2.0, 4.0
2	fine	0.0376	0.450	1.91	0.8525	1.21	1.12	1.16	14, 19, 24	0, 3.425, 6.85

Table 5.1: Parameters used in our calculation. am_{s0} and am_{c0} are the bare masses of the strange, charm valence quarks, tuned in [102], am_{b0} is the bare mass of the valence bottom quark, tuned in [76] u_0 is the 'tadpole improvement parameter' as used in [76]. $\{c_i\}$ are the coefficients for the kinetic and chromomagnetic terms in the NRQCD action (eq. (3.58)) [103]. $\{T\}$ is the set of temporal separations between source (B_s creation operator) and sink (D_s annihilation operator). a_{sm} are the radii of the exponential smearing function applied to the $B_{(s)}$ and $D_{(s)}$ creation operators.

We generated correlation functions on three MILC ensembles, sets 0, 1 and 2 in table 7.1. When using the NRQCD action, we are limited to the coarser end of the spectrum of ensembles, since in the $a \rightarrow 0$ limit subleading terms in δH (eq. (3.58)) and $J_\mu^{(n>0)}$ (eq. (5.2)) diverge. However, NRQCD discretisation effects are small relative to other discretizations due to the lack of the b rest mass, so we can afford to use coarser lattices. Also, obviously, using coarse lattices means the project is computationally inexpensive. The bare parameters used to generate the correlation functions are shown in table 5.1.

We generate 2-point correlation functions for $B_{(s)}$ and $D_{(s)}$ mesons, and 3-point correlators between $B_{(s)}$ and $D_{(s)}$ creation/annihilation operators with $V_\mu^{(n)}$ currents

inserted for all μ and $n = 0, 1, 2, 3, 4$. For the $B_{(s)}$ operator we use smearings like those introduced in eq. (5.5), smearing radii a_{sm} are given in table 5.1.

The $B_{(s)}$ 2-point correlators, $C_{B_{(s)}}^{\alpha\beta}(t)$ are generated using eq. (5.6), with the charm propagator replaced with a strange or light propagator, and $\mathcal{O}_m = \gamma_0\gamma_5$. We generate $D_{(s)}$ 2-point correlators at a number of spacial momenta $\{\mathbf{p}\}$, generated by

$$C_{D_{(s)}}^{\alpha\beta}(\mathbf{p}, t) = \sum_{\mathbf{x}, \mathbf{y}} \phi^\alpha(\mathbf{x})\phi^\beta(\mathbf{y}) \text{Tr}_c[g_c^\theta(x, y)g_{l(s)}^\dagger(x, y)]. \quad (5.16)$$

where $\phi^\alpha(\mathbf{x})$ are the smearing functions defined in eq. (5.5), $g_{l(s)}$ are light or strange staggered propagators, and g_c^θ is a charm staggered propagator with momentum twist θ . Tr_c is over color.

We generate 3-point correlators for each individual piece of the NRQCD-HISQ currents, and each chosen $D_{(s)}$ spacial momentum, using

$$C_{V_\mu^{(n)}}^{\alpha\beta}(\mathbf{p}, t, T) = \sum_{\mathbf{x}, \mathbf{y}, \mathbf{z}} \text{Tr}_c \left(g_c^\theta(x, y)g_{l(s)}^\dagger(x, z) \text{Tr}_s [\gamma_0\gamma_x\gamma_y\mathcal{O}_{n,\mu}G_b(y, z)\gamma_z] \right). \quad (5.17)$$

$\mathcal{O}_{n,\mu}$ are defined by $J_\mu^{(n)} = \bar{\psi}_c\mathcal{O}_{n,\mu}\Psi_b$, where $J_\mu^{(n)}$ are the NRQCD-HISQ vector currents given in Eq. (5.2). The list of twists we ran on each ensemble is given in table 5.2. Due to the signal/noise degradation of the $D_{(s)}$ correlators as one adds more spacial momentum, our lattice data was limited to the high q^2 region. One motivation for this study was to test how far down the q^2 range we could reach with lattice data before the noise in the correlators made the data useless.

	Set	θ	$ ap $	$q^2[\text{GeV}^2]$
$B \rightarrow D$	0	0, 0.74, 1.47, 2.20, 2.94	0, 0.25, 0.5, 0.75, 1.00	11.8, 11.6, 10.8, 9.4, 7.3
	1	0, 1.58, 2.24, 4.53	0, 0.36, 0.51, , 1.02	11.8, 10.8, 9.9, 5.0
	2	0, 1.76, 2.64	0, 0.30, 0.49	11.8, 10.7, 9.3
$B_s \rightarrow D_s$	0	0, 0.74, 1.47, 2.20, 2.94	0, 0.25, 0.5, 0.75, 1.03	11.8, 11.6, 10.9, 9.5, 7.6
	1	0, 1.10, 2.20, 3.31, 4.41	0, 0.25, 0.50, 0.75, 1.00	11.8, 11.3, 10.1, 8.1, 5.7
	2	0	0	11.8

Table 5.2: Twists given to the charm propagator on each ensemble.

5.3.2 Correlator Fits

We extract current matrix elements from the generated correlation functions, via simultaneous Bayesian fits as described in Sec. 4.2.1. For the set of 2-point correlators with a number of smearings we use (??), and 3-point correlators are fit to

$$C_3^{\alpha\beta}(t, T)|_{\text{fit}} = \sum_{j,k=0}^{N_{\text{exp}}, N_{\text{exp}}} \left(a_j^M J_{jk}^{nn} a_k^M f(E^{H_s}, t) f(E_n^{M'}, T-t) \right. \\ + a_{\alpha,j}^{M,o} J_{jk}^{on} a_{\beta,k}^{M'} (-1)^t f(E_n^{M,o}, t) f(E^{M'}, T-t) \\ + a_{\alpha,j}^M J_{jk}^{no} a_{\beta,k}^{M',o} (-1)^{T-t} f(E^M, t) f(E_n^{M'*}, T-t) \\ \left. + a_{\alpha,j}^{M,o} J_{jk}^{oo} a_{\beta,k}^{M',o} (-1)^T f(E_n^{M,o}, t) f(E^{M',o}, T-t) \right). \quad (5.18)$$

We set $N_{\text{exp}} = 5$ in each fit. We perform a single simultaneous fit containing each correlator computed for each ensemble.

We set gaussian priors for the parameters J_{jk} , and log-normal priors for all other parameters. Using log-normal distributions forbids energies E_n^M and amplitudes a_n^M from moving arbitrarily close to zero, improving stability of the fit.

Priors for the ground state energies and amplitudes (oscillating and non-oscillating) are set via an empirical Bayes approach, plots of effective masses and amplitudes are inspected to find reasonable central values of priors (see Sec. 6.2.2 for definitions of effective masses and amplitudes), and a generic variance of 10% is given. The typical precision of fit results for these parameters are of order 0.1%, much more precise than their priors. All 3-point transition parameters J_{jk} are given priors of 0 ± 1 .

We typically set $t_{\text{cut}} = 3$ for 2- and 3-point correlators in the fit on the fine ensemble (set 2) and $t_{\text{cut}} = 2$ on very coarse and coarse (sets 0 and 1). For some specific correlators, a larger t_{cut} is necessary to achieve a good fit ($\chi^2/N_{\text{dof}} < 1$), these higher t_{cut} values are always in the 2-8 range. An svd cut is applied in each fit, with a specific choice of cut determined according to what achieves a good fit. The svd-cut is typically of the order 10^{-3} .

The current matrix element we require to find $h_{A_1}^s(1)$ is given by

$$\langle D_s | V_\mu^{(m)} | B_s \rangle|_{\text{lat}} = 2\sqrt{M_{B_s} E_{D_s}} J_{00}^{nn}. \quad (5.19)$$

5.3.3 Form Factors

We construct 'continuum' vector currents $\langle D_{(s)} | V_\mu | B_{(s)} \rangle \equiv \langle V_\mu \rangle$ from the lattice expectation values $\langle D_s | V_\mu^{(n)} | B_s \rangle|_{\text{lat}}$ according to Eq. (5.3), i.e. only including the

first two current pieces $V_\mu^{(0)}$ and $V_\mu^{(1)}$. We also compute $V_0^{(2)}$ and $V_k^{(2,3,4)}$ to assess their size and the validity of ignoring them, this is addressed in sec. !!!.

We take the average over the spacial currents, resulting in two distinct current matrix elements $\langle V_0 \rangle$ and $\langle V_k \rangle$. Then, from Eq. (2.28), we find (defining $M_{B_{(s)}} \equiv M$, $M_{D_{(s)}} \equiv m$, $E_{D_{(s)}} \equiv E$, and $\mathbf{p}_{D_{(s)}} \equiv \mathbf{p}$)

$$\langle V_0 \rangle = f_+^{(s)}(q^2) \left[M + E - \frac{M^2 - m^2}{q^2} (M - E) \right] + f_0^{(s)}(q^2) \frac{M^2 - m^2}{q^2} (M - E) \quad (5.20)$$

$$\langle V_k \rangle = \frac{|\mathbf{p}|}{\sqrt{3}} \left[f_+^{(s)}(q^2) \left(1 + \frac{M^2 - m^2}{q^2} \right) - f_0^{(s)}(q^2) \frac{M^2 - m^2}{q^2} \right] \quad (5.21)$$

By inverting these relations we deduce $f_{0,+}^{(s)}(q^2)$ from $\langle V_0 \rangle, \langle V_k \rangle$ at the lattice spacings of each ensemble.

We aim then to extrapolate these values to $a = 0$ and to all q^2 . We did not obtain any lattice data at smaller light quark masses so cannot extrapolate to the physical light mass. In the $B_s \rightarrow D_s l \nu$ case, the size of such an effect is small (see chapters 6 and 7). In the $B \rightarrow D l \nu$ case, however, this could result in considerable uncontrolled systematic errors.

We parameterise the functional form of $f_{0,+}^{(s)}(q^2)$ using the BGL parameterization [104]. This involves first defining the map

$$z(q^2) = \frac{\sqrt{t_+ - q^2} - \sqrt{t_+ - t_0}}{\sqrt{t_+ - q^2} + \sqrt{t_+ - t_0}} \quad (5.22)$$

where we take $t_0 = t_+(1 - \sqrt{1 - t_-/t_+})$, and $t_\pm = (M_{B_s} \pm M_{D_s})^2$. $z(q^2)$ has a very small magnitude throughout the entire q^2 range, in our case $|z| < 0.032 \forall (\text{physical})q^2$. It can be shown that $f_{0,+}^{(s)}(q^2)$ is analytic in the unit disc of the z -plane. $f_{+,0}^{(s)}(q^2)$ can be expressed as a series expansion in z :

$$f_{0,+}(q^2) = \frac{1}{P_{0,+}(q^2)} \sum_k a_k^{0,+} z(q^2)^k. \quad (5.23)$$

we truncate this at z^2 , adding further terms have no effect on the fit. The so-called Blaschke factors $P(q^2)$ are defined by

$$P_{0,+}(q^2) = \left(1 - \frac{q^2}{M_{0,+}^2} \right) \quad (5.24)$$

These are required due to subthreshold poles in the crossed channel of $\langle D_s | V_\mu | B_s \rangle$, which in our case is a W decay into a B_c meson. The pole is located where the

W has the correct momentum q^2 to create the B_c , hence at $q^2 = M_{B_c}$. This is not within the q^2 range, but can create curvature in $f_{0,+}$ that can confound the expansion in z . $P_{0,+}$ effectively removes this pole from the z expansion.

The discretisation effects in our form factors are controlled for by modifying (5.23):

$$a_n^{0,+} \rightarrow a_n^{0,+} \times (1 + b_n^{0,+}(am_c)^2) \quad (5.25)$$

where $b_n^{0,+}$ are new fit parameters, and m_c is the charm mass. $am_c \rightarrow 0$ in the continuum limit, and, since the charm mass is the largest scale involved in our calculation, it serves as a good order parameter for discretization effects.

5.3.4 Results

The extrapolation of our lattice data to all q^2 and $a = 0$ is illustrated in figures 5.2 and 5.3. As can be seen here, statistical errors in the lattice data increase exponentially with momentum twist (as q^2 decreases). Besides this, the very coarse data suffers from large discretization effects as the twist is increased, pushing the results upwards.

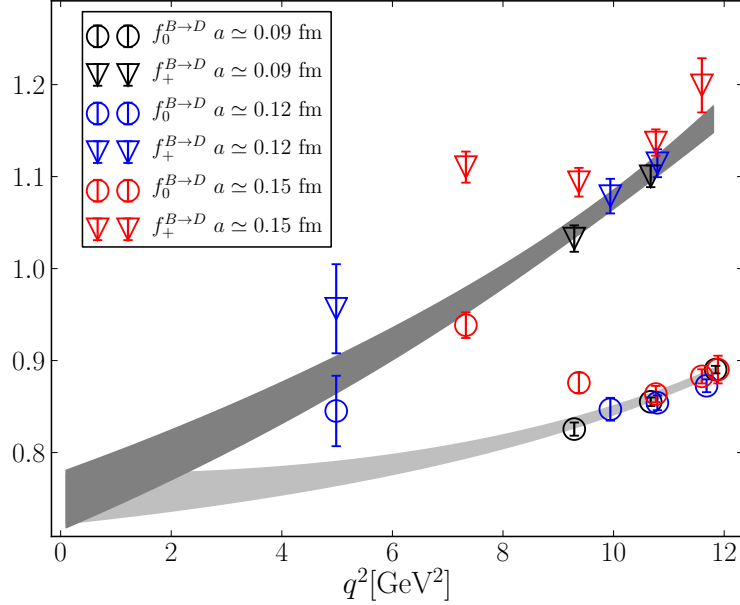


Figure 5.2: $B \rightarrow D l \nu$ form factors. The coloured points show lattice data, each color represents an ensemble. The grey band represents the continuum and kinematically extrapolated result.

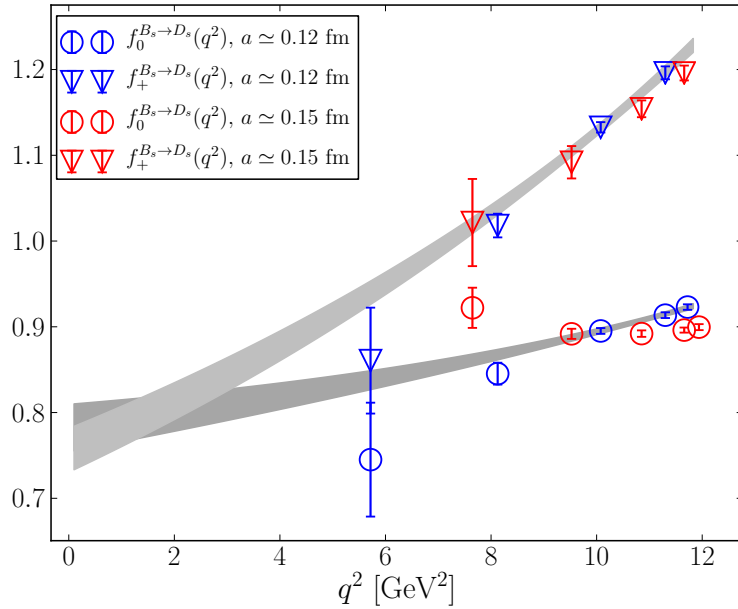


Figure 5.3: $B_s \rightarrow D_s l \nu$ form factors. The coloured points show lattice data, each color represents an ensemble. The grey band represents the continuum and kinematically extrapolated result.

We now go on to discuss the two issues which lead us to abandon this project.

Anomalous Results

In the $B_s \rightarrow D_s l \nu$ case we did not include lattice results from the fine ensemble in the q^2 and $a \rightarrow 0$ extrapolation. This is because the lattice results for $f_0^s(q^2)$ on this ensemble is clearly wrong.

Before the fits to correlation functions takes place we already know the ballpark of what J_{00}^{nn} should be from a couple of sources.

- The result should not vary more than $\mathcal{O}(a^2)$ (where a is the lattice spacing) from the same number on other ensembles.
- The result should not vary more than $\mathcal{O}(am_s - am_l)$ from the same number on the same on ensemble for the $B \rightarrow D$ calculation (Chiral symmetry).

However, we find the fits to q_{\max}^2 data on the fine ensemble produce a result for J_{00}^{nn} that is much larger than expected. This is accompanied by the fits being very unstable, varying by a number of sigma when different combinations of data are included. A number of tests have been carried out to find out exactly what is

causing this issue, but no compelling evidence has emerged for any explanation. Fig. 5.4 illustrates the situation.

it is worth keeping in mind that NRQCD results have no continuum limit, since the action and the currents are truncated sums of inverse masses in lattice units, therefore the truncation error grows like a^{-n} as $a \rightarrow 0$. What we are seeing here may be the result of large $1/(am_b)^2$ corrections to the NRQCD-HISQ current being ignored.

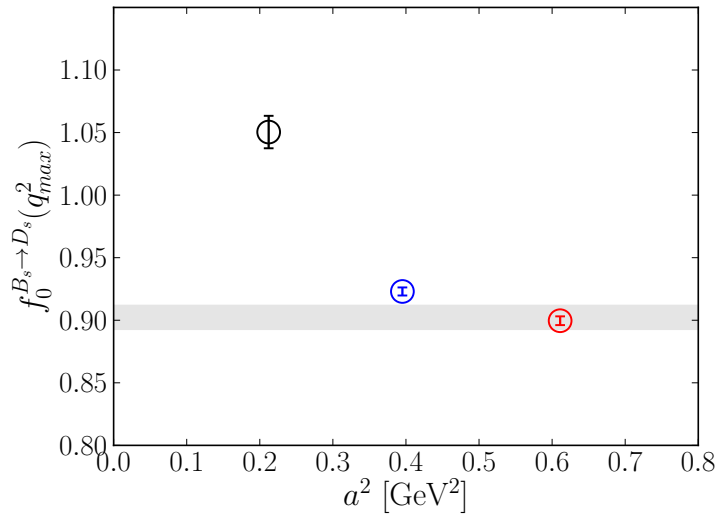


Figure 5.4: Lattice results for $f_0^s(q_{\max}^2)$ against a^2 . The grey band shows the result for $f_0^s(q_{\max}^2)$ computed in chapter 7 using the Heavy-HISQ approach for comparison. Clearly the result on the fine ensemble (the black point), and possibly on the coarse ensemble (the blue point), contain large unknown systematic errors.

Large Subleading Currents

Annother problem that has uncovered itself in the NRQCD calculation is large subleading currents. Namely, the pieces $V_k^{(2,4)}$ of the spacial vector current. We determined these currents as part of the calculation in order to assess if they are suitably small such that they can be ignored. These turned out to have a magnitude $\sim 35\%$ of the leading order.

In Fig. 5.5, we show the ratios of (matrix elements of) NRQCD-HISQ currents in the $B_s \rightarrow D_s$ case. All ratios are between the subleading currents $V_\mu^{(n>0)}$ and the leading order current $V_\mu^{(0)}$, in order to show the size of the subleading currents relative to the leading order. $V_\mu^{(0)}$ is included in our result, so we do not need to

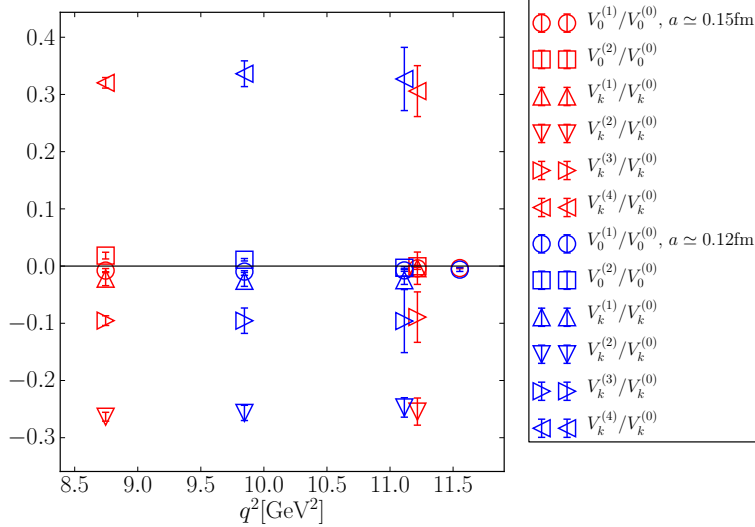


Figure 5.5: Lattice results for the ratios of (matrix elements of) NRQCD-HISQ currents in the $B_s \rightarrow D_s$ case. Namely ratios of the subleading currents $V_\mu^{(n>0)}$ to the leading order current $V_\mu^{(0)}$.

worry about it's size. $V_0^{(2)}$ and $V_k^{(3)}$ are $\lesssim 10\%$ of the leading order, given that these also receive $\mathcal{O}(\alpha_s)$ suppression, their negligence is relatively harmless.

$V_k^{(2,4)}$ however have considerable magnitude. Neglecting them implies a naive systematic error of $\mathcal{O}(35\% \times \alpha_s) \sim 8\%$. This would prevent any results from our calculation from being anywhere near competitive.

Since the problematic current pieces are exclusively part of the spacial vector current, we could remove this problem if we did not rely on the spacial vector current for extracting the form factors. The next section shows our attempt at such an alternative approach.

5.3.5 Form factors from V_0 and S in $B_{(s)} \rightarrow D_{(s)}$

Instead of using $\langle V_0 \rangle$ and $\langle V_k \rangle$ to extract $f_{0,+}^{(s)}(q^2)$, one could in principle instead use the combination $\langle V_0 \rangle$ and $\langle S \rangle$, where S is the scalar $b \rightarrow c$ density. In terms of NRQCD-HISQ currents, S can be written as

$$\begin{aligned} S &= (1 + z_0^S \alpha_s)(V_0^{(0)} - V^{(1)}) \\ &\quad + \mathcal{O}(\alpha_s \Lambda_{\text{QCD}}/m_b, \alpha_s p/m_b, \alpha_s^2, (\Lambda_{\text{QCD}}/m_b)^2, (p/m_b)^2), \end{aligned} \quad (5.26)$$

where z_0^S can be derived from $z_0^{V_\mu}$. Hence we infact already have numerical results for matrix elements of the scalar current, via the vector current pieces $V_0^{(0,1)}$. The scalar and temporal vector currents are related via the parially conserved vector current (PCVC) relation -

$$(M_{B_{(s)}} - E_{D_{(s)}})\langle V_0 \rangle = \delta m \langle S \rangle, \quad (5.27)$$

where $\delta m \equiv (m_b - m_c)$. Using this one can relate the scalar current to the form factors, resulting in a new way to extract form factors via $\langle V_0 \rangle$ and $\langle S \rangle$:

$$f_0^{(s)}(q^2) = \frac{\delta m}{M_{B_s}^2 - M_{D_s}^2} \langle S \rangle, \quad (5.28)$$

$$f_+^{(s)}(q^2) = \frac{1}{2M_{B_s}} \frac{(M_{B_{(s)}} - E_{D_{(s)}})\delta m \langle S \rangle - q^2 \langle V_0 \rangle}{\mathbf{p}_{D_{(s)}}^2}. \quad (5.29)$$

Care must be taken in choosing what masses to use in δm . One may want to use the bare charm and bottom mass, however these belong to different regularization schemes (HISQ and NRQCD), so taking their difference is not well defined. The solution is to use instead $\delta m = m_{b0} \times (1 - m_c/m_b)$, where m_{b0} is the bare b -quark mass used in the NRQCD action, and m_c/m_b is a regularization-independent quantity computed to be $m_c/m_b = 1/4.51(4)$ in [105].

Results from adopting this alternative approach (in the $B \rightarrow D$ case) is shown in fig. 5.6. One immediately notices that $f_+(q^2)$ results are diverging in the $|\mathbf{p}_D| \rightarrow 0$ limit. Why this occurs can be seen by inspecting eq. (5.29). For f_+ to remain finite, the difference between currents on the numerator must tend to zero at the same rate as \mathbf{p}_D^2 . Our results for the currents $\langle S \rangle$ and $\langle V_0 \rangle$ are not precise enough to produce the delicate cancellation required to accurately determine f_+ in the high q^2 region.

Let's summarize the situation. We have 3 currents, $\langle S \rangle$, $\langle V_0 \rangle$, and $\langle V_k \rangle$. We require input from two of these currents in order to determine the form factors. Large contributions to $\langle V_k \rangle$ may be being ignored, so at the moment we do not consider $\langle V_k \rangle$ a 'trustworthy' estimation of the continuum spacial vector current. Using only $\langle S \rangle$ and $\langle V_0 \rangle$ leads to a divergence of $f_+(q^2)$ as $q^2 \rightarrow q_{\max}^2$, so is also untenable. In the next section, we show an approach we attempted to finding new normalizations of these three currents such that all three can be 'trusted' as good approximations to the continuum current. One could then in principle use these trustworthy $\langle V_0 \rangle$ and $\langle V_k \rangle$ currents to extract the form factors.

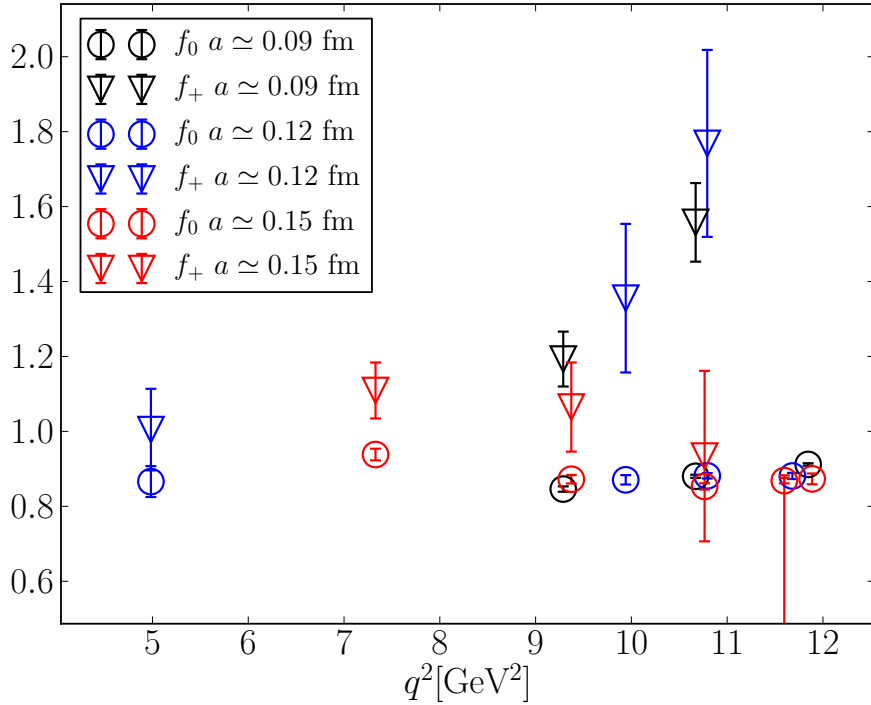


Figure 5.6: $B \rightarrow D$ form factors extracted from $\langle V_0 \rangle$ and $\langle S \rangle$. Clearly these results are nonsense. See text.

5.4 Non-Perturbative Renormalization using $B_c \rightarrow \eta_c$ Data

Here we define non-perturbative normalization constants Z_J for the NRQCD-HISQ currents via

$$\begin{aligned} J &= (1 + z_0^J \alpha_s)(J^{(0)} + J^{(1)}) + \mathcal{O}(\alpha_s \Lambda_{\text{QCD}}/m_b, \alpha_s \mathbf{p}/m_b, \alpha_s^2, (\Lambda_{\text{QCD}}/m_b)^2, (\mathbf{p}/m_b)^2) \\ &\equiv Z_J(1 + z_0^J \alpha_s)(J^{(0)} + J^{(1)}), \\ Z_J &= 1 + \mathcal{O}(\alpha_s \Lambda_{\text{QCD}}/m_b, \alpha_s \mathbf{p}/m_b, \alpha_s^2, (\Lambda_{\text{QCD}}/m_b)^2, (\mathbf{p}/m_b)^2). \end{aligned} \quad (5.30)$$

\mathbf{p} here is the spacial momentum exchange, i.e. in the previous chapter we would have $\mathbf{p} = \mathbf{p}_{D_{(s)}}$. The Z_J factor compensates for the truncation of the series. One can imagine fixing Z_J by demanding some property of J . One may be concerned that Z_J is dependent on the spacial momenta in the current $Z_J = Z_J(\mathbf{p})$, however, we will see below that this variation is a negligible effect.

In this section we outline an approach used to determine Z_S , Z_{V_0} and Z_{V_k} . In this process we use NRQCD data from another HPQCD project of determining form factors for $B_c \rightarrow \eta_c l \nu$ decays [106]. A schematic of how this is achieved is given in fig. 5.7. I thank Brian Colquhoun for supplying correlation functions from their calculation. The current in this calculation is the same as in the $B_{(s)} \rightarrow D_{(s)} l \nu$ calculation, so normalizations determined using this data can then be applied to the $B_{(s)} \rightarrow D_{(s)} l \nu$ calculation. I use the $B_c \rightarrow \eta_c l \nu$ data here since

- $B_c \rightarrow \eta_c$ correlators have much smaller statistical errors. This is because of the lack of the s spectator quark, degradation of the signal/noise ratio is less severe (see sec. 4.2.2).
- A heavy-HISQ determination of $B_{(s)} \rightarrow \eta_c$ form factors was also available from their project [106]. This comes in useful in our approach to the normalization.

All analysis below is performed using data on the fine ensemble (set 2). In principle it could be repeated for any other ensemble on which correlators for any $b \rightarrow c$ transition is available.

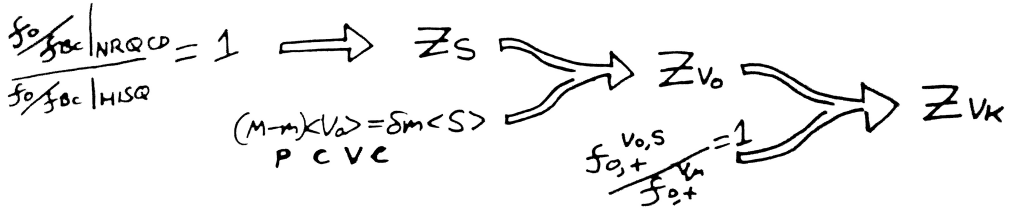


Figure 5.7: A schematic of the chain of steps towards normalizing the scalar, temporal vector and spacial vector currents NRQCD-HISQ currents. Details given in the next three sections; 5.4.1, 5.4.2 and 5.4.3.

5.4.1 Z_S

We have available to us lattice results for $f_0(q^2)$ for a number of q^2 values spanning the entire q^2 range (including q_{\max}^2 and $q^2 = 0$) from NRQCD-HISQ currents on the fine ensemble. We also have a determination of f_{B_c} also from NRQCD-HISQ lattice currents on the same ensemble. We denote these finite- a lattice results as $\hat{f}_0(q^2)$, \hat{f}_{B_c} . We also have a continuum-extrapolated heavy-HISQ result for $f_0(q^2)/f_{B_c}$, for a range of q^2 values also including q_{\max}^2 and $q^2 = 0$. This is given in the form of this

ratio since discretization effects largely cancel in this ratio improving the continuum extrapolation. Namely we have

$$\frac{f_0(q_{\max}^2)}{f_{B_c}} = 2.104(36), \quad \frac{f_0(0)}{f_{B_c}} = 1.288(42). \quad (5.31)$$

I thank Andrew Lytle for these results. By demanding that the NRQCD-HISQ finite- a match the continuum heavy-HISQ results, we can find, for example

$$\left. \frac{Z_S}{Z_{A_0}} \right|_{q_{\max}^2} = \frac{f_0(q_{\max}^2)/f_{B_c}}{\hat{f}_0(q_{\max}^2)/\hat{f}_{B_c}} = 0.995(15). \quad (5.32)$$

As a test to see if Z_S varies with \mathbf{p} , we can compare this result to an analogous approach at $q^2 = 0$;

$$\left. \frac{Z_S}{Z_{A_0}} \right|_0 = \frac{f_0(0)/f_{B_c}}{\hat{f}_0(0)/\hat{f}_{B_c}} = 0.962(33). \quad (5.33)$$

A similar approach cannot be applied for Z_{V_0} or Z_{V_k} , since f_0 has a complicated relationship to both $\langle V_0 \rangle$ and $\langle V_k \rangle$ that varies with q^2 , so it is not clear how one attribute discrepancies between \hat{f}_0/\hat{f}_{B_c} and f_0/f_{B_c} to Z_{V_0} and Z_{V_k} .

The comparison of these two ratios at q_{\max}^2 and $q^2 = 0$ show that any variation is small in comparison to statistical errors. We can absorb the variation in \mathbf{p} into a sub-leading term in the scalar current by demanding that $Z_{J_\mu}/Z_{A_0}|_{q_{\max}^2} = Z_{J_\mu}/Z_{A_0}|_{q^2=0}$. Redefine the scalar current according to:

$$S = Z_S \left[(1 + z_0^S \alpha_s) (S^{(0)} + S^{(1)}) + \alpha_s z_2^S J_\mu^{(2)} \right] \quad (5.34)$$

The definition of $S^{(2)}$ is identical to $V_0^{(2)}$. By defining \hat{f}_2 to be \hat{f}_0 but with $(1 + \alpha z^S)(S^{(0)} + S^{(1)})$ replaced with $\alpha S^{(2)}$, we can write:

$$\frac{Z_{A_0}}{Z_S} = \frac{(\hat{f}_0 + z_2^S \hat{f}_2)/\hat{f}_{B_c}}{f_0/f_{B_c}|_{cont}} \equiv \frac{Z_{A_0}}{Z_S}^{(0,1)} + z_2^S \frac{Z_{A_0}}{Z_S}^{(2)} \quad (5.35)$$

with this further definition, and demanding that $Z_{A_0}/Z_S|_{q_{\max}^2} = Z_{A_0}/Z_S|_{q^2=0}$, we end up with

$$z_2^S = \frac{\frac{Z_{A_0}}{Z_S}^{(0,1)}|_{q^2=0} - \frac{Z_{A_0}}{Z_S}^{(0,1)}|_{q_{\max}^2}}{\frac{Z_{A_0}}{Z_S}^{(2)}|_{q_{\max}^2} - \frac{Z_{A_0}}{Z_S}^{(2)}|_{q^2=0}} = -1.1(1.5) \quad (5.36)$$

Now that we are able to include $S^{(2)}$ in the scalar current, we can consider the scalar current normalized up to $\mathcal{O}(\alpha_s^2, (\Lambda_{\text{QCD}}/m_b)^2, (\mathbf{p}/m_b)^2)$ (yes, we have not strictly determined Z_S in this case, but we will for the vector currents). The

next steps are essentially to match results using the vector currents to this newly normalized scalar current, meaning the vector currents will be normalized up to $\mathcal{O}(\alpha_s^2, (\Lambda_{\text{QCD}}/m_b)^2, (\mathbf{p}/m_b)^2)$, hence we have theoretically accounted for the large subleading pieces in the spacial vector current.

5.4.2 Z_{V_0}

Recall from sec. 5.3.5 that $f_+(q^2)$ diverges as $|\mathbf{p}_{\eta_c}| \rightarrow 0$ when extracted from $\langle V_0 \rangle$ and $\langle S \rangle$. Fig. 5.8 compares form factors determined using $\langle V_0 \rangle$, $\langle S \rangle$, and $\langle V_0 \rangle$, $\langle V_k \rangle$.

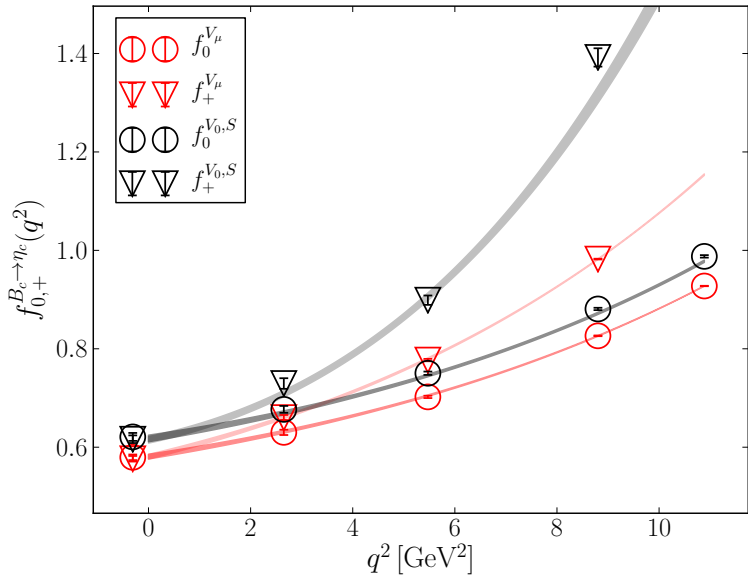


Figure 5.8: Comparison of form factors from $\langle V_0 \rangle$, $\langle S \rangle$ and $\langle V_0 \rangle$, $\langle V_k \rangle$, no additional normalizations. The bands show the results of fitting the data to the BGL parameterization (5.23), where coefficients $a_n^{0,+}$ are fit parameters.

The divergence is due to the numerator of (5.29) not tending to zero as $\mathbf{p}_{\eta_c}^2 \rightarrow 0$. At $\mathbf{p}_{\eta_c}^2 = 0$, the numerator becomes $(m_b - m_c)\langle S \rangle - (M_{B_c} - M_{\eta_c})\langle V_0 \rangle$, which vanishes when the PCVC relation is satisfied. So one would expect if we renormalize one of the currents so the Ward identity is satisfied (at q_{max}^2), this divergence should be removed or at least reduced.

Hence we should normalize the temporal vector current using the already normalized scalar density. So to satisfy the PCVC, Multiply $\langle V_0 \rangle$ by

$$Z_{V_0} = \frac{m_b - m_c}{M_{B_c} - M_{\eta_c}} \frac{\langle S \rangle}{\langle V_0 \rangle} \Big|_{q_{max}^2} = 1.0661(36) \quad (5.37)$$

This seems to deal with the f_+ divergence, in Fig. 5.9 we show the result again but with $\langle V_0 \rangle$ multiplied by Z_{V_0} . Unfortunately the same technique does not solve

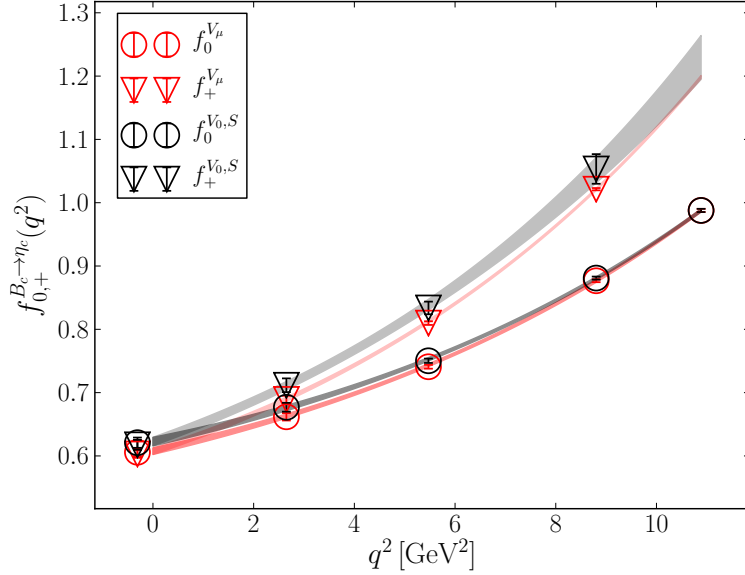


Figure 5.9: Comparison of form factors from $\langle V_0 \rangle, \langle S \rangle$ and $\langle V_0 \rangle, \langle V_k \rangle$, $\langle V_0 \rangle$ is multiplied by Z_{V_0} given in (5.37). The bands show the results of fitting the data to the BGL parameterization (5.23), where coefficients $a_n^{0,+}$ are fit parameters.

the diverging f_+ issue in the $B_{(s)} \rightarrow D_{(s)}$ case, the statistics are not as good so the divergence is too severe.

5.4.3 Z_{V_k}

We can determine a Z_{V_k} by demanding that $f_{0,+}^{V_0,S}/f_{0,+}^{V_\mu} = 1$, with the knowledge that $\langle V_0 \rangle, \langle S \rangle$ require no further normalization. This can be done with both f_+ and f_0 , at any q^2 :

$$Z_{V_k} = 1 + \frac{f_+^{V_0,S} - f_+^{V_\mu}}{R_{+k}\langle V_k \rangle} \quad (5.38)$$

$$= 1 + \frac{f_0^{V_0,S} - f_0^{V_\mu}}{R_{0k}\langle V_k \rangle}, \quad (5.39)$$

where the R 's are some kinematic gunk: $R_{+k} = (M_{B_c} - E_{\eta_c})/2M_{B_c}\mathbf{p}_{\eta_c}/\sqrt{3}$, $R_{0k} = R_{+k} - (M_{B_c}^2 - M_{\eta_c}^2)(M_{B_c} - E_{\eta_c})/2M_{B_c}\mathbf{p}_{\eta_c}/q^2\sqrt{3}$. The results are shown in fig. 5.10. The fact that these are not varying by a statistically significant extent

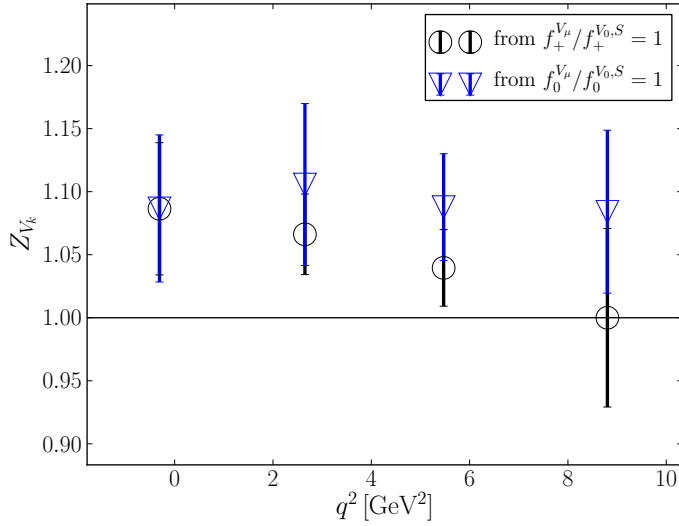


Figure 5.10: Z_{V_k} from constraining form factors to be the same from $\langle V_0 \rangle, \langle S \rangle$ and $\langle V_0 \rangle, \langle V_k \rangle$

in q^2 implies that the spacial vector normalization does not vary strongly in \mathbf{p}_{η_c} . Hence, since these are all estimates of the same value, we can average over them to get

$$Z_{V_k} = 1.070(36). \quad (5.40)$$

When this normalization is given to $\langle V_k \rangle$, the $B_c \rightarrow \eta_c$ form factors from the two methods become consistent, see Fig. 5.11.

One could imagine using these normalizations Z_{V_0} and Z_{V_k} in the $B_{(s)} \rightarrow D_{(s)}$ calculation. The errors of this normalization is around 4%, which would push the final results of the $B_{(s)} \rightarrow D_{(s)}$ study up to the 5 – 10% range. At present this level of precision is not competitive in comparison to other calculations of these quantities.

5.5 Conclusion of NRQCD work

As mentioned in the introduction - the main takehome of this thesis is that using NRQCD (namely NRQCD-HISQ currents) to compute form factors for $b \rightarrow c$ transitions, is far from optimal.

We rely here on truncations in many different interlocking series ($1/m_b, \alpha_s, \alpha_s/m_b, \dots$), which may leave out important information. The terms

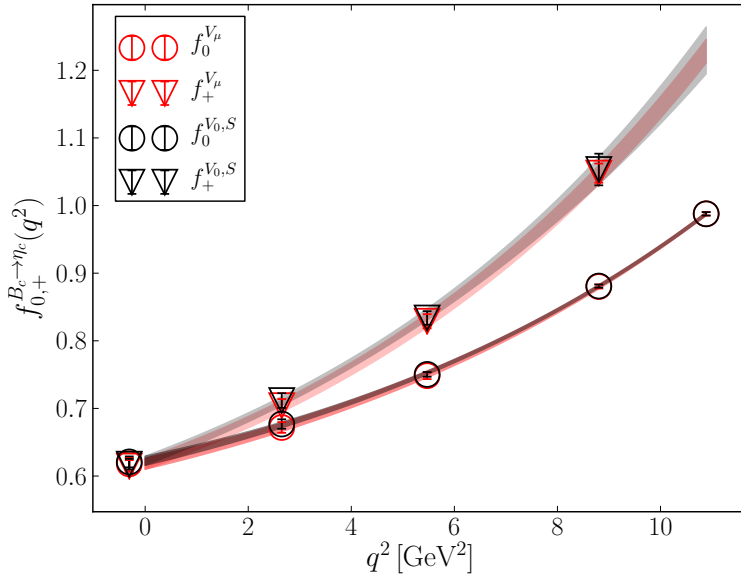


Figure 5.11: Comparison of form factors from $\langle V_0 \rangle$, $\langle S \rangle$ and $\langle V_0 \rangle$, $\langle V_k \rangle$, with $\langle V_0 \rangle$ normalized via Z_{V_0} and $\langle V_k \rangle$ normalized with Z_{V_k} . The bands show the results of fitting the data to the BGL parameterization (5.23), where coefficients $a_n^{0,+}$ are fit parameters.

in the series we *do* have access to rely on perturbation theory via the matching factors. Some progress was made to normalize currents non-perturbatively in the above work, but our results fall short of what would be required to obtain precise continuum results.

I hope that in reading this chapter you experienced a similar feeling of confusion and anxiety as I felt when carrying out this work. It was only after many months of grappling with the problems of these calculations that we decided to put them aside and attempt instead the heavy-HISQ approach from scratch. Reading the following two chapters, both dedicated to successful heavy-HISQ studies, will feel like a warm bath in comparison to the NRQCD experience. The heavy-HISQ approach is in contrast very elegant, contains far assumptions, and results in cleaner signals.

CHAPTER 6

$B_s \rightarrow D_s^* l \nu$ Axial Form Factor at Zero Recoil from Heavy-HISQ

This chapter concerns the simpler of our two heavy-HISQ studies, the calculation of the $B_s \rightarrow D_s^* l \nu$ form factor at zero recoil, $h_{A_1}^s(1)$ as defined in Sec. 2.2.2. We give this quantity the superscript s to differentiate it from the quantity more commonly referred to as $h_{A_1}(1)$, the zero recoil axial form factor for $B \rightarrow D^* l \nu$ decays.

We briefly review the definition of this form factor (at zero recoil) for clarity. The differential decay rate for the $\bar{B}_s^0 \rightarrow D_s^{*+} l^- \bar{\nu}_l$ decay is given in the SM by

$$\frac{d\Gamma}{dw}(\bar{B}_s^0 \rightarrow D_s^{*+} l^- \bar{\nu}_l) = \frac{G_F^2 M_{D_s^*}^3 |\eta_{EW} V_{cb}|^2}{4\pi^3} \times (M_{B_s}^2 - M_{D_s^*}^2) \sqrt{w^2 - 1} \chi(w) |\mathcal{F}^{B_s \rightarrow D_s^*}(w)|^2. \quad (6.1)$$

where $w = v_{B_s} \cdot v_{D_s^*}$, $v_H = p_H/M_H$ is the 4-velocity of a H -meson, and $\chi(w)$ is a known function of w (see appendix G of [8]). η_{EW} accounts for electroweak corrections due to diagrams where photons or Z s are exchanged in addition to a W^- , as well as the Coulomb attraction of the final-state charged particles [5–7]. The differential decay rate for the $B_s^0 \rightarrow D_s^{*-} l^+ \bar{\nu}_l$ is identical.

The form factor $\mathcal{F}^{B_s \rightarrow D_s^*}(w)$ is a linear combination of hadronic form factors that parameterize the vector and axial-vector matrix elements between initial and final state hadrons. At zero recoil ($w = 1$), the vector matrix element vanishes, the axial-vector element simplifies to

$$\langle D_s^*(\epsilon) | A^\mu | B_s \rangle = 2\sqrt{M_{B_s} M_{D_s^*}} h_{A_1}^s(1) \epsilon^{*\mu}, \quad (6.2)$$

and $\mathcal{F}^{B_s \rightarrow D_s^*}(w)$ reduces to

$$\mathcal{F}^{B_s \rightarrow D_s^*}(1) = h_{A_1}^s(1). \quad (6.3)$$

Our goal is to compute $h_{A_1}^s(1)$.

All we need to do this is the matrix element $\langle D_s^*(\epsilon) | A^\mu | B_s \rangle$ with both the B_s and D_s^* at rest, with the D_s^* polarization ϵ in the same direction as the axial current.

6.1 Motivation

The $\bar{B} \rightarrow D^* l \bar{\nu}_l$ decay supplies one of the three methods used for precisely determining the CKM element $|V_{cb}|$ [13, 17, 107–122]. Measurements of branching fractions are extrapolated through q^2 to the zero recoil point to deduce $h_{A_1}(1)|V_{cb}|$, where $h_{A_1}(1)$ is the only form factor contributing at zero recoil. Then an SM determination of $h_{A_1}(1)$ (via Lattice QCD [8, 13]) can be divided out to infer $|V_{cb}|$.

A similar process that could also be used to determine $|V_{cb}|$, and test the SM, is $\bar{B}_s \rightarrow D_s^* l \bar{\nu}_l$. There is at time of writing no published measurements of this decay, but it is feasible to measure such a decay at a detector like LHCb. This decay is also attractive from the Lattice QCD side.

The absence of valence light quarks means lattice QCD results have smaller statistical errors, are less computationally expensive, a simpler chiral extrapolation to the physical light mass, and negligible finite volume effects. This makes the $\bar{B}_s \rightarrow D_s^* l \bar{\nu}_l$ both a useful test bed for lattice techniques (that may be later used to study $\bar{B} \rightarrow D^* l \bar{\nu}_l$ decays), and a key decay to make predictions about when experimental results become available.

Chiral symmetry implies that form factors for decays such as $B_s \rightarrow D_s^*$ and $B \rightarrow D^*$ are insensitive to the mass of the spectator quark, since implying that form factors for these two decays are approximately equal [123]. This was seen in the recent lattice calculation [8] that found $h_{A_1}^{B_s \rightarrow D_s^*}(1)/h_{A_1}^{B \rightarrow D^*}(1) = 1.013(14)_{\text{stat}}(17)_{\text{sys}}$. We can then expect to learn about $B \rightarrow D^*$ by studying $B_s \rightarrow D_s^*$. We perform test of this claim, in the context of our formalism, in this study.

Lattice calculations of the $B_{(s)} \rightarrow D_{(s)}^*$ form factors at zero recoil have so far been performed by two collaborations. The Fermilab Lattice collaboration produced $h_{A_1}^{B \rightarrow D^*}(1)$ in [13]. HPQCD computed both $h_{A_1}^{B \rightarrow D^*}(1)$ and $h_{A_1}^{B_s \rightarrow D_s^*}(1)$ in [8]. The RBC/UKQCD [124] and LANL-SWME [125] collaborations are also working towards these form factors.

The presence of heavy quarks is a large consideration in designing a lattice calculation. A b quark introduces discretization effects of size $(am_b)^n$ where n is a positive integer dependent on the choice of action. To avoid such potentially large discretization effects, most lattice studies (including all of those mentioned in the previous paragraph), use some EFT approach for simulating heavy quarks. The Fermilab Lattice, RBC/UKQCD, and LANL-SWME calculations all use some variation of the Fermilab action [126–128] to simulate c and b quarks. The HPQCD calculation uses the NRQCD action [57] for b quarks.

To relate the results from these approaches to full continuum QCD, each of the above studies requires perturbative matching of lattice currents to continuum QCD. The matching has only been performed to 1-loop, leading to each having matching errors as a key uncertainty. The use of NRQCD in the HPQCD calculation brings in matching errors of $\mathcal{O}(\alpha_s^2, \alpha_s \Lambda_{\text{QCD}}/m_b, (\Lambda_{\text{QCD}}/m_b)^2)$. It is difficult to estimate the size of matching errors in lattice NRQCD, so to be conservative a large matching error was assigned to the result. This error contributes $\sim 80\%$ of the full error budget. The use of the Fermilab action in the Fermilab Lattice calculation leads to $\mathcal{O}(\alpha_s^2)$ errors. They avoid this issue to a large extent by analysing only ratios of correlation functions, however, the matching still contributes $\sim 30\%$ to the final error.

In this chapter, we report details and results of the first calculation of the $B_s \rightarrow D_s^*$ form factor at zero recoil using an approach free of perturbative matching.

Since the $B_s \rightarrow D_s$ form factor is approximately equal to the $B \rightarrow D$ form factor, and our results are non-perturbatively renormalised, this calculation can be seen as a check of the normalisation of the Fermilab Lattice and HPQCD determinations of $h_{A_1}(1)$ that contributed to $|V_{cb}|_{\text{excl}}$. While producing a quantity less relevant to current phenomenology than the $B \rightarrow D^*$ form factor, this calculation can be seen as a proof-of-principle for the heavy-HISQ approach.

Using the heavy-HISQ approach has the added benefit of elucidating the dependence of form factors on heavy quark masses, meaning we can test expectations from Heavy Quark Effective Theory (HQET). In this article we give a determination of the HQET low energy constants $l_{V,A,P}^s$ associated with the $B_s \rightarrow D_s^*$ form factor at zero recoil.

6.2 Calculation Details

6.2.1 Lattice Setup

We use the MILC gluon field configurations detailed in Sec. 4.1.1 [91,92]. We use sets 2-5 in table 7.1, i.e., the fine, fine-physical, superfine and ultrafine ensembles. Table 6.1 gives the valence quark masses we use in the generation of quark propagators. In three of the four ensembles (fine,superfine and ultrafine), the bare light mass is set to $m_{l0}/m_{s0} = 0.2$. The fact that the m_{l0} value is unphysically high is expected to have a small effect on $h_{A_1}^s(1)$, due to the lack of valence light quarks, and previous experience of the dependence of $h_{A_1}^s(1)$ on m_{l0} [8]. The small effect due to the

set	handle	am_{s0}^{val}	am_{c0}^{val}	am_{h0}^{val}	T
2	fine	0.0376	0.45	0.5, 0.65, 0.8	14,17,20
3	fine-physical	0.036	0.433	0.5, 0.8	14,17,20
4	superfine	0.0234	0.274	0.427, 0.525, 0.65, 0.8	22,25,28
5	ultrafine	0.0165	0.194	0.5, 0.65, 0.8	31,36,41

Table 6.1: Parameters relevant to our calculation. Columns 3 and 4 give the s and c valence quark masses, these values were tuned in [94] to reproduce the correct η_s and η_c masses. We use a number of heavy quark masses to assist the extrapolation to physical the b mass, given in column 5. Column 6 gives the temporal separations between source and sink, T , of the 3-point correlation functions computed on each ensemble.

unphysical m_{l0} is quantified by including a fourth ensemble (fine-physical) with physical m_{l0} , and corrected for.

We use a number of different masses for the valence heavy quark. This is in order to resolve the dependence of $h_{A_1}^s(1)$ on the heavy mass, so that an extrapolation to $m_h = m_b$ can be performed. By varying the heavy mass varying both within ensembles and between ensembles, we can resolve both the discretization effects that grow with large ($am_{h0}^{\text{val}} \lesssim 1$) masses and the physical dependence of the continuum form factor on m_h .

As detailed in Sec. 4.1.3, staggered correlation functions are built by a combination of staggered propagators $g(x, y)$ and staggered phases. In this calculation we only need local (non point-split) operators, this is an advantage since point-split operators lead to correlation functions more noisy than local operators.

We compute a number of correlation functions on each ensemble. To generate these correlators we use random wall sources, and use extended sources for the 3-point correlators, as described in Sec. 4.1.3. First we compute 2-point correlation functions between zero-momentum eigenstates, objects of the form

$$C_M(t) = \langle \Phi_M(t) \Phi_M^\dagger(0) \rangle, \quad (6.4)$$

$$\Phi_M(t) = \sum_{\mathbf{x}} \bar{q}(\mathbf{x}, t) \Gamma q'(\mathbf{x}, t),$$

where $\langle \rangle$ represents a functional integral, q, q' are valence quark fields of the flavours

the M meson is charged under, and Γ is the spin-taste structure of M . We compute these for all t values, i.e. $0 \leq t \leq N_t$.

We compute correlation functions for a heavy-strange pseudoscalar, H_s , with spin-taste structure $(\gamma_5 \otimes \gamma_5)$. In terms of staggered propagators this takes the form

$$C_{H_s}(t) = \sum_{\mathbf{x}, \mathbf{y}} \text{Tr} [g_h(x, y) g_s^\dagger(x, y)], \quad (6.5)$$

where $g_q(x, y)$ is a staggered propagator for flavour q , and the trace is over color. Here $x_0 = 0$ and $y_0 = t$, and the sum is over spacial sites \mathbf{x}, \mathbf{y} . We also compute correlators for a charm-strange vector meson D_s^* , with structure $(\gamma_\mu \otimes \gamma_\mu)$, using

$$C_{D_s^*}(t) = \sum_{\mathbf{x}, \mathbf{y}} (-1)^{x_\mu + y_\mu} \text{Tr} [g_c(x, y) g_s^\dagger(x, y)]. \quad (6.6)$$

In order to non-perturbatively renormalise the axial vector current, we compute correlation functions for goldstone and non-goldstone pseudoscalar and heavy-charm mesons denoted H_c and \hat{H}_c respectively, where H_c has spin-taste structure Γ_P , and \hat{H}_c has structure Γ_A^0 . H_c correlators are computed using (7.9) (with g_s replaced with g_c), while \hat{H}_c correlators are given by

$$C_{\hat{H}_c}(t) = \sum_{\mathbf{x}, \mathbf{y}} (-1)^{\bar{x}_0 + \bar{y}_0} \text{Tr} [g_h(x, y) g_c^\dagger(x, y)], \quad (6.7)$$

where we use the notation $\bar{z}_\mu = \sum_{\nu \neq \mu} z_\nu$.

The heavy-mass extrapolation requires masses of η_h mesons, heavy-heavy pseudoscalars artificially forbidden to annihilate. To quantify mistuning of the charm and strange quark masses, we also require masses for η_c and η_s mesons, identical to η_h with h replaced c and s quarks respectively. We compute correlators for each of these, using a spin-taste $(\gamma_5 \otimes \gamma_5)$, taking the form of (7.9).

We then generate the 3-point correlation functions

$$\begin{aligned} C_3(t, T) &= \sum_{\mathbf{y}} \langle \Phi_{D_s^*(\epsilon)}(T) A^\mu(\mathbf{y}, t) \Phi_{H_s}(0) \rangle, \\ A^\mu(\mathbf{y}, t) &= \bar{c}(\mathbf{y}, t) \gamma^5 \gamma^\mu h(\mathbf{y}, t). \end{aligned} \quad (6.8)$$

In terms of the staggered formalism, the H_s source is given structure $(\gamma_5 \otimes \gamma_5)$, the D_s^* sink is given $(\gamma_\mu \otimes \gamma_\mu)$, and the current insertion $(\gamma_5 \gamma_\mu \otimes \gamma_5 \gamma_\mu)$. In terms of staggered propagators this is given by

$$\begin{aligned} C_3(t, T) &= \sum_{\mathbf{x}, \mathbf{y}, \mathbf{z}} (-1)^{\bar{y}_\mu + \bar{z}_\mu} \\ &\quad \times \text{Tr} [g_h(x, y) g_c(y, z) g_s^\dagger(x, z)], \end{aligned} \quad (6.9)$$

where we fix $x_0 = 0$, $y_0 = t$ and $z_0 = T$. We compute these for all t values within $0 \leq t \leq T$, and 3 T values that vary between ensembles, given in table 6.1.

In the $C_{D_s^*}$ and C_3 cases, dependant on a polarization μ , we compute the cases with $\mu = x, y, z$, and take the average over these.

6.2.2 Correlator Fits

We extract current matrix elements from the generated correlation functions, via simultaneous Bayesian fits as described in Sec. 4.2.1. We use fit forms given by (4.40) for 2-point and (5.18) for 3-point correlators. We set $N_{\text{exp}} = 5$ in each fit. We perform a single simultaneous fit containing each correlator computed ($H_s, D_s^*, \eta_h, \eta_s, H_c, \hat{H}_c$, and 3-point) for each ensemble. We also marginalize out the highest energy excited states in the fit function using the prior distributions, in the interest of speed of the fits.

We set gaussian priors for the parameters J_{jk} , and log-normal priors for all other parameters.

Ground state energies E_0^M are given priors of $(am_{q0} + am_{q'0} + a\Lambda_{\text{QCD}}) \pm 2a\Lambda_{\text{QCD}}$, where $m_{q0, q'0}$ are the masses of the flavours the meson M is charged under, and Λ_{QCD} is the confinement scale, which we set to 0.5GeV. For $q = h$ or c , this corresponds to the leading order HQET expression for a heavy meson mass. In the η_s case, the prior becomes approximately $2am_{s0} + a\Lambda_{\text{QCD}} \simeq a\Lambda_{\text{QCD}}$, which one would expect. Ground-state energies of oscillating states, $E_0^{M,o}$, are given priors of $(am_{q0} + am_{q'0} + 2a\Lambda_{\text{QCD}}) \pm 2\Lambda_{\text{QCD}}$. Excited state energies, E_i^M , $i > 0$ are given prior values $2a\Lambda_{\text{QCD}} \pm a\Lambda_{\text{QCD}}$. Priors for ground state amplitudes a_0^M , are set according to an empirical-Bayes approach, plots of the effective amplitude of the correlation functions are inspected to deduce reasonable priors. The resulting priors always have a variance at least 10 times that of the final result. The excited state amplitudes $a_i^M, i > 0$ are given priors of 0.15 ± 0.5 for non-oscillating states, and 0.05 ± 0.1 for oscillating states. The ground-state non-oscillating to non-oscillating 3-point parameter, J_{00}^{nn} is given a prior of 1 ± 0.6 , and the rest of the 3-point parameters J_{jk}^{nn} are given 0 ± 1 .

The current matrix element we require to find $h_{A_1}^s(1)$ is given by

$$\langle D_s^*(\hat{k}) | A^k | H_s \rangle |_{\text{lat}} = 2\sqrt{M_{H_s} M_{D_s^*}} J_{00}^{nn}. \quad (6.10)$$

We performed a number of tests on the fits, to demonstrate the robustness of the fits to various hyperparameter choices. Results are given in fig. 4.2.1. We will refer to these tests throughout the remainder of this section. In test #1 we loosened

priors to test stability. We tested the effects of changing N_{exp} , to $N_{\text{exp}} = 6$ in test #2 and $N_{\text{exp}} = 4$ in test #3.

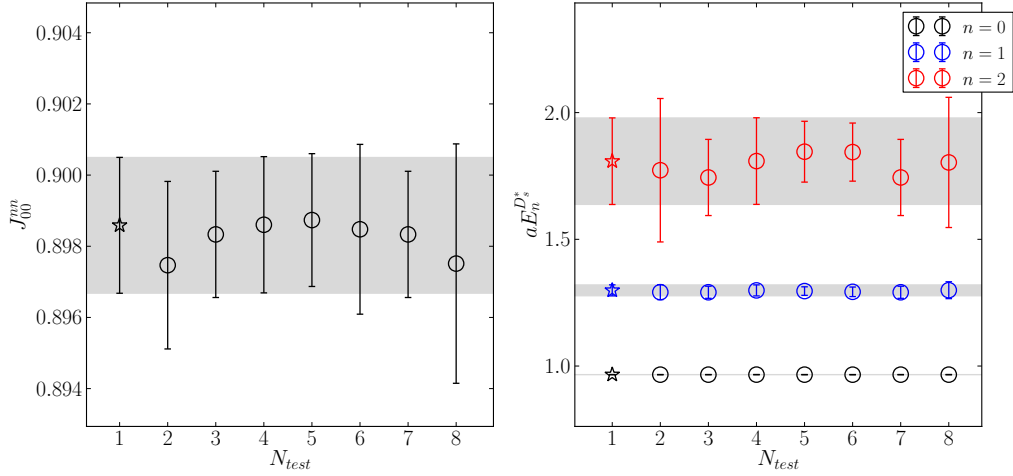


Figure 6.1: Tests on the correlator fits on the fine ensemble. At $N_{\text{test}} = 1$ we give the final accepted result. $N_{\text{test}} = 2$ gives the results when all priors are loosened by 50%. $N_{\text{test}} = 3$ and 4 gives the results of setting $N_{\text{exp}} = 4$ and 6 respectively. $N_{\text{test}} = 5, 6$ gives the results of setting $t_{\text{cut}} = 2, 4$ respectively for all correlators. $N_{\text{test}} = 7$ gives the result without marginalising out the $n = 5$ excited state. $N_{\text{test}} = 8$ gives the result of moving the SVD cut from 10^{-3} to 10^{-2} .

To ensure that truncating the sum at N_{exp} is a good approximation to the infinite sum containing all excited states, we only include data with $t \geq t_{\text{cut}}$ and $t \leq N_t - t_{\text{cut}}$ in the 2-point case and $t \leq T - t_{\text{cut}}$ in the 3-point case. We can in principle use a different t_{cut} for every correlation function included in our fit, so must choose a set $\{t_{\text{cut}}^c\}$ (where c labels the correlator).

To ensure the optimal choice for the $\{t_{\text{cut}}^c\}$ set, we employ the `scikit-optimize` python package [129]. The process consists of defining a function f with an input of $\{t_{\text{cut}}^c\}$ and an output of some loss function f . Then, the minimum of f with respect to $\{t_{\text{cut}}^c\}$ is found via a Gaussian process. We use the loss function

$$f(\{t_{\text{cut}}^c\}) = -\log \text{GBF} + \theta \left(\frac{\chi^2}{N_{\text{dof}}} - 1 \right) \rho \frac{\chi^2}{N_{\text{dof}}}. \quad (6.11)$$

GBF is the Gaussian Bayes factor corresponding to the comparison between the resulting model of the fit (the fit function with parameters set by the fit), and a random model (the fit function with randomly sampled parameters). The second

term gives a strong punishment to fits with $\chi^2/N_{\text{dof}} > 1$. We set $\rho = 10^5$, in order to make the second term of comparable size of the first, which for typical fits we attempted had a magnitude of order 10^4 . A couple of more naive choices for $\{t_{\text{cut}}^c\}$ are given in tests #3 & #4.

An appropriate value for the SVD-cut is found by comparing estimates of covariance matrix eigenvalues between different bootstrap samples of the data. Typically the smallest eigenvalues are sensitive to taking new bootstrap copies, suggesting they are poorly estimated. A cut is placed such that any poorly estimated eigenvalues are replaced with more conservative (larger) values. The resulting SVD cut varies between ensembles since it depends on the quality of the dataset, but are always of order 10^{-3} .

Fig. 6.2 illustrates this process on the fine ensemble. In fits to the fine ensemble correlators, we set the SVD cut to 10^{-3} , we then tested to see if this had any effect by also running the fit with SVD cut 10^{-2} in test #7.

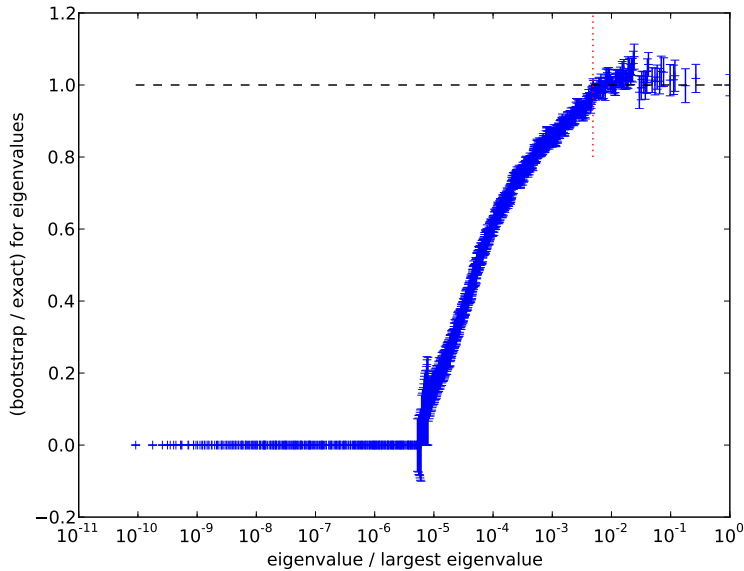


Figure 6.2: An illustration of the process of deducing an appropriate SVD cut on the fine ensemble. Each point shows the ratio of a covariance matrix eigenvalue, to the same eigenvalue from a bootstrap copy, against the relative size of the eigenvalue. The eigenvalues below the red dotted line are at risk of being underestimated.

We can perform further sanity checks on the fits by plotting certain functions of the 2-point correlators. To obtain useful forms, first, one can approximately flush

out the oscillating states from correlators by performing a so-called *superaverage*, $C(t) \rightarrow [C(t) + C(t + a)]/2$. We perform a symmetric and doubled version of this operator on correlators to obtain

$$C(t) \rightarrow \tilde{C}(t) = \frac{1}{4}(C(t - a) - 2C(t) + C(t + a)). \quad (6.12)$$

We can check the ground-state energy of the correlator by looking at the large- t behaviour of

$$E_{\text{eff}}(t) = \log \left(\frac{\tilde{C}(t)}{\tilde{C}(t - a)} \right). \quad (6.13)$$

It is straightforward to show from inspecting eq. (4.35) that in the large t (but $t < T_{\text{lat}}/2$) limit, this should tend towards the ground-state energy for the correlator. One can also construct a similar function for the amplitude:

$$a_{\text{eff}}(t) = \sqrt{\frac{\cosh E_{\text{eff}}(t) - 1}{2}} \sqrt{\tilde{C}(t) e^{E_{\text{eff}} t}}. \quad (6.14)$$

The second term would produce the correct amplitude (in the large- t limit) in the absence of superaveraging, and the first corrects for the effect of the superaveraging (6.12). These functions, for various relevant correlators on the fine ensemble, are plotted in comparison with the full fit results in fig. 6.3.

A similar approach can be applied to the 3-point correlators. The ratio $\tilde{C}_3(t, T)/\tilde{C}^{H_s}(t)\tilde{C}^{D_s^*}(T - t)$ approaches J_{00}^{nn} for $t \gg 0$ and $t \ll T$. This is illustrated in fig. 6.4. From inspecting these figures for 2- and 3-point sanity tests, one can reassure themselves that the fits to the correlators are well behaved.

6.2.3 Normalization of Axial Current

Conserved and partially conserved currents require no renormalization. However, the staggered conserved axial-vector current is not simply $(\gamma_5 \gamma_\mu \otimes \gamma_5 \gamma_\mu)$, it is a complicated linear combination of many local and point-split lattice currents. In this study we use only local axial vector currents, this simplifies the lattice calculation but creates the need for our resulting current matrix element to be multiplied by a matching factor Z_A to produce the appropriate continuum current. We find Z_A via a fully non-perturbative method [130, 131].

We leverage the fact that the staggered local pseudoscalar current $(\gamma^5 \otimes \gamma^5)$, multiplied by the sum of masses of quark flavours the current is charged under, is absolutely normalized. We extract from the 2-point H_c and \hat{H}_c correlators the decay

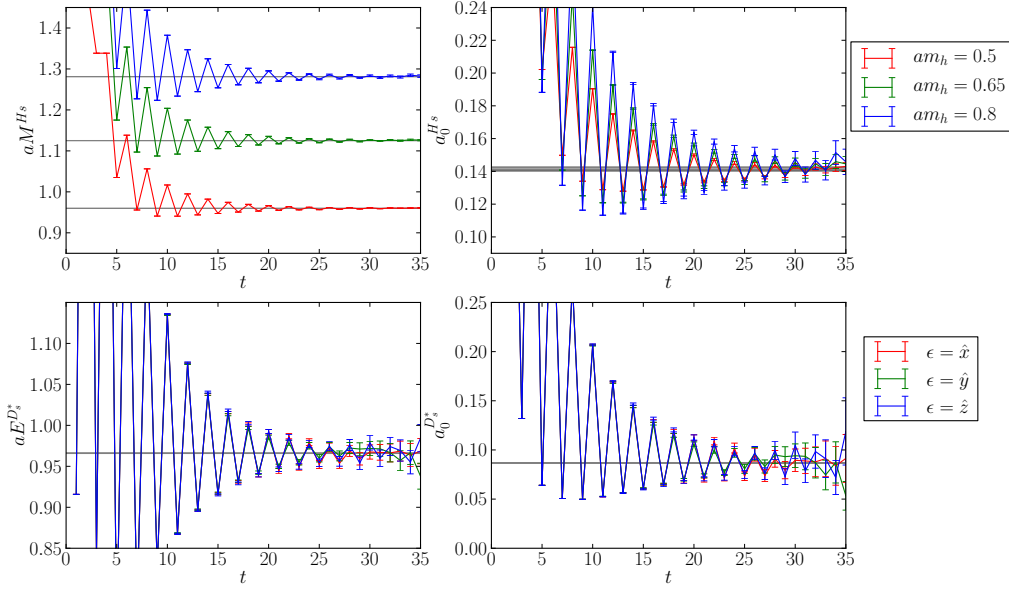


Figure 6.3: Effective energies and amplitudes for H_s and D_s^* correlators on the fine ensemble. The energies are obtained from eq. (6.13), and amplitudes from eq. (6.14). The grey bands give the results of the full multiexponential fit.

amplitudes $\langle \Omega | \bar{c}(\gamma_5 \otimes \gamma_5) h | H_c \rangle \equiv \langle \Omega | P | H_c \rangle$, $\langle \Omega | \bar{c}(\gamma_0 \gamma_5 \otimes \gamma_0 \gamma_5) h | \hat{H}_c \rangle = \langle \Omega | A_0 | \hat{H}_c \rangle$. Then, the normalization for A_0 (common to that of spacial axial currents A_k) Z_A , is fixed by demanding that the partially conserved axial current relation holds-

$$(m_{h0}^{\text{val}} + m_{c0}^{\text{val}}) \langle \Omega | P | H_c \rangle|_{\text{lat}} = M_{\hat{H}_c} Z_A \langle \Omega | A^0 | \hat{H}_c \rangle|_{\text{lat}}. \quad (6.15)$$

The Z_A values found on each ensemble and am_{h0}^{val} are given in table 7.4.

There is an ambiguity in what mass to use on the right hand side of (7.17), we here use the non-goldstone mass $M_{\hat{H}_c}$, but one could just as well replace this with M_{H_c} . Using M_{H_c} here changes Z_A only by discretization effects, the difference never exceeding 0.0015 throughout the ensembles and heavy masses. The choice between these two definitions of Z_A does not effect the continuum result.

We also remove tree-level mass-dependent discretization effects, at leading order

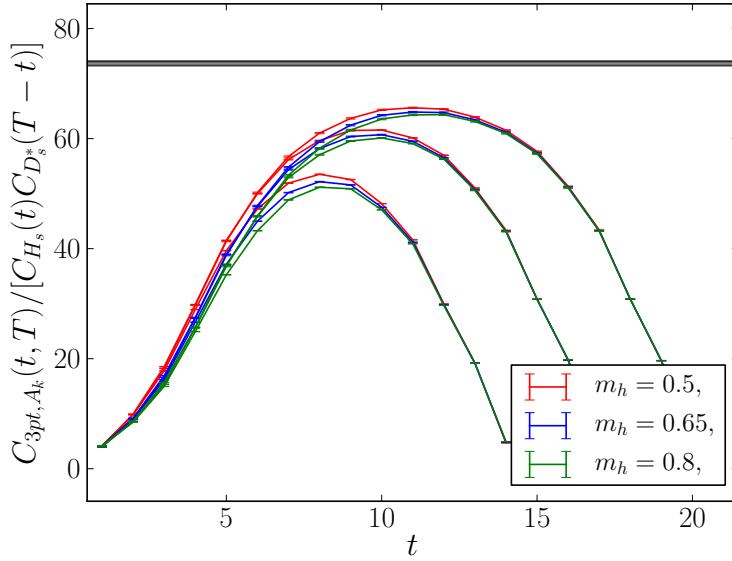


Figure 6.4: Sanity check for fits to the 3-point correlation functions. This ratio should approach J_{00}^{nn} for $t \gg 0$ and $t \ll T$. The grey band shows the result for J_{00}^{nn} from the full multiexponential fit.

in $|\mathbf{p}_h|/m_h$, using a normalization constant derived in [132]:

$$\begin{aligned} Z_{\text{disc}} &= \sqrt{\tilde{C}_h \tilde{C}_c}, \\ \tilde{C}_q &= \cosh am_{q1} \left(1 - \frac{1 - \epsilon_{\text{Naik}}}{2} \sinh^2 am_{q1} \right), \\ am_{q1} &= am_{q0} \left(1 - \frac{3}{88} am_{q0}^4 + \frac{23}{2240} am_{q0}^6 \right. \\ &\quad \left. + \frac{1783}{537600} am_{q0}^8 - \frac{76943}{23654400} am_{q0}^{10} + \mathcal{O}(am_{q0}^{12}) \right), \end{aligned} \quad (6.16)$$

where ϵ_{Naik} is the Naik parameter in the HISQ action and am_{q1} is the tree-level pole mass in HISQ. The expansion for am_{q1} in terms of am_{q0} was derived in [65]. The effect of Z_{disc} is very small, never exceeding 0.2%. Z_{disc} values on each ensemble for each am_{h0}^{val} are given in table 7.4.

Combining these normalizations with the lattice current from the 3-point fits, we find a value for the form factor at a given heavy mass and lattice spacing:

$$h_{A_1}^s(1) = \frac{1}{3} \sum_{k=0}^3 \frac{Z_A Z_{\text{disc}} \langle D_s^*(\hat{k}) | A^k | H_s \rangle_{\text{lat}}}{2 \sqrt{M_{H_s} M_{D_s^*}}}. \quad (6.17)$$

Set	am_{h0}^{val}	Z_A	Z_{disc}
2	0.5	1.03178(57)	0.99819
	0.65	1.03740(58)	0.99635
	0.8	1.04369(56)	0.99305
3	0.5	1.03203(39)	0.99829
	0.8	1.04389(38)	0.99315
4	0.427	1.0138(11)	0.99931
	0.525	1.0170(12)	0.99859
	0.65	1.0213(12)	0.99697
	0.8	1.0272(12)	0.99367
5	0.5	1.00898(45)	0.99889
	0.65	1.01365(50)	0.99704
	0.8	1.01970(55)	0.99375

Table 6.2: Normalization constants applied to the lattice axial vector current in (7.18). Z_A is found from (7.17) and Z_{disc} from (6.16).

6.2.4 Extrapolation to Physical Point

We now address the extrapolation of the $h_{A_1}^s(1)$ values to continuum and physical b and l masses. In the process of the extrapolation, we also aim to determine the HQET low energy constants $l_{V,A,P}^s$. This process requires a number of considerations.

Heavy Mass Dependence

Our extrapolation in the m_h direction can be guided by HQET. The HQET expression for $h_{A_1}^s(1)$ (where here we consider both h and c to be heavy quarks in the HQET context) is given by [133, 134]:

$$h_{A_1} = \eta_A \left(1 - \frac{l_V}{(2m_c)^2} + \frac{2l_A}{2m_c m_h} - \frac{l_P}{(2m_h)^2} \right) + \mathcal{O}\left(\frac{1}{m_c^n m_h^m}, n+m \geq 3\right). \quad (6.18)$$

η_A accounts for matching between HQET and QCD, and has been computed at 2-loop: $\eta_A = 0.960(7)$ [135]. It is dependent on m_h , so one may worry that, if we are going to use this expression for the extrapolation in m_h , we must account for the m_h dependence in η_A . However this dependence is weak in the region of m_h we are interested in ($m_c \leq m_h \leq m_b$). This can be seen by examining how the 1-loop expression for η_A varies with m_h [136]:

$$\eta_A(m_h) = 1 - \frac{3\alpha_s(m_b)}{4\pi} \left(\frac{m_h + m_c}{m_h - m_c} \log\left(\frac{m_c}{m_h}\right) - 2 \right). \quad (6.19)$$

Fig. 6.5 shows the variation of η_A throughout this range; the value changes by around 1%, This is negligible in relation to the errors we find in the parameters governing the slope, $l_{V,A,P}$. so we can safely ignore the m_h dependence in η_A . The fit was attempted with an extra factor multiplying η_A of $(1 + \rho \log(M_{\eta_c}/M_{\eta_h}))$, where ρ was a free fit parameter, and this caused the Bayes factor to drop by a factor of 25. This implies that our lattice data cannot resolve any logarithmic behaviour in m_h , and we can safely ignore η_A 's m_h dependence.

Quark Mass Ambiguities

If we are to determine $l_{V,A,P}^s$, attention must be paid to what to input for the masses $m_{h,c}$ in (6.18). Finding continuum quark masses corresponding to lattice bare masses would be a considerable task. Even if we took this on, what renormalisation scheme

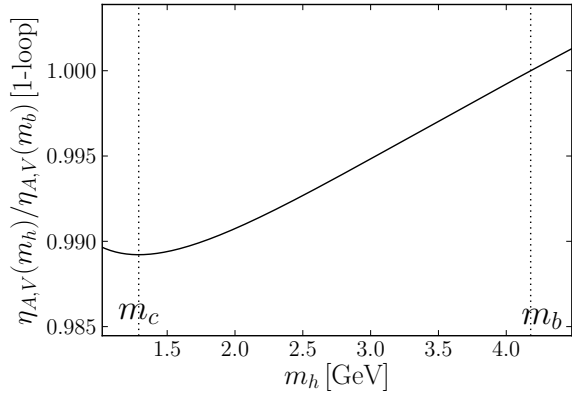


Figure 6.5: The variation of the 1-loop expression for η_A & η_V throughout the $m_c \leq m_h \leq m_b$ range.

do the masses belong to? In HQET, the masses that define the power counting should be pole masses. Due to renormalons, the definition of pole masses is also ambiguous.

Thankfully, for our purposes, we do not need to worry about any of this. The quark masses in this equation can be replaced with expressions depending only on the meson masses M_{H_s} , $M_{D_s^*}$, which we can obtain for each ensemble and heavy mass from the H_s and D_s^* correlator fits.

To see this, first consider the HQET expansion of a heavy-light meson [137]:

$$M_{H_q} = m_{h,S} + \bar{\Lambda}_S + \frac{\mu_S^2}{m_{h,S}} + \mathcal{O}\left(\frac{1}{m_h^2}\right). \quad (6.20)$$

For notational brevity we are using the shorthand $\mu_S^2 = \mu_{\pi,S}^2 - d_{H(*)}\mu_{G,S}^2$, where $d_{H(*)} = 1$ for pseudoscalar mesons and $-1/3$ for vectors. $\bar{\Lambda}_S, \mu_{\pi,S}, \mu_{G,S}$ are HQET parameters and q labels the light quark. As already mentioned, m_h is defined in some renormalization scheme S , and since the meson mass M_{H_q} is scheme-independent, the HQET parameters must also take on scheme dependence to cancel the dependence in m_h .

Changing the subject of eq. (6.20) to m_h and taking the inverse, we find

$$\begin{aligned} \frac{1}{m_{h,S}} &= \frac{1}{M_{H_q} - \bar{\Lambda}_S - \frac{\mu_S^2}{m_{h,S}}} + \mathcal{O}\left(\frac{1}{m_h^2}\right), \\ &= \frac{1}{M_{H_q} - \bar{\Lambda}_S} \left(1 + \frac{\mu_S^2}{(M_{H_q} - \bar{\Lambda}_S)m_{h,S}}\right) + \mathcal{O}\left(\frac{1}{m_h^2}\right), \end{aligned}$$

then solving for $1/m_{h,S}$ -

$$\begin{aligned} \frac{1}{m_{h,S}} &= \frac{1}{(M_{H_q} - \bar{\Lambda}_S) \left(1 - \frac{\mu_S^2}{(M_{H_q} - \bar{\Lambda}_S)^2}\right)} + \mathcal{O}\left(\frac{1}{m_h^2}\right) \\ &\equiv \varepsilon_{h,S} + \mathcal{O}\left(\frac{1}{m_h^2}\right) \end{aligned} \quad (6.21)$$

For two heavy-light mesons, for example $M_{H_s}, M_{D_s^*}$, one can show (recognising that $\varepsilon_{h,S} \sim \mathcal{O}(1/m_h)$)

$$\frac{1}{m_{h,S} m_{c,S}} = \varepsilon_{h,S} \varepsilon_{c,S} + \mathcal{O}\left(\frac{1}{m_c^n m_h^m}, n+m \geq 3\right). \quad (6.22)$$

Since we are aiming to find the low energy constants in the context of HQET at order below $\mathcal{O}(1/m_c^n m_h^m, n+m \geq 3)$, we can safely replace the quark masses m_c, m_h in (6.18) with $\varepsilon_{h,c,S}^{-1}$.

For our calculation, we use HQET parameters calculated in [137] in the minimal renormalon-subtraction scheme: $\bar{\Lambda}_{\text{MRS}} = 0.552(30)\text{GeV}$, $\mu_{\pi,\text{MRS}}^2 = 0.06(22)\text{GeV}^2$, $\mu_{G,\text{MRS}}^2 = 0.38(1)\text{GeV}^2$.

One would expect that performing a fit using these scheme-dependent parameters will produce outputs $l_{V,A,P}^s$ containing a scheme ambiguity. However, renormalon ambiguities in a pole mass m are of order $\mathcal{O}(1/m)$. The ambiguity in the low-energy constants will, in fact, be absorbed by the next order in $1/m$, which we can safely ignore. Hence we can drop the renormalization scheme subscripts.

The fit form we use for the full extrapolation of $h_{A_1}^s(1)$ is

$$\begin{aligned} h_{A_1}^s(1)|_{\text{fit}} &= \eta_A \left(1 - \left(\frac{\varepsilon_c}{2}\right)^2 l_V + \varepsilon_c \varepsilon_h l_A - \left(\frac{\varepsilon_h}{2}\right)^2 l_P\right) \\ &\quad + \mathcal{N}_{\text{disc}} + \mathcal{N}_{\text{mistuning}}. \end{aligned} \quad (6.23)$$

$\mathcal{N}_{\text{disc}}$ and $\mathcal{N}_{\text{mistuning}}$ are nuisance parameters to account for discretization and mass mistuning effects, defined in the following subsections. $l_{V,A,P}^s$ are taken here as fit parameters with prior distributions $0 \pm (2\Lambda_{\text{QCD}})^2$.

Discretization Effects

Discretization effects in the data are accounted for by including (following the methodology of [3]):

$$\mathcal{N}_{\text{disc}} = \sum_{i,j+k \neq 0}^{2,2,2} d_{ijk} \left(\frac{\Lambda_{\text{QCD}}}{M_{\eta_h}}\right)^i \left(\frac{am_{h0}^{\text{val}}}{\pi}\right)^{2j} \left(\frac{am_{c0}^{\text{val}}}{\pi}\right)^{2k}. \quad (6.24)$$

M_{η_h} is used here as a proxy for the heavy quark mass. d_{ijk} are fit parameters with prior distributions 0 ± 0.5 . We account here for discretization effects from the two largest scales in the system, am_{h0}^{val} and am_{c0}^{val} . All discretization effects are of even order by construction of the HISQ action.

We tried including extra terms of size $a\Lambda_{\text{QCD}}, am_{s0}^{\text{val}}, am_{l0}^{\text{val}}$, but the data could not resolve effects of that size, so it made no difference to the fit. We also tested the effects of increasing the number of terms in each sum, but the final result remained unchanged.

Mass Mistunings

Any possible mistunings of the charm mass is automatically accounted for in the first part of (6.23). To obtain the final result we set $M_{D_s^*}$ in ε_c to the physical value, hence any charm mistuning is removed.

The strange and light mistunings are accounted for using the formalism introduced in [94]. To deal with possible strange mistuning, we define the term $\delta_s = m_s - m_s^{\text{tuned}}$, where m_s^{tuned} is defined by

$$m_s^{\text{tuned}} = m_{s0} \left(\frac{M_{\eta_s}^{\text{physical}}}{M_{\eta_s}} \right)^2. \quad (6.25)$$

$M_{\eta_s}^{\text{physical}}$ is determined in lattice simulations from the masses of the pion and kaon [93].

We similarly account for (sea) light quark mistuning by defining $\delta_l = m_{l0} - m_l^{\text{tuned}}$. We find m_l^{tuned} from m_s^{tuned} , leveraging the fact that the ratio of quark masses is regularization independent, and was calculated in [138]:

$$\left. \frac{m_s}{m_l} \right|_{\text{phys}} = 27.35(11). \quad (6.26)$$

We set m_l^{tuned} to m_s^{tuned} divided by this ratio.

The full term we include to account for mistuning is given by

$$\mathcal{N}_{\text{mistuning}} = c_s \frac{\delta_s}{\Lambda_\chi} + c_l \frac{\delta_l}{\Lambda_\chi} \quad (6.27)$$

where c_l and c_s are fit parameters with prior distributions 0 ± 1 , and Λ_χ is the chiral breaking scale, which we set to 1GeV. We neglect $\delta_{s,l}^2$ contributions since these are an order of magnitude smaller and are not resolved by the data.

Other Effects

The finite volume effects in our lattice results are negligible. Since the lightest valence quarks in our simulation are s quarks, the lightest particles that can arise from loop diagrams in the decay are Kaons. In appendix F of [8], the $\text{HMS}\chi\text{PT}$ finite volume effect on the fine-physical ensemble, as a function of the lightest meson appearing in loops, was found (from the formulas derived in [123]). At the Kaon mass, the finite volume effect is many orders of magnitude smaller than any of our other sources of error. Since one would expect the fine-physical ensemble to be where the dominant finite volume effects arise in our calculation, we can safely ignore finite volume effects in this analysis.

In our simulation we set $m_u = m_d \equiv m_l$, this means our results do not account for isospin breaking. We tested for any possible influence this has on our fit, by moving the m_l^{tuned} value up and down by the PDG value for $m_d - m_u$, and the effect was negligible in comparison to the other sources of error.

In section 6.3.2 we detail a number of other tests run on this fit.

6.3 Results and Discussion

6.3.1 $h_{A_1}^s(1)$

The values extracted from correlation function fits for $h_{A_1}^s(1)$, along with quantities required for its extrapolation to the physical point, are given in table 6.3.

The results for the extrapolation through heavy mass of $h_{A_1}^s(1)$ is given in fig. 6.6. Our final, fully non-perturbative result for the $B_s \rightarrow D_s^*$ form factor at zero recoil is

$$\mathcal{F}^{B_s \rightarrow D_s^*}(1) = h_{A_1}^s(1) = 0.8968(88)_{\text{stat}}(60)_{\text{sys}}. \quad (6.28)$$

Adding the statistical and systematic errors in quadrature, we find a total fractional error of 1.19%. The error budget for this result is given in table 6.5.

Our result is statistics dominated. The systematic error is dominated by the continuum extrapolation.

We include in fig. 6.6 a determination from the only other lattice determination of this quantity [8]. They report a value of $h_{A_1}^s(1) = 0.883(12)_{\text{stat}}(28)_{\text{sys}}$. Our two studies, containing independent systematic uncertainties, are in agreement.

This study used the same gluon ensembles, with HISQ s and c valence quarks, and an NRQCD b quark. Using NRQCD meant they could perform their simula-

Set	am_h^{val}	$h_{A_1}^s(1)$	aM_{H_s}	$aM_{D_s^*}$
0	0.5	0.9255(20)	0.95972(12)	0.96616(44)
	0.65	0.9321(22)	1.12511(16)	
	0.8	0.9434(24)	1.28128(21)	
1	0.5	0.9231(21)	0.95462(12)	0.93976(42)
	0.8	0.9402(27)	1.27577(22)	
2	0.427	0.9107(46)	0.77453(24)	0.63589(49)
	0.525	0.9165(49)	0.88487(31)	
	0.65	0.9246(65)	1.02008(39)	
	0.8	0.9394(66)	1.17487(54)	
3	0.5	0.9143(51)	0.80245(24)	0.47164(39)
	0.65	0.9273(62)	0.96386(33)	
	0.8	0.9422(72)	1.11787(43)	

Table 6.3: Values extracted from correlation function fits for $h_{A_1}^s(1)$, along with quantities required for its extrapolation to the physical point. $h_{A_1}^s(1)$ values are found from eq. (7.18). f_{H_c} is the H_c decay constant derived from eq. (??).

Set	am_h^{val}	aM_{H_c}	af_{H_c}	aM_{η_h}	aM_{η_c}	aM_{η_s}
0	0.5	1.419515(41)	0.186299(70)	1.471675(38)	1.367014(40)	0.313886(75)
	0.65	1.573302(40)	0.197220(77)	1.775155(34)		
	0.8	1.721226(39)	0.207068(78)	2.064153(30)		
1	0.5	1.400034(28)	0.183472(62)	1.470095(25)	1.329291(27)	0.304826(52)
	0.8	1.702456(23)	0.203407(45)	2.062957(19)		
2	0.427	1.067224(46)	0.126564(70)	1.233585(41)	0.896806(48)	0.207073(96)
	0.525	1.172556(46)	0.130182(72)	1.439515(37)		
	0.65	1.303144(46)	0.133684(75)	1.693895(33)		
	0.8	1.454205(46)	0.137277(79)	1.987540(30)		
3	0.5	1.011660(32)	0.098970(52)	1.342639(65)	0.666586(89)	0.15412(17)
	0.65	1.169761(34)	0.100531(60)	1.650180(56)		
	0.8	1.321647(37)	0.101714(70)	1.945698(48)		

Table 6.4: Values extracted from correlation function fits for $h_{A_1}^s(1)$, along with quantities required for its extrapolation to the physical point. $h_{A_1}^s(1)$ values are found from eq. (7.18). f_{H_c} is the H_c decay constant derived from eq. (4.36).

Source	% Fractional Error
Statistics	0.98
$a \rightarrow 0$	0.57
$m_h \rightarrow m_b$, c -mistuning	0.36
l -mistuning	0.08
s -mistuning	0.03
Total	1.19

Table 6.5: Error budget for $h_{A_1}^s(1)$.

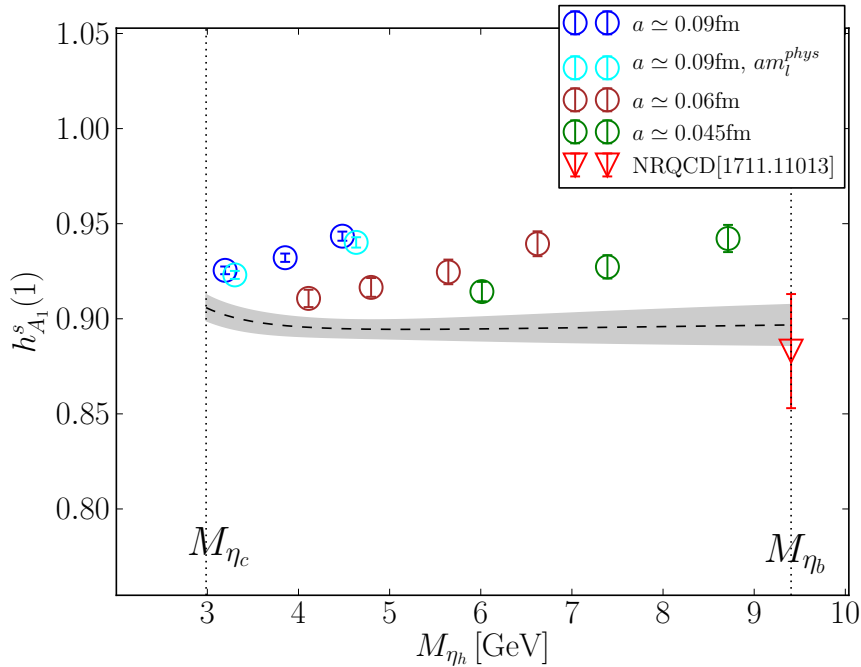


Figure 6.6: $h_{A_1}^s(1)$ against M_{η_h} (a proxy for the heavy quark mass). The grey band shows the result of the extrapolation at $a = 0$ and physical l,s and c masses. Sets listed in the legend follow the order of sets in table 6.1. The red point represents a determination of the same quantity from a previous study using the NRQCD action for the b [8].

tion directly at the physical b mass. However, the matching of lattice NRQCD to continuum QCD causes their dominant error. Adding their errors from $\mathcal{O}(\alpha_s^2)$, $\mathcal{O}(\alpha_s \Lambda_{\text{QCD}}/m_b)$ and $\mathcal{O}((\Lambda_{\text{QCD}}/m_b)^2)$ corrections in quadrature, we find a 2.8% error, while their total error is reported as 2.9%.

6.3.2 Extrapolation Stability

We performed a number of tests of the continuum/heavy mass extrapolation. The results of each of these tests are given in fig. 6.7.

One of the tests requires some explanation, the result of which is given in fig. 6.7, labelled ‘Ratio’. We performed a continuum/heavy mass extrapolation in the ratio $h_{A_1}^s(1)/(f_{H_c} \sqrt{M_{H_c}})$. f_{H_c} is found from fitting the H_c correlation functions to obtain $a_0^{H_c}$, and using eq. (4.36). Since we create the H_c mesons with a local HISQ pseudoscalar current, which is absolutely normalized, no normalization of f_{H_c}

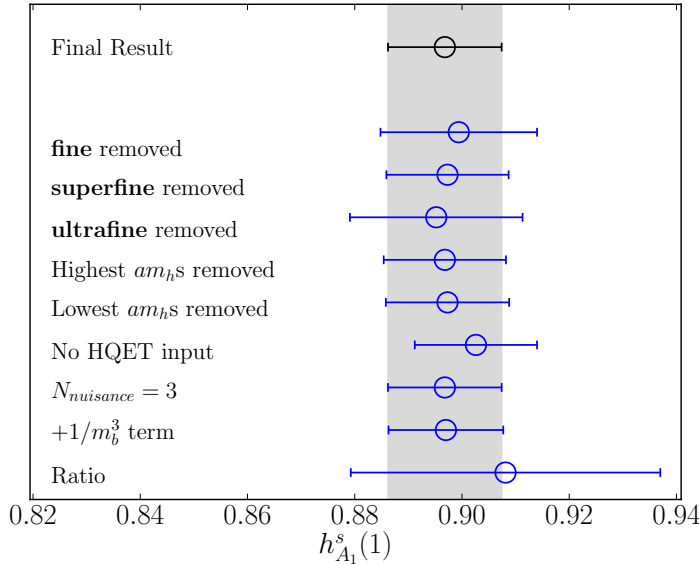


Figure 6.7: Results of $h_{A_1}^s(1)$ extrapolation tests. The top three blue points show $h_{A_1}^s(1)$ at continuum and physical b mass, if data from the fine, superfine or ultrafine ensembles are not used in the fit. The fourth and fifth blue points show the result if data at the highest/lowest am_{h0}^{val} value on each ensemble are removed. The point labelled 'No HQET input' is the result of a more naive heavy-mass extrapolation; the first line of (6.23) is removed, and the sum in (6.24) is extended to include terms with $j+k=0$. An extra term to account for charm mass mistunings is added. The point labelled $N_{nuisance}=3$ is the result of extending the sum in (6.24) such that it truncates at 3 rather than 2 in each of the i,j,k directions. The point labelled ' $+1/m_b^3$ ' results from adding an extra term to (6.23) of the form $p\varepsilon_h^3$ where p is a fit parameter with the same prior as $l_{V,A,P}^s$. In this case, the Bayes factor falls by a factor of 7, suggesting that the data does not contain a cubic dependence on the heavy mass. The point labelled 'Ratio' is the result of an alternative extrapolation described in sec. 6.3.2.

is required here. Details of the extrapolation are given in appendix 6.3.5, and results are shown in fig. 6.8. Discretization effects cancel to a large extent in this ratio, it however varies strongly with changing heavy mass. This makes the extrapolation very different to the extrapolation in $h_{A_1}^s(1)$, which has large discretization effects but has little variation in the heavy mass. Hence the two extrapolations have quite

different systematics.

We also performed an extrapolation of f_{H_c} to continuum and physical b , following precisely the methodology of [3], and summarized in sec 6.3.5. The result of the extrapolation of $h_{A_1}^s(1)/(f_{H_c}\sqrt{M_{H_c}})$ at continuum and physical b mass was multiplied by our f_{B_c} result, and the PDG value for M_{B_c} [1], to obtain a second determination of $h_{A_1}^s(1)$. This is the result given in fig. 6.7 labelled 'Ratio'.

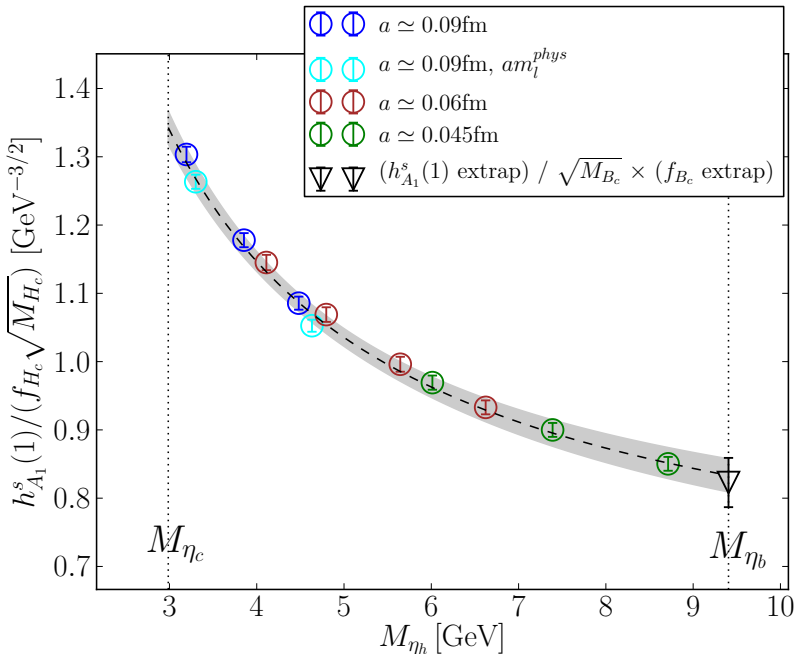


Figure 6.8: $h_{A_1}^s(1)/(f_{H_c}\sqrt{M_{H_c}})$ against M_{η_h} (a proxy for the heavy quark mass). The grey band shows the result of the extrapolation at $a = 0$ and physical l,s and c masses. Sets listed in the legend follow the order of sets in table 6.1. The black point shows our final result for $h_{A_1}^s(1)$ divided by $\sqrt{M_{B_c}}$ from the PDG [1] and f_{B_c} from our extrapolation of f_{H_c} to continuum and physical b mass.

In fig. 6.9, we show all current lattice results for $h_{A_1}(1)$ and $h_{A_1}^s(1)$. In fig. 6.10, we show lattice data from the previous FNAL/MILC and HPQCD, along with their final results, and the final result of this study, against 'pion mass'. Here pion mass refers to the mass of a pion containing quarks with the mass of the spectator quark. Here we can see that the FNAL/MILC lattice data is very flat in the spectator quark mass, so if they were to extrapolate their data to find $h_{A_1}^s(1)$, it would broadly be in agreement with our result.

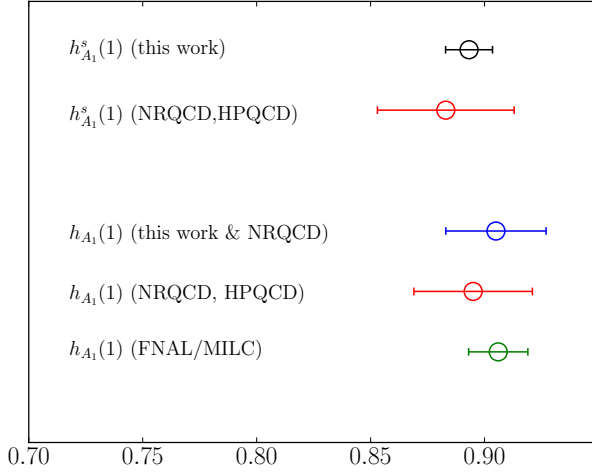


Figure 6.9: $h_{A_1}^{(s)}(1)$ from different calculations. Those marked (NRQCD,HPQCD) are from [8]. The quantity marked (this work & NRQCD) is the result of multiplying our result for $h_{A_1}^s(1)$ with the ratio $h_{A_1}(1)/h_{A_1}^s(1)$ computed in [8]. The quantity marked (FNAL/MILC) is from [13].

6.3.3 Hints about $B \rightarrow D^*$

As mentioned in the introduction, the $B_s \rightarrow D_s^*$ form factor seems to be very close to the equivalent $B \rightarrow D^*$ form factor.

As an additional test of this claim, we obtained lattice data for $h_{A_1}(1)$ on the fine ensemble, for comparison with the $h_{A_1}^s(1)$ data within our formalism. This involved an identical process to that of obtaining $h_{A_1}^s(1)$, except with the strange valence quark replaced with a valence quark of a mass equal to am_{l0} , the sea light quark mass.

The $h_{A_1}(1)$ data is shown in comparison to the $h_{A_1}^s(1)$ data in fig. 6.11. Errors are statistical. The error on $h_{A_1}(1)$ is much larger due to the presence of the valence light quark. There is no significant difference between $h_{A_1}(1)$ and $h_{A_1}^s(1)$ here.

In [8], the ratio between these two quantities was computed - $h_{A_1}(1)/h_{A_1}^s(1) = 1.013(14)_{\text{stat}}(17)_{\text{sys}}$. Multiplying this by our result for $h_{A_1}^s(1)$, one finds a result consistent with the two previous $h_{A_1}(1)$ determinations.

$$\mathcal{F}^{B \rightarrow D^*}(1) = h_{A_1}(1) = 0.909(24). \quad (6.29)$$

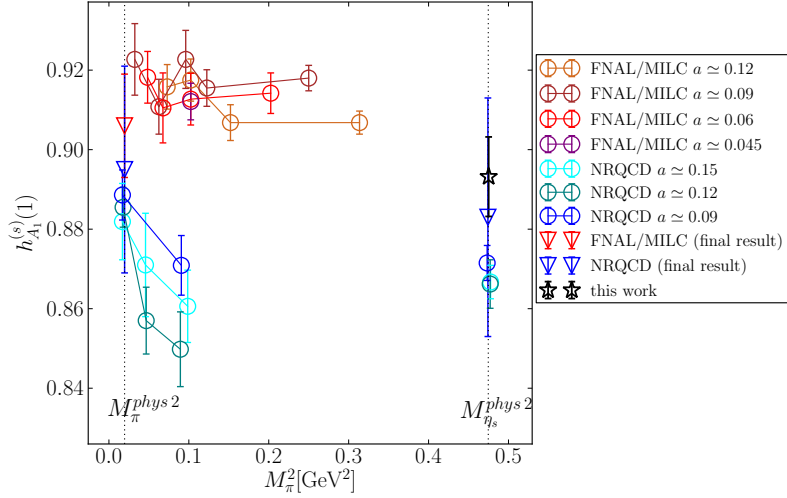


Figure 6.10: Lattice data and continuum extrapolated data for three studies of $h_{A_1}(1)$ and $h_{A_1}^s$, against the pion mass. Points labeled FNAL/MILC are from [13], and those labeled NRQCD are from [8]. The x-axis must be taken with a pinch of salt, the points at $M_\pi = M_{\eta_s}$ have pions in the sea of smaller masses than M_{η_s} , but we place them here to signify that the spectator quark as the mass of a strange quark.

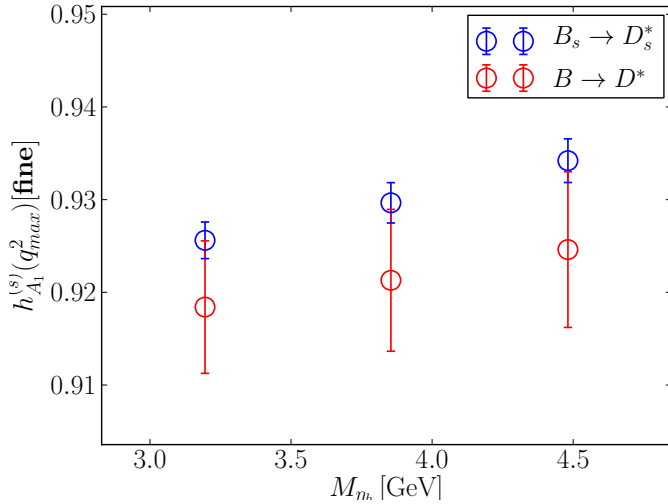


Figure 6.11: $h_{A_1}(1)$ and $h_{A_1}^s(1)$ data on the fine ensemble.

6.3.4 HQET Low Energy Constants

Our fit of the lattice data to (6.23) produced the fit parameters $l_{V,A,P}^s$, which as discussed in sections 6.2.4 and 6.2.4, are numerically equal to the low energy HQET

Source	l_V^s	l_A^s	l_P^s
Statistics	30.3	101.8	64.4
$a \rightarrow 0$	22.4	80.5	38.2
mistuning	2.0	3.5	1.5
η_A	0.7	0.7	0.7
$\mathcal{O}(1/m_c^3)$	4.4	-	-
Total	40.0	136.9	78.9

Table 6.6: Error budget for HQET low energy constants. Each column gives the % fractional error for the associated quantity.

constants of the same name. We find

$$\begin{aligned} l_V^s &= 0.59(24)\text{GeV}^2, \\ l_A^s &= -0.08(11)\text{GeV}^2, \\ l_P^s &= -0.25(20)\text{GeV}^2. \end{aligned} \quad (6.30)$$

Since the lattice data contains all orders of HQET, l_V has been given a systematic uncertainty due to contamination from higher orders in $1/m_c$. Accordingly a systematic error of size $(\varepsilon_c \Lambda_{\text{QCD}})^3 \simeq 0.03$ is included in the l_V result. We also include an error accounting for the error in η_A that we neglect in the fit.

An estimate from the ISGW model for $B \rightarrow D^*$ decays gives [139]

$$l_P \simeq l_V \simeq 0.39\text{GeV}^2. \quad (6.31)$$

One does not expect these to differ significantly from $l_{V,A,P}^s$. These are of the same order of magnitude as our results. It is notable however that we find a different sign for l_P to the ISGW result.

6.3.5 Extrapolation of $h_{A_1}^s(1)/(f_{H_c}\sqrt{M_{H_c}})$ and f_{H_c}

As a consistency test of our result we also perform extrapolations in $h_{A_1}^s(1)/(f_{H_c}\sqrt{M_{H_c}})$ and f_{H_c} , then combine them to find a second determination of $h_{A_1}^s(1)$.

Both extrapolations use a fit function of the form

$$\text{fit} = \left(\frac{\alpha_s(M_{\eta_h})}{\alpha_s(M_{\eta_c})} \right)^p M_{\eta_h}^{n/2} \times \\ \sum_{i,j,k=0}^{2,2,2} d_{ijk} \left(\frac{\Lambda_{\text{QCD}}}{M_{\eta_h}} \right)^i \left(\frac{am_{h0}^{\text{val}}}{\pi} \right)^{2j} \left(\frac{am_{c0}^{\text{val}}}{\pi} \right)^{2k} \\ + \mathcal{N}_{\text{mistuning}}. \quad (6.32)$$

$\alpha_s(M)$ is the QCD coupling constant evaluated at scale M . p is a fit parameter with prior distribution $\pm 2/9 \pm 1/9$, + for $h_{A_1}^s(1)/(f_{H_c}\sqrt{M_{H_c}})$ and - for f_{H_c} . $n = 0$ for $h_{A_1}^s(1)/(f_{H_c}\sqrt{M_{H_c}})$ and $n = -1$ for f_{H_c} . The $M_{\eta_h}^{n/2}$ accounts for the leading order dependance of f_{H_c} in HQET, and the α_s ratio comes from matching between QCD and HQET of f_{H_c} . $\mathcal{N}_{\text{mistuning}}$ is defined in 7.23.

The extrapolation in f_{H_c} is shown in fig. 6.12. We here include the result from a previous heavy-HISQ determination of f_{B_c} on 2+1 gauge ensembles [3]. Our result is slightly higher than theirs, since their study used only unphysically heavy light quarks ($m_l/m_s \simeq 0.2$), and did not control for associated effects. Our final result for this quantity is

$$f_{B_c} = 0.4350(55). \quad (6.33)$$

6.4 Conclusions

We have produced a fully non-perturbative determination of $h_{A_1}^s(1)$, sometimes called $\mathcal{F}^{B_s \rightarrow D_s}(1)$, using unquenched lattice data from a fully relativistic and highly improved lattice action, along with the low energy constants $l_{V,A,P}^s$, given in (6.28) and (6.30) respectively. We used gauge ensembles with 3 lattice spacings, including an ensemble with approximately physical light sea quark masses, and obtained data corresponding to 12 different heavy quark masses.

This study supplies an independent check of the NRQCD formalism used in previous HPQCD studies. It is also much more precise, in the case of $h_{A_1}^s$, the total fractional error has been halved in comparison to the NRQCD determination. The comparative precision resulting from the heavy-HISQ method suggests that it is well suited to computing other form factors associated with b -decays. A sister paper, studying the $B_s \rightarrow D_s$ form factors throughout the physical q^2 range, is in progress.

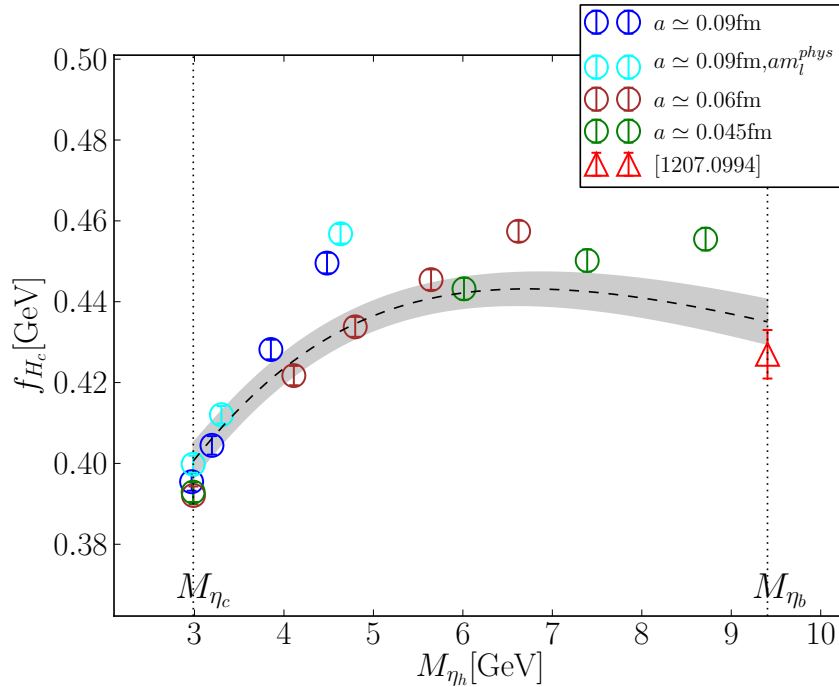


Figure 6.12: $h_{A_1}^s(1)$ against M_{η_h} (a proxy for the heavy quark mass). The grey band shows the result of the extrapolation at $a = 0$ and physical l,s and c masses. Sets listed in the legend follow the order of sets in table 6.1. The red point shows the result from a previous heavy-HISQ determination of f_{B_c} on 2+1 gauge ensembles [3]

Various improvements to this study could be implemented in future calculations. For example - since the uncertainty is dominated by statistics, more lattice data should be included. One useful innovation that was not used here is the Covariant Approximation Averaging approach to solving quark propagators [140], this could significantly boost statistics while keeping computational cost manageable.

CHAPTER 7

$B_s \rightarrow D_s l \nu$ Form Factor at All Physical q^2 from Heavy-HISQ

In this chapter we detail the second of our two heavy-HISQ studies, the calculation of the $B_s \rightarrow D_s l \nu$ form factors $f_0^s(q^2), f_+^s(q^2)$ throughout all physical q^2 , as defined in Sec. 2.2.2. Like for $h_{A_1}^s(1)$, we give this quantity the superscript s to differentiate it from the more often referred to form factors for $B \rightarrow D l \nu$ decays.

We briefly review the definition of the form factors here for ease of reading. The differential decay rate for $B_s \rightarrow D_s l \nu$ decays are given in the SM by

$$\frac{d\Gamma}{dq^2} = \eta_{\text{EW}} \frac{G_F^2 |V_{cb}|^2}{24\pi^3 M_{B_s}^2} \left(1 - \frac{m_l^2}{q^2}\right)^2 |\mathbf{p}_{D_s}| \times \\ \left[\left(1 + \frac{m_l^2}{2q^2}\right) M_{B_s}^2 |\mathbf{p}_{D_s}|^2 f_+^{s2}(q^2) + \frac{3m_l^2}{8q^2} (M_{B_s}^2 - M_{D_s}^2)^2 f_0^{s2}(q^2) \right] \quad (7.1)$$

where m_l is the mass of the lepton, η_{EW} is the electroweak correction, $q^2 = (p_{B_s} - p_{D_s})^2$ is the momentum transfer, and $f_0^s(q^2), f_+^s(q^2)$ are the scalar and vector form factors that parameterize the non-perturbative contribution to the decay. The allowed range of q^2 values if the final states are on-shell is

$$m_l^2 \leq q^2 \leq (M_{B_s} - M_{D_s})^2. \quad (7.2)$$

The form factors parameterize matrix elements of the electroweak current between B_s and D_s states, $\langle D_s | (V - A)^\mu | B_s \rangle$ where $V^\mu = \bar{b} \gamma_\mu c$ is the vector component and $A^\mu = \bar{b} \gamma_5 \gamma_\mu c$ is the axial vector component. In a pseudoscalar-to-pseudoscalar amplitude, only V^μ contributes, since $\langle D_s | A^\mu | B_s \rangle$ does not satisfy the parity invariance of QCD. The vector current in terms of form factors is given by

$$\langle D_s | V^\mu | B_s \rangle = f_+^s(q^2) \left[p_{B_s}^\mu + p_{D_s}^\mu - \frac{M_{B_s}^2 - M_{D_s}^2}{q^2} q^\mu \right] \\ + f_0^s(q^2) \frac{M_{B_s}^2 - M_{D_s}^2}{q^2} q^\mu. \quad (7.3)$$

Analyticity of this matrix element demands that

$$f_+^s(0) = f_0^s(0). \quad (7.4)$$

Via the partially conserved vector current relation (PCVC), the form factor $f_0^s(q^2)$ is also directly related to the matrix element of the scalar current $S = \bar{b}c$;

$$(m_b - m_c)\langle D_s | S | B_s \rangle = (M_{B_s}^2 - M_{D_s}^2)f_0^s(q^2). \quad (7.5)$$

In our calculation we access the form factors by computing matrix elements of the temporal vector current V_0 and the scalar current S . The form factors can be extracted from this combination using expresions derived from (7.3) and (7.5);

$$f_0^s(q^2) = \frac{m_b - m_c}{M_{B_s}^2 - M_{D_s}^2}\langle D_s | S | B_s \rangle, \quad (7.6)$$

$$f_+^s(q^2) = \frac{1}{2M_{B_s}} \frac{\delta^M \langle D_s | S | B_s \rangle - q^2 \langle D_s | V_0 | B_s \rangle}{\mathbf{p}_{D_s}^2}, \quad (7.7)$$

$$(\delta^M = (m_b - m_c)(M_{B_s} - E_{D_s})).$$

Our goal is to compute $f_0^s(q^2)$ and $f_+^s(q^2)$ throughout the range of q^2 values $0 \leq q^2 \leq (M_{B_s} - M_{D_s})^2 \equiv q_{\max}^2$. We extend the range to $q^2 = 0$ in order to take advantage of the constraint (7.4). To acheive this, we compute $\langle D_s | S | H_s \rangle$ and $\langle D_s | V_0 | H_s \rangle$ on the lattice, where the H_s meson is at rest and D_s mesons are given an appropriate array of spacial momenta.

Those interested in simply using the form factors calculated here should refer to Sec. 7.4, which gives all information necessary for reconstructing our form factors.

7.1 Motivation

$B_s \rightarrow D_s l \nu$ decays can supply a new method for precisely determining the CKM element $|V_{cb}|$. Determination of $|V_{cb}|$ in this way requires both a measurement of the branching fraction and a theoretical determination of the form factors, as explained in Sec. 2.2.2. To obtain the highest possible precision, data for both the form factors and branching fractions are required throughout the largest possible range of momentum transfer. Analogous approaches were already performed using $B \rightarrow D l \nu$ decays [11, 12, 17–19, 141, 142].

The $B_s \rightarrow D_s l \nu$ decay can also supply a new test of the Standard Model, by comparing the theoretical and experimental determinations of the ratio R_{D_s} , defined in (2.35). This would be especially illuminating since tension has been found in the

intimately related ratios $R_{D(*)}$. The presence or absense of an anomaly in R_{D_s} would help to confirm or dismiss a new physics explaination for such a family of anomalies.

The $B_s \rightarrow D_s l \nu$ scalar form factor is one of the theoretical inputs to predicting the branching fraction for the $B_s \rightarrow \mu^+ \mu^-$ decay. Taking a ratio of the $B_s \rightarrow D_s$ and $B \rightarrow D$ scalar form factors gives the so-called fragmentation ratio, the ratio of probabilities of a b quark hadronizing into a B or B_s meson. The $B_s \rightarrow \mu^+ \mu^-$ branching fraction is directly proportional to the fragmentation ratio.

Chiral perturbation theory implies that form factors for decays such as $B_s \rightarrow D_s$ and $B \rightarrow D$ are insensitive to the mass of the spectator quark, implying that form factors for these two decays are approximately equal [123]. This expectation has been validated by previous lattice calculations, for example in [143] the ratio of scalar form factors for the two decays at momentum transfer $q^2 = M_\pi^2$ was found to be $f_0^s(M_\pi^2)/f_0(M_\pi^2) = 1.054(50)$, while [101] found the value $f_0^s(M_\pi^2)/f_0(M_\pi^2) = 1.006(62)$. Hence we can expect to learn about $B \rightarrow D$ form factors by studying $B_s \rightarrow D_s$.

While $B \rightarrow D$ form factors are currently more phenomenologically useful, $B_s \rightarrow D_s$ form factors are more attractive on the lattice QCD side. The absense of valence light (u or d) quarks means lattice QCD results have smaller statistical errors, are less computationally expensive, have a more simple chiral extrapolation to the physical light mass, and negligible finite volume effects. This makes the $B_s \rightarrow D_s l \nu$ decay a useful test bed for lattice techniques that may be later used to study $B \rightarrow D l \nu$ decays.

A number of lattice calculations of $B_{(s)} \rightarrow D_{(s)}$ form factors have already been performed. The FNAL/MILC collaboration produced $B \rightarrow D$ form factors on the $N_f = 2 + 1$ MILC gluon ensembles, using the Fermilab action for b and c valence quarks and ASQTAD light quarks [12]. They also, in an earler work, computed the ratio of scalar form factors for $B_s \rightarrow D_s$ and $B \rightarrow D$ to obtain the fragmentation ratio [143]. The HPQCD collaboration computed both $B \rightarrow D$ and $B_s \rightarrow D_s$ form factors on the $N_f = 2 + 1$ MILC gluon ensembles using a non-relativistic action (NRQCD) for the valence b , and the HISQ action for all other quarks [11, 101]. Atoui et. al. also produced $B_s \rightarrow D_s$ form factors using maximally twisted Wilson quarks on $N_f = 2$ gluon ensembles [144]. A calculaton of the $B_s \rightarrow D_s$ form factors by the RBC/UKQCD collaboration is currently underway.

A considerable limitation in the FNAL/MILC and HPQCD studies is the re-

quirement for perturbative matching between the lattice effective field theories and continuum QCD. FNAL/MILC required a matching that was only available to 1-loop, resulting in a $\mathcal{O}(\alpha_s^2)$ systematic error. In the HPQCD calculation, the NRQCD approach required constructing a continuum current from a series of lattice currents of increasing order in $1/m_b$. Each lattice current required perturbative matching, and matching was available to a limited order in $1/m_b$. The physical current was constructed by a truncation of this series. However, some lattice currents that were ignored in this process turned out to be numerically large, having a magnitude around 30% the size of the leading order currents. Also, such subleading currents were strongly dependent on the momentum of the decay product, so they grew as one moved away from the zero recoil point. On top of all this, it was not clear whether the matching of these currents should have a q^2 dependence.

Another limitation present in each of the afferntioned studies is that the lattice data is limited to a region of high q^2 . To generate lattice points at lower q^2 , a large spacial momentum must be given to one of the quarks on the lattice. Due to Parisi-Lepage scaling, adding momentum leads to an exponential increase of noise in correlation functions. Hence, in cases like $B_{(s)} \rightarrow D_{(s)}$, lattice data close to $q^2 = 0$ would be uselessly noisy, and lattice results must be limited to high q^2 . This fact necessitates an extrapolation from the data in the high q^2 region to the rest of the physical range. Since there has been some controversy in choices of form factor extrapolations through q^2 recently (for example see [14, 20]), it would be desirable to instead have lattice data covering the entire q^2 range.

7.2 Calculation Details

7.2.1 Lattice Setup

This calculation closely follows the approach employed in our calculation of the $B_s \rightarrow D_s^*$ axial form factor at zero recoil, given in the last chapter. The main modifications required for this calculation are 1) the form factors are not protected by Luke's theorem, so a more general fit form for the extrapolation in m_h is required, and 2) to cover the q^2 range we give the charm quark a number of spacial momentum values via a momentum twist, and interpolate the results to all q^2 .

We use the same set of ensembles as in the $B_s \rightarrow D_s^*$ study. In three of the four ensembles (sets 2, 4 and 5), the bare light mass is set to $m_{l0}/m_{s0} = 0.2$. The fact that the m_{l0} value is unphysically high is expected to have a small effect on the

set	handle	a/fm	$N_x^3 \times N_t$	am_{l0}	am_{s0}	am_{c0}
1	fine	0.0884(6)	$32^3 \times 96$	0.0074	0.037	0.440
2	fine-physical	0.0873(5)	$64^3 \times 96$	0.0012	0.0363	0.432
3	superfine	0.05922(12)	$48^3 \times 144$	0.0048	0.024	0.286
4	ultrafine	0.04406(23)	$64^3 \times 192$	0.00316	0.0158	0.188

Table 7.1: Parameters for gluon ensembles [91, 92]. a is the lattice spacing, values for sets 1 & 2 deduced in [93], set 3 from [94]. We thank C. McNeile for computing the a value on set 4. These a values are determined by measuring the Wilson flow parameter w_0/a on the lattice, then using the known value for w_0 to isolate a . N_x is the spatial extent and N_t the temporal extent of the lattice. Light, strange and charm quarks are included in the sea, their masses are given in columns 5-7.

form factors, due to the lack of valence light quarks, and previous experience of the form factor dependence on m_{l0} [101]. The small effect due to the unphysical m_{l0} is quantified by including a fourth ensemble (set 3) with roughly physical m_{l0} , and corrected for.

We use a number of different masses for the valence heavy quark am_{h0}^{val} . Unphysically light h -quarks reduces the q^2 range, meaning we can obtain lattice data at both ends of the range while the statistical noise remains under control.

As detailed in Sec. 4.1.3, staggered correlation functions are built by a combination of staggered propagators $g(x, y)$ and staggered phases. In this calculation we only need local (non point-split) operators, this is an advantage since point-split operators lead to correlation functions more noisy than local operators.

We compute a number of correlation functions on the ensembles detailed in table 7.1. Valence masses, momenta and other inputs to the calculation are given in table 7.2. We use random wall sources for generating all staggered propagators. First we compute 2-point correlation functions between eigenstates of momentum $a\mathbf{p}$, objects of the form

$$C_M^{a\mathbf{p}}(t) = \langle \tilde{\Phi}_M(\mathbf{p}, t) \tilde{\Phi}_M^\dagger(\mathbf{p}, 0) \rangle, \quad (7.8)$$

$$\tilde{\Phi}_M(\mathbf{p}, t) = \sum_{\mathbf{x}} e^{-i\mathbf{p}\cdot\mathbf{x}} \bar{q}(\mathbf{x}, t) \Gamma q'(\mathbf{x}, t),$$

where $\langle \rangle$ represents a functional integral over all fields, q, q' are valence quark fields

set	am_{s0}^{val}	am_{c0}^{val}	am_{h0}^{val}	$ a\mathbf{p}_{D_s} $	T
1	0.0376	0.45	0.5	0, 0.056	14, 17, 20
			0.65	0, 0.142, 0.201	
			0.8	0, 0.227, 0.323	
2	0.036	0.433	0.5	0, 0.0279	14, 17, 20
			0.8	0, 0.162	
3	0.0234	0.274	0.427	0, 0.113, 0.161	22, 25, 28
			0.525	0, 0.161, 0.244	
			0.65	0, 0.244, 0.338	
			0.8	0, 0.338, 0.438	
4	0.0165	0.194	0.5	0, 0.202, 0.281	31, 36, 41
			0.65	0, 0.202, 0.281, 0.382	
			0.8	0, 0.281, 0.382, 0.473	

Table 7.2: Simulation details. Columns 2 and 3 give the s and c valence quark masses, which were tuned in [94]. In column 4 we give the heavy quark masses, we use a number of heavy quark masses to assist the extrapolation to physical the b mass. Column 5 gives the square of the spacial momentum given to the D_s meson, using a momentum twist, in lattice units. These values are chosen with the following rationale: When only 2 are used, these correspond to the $q^2 = 0$ and q_{\max}^2 points (except on the fine-physical ensemble, where we find the points q_{\max}^2 and $q_{\max}^2/2$). When 3 are used, the momenta correspond to $q^2 = 0$, $q^2 = q_{\max}^2/2$, and q_{\max}^2 points. When 4 are used, these are points for q_{\max}^2 , $3q_{\max}^2/4$, $q_{\max}^2/2$, $q_{\max}^2/4$, $q^2 = 0$. We used charm momentum in the $(1, 1, 1)$ direction. Column 6 gives the temporal separations between source and sink, T , of the 3-point correlation functions computed on each ensemble.

of the flavours the M meson is charged under, and Γ is the spin-taste structure of M . We compute these for all t values, i.e. $0 \leq t \leq N_t$.

In some cases momentum is given to the meson by imposing twisted boundary conditions on the gluon fields when computing propagators, as described in Sec.

4.1.3.

We compute correlation functions for a heavy-strange pseudoscalar, H_s , with spin-taste structure $(\gamma_5 \otimes \gamma_5)$, at rest. In terms of staggered propagators this takes the form

$$C_{H_s}(t) = \sum_{\mathbf{x}, \mathbf{y}} \text{Tr} \left[g_h(x, y) g_s^\dagger(x, y) \right], \quad (7.9)$$

where $g_q(x, y)$ is a staggered propagator for flavour q , and the trace is over color. Here $x_0 = 0$ and $y_0 = t$, and the sum is over spacial sites labelled \mathbf{x} , \mathbf{y} . We also compute correlators for a charm-strange pseudoscalar meson D_s , with structure $(\gamma_\mu \otimes \gamma_\mu)$ and momentum $a\mathbf{p}$, using

$$C_{D_s}^{a\mathbf{p}}(t) = \sum_{\mathbf{x}, \mathbf{y}} \text{Tr} \left[g_c^\theta(x, y) g_s^\dagger(x, y) \right], \quad (7.10)$$

where $g_q^\theta(x, y)$ denotes a propagator with momentum twist θ . We compute this using a number of twists to produce the range of momenta given in table 7.2. We design the c propagators to have momentum $a\mathbf{p} = |a\mathbf{p}|(1, 1, 1)$, by imposing a twist $\theta = N_x|a\mathbf{p}|/\pi\sqrt{3}$ in each spacial direction.

Necessary for extracting the vector current, we also compute non-goldstone pseudoscalar heavy-strange mesons at rest, denoted \hat{H}_s . This has spin-taste structure $(\gamma_0 \gamma_5 \otimes \gamma_0 \gamma_5)$. \hat{H}_s correlators are computed using

$$C_{\hat{H}_s}(t) = \sum_{\mathbf{x}, \mathbf{y}} (-1)^{\bar{x}_0 + \bar{y}_0} \text{Tr} \left[g_h(x, y) g_s^\dagger(x, y) \right], \quad (7.11)$$

where we use the notation $\bar{z}_\mu = \sum_{\nu \neq \mu} z_\nu$.

We also compute correlators for H_c mesons, heavy-charmed pseudoscalars, using the same form as H_s (7.9). This is used to find H_c decay constants, which are useful in our continuum and m_h extrapolation.

The heavy-mass extrapolation requires masses of η_h mesons, heavy-heavy pseudoscalars artificially forbidden to annihilate. To quantify mistuning of the charm and strange quark masses, we also require masses for η_c and η_s mesons, identical to η_h with h replaced c and s quarks respectively. We compute correlators for each of these at rest, using a spin-taste structure $(\gamma_5 \otimes \gamma_5)$, taking the form of spin-taste structure as the H_s (7.9).

We then compute 3-point correlation functions. We require two sets of such correlation functions, one with a scalar and one with a temporal vector current

insertion. The first takes the form

$$C_S^{a\mathbf{p}_{D_s}}(t, T) = \sum_{\mathbf{y}} \langle \tilde{\Phi}_{D_s}(\mathbf{p}, T) S(\mathbf{y}, t) \tilde{\Phi}_{H_s}(\mathbf{0}, 0) \rangle, \quad (7.12)$$

$$S(\mathbf{y}, t) = \bar{c}(\mathbf{y}, t) h(\mathbf{y}, t).$$

In terms of the staggered formalism, both the H_s source and D_s sink are given structure $(\gamma_5 \otimes \gamma_5)$, and the current insertion $(1 \otimes 1)$. We generate these with staggered propagators using

$$C_S^{a\mathbf{p}_{D_s}}(t, T) = \sum_{\mathbf{x}, \mathbf{y}, \mathbf{z}} \text{Tr} \left[g_h(x, y) g_c^\theta(y, z) g_s^\dagger(x, z) \right], \quad (7.13)$$

where we fix $x_0 = 0$, $y_0 = t$ and $z_0 = T$, and once again the charm propagator is given the appropriate twist θ . We compute these for all t values within $0 \leq t \leq T$, and 3 T values that vary between ensembles, given in table 7.2.

To extract the temporal vector current, we require the function

$$C_{V_0}^{a\mathbf{p}_{D_s}}(t, T) = \sum_{\mathbf{y}} \langle \tilde{\Phi}_{D_s}(\mathbf{p}, T) V_0(\mathbf{y}, t) \tilde{\Phi}_{\hat{H}_s}(\mathbf{0}, 0) \rangle, \quad (7.14)$$

$$V_0(\mathbf{y}, t) = \bar{c}(\mathbf{y}, t) \gamma_0 h(\mathbf{y}, t).$$

This is generated using structures $(\gamma_0 \gamma_5 \otimes \gamma_0 \gamma_5)$ at the \hat{H}_s source, $(\gamma_5 \otimes \gamma_5)$ at the D_s sink, and $(\gamma_0 \otimes \gamma_0)$ at the current insertion. To achieve this we compute

$$C_{V_0}^{a\mathbf{p}_{D_s}}(t, T) = \sum_{\mathbf{x}, \mathbf{y}, \mathbf{z}} (-1)^{\bar{x}_0 + \bar{y}_0}$$

$$\times \text{Tr} \left[g_h(x, y) g_c^\theta(y, z) g_s^\dagger(x, z) \right]. \quad (7.15)$$

The non-goldstone \hat{H}_s is required here to ensure all taste structure cancels in the fermion loop.

7.2.2 Analysis of Correlation Functions

We then extract current matrix elements from the generated correlation functions, via simultaneous Bayesian fits, as described in Sec. 4.2.1. We perform a single simultaneous fit containing each correlator computed ($C_{H_s}, C_{\hat{H}_s}, C_{D_s}, C_{\eta_h}, C_{\eta_s}, C_{H_c}, C_S, C_{V_0}$) at every m_h and every $|a\mathbf{p}_{D_s}|$, for each ensemble.

We choose not to perform tuning on $\{t_{\text{cut}}\}$ as was performed in the $B_s \rightarrow D_s^*$ study. This is because the fits are much larger than in the $B_s \rightarrow D_s^*$ case, and

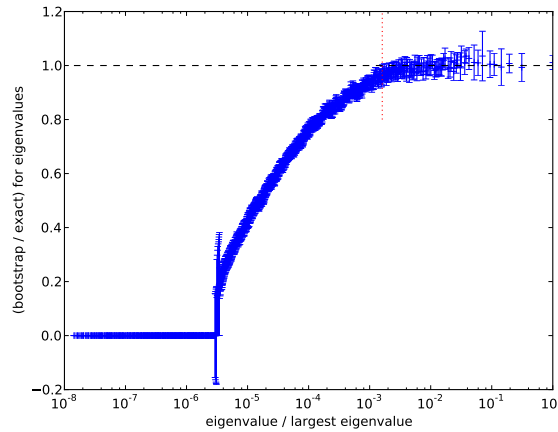


Figure 7.1: An plot analogous to fig. 6.2 for the dataset of correlators on the fine ensemble in the $B_s \rightarrow D_s$ case.

set	handle	H_s	\hat{H}_s	D_s	H_c	η_q	S	V_0
2	fine	2	2	2	2	2	2	2
3	fine-physical	4	4	4	5	4	2	2
4	superfine	5	5	5	10	5	4	4
5	ultrafine	2	2	2	8	2	4	4

Table 7.3: t_{cut} values used for each correlator on each ensemble. S and V_0 denote the 3-point correlators with the corresponding current S or V_0 . There is one exception to the values here: on the 3-point correlators on the ultrafine ensemble with $am_h = 0.8$ and $q^2 = 0$, the t_{cut} given here is replaced with 8, 10 and 12 in the $T = 14, 17, 20$ cases respectively.

tuning, which involves many serial fits, would take an unreasonable amount of time. The t_{cut} 's we set are given in table 7.3.

These simultaneous fits are very large. For example, on set 4 (ultrafine) we fit 109 correlation functions to 1080 fit parameters, taking all correlations into account. Both the stability (e.g. invariance under changes of arbitrary hyperparameters such as N_{exp}) and the speed of such simultaneous fits take a hit when there is such a large amount of data and a large number of parameters.

The stability issue is likely due to the size of the covariance matrix for the data,

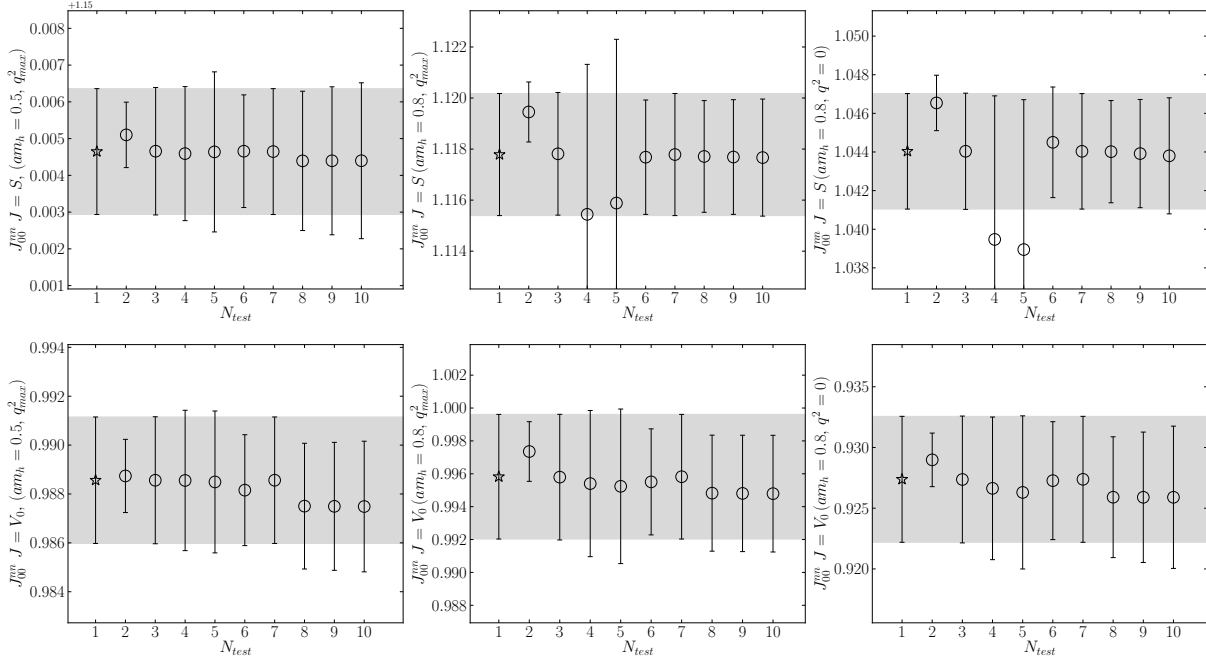


Figure 7.2: Tests on the correlator fits on the fine ensemble. At $N_{\text{test}} = 1$ we give the final accepted result. $N_{\text{test}} = 2$ and 3 gives the results of setting $N_{\text{exp}} = 4$ and 6 respectively. $N_{\text{test}} = 4$ gives the results when all priors are loosened by 50%. $N_{\text{test}} = 5$ gives the result of setting $t_{\text{cut}} = 4$ rather than 2 for all correlators. $N_{\text{test}} = 6$ gives the result without marginalising out the $n = 5$ excited state. $N_{\text{test}} = 7$ gives the result of moving the SVD cut from 10^{-3} to 10^{-2} . $N_{\text{test}} = 8, 9, 10$ gives the result of using a chained fit described above with priors for the full correlated fit loosened by 100%, 150% and 200% respectively.

which must be inverted to estimate χ^2 . We take two steps toward mitigating this. The first is to impose an svd cut. The second step we take towards a stable fit is employing a chained-fitting approach (on the superfine and ultrafine data only). We first perform an array of smaller fits, each fitting the correlators relevant only to one m_h and one $|\mathbf{ap}_{D_s}|$ value. In the case of set 4, for example, this results in 11 separate fits. Then, a full fit of all of the correlators is carried out, with priors set to the results of the smaller fits, with errors inflated by 150%. This both speeds up the full fit and improves stability of the results. We tested the validity of the results by varying the error inflation between 100% and 200%, this caused negligible changes

in the results. Since we did not need to take this measure on the fine ensemble, we performed both a standard simultaneous fit and chained fits of the type above as a check for the chained fits. Tests 8, 9 and 10 on fig. 7.2 show the results of these chained fits in comparison to the simultaneous fit.

The priors were set up as follows. We set gaussian priors for the parameters J_{jk} , and log-normal priors for all other parameters. Using log-normal distributions forbids energies E_n^M and amplitudes a_n^M from both becoming negative and moving arbitrarily close to zero, improving stability of the fit.

Priors for ground state energies E_0^M and amplitudes a_0^M are set according to an empirical-Bayes approach, plots of the effective amplitude of the correlation functions are inspected to deduce reasonable priors. The ground-state oscillating parameters $a_0^{M,o}, E_0^{M,o}$, are given the same priors as the non-oscillating states, with errors inflated by 50%. The resulting priors always have a variance at least 10 times that of the final result. Oscillating and non-oscillating excited state energies, $E_i^{M,(o)}$, $i > 0$ are given prior values 0.5 ± 0.25 . The excited state amplitudes $a_i^M, i > 0$ are given priors of 0.15 ± 0.5 for non-oscillating states, and 0.05 ± 0.1 for oscillating states. The ground-state non-oscillating to non-oscillating 3-point parameter, J_{00}^{nn} is given a prior of 1 ± 0.5 , and the rest of the 3-point parameters J_{jk}^{nn} are given 0 ± 1 .

The current matrix elements we require can be extracted from the fit parameters via

$$\langle D_s | J | H_s \rangle |_{\text{lat}} = 2\sqrt{M_{H_s} E_{D_s}} J_{00}^{nn}. \quad (7.16)$$

7.2.3 Vector Current Renormalization

In HISQ, the local scalar current ($1 \otimes 1$) (multiplied by the mass difference of flavours it is charged under) is conserved, and hence requires no renormalization. This is not the case for the temporal vector current ($\gamma_0 \otimes \gamma_0$). The conserved vector current is a complicated linear combination of many local and point-split lattice currents. In this calculation we use only the local part of the vector current, this improves the statistics of our results but creates the need for the resulting current matrix element to be multiplied by a matching factor Z_V , to produce the appropriate continuum current. We find Z_V via a fully non-perturbative method [130, 131].

When both meson states in the matrix elements are at rest (the zero recoil point),

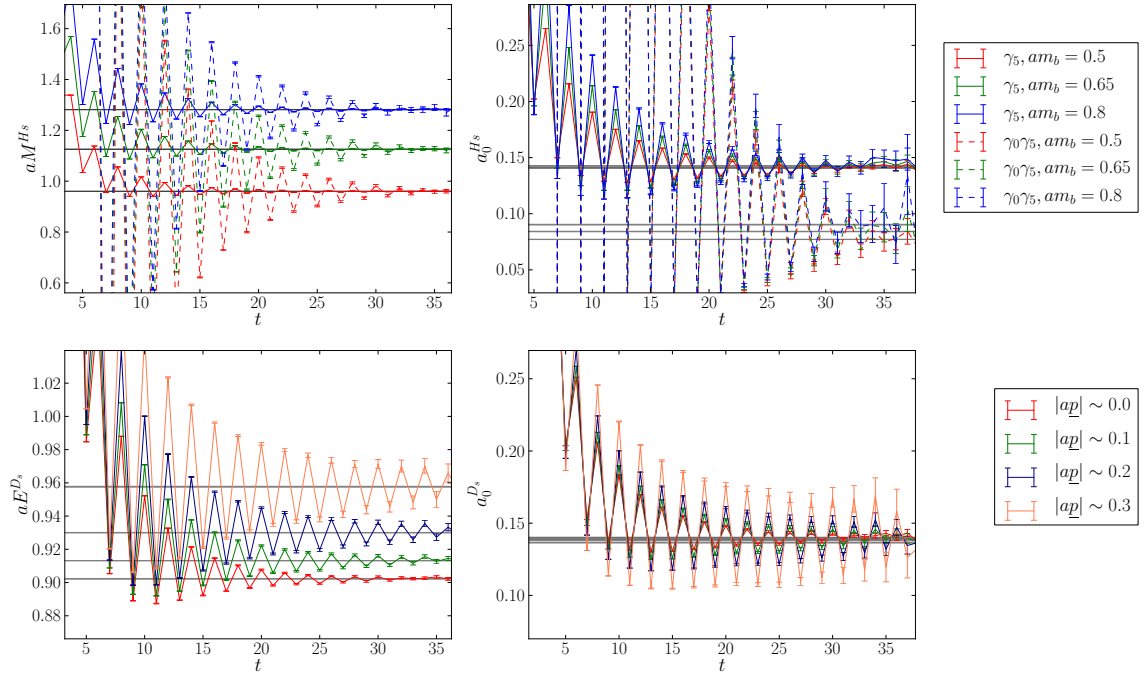


Figure 7.3: Super-averaged effective energies (given by eq. (6.13)) and amplitudes (given by eq. (6.14)) for a selection of 2-point correlators on the fine ensemble. The grey bands show the corresponding results for these quantities from the simultaneous bayesian fits.

the scalar and local vector matrix elements are related via the PCVC relation:

$$(M_{H_s} - M_{D_s}) Z_V \langle D_s | V_0 | \hat{H}_s \rangle |_{\text{lat}} \\ = (m_{h0}^{\text{val}} - m_{c0}^{\text{val}}) \langle D_s | S | H_s \rangle |_{\text{lat}}. \quad (7.17)$$

Z_V can be extracted from this relation since the matrix elements are already computed as part of the calculation. The calculation self-renormalizing, in the sense that the normalization can be found at no extra computational cost. The Z_V values found on each ensemble and am_{h0}^{val} are given in table 7.4.

We also remove tree-level mass-dependent discretization effects using a normalization constant Z_{disc} defined in (6.16).

Combining these normalizations with the lattice current from the simultaneous correlation function fits, we find values for the form factors at a given heavy mass,

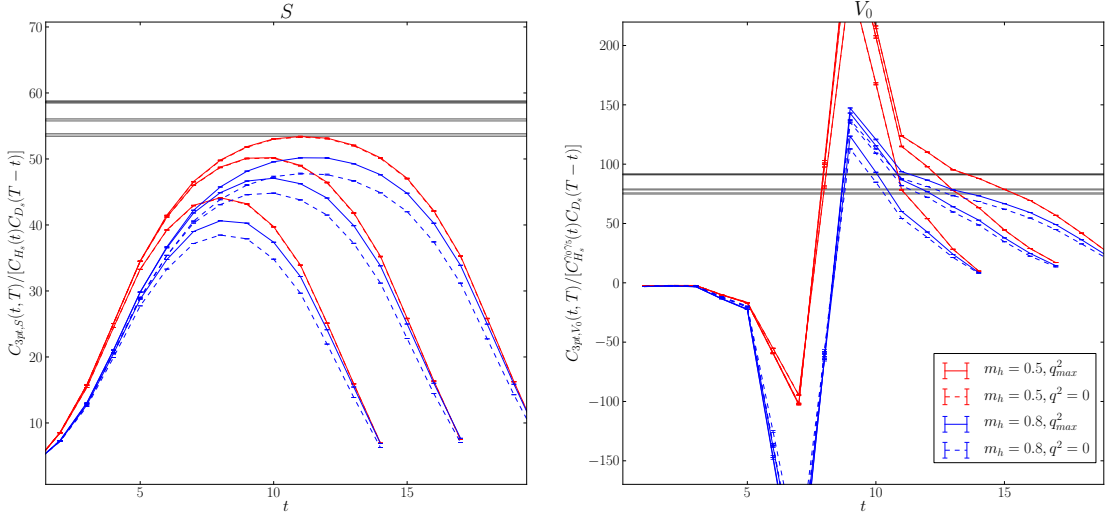


Figure 7.4: $\tilde{C}_3(t, T)/\tilde{C}^{H_s}(t)\tilde{C}^{D_s}(T-t)$, which should plateau at J_{00}^{nn} , in the fine ensemble for the $J = S$ and $J = V_0$ cases. The grey bands show the corresponding results for these quantities from the simultaneous bayesian fits.

lattice spacing, and q^2 :

$$\begin{aligned} f_0^s(q^2) &= \frac{m_{h0}^{\text{val}} - m_{c0}^{\text{val}}}{M_{H_s}^2 - M_{D_s}^2} Z_{\text{disc}}\langle D_s|S|H_s\rangle|_{\text{lat}}(q^2) \\ f_+^s(q^2) &= \frac{Z_{\text{disc}}}{2M_{H_s}} \times \\ &\quad \frac{\delta^M\langle D_s|S|B_s\rangle|_{\text{lat}}(q^2) - q^2 Z_V\langle D_s|V_0|B_s\rangle|_{\text{lat}}(q^2)}{\mathbf{p}_{D_s}^2}. \end{aligned} \quad (7.18)$$

We have here explicitly denoted the dependence of the matrix elements on q^2 as a reminder that the matrix elements have q^2 dependence via the D_s momentum.

7.2.4 Extrapolation to the Physical Point

We now address the extrapolation of the $f_0^s(q^2)$ and $f_+^s(q^2)$ values to continuum, physical b and l masses and arbitrary q^2 . We take two complementary approaches to the extrapolation.

One we refer to as the *ratio* approach, in which we extrapolate the quantity

$$R_{0,+}^s(q^2) \equiv \frac{f_{0,+}^s(q^2)}{f_{H_c}\sqrt{M_{H_c}}} \quad (7.19)$$

Set	am_h^{val}	Z_V	Z_{disc}
0	0.5	1.0151(32)	0.99819
	0.65	1.0240(37)	0.99635
	0.8	1.0368(49)	0.99305
1	0.5	1.0134(24)	0.99829
	0.8	1.0348(29)	0.99315
2	0.427	1.0027(25)	0.99931
	0.525	1.0059(29)	0.99859
	0.65	1.0108(37)	0.99697
	0.8	1.0197(49)	0.99367
3	0.5	1.0037(40)	0.99889
	0.65	1.0087(46)	0.99704
	0.8	1.0160(53)	0.99375

Table 7.4: Normalization constants applied to the lattice axial vector current in (7.18). Z_V is found from (7.17) and Z_{disc} from (6.16).

to the physical point. Discretisation effects appear to cancel to a large extent in this ratio, resulting in a better controlled continuum extrapolation. The value at the physical point is then multiplied by $f_{B_c} \sqrt{M_{B_c}}$ to isolate the form factors, where we find f_{B_c} via a separate extrapolation (detailed in Sec. 6.3.5), and take the PDG value for $M_{B_c} = 6.2756(11)\text{GeV}$ [1]. While this approach improves the continuum extrapolation, it has the downside of introducing errors from scale-setting on account of $R_{0,+}^s(q^2)$ being dimensionful quantities (as opposed to $f_{0,+}^s(q^2)$ which are dimensionless).

In the other method, that we refer to as the *direct* approach, we simply extrapolate the form factors to the physical point. The form factors by themselves have larger discretisation effects than $R_{0,+}^s(q^2)$, but since $f_{0,+}^s$ are dimensionless, the results are insensitive to scale-setting uncertainty.

We use identical fit functions for both approaches. In the below discussion, we use the notation $\tilde{f}_{0,+}^s(q^2)$ to denote either $f_{0,+}^s(q^2)$ or $R_{0,+}^s(q^2)$, depending on the approach being applied.

Kinematic Behaviour

Our fit form for the extrapolation is a modified version of the Bourrely-Caprini-Lellouch (BCL) parameterisation for pseudoscalar-to-pseudoscalar form factors [145]:

$$\begin{aligned}\tilde{f}_0^s(q^2)|_{\text{fit}} &= \frac{1}{1 - \frac{q^2}{M_{H_c^0}^2}} \sum_{n=0}^{N-1} a_n^0 z^n(q^2), \\ \tilde{f}_+^s(q^2)|_{\text{fit}} &= \frac{1}{1 - \frac{q^2}{M_{H_c^*}^2}} \sum_{n=0}^{N-1} a_n^+ \left(z^n(q^2) - \frac{n}{N} (-1)^{n-N} z^N(q^2) \right).\end{aligned}\quad (7.20)$$

The function $z(q^2)$ maps q^2 to a small region inside the unit circle on the complex q^2 plane, defined by

$$z(q^2) = \frac{\sqrt{t_+ - q^2} - \sqrt{t_+ - t_0}}{\sqrt{t_+ - q^2} + \sqrt{t_+ - t_0}}, \quad (7.21)$$

where $t_+ = (M_{H_s} + M_{D_s})^2$, and we choose t_0 to be $t_0 = 0$. This t_0 choice means at $q^2 = 0$ the fit functions simplify to $\tilde{f}_{0,+}^s(0) = a_0^{0,+}$. Throughout the physical range of q^2 , z is restricted to the range $0 < z < 0.06$, resulting in a fast converging series in powers of z . We truncate at $L = 3$, adding further orders of z^l does not effect the results of the fit.

The factors in front of the sums in the BCL parameterisation account for sub-threshold poles in the form factors due to the production of on-shell H_c^0 and H_c^* states in the crossed channel of the semileptonic decay.

To estimate $M_{H_c^0}$, the scalar heavy-charm meson mass, at each of the heavy masses we use, we leverage the fact that the splitting $\Delta_0 = M_{H_c^0} - M_{H_c}$ is due to a radial excitation and therefore independent of the heavy quark mass. This has been calculated in [146] to be $\Delta_0 = 0.429(13)\text{GeV}$. Combined with an H_c mass from our lattice data, we can construct the H_c^0 mass: $M_{H_c^0} = M_{H_c} + \Delta_0$. We do not take the error on Δ_0 into account in the fit, since the precise position of the pole has a small effect on the fit results.

To estimate $M_{H_c^*}$, the vector heavy-charm mass, we use the fact that the splitting $M_{H_c^*} - M_{H_c}$ vanishes in the infinite m_h limit. $M_{H_c^*}$ then takes the approximate form $M_{H_c^*} \simeq M_{H_c} + \mathcal{O}(1/m_h)$. To reproduce this behaviour we use the ansatz $M_{H_c} + x/M_{\eta_h}$, and fix x at the physical point to find $x = 0.508\text{GeV}^2$.

Heavy Mass and Discretisation Effects

To account for variation in heavy mass and discretisation effects in a general way, we give the following form to each of the $a_l^{0,+}$ coefficients:

$$\begin{aligned} a_n^{0,+} = & \left(1 + \rho_n^{0,+} \log \left(\frac{M_{\eta_h}}{M_{\eta_c}} \right) \right) \times \\ & \sum_{i,j,k=0}^{2,2,2} d_{ijkn}^{0,+} \left(\frac{\Lambda_{\text{QCD}}}{M_{\eta_h}} \right)^i \left(\frac{am_{h0}^{\text{val}}}{\pi} \right)^{2j} \left(\frac{aE_{D_s}}{\pi} \right)^{2k} \\ & + \mathcal{N}_{\text{mistraining},n}^{0,+} \end{aligned} \quad (7.22)$$

To understand this form, focus first on the sum. Powers of $(\Lambda_{\text{QCD}}/M_{\eta_h})$ give a Heavy Quark Effective Theory (HQET) inspired way of quantifying the variation in the results due to the changing heavy mass. M_{η_h} varies strongly and monotonically with the heavy quark mass, so acts as a suitable proxy. Λ_{QCD} is the confinement scale, which we set to 0.5GeV .

The two scales expected to be the largest sources of discretisation effects are the heavy mass am_{h0}^{val} , and the energy in the D_s meson, aE_{D_s} , especially when it is given a large spacial momentum. Adding further, smaller scales, like $a\Lambda_{\text{QCD}}$, had no effect on the results.

The coefficients $d_{ijkn}^{0,+}$ are fit parameters given gaussian prior distributions of 0 ± 1 .

To account for any required matching between HQET and QCD, we include a log term in front of the sum. $\rho_n^{0,+}$ are fit parameters with prior distribution 0 ± 1 .

The fact that $f_+^s(0) = f_0^s(0)$ ($\Rightarrow a_0^+ = a_0^0$) is a very powerful constraint within the heavy-HISQ approach. Since this must be true at all m_h , this translates to constraints in the fit parameters - $d_{i000}^+ = d_{i000}^0 \forall i$ and $\rho_0^+ = \rho_0^0$. We impose these constraints in the fit, which serves to stabilize the heavy mass extrapolation.

Mass Mistunings

We deal with possible mistunings in the c , s and l masses in the same way as in the $B_s \rightarrow D_s^*$ study, that we repeat here for completeness. We include the terms $\mathcal{N}_{\text{mistuning},n}^{0,+}$ in each $a_n^{0,+}$ coefficient, given by

$$\begin{aligned} \mathcal{N}_{\text{mistuning},n} &= c_{s,n} \frac{\delta_s}{\Lambda_\chi} + c_{l,n} \frac{\delta_l}{\Lambda_\chi} \\ &+ \left(c_{c,n}^{0,+} + c_{c,n}'^{0,+} \frac{\Lambda_{\text{QCD}}}{M_{\eta_h}} \right) \times (M_{\eta_c} - M_{\eta_c}^{\text{phys}}) \end{aligned} \quad (7.23)$$

where $c_{l,n}^{0,+}$, $c_{l,n}'^{0,+}$, $c_s^{0,+}$ and $c_{ci}^{0,+}$ are fit parameters with prior distributions 0 ± 1 . Λ_χ is the chiral breaking scale, which we set to 1GeV.

The strange mistuning is accounted for here using an approach first used in [94]. We define the term $\delta_s = m_{s0}^{\text{val}} - m_s^{\text{tuned}}$, where m_s^{tuned} is defined by

$$m_s^{\text{tuned}} = m_{s0}^{\text{val}} \left(\frac{M_{\eta_s}^{\text{phys}}}{M_{\eta_s}} \right)^2. \quad (7.24)$$

$M_{\eta_s}^{\text{phys}}$ was determined in a lattice simulation from the masses of the pion and kaon [93].

We similarly account for (sea) light quark mistuning by defining $\delta_l = m_{l0} - m_l^{\text{tuned}}$. We find m_l^{tuned} from m_s^{tuned} , using the fact that the ratio of quark masses is regularization independent, and was calculated in [138]:

$$\left. \frac{m_s}{m_l} \right|_{\text{phys}} = 27.35(11). \quad (7.25)$$

We set m_l^{tuned} to m_s^{tuned} divided by this ratio.

Since the physical charm mass is relatively close to the m_h values we use, mistuning in this mass can interfere with the m_h dependence in the results. This is accounted for in (7.23) by including an extra mistuning term multiplied by $\Lambda_{\text{QCD}}/M_{\eta_h}$.

All higher order contributions, like $\delta_{s,l}^2$, $(M_{\eta_c} - M_{\eta_c}^{\text{phys}})^2$, or $(\Lambda_{\text{QCD}}/M_{\eta_h})^2$ are too small to be resolved by our lattice data, so are not included in the fit.

Finite Volume and Isospin Breaking Effects

Finite volume effects are negligible in our calculation, we do not include any associated error. Finite volume corrections to the $B \rightarrow Dl\nu$ form factors in chiral perturbation theory were calculated in [123]. They found the $B \rightarrow Dl\nu$ form factor at zero recoil, with a lattice size of $L = 2.5\text{fm}$, and pion mass equal to or greater than physical, never exceeded 10^{-4} . There is no reason to believe changing the spectator quark from light to strange, and moving away from zero recoil, will increase this effect.

In our simulation we set $m_u = m_d \equiv m_l$, this means our results do not account for isospin breaking. By moving the m_l^{tuned} value up and down by the PDG value for $m_d - m_u$, we tested for any signs of isospin breaking having an effect on the results. The resulting effect was negligible in comparison to all other sources of error.

7.3 Results and Discussion

In tables 7.10 and 7.11 in Sec. 7.7, we give numerical values for the form factors, the ratios $R_{0,+}^s(q^2)$, and parameters extracted from the correlation function fits required for the extrapolations to the physical point.

We show first results from the ratio method, then the direct method. In both cases, we performed a simpler fit at zero recoil first, then a larger fit taking into account all data throughout q^2 . In each case, our results are statistics dominated. The results from the two methods are in good agreement.

7.3.1 Ratio Method

Zero Recoil

We performed an isolated extrapolation of $R_0^s(q_{\max}^2)$ to the physical point. To do this we used a simplified fit form for $R_0^s(q_{\max}^2)$ consisting of the right hand side of (7.22), with the index l discarded. We find

$$R_0^s(q_{\max}^2) = \frac{f_0^s(q_{\max}^2)}{f_{B_c}\sqrt{M_{B_c}}} = 0.831(14)\text{GeV}^{-3/2} \quad (7.26)$$

The extrapolation against M_{η_h} is illustrated in figure 7.5. As can be seen from this plot, the data has a very weak dependence on the lattice spacing. The error budget for this result is given in table 7.5.

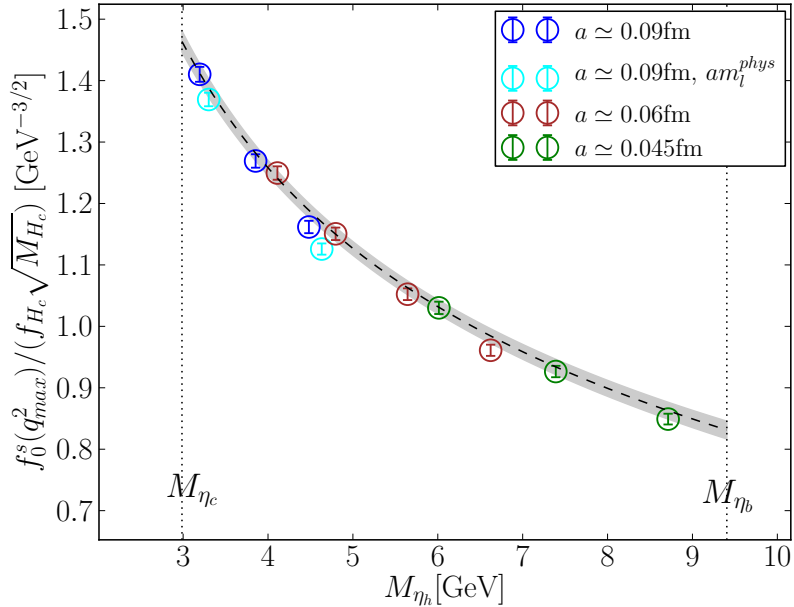


Figure 7.5: $R_0^s(q_{\max}^2) = f_0^s(q_{\max}^2)/(f_{H_c} \sqrt{M_{H_c}})$ against M_{η_h} (a proxy for the heavy quark mass). The grey band shows the result of the extrapolation at $a = 0$ and physical l,s and c masses. Sets listed in the legend follow the order of sets in table 7.1.

Source	% Fractional Error
Statistics	1.48
Scale Setting	1.15
$m_h \rightarrow m_b$,	0.44
$a \rightarrow 0$	0.05
mistuning	0.24
Total	1.73

Table 7.5: Error budget for $R_0^s(q_{\max}^2)$.

We perform a number of tests on this zero recoil extrapolation to test the stability of our fit form, results are given in fig. 7.6.

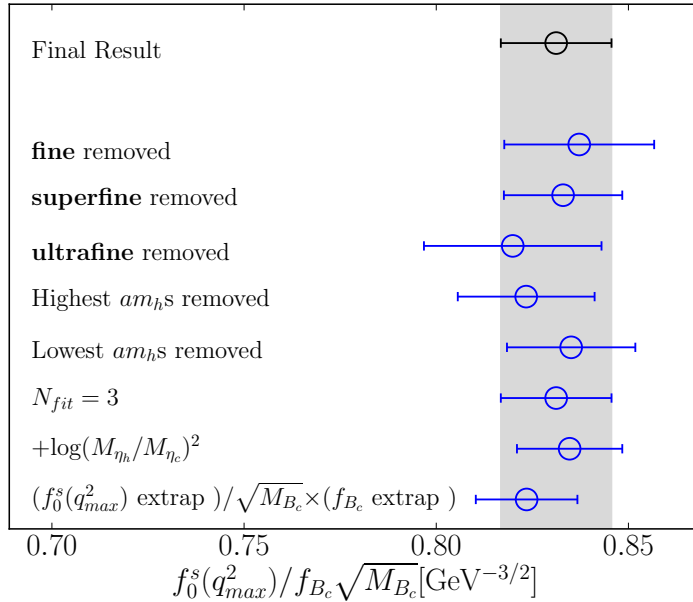


Figure 7.6: Results of tests of the $R_0^s(q_{\max}^2)$ extrapolation. The top three blue points show $R_0^s(q_{\max}^2)$ at continuum and physical b mass, if data from the fine, superfine or ultrafine ensembles are not used in the fit. The fourth and fifth blue points show the result if data at the highest/lowest am_{h0}^{val} value on each ensemble are removed. The point labelled $N_{fit} = 3$ is the result of extending the sum in (7.22) such that it truncates at 3 rather than 2 in each of the i, j, k directions. The point labelled $+log(M_{\eta_h}/M_{\eta_c})^2$ represents the result of adding a $\rho_2 log(M_{\eta_h}/M_{\eta_c})^2$ term in the first set of brackets in (7.22), where ρ_2 is a new fit parameter with the same prior distribution as ρ_{\log} . The lowest point shows the result of our direct extrapolation of $f_0^s(q_{\max}^2)$ to the physical point, divided by the PDG value for $\sqrt{M_{B_c}}$ [1] and the result of our extrapolation of f_{B_c} to the physical point detailed in sec. 6.3.5.

Non-zero Recoil

In fig. 7.7, we show results of the full extrapolation of the ratio throughout the q^2 range described in section 7.2.4. As the heavy mass increases, the q^2 range, $0 < (M_{H_s} - M_{D_s})^2$ expands.

To isolate the form factors, the resulting functions $R_{0,+}^s(q^2)$ were multiplied by $\sqrt{M_{B_c}}$ (using the PDG value) and f_{B_c} from our determination detailed in sec. 6.3.5. The resulting form factors are shown in fig. 7.13, against the form factors found via

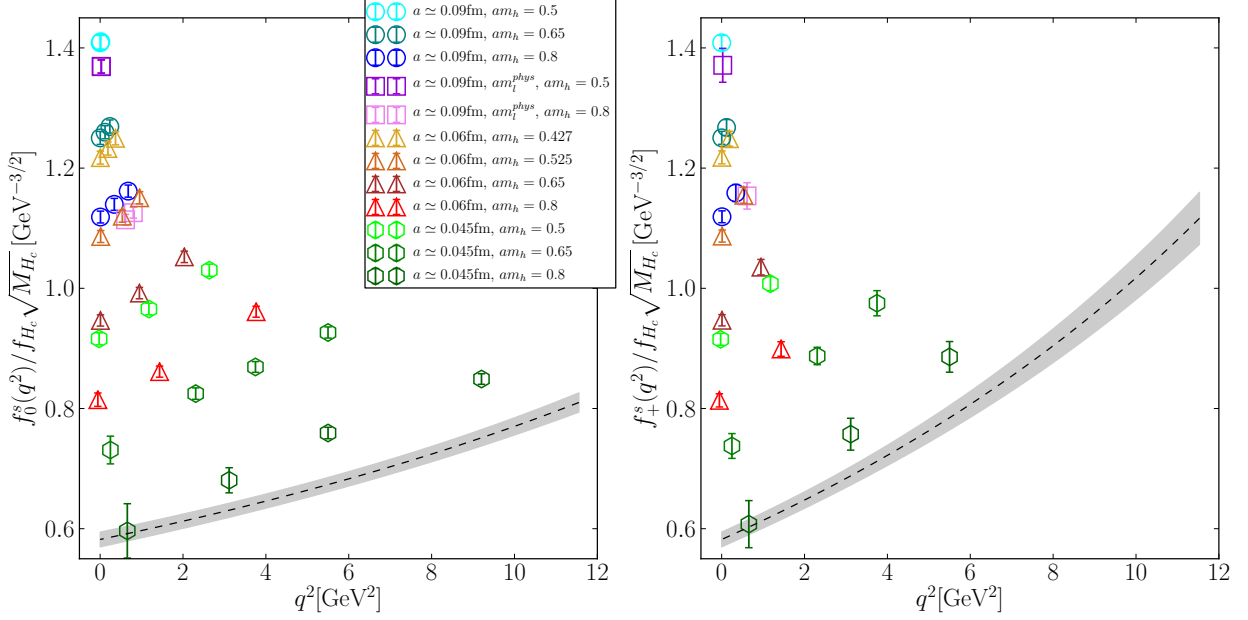


Figure 7.7: $R_{0,+}^s(q^2) = f_{0,+}^s(q^2)/(f_{H_c}\sqrt{M_{H_c}})$ against q^2 . The grey band shows the result of the extrapolation at $a = 0$ and physical l, s, c and b masses. Sets listed in the legend follow the order of sets in table 7.1.

the direct method.

7.3.2 Direct Method

Zero Recoil

Source	% Fractional Error
Statistics	0.90
$m_h \rightarrow m_b$,	0.40
$a \rightarrow 0$	0.02
mistuning	0.15
Total	1.05

Table 7.6: Error budget for $f_0^s(q_{\max}^2)$ found via the direct method.

We performed an isolated extrapolation of $f_0^s(q_{\max}^2)$ to the physical point. Once

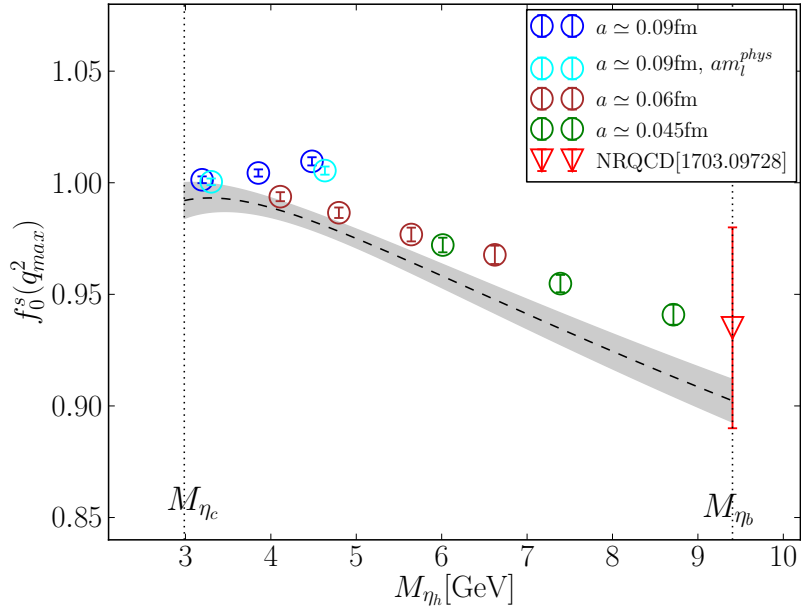


Figure 7.8: $f_0^s(q_{\max}^2)$ against M_{η_h} (a proxy for the heavy quark mass). The grey band shows the result of the extrapolation at $a = 0$ and physical l,s and c masses. We also include the result from a previous lattice calculation, which used the NRQCD discretisation for the b quark [101]. Sets listed in the legend follow the order of sets in table 7.1.

again, this was performed using a fit function for $f_0^s(q_{\max}^2)$ consisting of the right hand side of (7.22) with the index l discarded. We find

$$f_0^s(q_{\max}^2) = 0.9023(95). \quad (7.27)$$

The extrapolation against M_{η_h} is shown in figure 7.8. The error budget for this result is given in table 7.6.

We include in fig. 7.8 a previous lattice determination of this quantity [101], shown as a red triangle. Our two studies, containing largely independent systematic uncertainties, are in agreement. This study used the 2+1 MILC gluon ensembles, with HISQ s and c valence quarks, and an NRQCD b quark. Using NRQCD meant they could perform their simulation directly at the physical b mass. However, the matching of lattice NRQCD to continuum QCD causes their dominant error.

As when using the ratio method, we perform a number of tests on this extrapolation at zero recoil, and present results in fig. 7.9.

Non-Zero Recoil

In fig. 7.10, we show results of the full extrapolation of the ratio throughout the q^2 range described in section 7.2.4.

In fig. 7.11, we show the resulting form factors from the direct approach, and in fig. 7.12 we give an associated error budget for these throughout q^2 .

We take the results from the direct method as our final result, and supply the ratio method results as a consistency test, since the product of the direct method is more precise. In fig. 7.13, we plot form factors from the two methods on top of each other. As one can see from this plot, the results are in good agreement.

In figure 7.14, we show our final results (direct approach) against lattice form factors determined from the NRQCD calculation mentioned in section 7.3.2 [101]. Our results are in excellent agreement with the NRQCD calculation, and are more precise for both $f_0^s(q^2)$ and $f_+^s(q^2)$ throughout all q^2 .

7.3.3 Unitarity Test

Unitarity and crossing symmetry imposes bounds on the coefficients of the BCL parameterization of $f_{0,+}(q^2)$, $\{a_n\}$ [147, 148]. As another consistency test, we show here that the coefficients found in our fit satisfy these bounds.

To obtain bounds on the BCL coefficients, one must relate them to those of a different parameterisation, that of Boyd-Grinstein-Lebed (BGL) [149]:

$$f^s(q^2) = \frac{1}{B(z)\phi(z)} \sum_{n \geq 0}^N b_n z^n. \quad (7.28)$$

$B(z)$ is known as the Blaske factor;

$$B(z) = \frac{z - z_*}{1 - zz_*}, \quad (7.29)$$

where $z_* = z(M_{B_c^0}^2)$ for f_0^s , or $z(M_{B_c^*}^2)$ for f_+^s . $\phi(z)$ is the outer function;

$$\begin{aligned} \phi(z) &= M_{B_s}^{2-s} 2^{2+p} \sqrt{\kappa n_f} \left[\frac{M_{D_s}}{M_{B_s}} (1+z) \right]^{s-3/2} \\ &\times \left[(1-z) \left(1 + \frac{M_{D_s}}{M_{B_s}} \right) + 2 \sqrt{\frac{M_{D_s}}{M_{B_s}}} (1+z) \right]^{-s-p}. \end{aligned} \quad (7.30)$$

In the f_0^s case, $\kappa = 12\pi M_{B_s}^2 \chi_A$, $p = 1, s = 3$. In the f_+^s case, $\kappa = 6\pi M_{B_s}^2 \chi_V$, $p = 3, s = 2$. The quantities $\chi_{V,A}$ are the once-subtracted dispersion relations at

$q^2 = 0$ for vector and axial $b \rightarrow c$ currents respectively, computed in [149] to be $\chi_V = 5.7 \times 10^{-3}/m_b^2$ and $\chi_A = 9.6 \times 10^{-3}/m_b^2$.

The BGL coefficients, $\{b_n\}$, obey the unitarity constraint

$$\sum_{m=0}^{\infty} |b_m|^2 \leq 1 \quad (7.31)$$

by construction of the parameterisation. To see how this applies to the BCL coefficients $\{a_n\}$, one must relate them to $\{b_m\}$ by equating the two parameterisations to find

$$\sum_{m=0}^M b_m z^m = \psi(z) \sum_{n=0}^N a_n z^n, \quad (7.32)$$

where $\psi(z)$ is given by

$$\psi(z) = \frac{M_{\text{pole}}^2}{4(t_+ - t_0)} \phi(z) \frac{(1-z)^2(1-z_*)^2}{(1-zz_*)^2}, \quad (7.33)$$

where $M_{\text{pole}} = M_{B_c^0}$ in the f_0^s case and $M_{B_c^*}$ in the f_+^s case. Expanding $\psi(z)$ around $z = 0$, comparing coefficients of z in (7.32), and imposing the constraint (7.31), we arrive at a constraint for the BCL coefficients

$$\mathcal{B} \equiv \sum_{j,k=0}^{L,L} B_{jk} a_j a_k \leq 1 \quad (7.34)$$

$$B_{jk} = \sum_{n=0}^{\infty} \eta_n \eta_{n+|j-k|} \quad (7.35)$$

where $\{\eta_n\}$ are the taylor coefficients of $\psi(z)$.

	B_{00}	B_{01}	B_{02}
f_0^s	0.00186	-0.000258	-0.000703
f_+^s	0.00179	-0.000367	0.00108

Table 7.7: Numerical values for B_{jk} appearing in the unitarity bound for BCL coefficients, defined in (7.35), for the f_0^s and f_+^s cases. The rest of the elements can be obtained from these using the properties $B_{j(j+k)} = B_{0k}$ and $B_{jk} = B_{kj}$.

$\psi(z)$ is bounded on the closed disk $|z| < 1$, so it's taylor coefficients are rapidly decreasing. We computed values for B_{jk} by truncating the sum in it's definition

(7.35) at 100. These values are given in table 7.7. With these B_{jk} values, and the a_n coefficients from our fit (via the direct method), we find

$$\mathcal{B}_0 = 0.00059(67)$$

$$\mathcal{B}_+ = 0.0245(58).$$

These comfortably satisfy the unitarity bound. Additionally, as discussed in [150], the leading contributions to $\mathcal{B}_{0,+}$ are of order $(\Lambda_{\text{QCD}}/m_b)^3 \simeq 10^{-3}$ in the heavy quark expansion. This expectation is approximately fulfilled by our result.

7.3.4 R_{D_s}

Using our calculated form factors $f_{0,+}^s(q^2)$, we can produce a new prediction for the quantity

$$R_{D_s} = \frac{\mathcal{B}(B_s \rightarrow D_s \tau \nu_\tau)}{\mathcal{B}(B_s \rightarrow D_s l \nu_l)}, \quad (7.36)$$

where $l = e$ or μ (the ambiguity between e and μ is negligible in comparison to the current precision on R_{D_s}). As mentioned in the introduction, the analogous quantities R_D and R_{D^*} are in tension between SM prediction and experimental measurement. There is, at time of writing, no published measurement of R_{D_s} , providing an opportunity for lattice QCD to give a clear prediction of the value of R_{D_s} expected by the SM.

Armed with form factors from a lattice QCD calculation, one can immediately produce an R_{D_s} determination by taking the ratio of SM branching fractions (7.2) between the $l = \tau$ and $l = \mu, e$ cases. $|V_{cb}|$ and η_{EW} cancel in the ratio.

A lattice prediction has already been made in [101] of $R_{D_s}|_{\text{SM}} = 0.301(6)$. We here report a new prediction:

$$R_{D_s}|_{\text{SM}} = 0.2955(35). \quad (7.37)$$

To arrive at this prediction we averaged over the $l = e$ and $l = \mu$ cases. We give an error budget for this result in terms of errors from our lattice calculation in table 7.8.

7.4 Reconstructing Form Factors

This section gives the necessary information to reproduce the functional form of the form factors through q^2 reproduced in this work. We here express the form factors

Source	% Fractional Error
Statistics	0.99
Scale Setting	0.40
Kinematic Interpolation	0.43
$m_h \rightarrow m_b,$	0.35
$a \rightarrow 0$	0.06
Quark Mass Mistuning	0.17
Total	1.18

Table 7.8: Error budget for $R_{D_s}|_{\text{SM}}$.

in terms of the BCL parameterisation [145]:

$$\begin{aligned} f_0^s(q^2) &= \frac{1}{1 - \frac{q^2}{M_{B_c^0}^2}} \sum_{n=0}^2 a_n^0 z^n(q^2), \\ f_+^s(q^2) &= \frac{1}{1 - \frac{q^2}{M_{B_c^*}^2}} \sum_{n=0}^2 a_n^+ \left(z^n(q^2) - \frac{n}{3} (-1)^{n-3} z^3(q^2) \right), \end{aligned} \quad (7.38)$$

where the function $z(q^2)$ is defined by defined by

$$z(q^2) = \frac{\sqrt{t_+ - q^2} - \sqrt{t_+}}{\sqrt{t_+ - q^2} + \sqrt{t_+}}, \quad (7.39)$$

and $t_+ = (M_{B_s} + M_{D_s})^2$ (one should take the PDG 2018 values for these masses). For the position of the poles, one can use $M_{B_c^0} = 6.70390(80)\text{GeV}$ and $M_{B_c^*} = 6.28030(80)\text{GeV}$. The coefficients $a_n^{0,+}$ found from our fit, along with their covariance, is given in table 7.9.

7.5 $h_+^s(1)$ and HQET low energy constants

Recall from Sec. 2.4.1 that there is an alternative parameterization of pseudoscalar-to-pseudoscalar transition amplitudes, given in eq. (2.76), motivated by HQET. The

a_0^0	a_1^0	a_2^0	a_0^+	a_1^+	a_2^+
0.65957	-0.10919	-0.02616	0.65957	-3.50695	0.01359
0.00008	0.00096	-0.00012	0.00008	0.00019	0.00000
	0.02882	0.03699	0.00096	0.00871	0.00002
		0.89613	-0.00012	0.04429	-0.00099
			0.00008	0.00019	0.00000
				0.19399	0.02158
					1.00159

Table 7.9: Our results for z -coefficients in the BCL parameterization (7.38). The first row gives mean values, and the rest of the table gives the covariance matrix associated with these parameters.

form factor h_+^s is protected by Luke's theorem at zero recoil, and can be written as

$$h_+^s(1) = \eta_V \left[1 - l_P^s \left(\frac{1}{2m_h} - \frac{1}{2m_c} \right)^2 \right] + \mathcal{O} \left(\frac{1}{m_c^n m_h^m}, n+m \geq 3 \right). \quad (7.40)$$

This invites an extrapolation of $h_+^s(1)$ through m_h in the same way as $h_{A_1}^s$ was extrapolated. We perform this for two reasons - to determine l_P^s , and to supply another consistency test for the m_h extrapolation of $f_0(q_{\max}^2)$.

We perform the $h_+(1)$ extrapolation using the fit form

$$h_+^s(1)|_{\text{fit}} = \eta_V \left[1 - l_P^s \left(\frac{\epsilon_h}{2} - \frac{\epsilon_c}{2} \right)^2 \right] + \mathcal{N}_{\text{disc}} + \mathcal{N}_{\text{mistuning}}. \quad (7.41)$$

where ϵ_q is defined in (6.21), $\mathcal{N}_{\text{disc}}$ is defined in (6.24), and $\mathcal{N}_{\text{mistuning}}$ in (7.23). η_V has a 1-loop expression [136]

$$\eta_V(m_h) = 1 - \frac{3\alpha_s(m_b)}{4\pi} \left(\frac{m_h + m_c}{m_h - m_c} \log \left(\frac{m_c}{m_h} \right) - \frac{3}{2} \right), \quad (7.42)$$

and has been computed to 2-loop to have the value $\eta_V = 1.022(4)$ [135]. Similarly to η_A , this varies weakly with m_h , the variance of this through the $m_c \leq m_h \leq m_b$ range is illustrated in fig. 6.5. Like in the $h_{A_1}(1)$ case, we attempted the fit with an extra $(1 + \rho \log(M_{\eta_c}/M_{\eta_h}))$ factor multiplying η_V (ρ is a fit parameter with prior distribution 0 ± 1), and this reduced the Bayes factor by a factor of 16. So the η_V dependence on m_h can be safely ignored.

We did however find that there is not enough freedom in a fit to the above form to achieve $\chi^2/N_{\text{dof}} \leq 1$. The only way to obtain a good fit is to promote η_V to a fit parameter, with prior distribution $1 \pm \alpha_s^2$, where we take $\alpha_s = 0.22$. All other priors are given the same distributions as in the $h_{A_1}(1)$ case, except for d_{ijk} which are each given the prior 0 ± 1 .

The extrapolation is illustrated in fig. 7.16. The result for $h_+^s(1)$ at continuum and all physical quark masses is

$$h_+^s(1) = 0.9998(81)_{\text{stat}}(45)_{\text{sys}}. \quad (7.43)$$

The fit finds new non-perturbative values for

$$\eta_V = 0.9931(52) , \quad l_P^s = -0.07(13)\text{GeV}^2. \quad (7.44)$$

Our estimate for l_P^s here is consistent with the l_P^s value found from the $h_{A_1}^s(1)$ study of $l_P^s = -0.25(20)\text{GeV}^2$ (in the sense that neither of them say anything really).

From this h_+^s result at the physical point we can produce a new $f_0^s(q_{\text{max}}^2)$ value for comparison with our final result:

$$f_0^s(q_{\text{max}}^2)|_{h_+} = \frac{2\sqrt{M_{B_s}M_{D_s}}}{M_{B_s} + M_{D_s}} h_+^s(1) = 0.8860(82). \quad (7.45)$$

This is in a mild 1.7σ tension with our result from the direct $f_0^s(q_{\text{max}}^2)$ extrapolation given in eq. (7.27).

7.6 Conclusions

We have produced a fully non-perturbative lattice QCD prediction of the scalar and vector form factors for the $B_s \rightarrow D_s l \nu$ decay throughout the entire q^2 range, and a value for R_{D_s} (eq. (7.37)). Our results are statistics dominated. In this calculation we used correlation functions from 3 lattice spacings, including an ensemble with an approximately physical light quark mass, and learned the b -mass dependence of the form factors by obtaining data at 12 different heavy quark masses.

Our results supply an independent check on the NRQCD formalism for computing pseudoscalar-to-pseudoscalar form factors. Our results validate the q^2 -extrapolation from high q^2 lattice data used in the NRQCD case, since our formalism produced lattice data throughout all q^2 . We have also validated the normalization of NRQCD lattice currents, and the truncation they use in the $1/m_b$ expansion of the currents. Our results are however considerably more precise, and does not rely on the assumptions implicit in the NRQCD formalism.

Our calculation has shown that a heavy-HISQ determination of the $B \rightarrow Dl\nu$ form factors is very plausible. Such a calculation could use an essentially identical process as given here, with the strange valence quark simply replaced with a light one. Perhaps correlation functions from additional ensembles with smaller light quark masses would be necessary to resolve the dependence of the form factors on the light mass. Also more statistics would likely be necessary, since the presence of a light valence quark increases the noise in the lattice data, and statistics is already dominant in this calculation.

7.7 Numerical Values for Lattice Results

In this section we give two tables, consisting of all numerical results for form factors, ratios $R_{0,+}^s(q^2)$, masses, energies and decay constants required for the extrapolations performed to the physical point. Table 7.10 gives results relevant to all q^2 values, while 7.11 gives results that vary over q^2 .

Set	aM_{h0}^{val}	aM_{H_s}	aM_{D_s}	aM_{H_c}	af_{He}	aM_{η_h}	aM_{η_c}	aM_{η_s}
0	0.5	0.95976(11)	0.90222(10)	1.419515(41)	0.186299(70)	1.471675(38)	1.367014(40)	0.313886(75)
	0.65	1.12519(15)		1.573302(40)	0.197220(77)	1.775155(34)		
	0.8	1.28139(19)		1.721226(39)	0.207068(78)	2.064153(30)		
1	0.5	0.95446(13)	0.87715(11)	1.400025(26)	0.183482(46)	1.470095(25)	1.329291(27)	0.304826(52)
	0.8	1.27560(24)		1.702438(24)	0.203382(50)	2.062957(19)		
	2	0.427	0.77433(17)	0.59150(11)	1.067224(46)	0.126564(70)	1.233585(41)	0.896806(48)
0.525	0.525	0.88447(21)		1.172556(46)	0.130182(72)	1.439515(37)		
	0.65	1.01931(29)		1.303144(46)	0.133684(75)	1.693895(33)		
	0.8	1.17383(42)		1.454205(46)	0.137277(79)	1.987540(30)		
3	0.5	0.80237(22)	0.439879(93)	1.011679(29)	0.099006(56)	1.342747(27)	0.666754(39)	0.153827(77)
	0.65	0.96357(30)		1.169775(31)	0.100553(66)	1.650264(23)		
	0.8	1.11734(41)		1.321656(35)	0.101720(82)	1.945763(21)		

Table 7.10: Values extracted from correlation function fits required for the extrapolation of $f_{0,+}^s(q^2)$, $R_{0,+}^s(q^2)$ to the physical point. The decay constant af_{D_s} is extracted from the fit via (??) and (??). D_s energies away from zero recoil are given in table 7.11.

Set	am_{h0}^{val}	$q^2[\text{GeV}^2]$	aE_{D_s}	$f_0^s(q^2)$	$f_+^s(q^2)$	$R_0(q^2)[\text{GeV}^{-3/2}]$	$R_+(q^2)[\text{GeV}^{-3/2}]$
0	0.5	0.016	0.90222(10)	1.0013(15)		1.410(12)	
	0.000	0.90391(11)	1.0001(15)	1.0001(15)		1.409(12)	1.409(12)
	0.65	0.234	0.90222(10)	1.0044(16)		1.269(11)	
	0.118	0.91315(12)	0.9968(16)	1.0031(61)		1.260(11)	1.268(13)
	0.003	0.92407(14)	0.9893(17)	0.9895(17)		1.250(11)	1.250(11)
	0.8	0.678	0.90222(10)	1.0096(18)		1.162(10)	
1	0.342	0.93000(15)	0.9904(20)	1.0069(88)		1.1397(99)	1.159(14)
	0.008	0.95766(25)	0.9721(24)	0.9725(24)		1.1186(99)	1.1190(99)
	0.5	0.030	0.87715(11)	1.0004(15)		1.369(11)	
	0.026	0.87759(11)	1.0001(15)	1.0002(19)		1.369(11)	1.371(28)
2	0.8	0.801	0.87715(11)	1.0054(18)		1.1258(91)	
	0.613	0.89178(15)	0.9948(22)	1.030(18)		1.1139(91)	1.154(22)
	0.427	0.371	0.59150(11)	0.9938(20)		1.250(11)	
	0.188	0.60215(14)	0.9802(23)	0.9932(52)		1.233(11)	1.249(12)
0.525	0.006	0.61276(17)	0.9682(24)	0.9686(25)		1.217(11)	1.218(11)
	0.536	0.61276(17)	0.9603(28)	0.9902(76)		1.120(10)	1.155(13)
	0.012	0.63940(30)	0.9313(33)	0.9319(33)		1.086(10)	1.087(10)
	0.65	2.032	0.59150(11)	0.9866(23)		1.151(10)	
0.8	0.948	0.63940(30)	0.9208(41)	0.9609(88)		0.9920(95)	1.035(13)
	0.008	0.68092(55)	0.8786(45)	0.8788(45)		0.9465(94)	0.9468(94)
	3.765	0.59150(11)	0.9677(41)			0.9611(91)	
	1.434	0.68092(55)	0.8673(57)	0.9052(94)		0.8614(93)	0.899(12)
-0.055	0.7381(13)	0.8203(87)	0.8192(86)	0.815(11)			0.814(11)

Table 7.11: Parameters extracted from correlation function fits at varying q^2 points (from the fine and fine-physical ensembles, sets 2 and 3). $f_{0,+}^s(q^2)$ are extracted via (7.16) and (7.18), and $R_{0,+}^s(q^2)$ is defined in (7.19).

Set	am_{h0}^{val}	$q^2[\text{GeV}^2]$	aE_{D_s}	$f_0^s(q^2)$	$f_+^s(q^2)$	$R_0(q^2)[\text{GeV}^{-3/2}]$	$R_+(q^2)[\text{GeV}^{-3/2}]$
3	0.5	2.635	0.439879(93)	0.9721(33)		1.030(10)	
	1.177	0.48519(24)	0.9111(36)	0.9509(70)	0.9655(96)	1.008(12)	
	-0.024	0.52252(60)	0.8644(52)	0.8636(51)	0.916(10)	0.9151(99)	
0.65	5.500	0.439879(93)	0.9548(39)		0.9265(93)		
	3.749	0.48519(24)	0.8957(43)	1.005(20)	0.8691(89)	0.975(21)	
	2.306	0.52252(60)	0.8500(61)	0.915(12)	0.8248(95)	0.887(14)	
0.8	0.248	0.57558(32)	0.753(23)	0.760(20)	0.731(23)	0.738(21)	
	9.204	0.439879(93)	0.9409(45)		0.8490(88)		
	5.500	0.52252(60)	0.8413(72)	0.982(27)	0.7592(95)	0.886(26)	
3.114	0.57558(32)	0.754(22)	0.839(28)	0.681(21)		0.757(27)	
	0.656	0.631(10)	0.661(50)	0.673(43)	0.596(45)	0.608(39)	

Table 7.12: Parameters extracted from correlation function fits at varying q^2 points, from the superfine and ultrafine ensembles (sets 4 and 5)

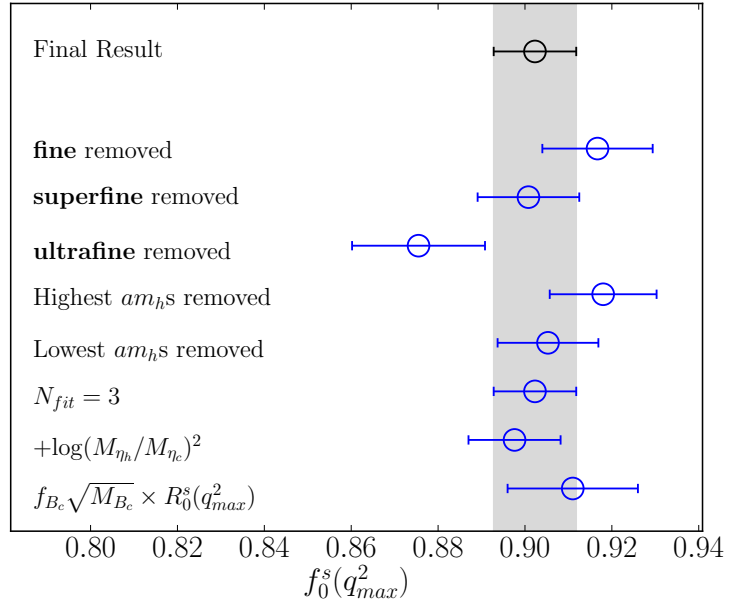


Figure 7.9: Results of tests of the $f_0^s(q_{max}^2)$ extrapolation. The top three blue points show $f_0^s(q_{max}^2)$ at continuum and physical b mass, if data from the fine, superfine or ultrafine ensembles are not used in the fit. The fourth and fifth blue points show the result if data at the highest/lowest am_{h0}^{val} value on each ensemble are removed. The point labelled $N_{fit} = 3$ is the result of extending the sum in (7.22) such that it truncates at 3 rather than 2 in each of the i, j, k directions. The point labelled $+\log(M_{\eta_h}/M_{\eta_c})^2$ represents the result of adding a $\rho_2 \log(M_{\eta_h}/M_{\eta_c})^2$ term in the first set of brackets in (7.22), where ρ_2 is a new fit parameter with the same prior distribution as ρ_{\log} . The lowest point shows the result from the extrapolation of $R_0^s(q_{max}^2)$, multiplied by the PDG value for $\sqrt{M_{B_c}}$ [1] and the result of our extrapolation of f_{B_c} to the physical point detailed Sec. 6.3.5.

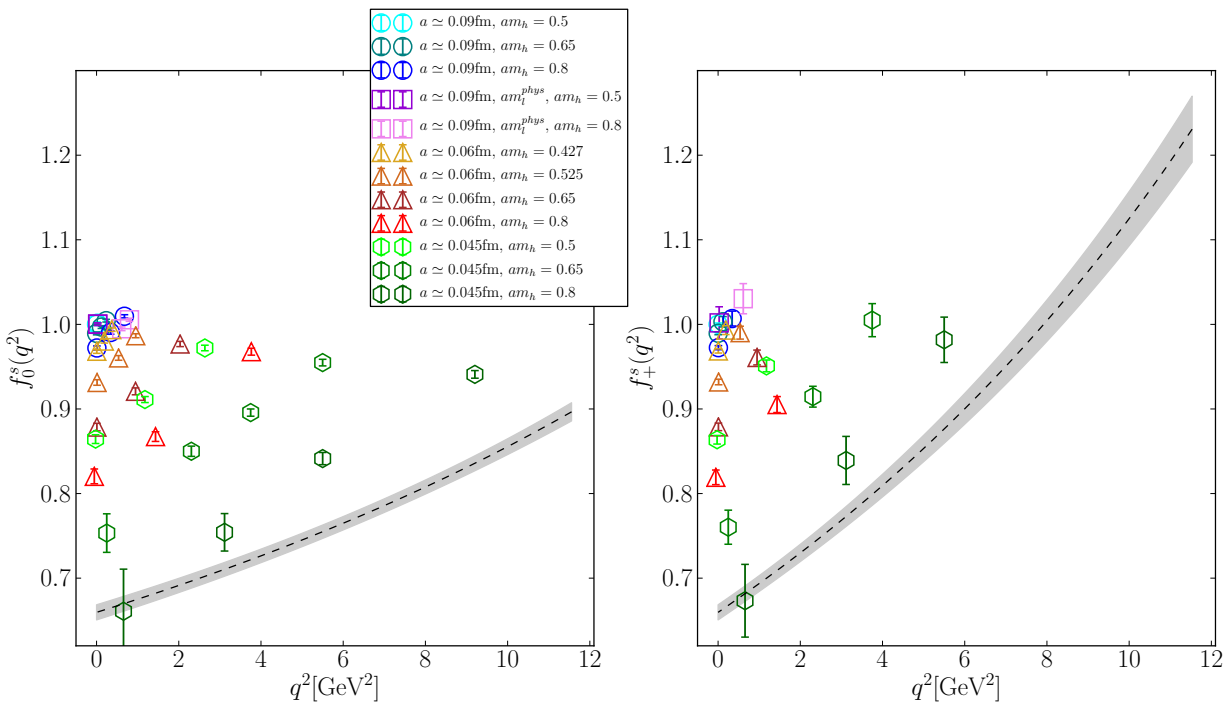
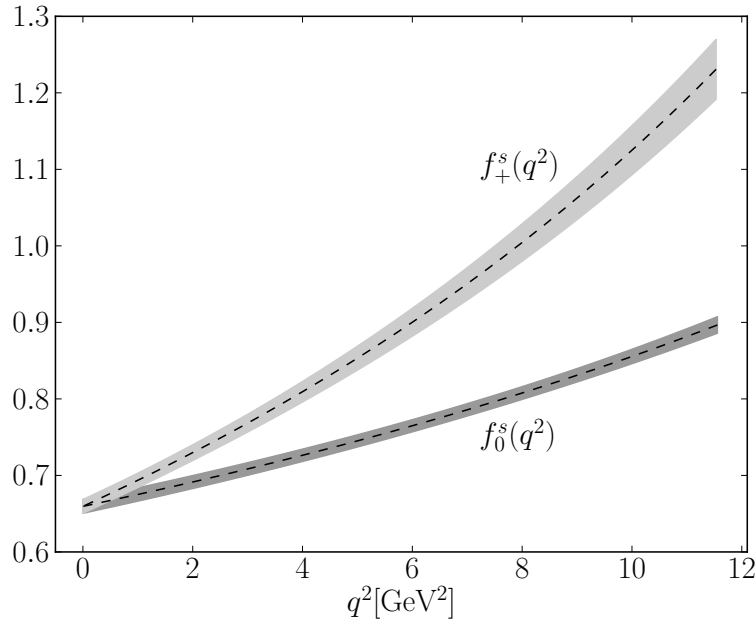
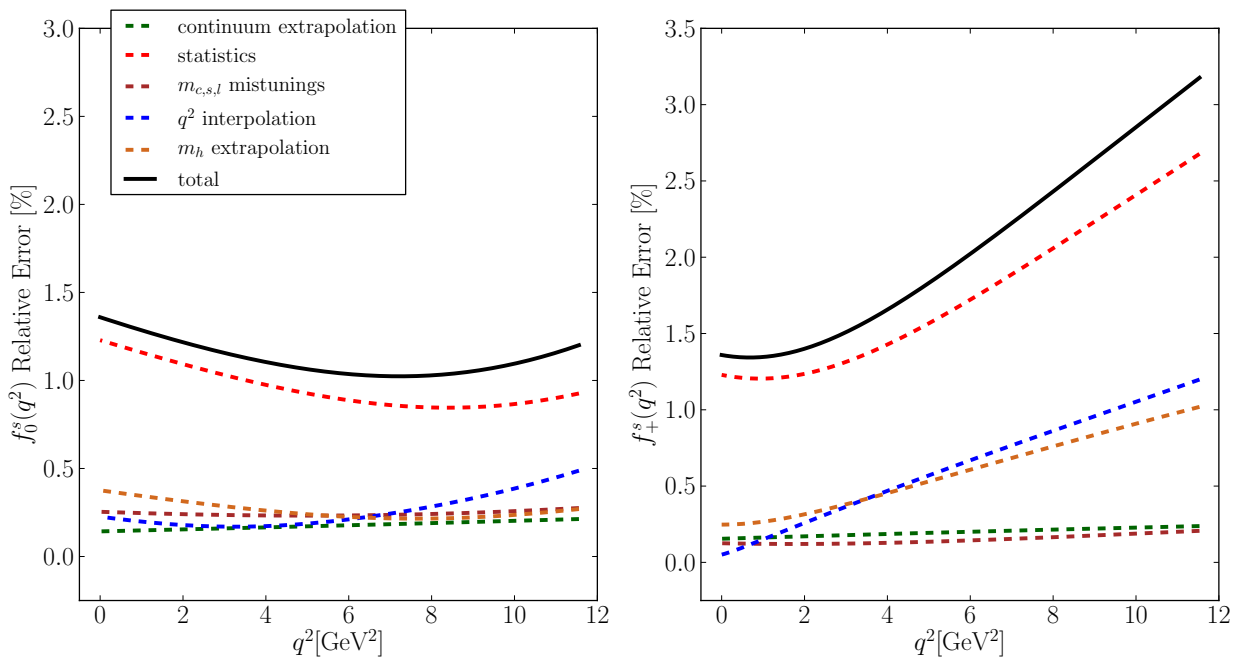


Figure 7.10: $f_{0,+}^s(q^2)$ against q^2 . The grey band shows the result of the extrapolation at $a = 0$ and physical l,s,c and b masses. Sets listed in the legend follow the order of sets in table 7.1.

Figure 7.11: Final result for $f_{0,+}^s(q^2)$ against q^2 at the physical point .Figure 7.12: Error budget for $f_{0,+}^s(q^2)$ against q^2 .

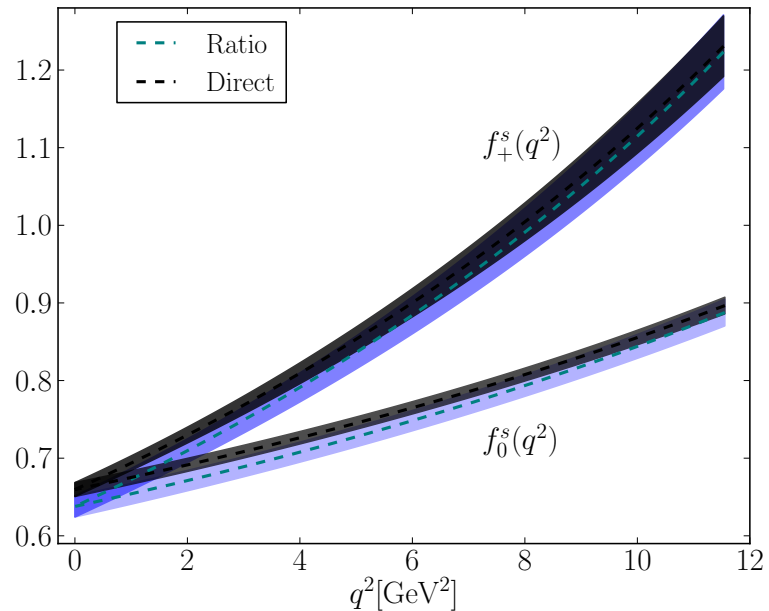


Figure 7.13: Results for $f_{0,+}^s(q^2)$ against q^2 at the physical point, from both the ratio method and the direct method.

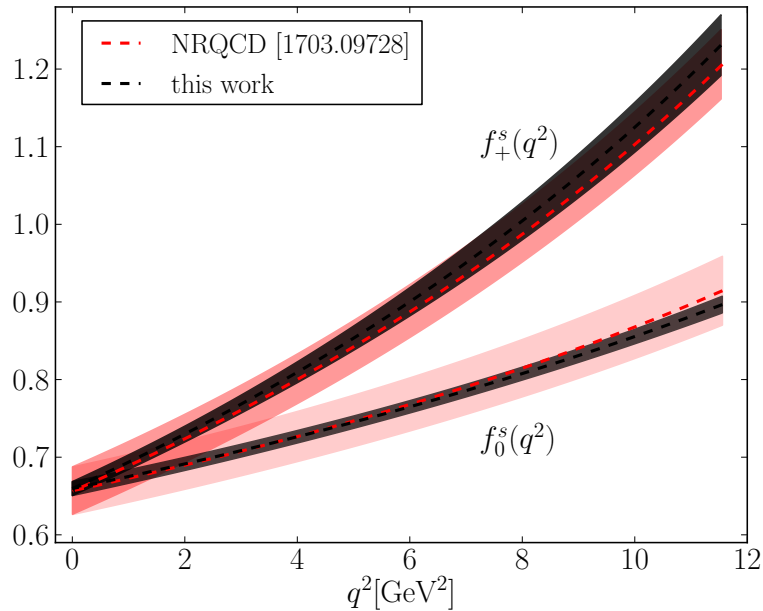


Figure 7.14: Our final result for $f_{0,+}^s(q^2)$ against form factors calculated from a previous study using the NRQCD action for the b quark [101] .

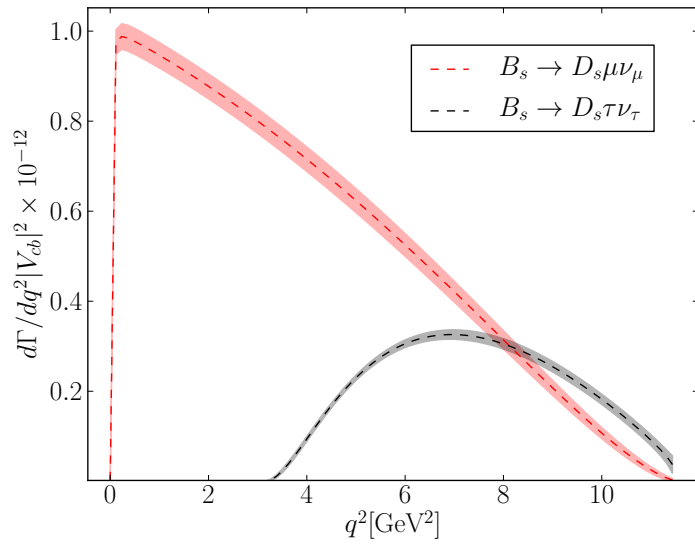


Figure 7.15: Decay rates for the $B_s \rightarrow D_s \mu \nu_\mu$ and $B_s \rightarrow D_s \tau \nu_\tau$ decays, derived using form factors calculated in this work.

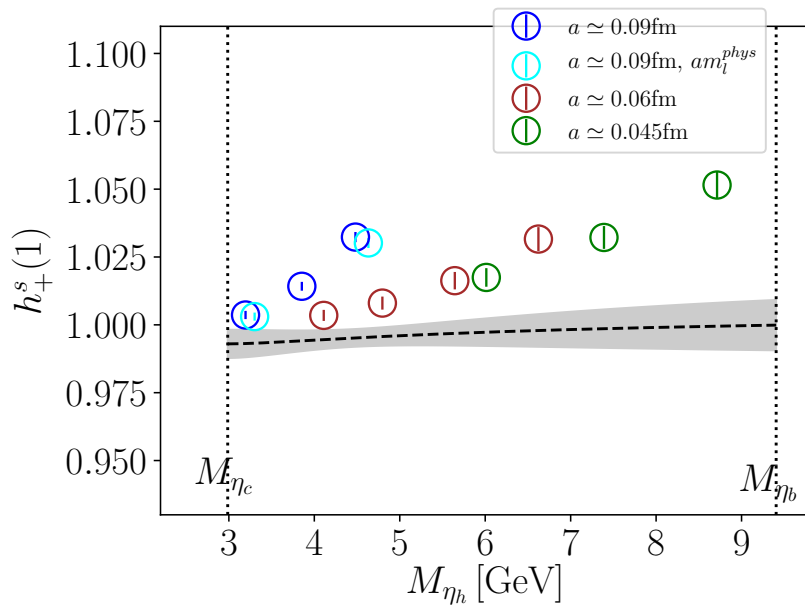


Figure 7.16: Extrapolation of $h_+^s(1)$ through M_{η_h} . The grey band shows the $a \rightarrow 0$ and physical charm, strange and light quarks result.

List of Figures

2.1	The flavour-changing charged current vertex.	8
2.2	A sketch of the unitarity triangle.	9
2.3	Exclusion regions for the vertices of the CKM triangle from various measurements, courtesy of the most recent PDG update [1].	10
2.4	Leptonic decay of meson M at tree level in the electroweak coupling.	11
2.5	Semileptonic decay, $M \rightarrow M' l \bar{\nu}$, at tree level in electroweak coupling.	12
2.6	Different determinations of $ V_{cb} $. Points labelled $w = 1$ are determinations from extrapolating measurements of decay rates to the zero recoil point, and combining them with a lattice determination of the form factor at zero recoil. Points labelled $w \geq 1$ are results from using a combination of both branching fractions and lattice form factors through some range of w . The first name mentioned in the labels give the source of the lattice form factors, and the second gives the source of the experimental data (e.g. the HPQCD+BaBar point used form factors from the HPQCD collaboration and data from the BaBar experiment). The highest point is from [11], the second and third highest from [12], fourth from [13], fifth from [14]. The bottom point is from the PDG [1], using data from the ALPEPH [15], Belle [16], BaBar [17, 18], and CLEO [19] experiments.	15
2.7	$R(D^{(*)})$ determinations from SM and measurement [2]	17
2.8	The relationship between scale Q and the strong coupling constant α_s , from the PDG [1].	20
3.1	Depiction of colour spaces (fibres) at two points in spactime (base space) with the value of the quark field q represented at each point as a colour vector, and the connection $W(x, y)$ needed to compare the two colour vectors. A gauge transform changes the two vectors in different ways, for the comparison to be gauge independent, the connection must also transform appropriately.	32
3.2	Depiction of a gauge invariant quark bilinear, connected by a Wilson line made of gauge links.	32
3.3	Elementary Plaquette.	33

3.4	Terms additional to the elementary plaquette in the improved pure QCD action.	35
3.5	Taste mixing at tree level.	41
3.6	Different scales relevant to non-perturbative physics, and brackets showing the range of scales that typical lattices can resolve. The larger the range of scales resolved, the more computationally expensive the calculation.	43
3.7	An extrapolation to $m_h = m_b$ of the η_h decay constant (where η_h is a pseudoscalar $\bar{h}h$ meson [3]. The colourful points are measurements of f_{η_h} on the lattice, the colour denotes lattice spacing. The x axis, M_{η_h} , is a proxy for the h -quark mass.	44
5.1	Decay amplitude ratios (colourful points) against the expected relativistic behaviour (grey dotted line and band). Adding the $A_{0,\text{lat}}^{(1)}$ piece of the current does not improve the relativistic behaviour of the ratio.	68
5.2	$B \rightarrow Dl\nu$ form factors. The coloured points show lattice data, each color represents an ensemble. The grey band represents the continuum and kinematically extrapolated result.	73
5.3	$B_s \rightarrow D_s l\nu$ form factors. The coloured points show lattice data, each color represents an ensemble. The grey band represents the continuum and kinematically extrapolated result.	74
5.4	Lattice results for $f_0^s(q_{\max}^2)$ against a^2 . The grey band shows the result for $f_0^s(q_{\max}^2)$ computed in chapter 7 using the Heavy-HISQ approach for comparison. Clearly the result on the fine ensemble (the black point), and possibly on the coarse ensemble (the blue point), contain large unknown systematic errors.	75
5.5	Lattice results for the ratios of (matrix elements of) NRQCD-HISQ currents in the $B_s \rightarrow D_s$ case. Namely ratios of the subleading currents $V_\mu^{(n>0)}$ to the leading order current $V_\mu^{(0)}$	76
5.6	$B \rightarrow D$ form factors extracted from $\langle V_0 \rangle$ and $\langle S \rangle$. Clearly these results are nonsense. See text.	78
5.7	A schematic of the chain of steps towards normalizing the scalar, temporal vector and spacial vector currents NRQCD-HISQ currents. Details given in the next three sections; 5.4.1, 5.4.2 and 5.4.3.	79

5.8 Comparison of form factors from $\langle V_0 \rangle, \langle S \rangle$ and $\langle V_0 \rangle, \langle V_k \rangle$, no additional normalizations. The bands show the results of fitting the data to the BGL parameterization (5.23), where coefficients $a_n^{0,+}$ are fit parameters.	81
5.9 Comparison of form factors from $\langle V_0 \rangle, \langle S \rangle$ and $\langle V_0 \rangle, \langle V_k \rangle$ is multiplied by Z_{V_0} given in (5.37). The bands show the results of fitting the data to the BGL parameterization (5.23), where coefficients $a_n^{0,+}$ are fit parameters.	82
5.10 Z_{V_k} from constraining form factors to be the same from $\langle V_0 \rangle, \langle S \rangle$ and $\langle V_0 \rangle, \langle V_k \rangle$	83
5.11 Comparison of form factors from $\langle V_0 \rangle, \langle S \rangle$ and $\langle V_0 \rangle, \langle V_k \rangle$, with $\langle V_0 \rangle$ normalized via Z_{V_0} and $\langle V_k \rangle$ normalized with Z_{V_k} . The bands show the results of fitting the data to the BGL parameterization (5.23), where coefficients $a_n^{0,+}$ are fit parameters.	84
6.1 Tests on the correlator fits on the fine ensemble. At $N_{\text{test}} = 1$ we give the final accepted result. $N_{\text{test}} = 2$ gives the results when all priors are loosened by 50%. $N_{\text{test}} = 3$ and 4 gives the results of setting $N_{\text{exp}} = 4$ and 6 respectively. $N_{\text{test}} = 5, 6$ gives the results of setting $t_{\text{cut}} = 2, 4$ respectively for all correlators. $N_{\text{test}} = 7$ gives the result without marginalising out the $n = 5$ excited state. $N_{\text{test}} = 8$ gives the result of moving the SVD cut from 10^{-3} to 10^{-2}	91
6.2 An illustration of the process of deducing an appropriate SVD cut on the fine ensemble. Each point shows the ratio of a covariance matrix eigenvalue, to the same eigenvalue from a bootstrap copy, against the relative size of the eigenvalue. The eigenvalues below the red dotted line are at risk of being underestimated.	92
6.3 Effective energies and amplitudes for H_s and D_s^* correlators on the fine ensemble. The energies are obtained from eq. (6.13), and amplitudes from eq. (6.14). The grey bands give the results of the full multiexponential fit.	94
6.4 Sanity check for fits to the 3-point correlation functions. This ratio should approach J_{00}^{nn} for $t \gg 0$ and $t \ll T$. The grey band shows the result for J_{00}^{nn} from the full multiexponential fit.	95
6.5 The variation of the 1-loop expression for η_A & η_V throughout the $m_c \leq m_h \leq m_b$ range.	98

- 6.6 $h_{A_1}^s(1)$ against M_{η_h} (a proxy for the heavy quark mass). The grey band shows the result of the extrapolation at $a = 0$ and physical l,s and c masses. Sets listed in the legend follow the order of sets in table 6.1. The red point represents a determination of the same quantity from a previous study using the NRQCD action for the b [8]. 104

6.7 Results of $h_{A_1}^s(1)$ extrapolation tests. The top three blue points show $h_{A_1}^s(1)$ at continuum and physical b mass, if data from the fine, superfine or ultrafine ensembles are not used in the fit. The fourth and fifth blue points show the result if data at the highest/lowest am_{h0}^{val} value on each ensemble are removed. The point labelled 'No HQET input' is the result of a more naive heavy-mass extrapolation; the first line of (6.23) is removed, and the sum in (6.24) is extended to include terms with $j + k = 0$. An extra term to account for charm mass mistunings is added. The point labelled $N_{\text{nuisance}} = 3$ is the result of extending the sum in (6.24) such that it truncates at 3 rather than 2 in each of the i,j,k directions. The point labelled '+1/ m_b^3 ' results from adding an extra term to (6.23) of the form $p\varepsilon_h^3$ where p is a fit parameter with the same prior as $l_{V,A,P}^s$. In this case, the Bayes factor falls by a factor of 7, suggesting that the data does not contain a cubic dependence on the heavy mass. The point labelled 'Ratio' is the result of an alternative extrapolation described in sec. 6.3.2. . . . 105

6.8 $h_{A_1}^s(1)/(f_{H_c}\sqrt{M_{H_c}})$ against M_{η_h} (a proxy for the heavy quark mass). The grey band shows the result of the extrapolation at $a = 0$ and physical l,s and c masses. Sets listed in the legend follow the order of sets in table 6.1. The black point shows our final result for $h_{A_1}^s(1)$ divided by $\sqrt{M_{B_c}}$ from the PDG [1] and f_{B_c} from our extrapolation of f_{H_c} to continuum and physical b mass. 106

6.9 $h_{A_1}^{(s)}(1)$ from different calculations. Those marked (NRQCD,HPQCD) are from [8]. The quantity marked (this work & NRQCD) is the result of multiplying our result for $h_{A_1}^s(1)$ with the ratio $h_{A_1}(1)/h_{A_1}^s(1)$ computed in [8]. The quantity marked (FNAL/MILC) is from [13]. 107

6.10 Lattice data and continuum extrapolated data for three studies of $h_{A_1}(1)$ and $h_{A_1}^s$, against the pion mass. Points labeled FNAL/MILC are from [13], and those labeled NRQCD are from [8]. The x-axis must be taken with a pinch of salt, the points at $M_\pi = M_{\eta_s}$ have pions in the sea of smaller masses than M_{η_s} , but we place them here to signify that the spectator quark as the mass of a strange quark.	108
6.11 $h_{A_1}(1)$ and $h_{A_1}^s(1)$ data on the fine ensemble.	108
6.12 $h_{A_1}^s(1)$ against M_{η_h} (a proxy for the heavy quark mass). The grey band shows the result of the extrapolation at $a = 0$ and physical l,s and c masses. Sets listed in the legend follow the order of sets in table 6.1. The red point shows the result from a previous heavy-HISQ determination of f_{B_c} on 2+1 gauge ensembles [3]	111
7.1 An plot analogous to fig. 6.2 for the dataset of correlators on the fine ensemble in the $B_s \rightarrow D_s$ case.	121
7.2 Tests on the correlator fits on the fine ensemble. At $N_{\text{test}} = 1$ we give the final accepted result. $N_{\text{test}} = 2$ and 3 gives the results of setting $N_{\text{exp}} = 4$ and 6 respectively. $N_{\text{test}} = 4$ gives the results when all priors are loosened by 50%. $N_{\text{test}} = 5$ gives the result of setting $t_{\text{cut}} = 4$ rather than 2 for all correlators. $N_{\text{test}} = 6$ gives the result without marginalising out the $n = 5$ excited state. $N_{\text{test}} = 7$ gives the result of moving the SVD cut from 10^{-3} to 10^{-2} . $N_{\text{test}} = 8, 9, 10$ gives the result of using a chained fit described above with priors for the full correlated fit loosened by 100%, 150% and 200% respectively.	122
7.3 Super-averaged effective energies (given by eq. (6.13)) and amplitudes (given by eq. (6.14)) for a selection of 2-point correlators on the fine ensemble. The grey bands show the correpsonding results for these quantities from the simultaious bayesian fits.	124
7.4 $\tilde{C}_3(t, T)/\tilde{C}^{H_s}(t)\tilde{C}^{D_s}(T - t)$, which should plateau at J_{00}^{nn} , in the fine ensemble for the $J = S$ and $J = V_0$ cases. The grey bands show the correpsonding results for these quantities from the simultaious bayesian fits.	125
7.5 $R_0^s(q_{\max}^2) = f_0^s(q_{\max}^2)/(f_{H_c}\sqrt{M_{H_c}})$ against M_{η_h} (a proxy for the heavy quark mass). The grey band shows the result of the extrapolation at $a = 0$ and physical l,s and c masses. Sets listed in the legend follow the order of sets in table 7.1.	131

- 7.6 Results of tests of the $R_0^s(q_{\max}^2)$ extrapolation. The top three blue points show $R_0^s(q_{\max}^2)$ at continuum and physical b mass, if data from the fine, superfine or ultrafine ensembles are not used in the fit. The fourth and fifth blue points show the result if data at the highest/lowest am_{h0}^{val} value on each ensemble are removed. The point labelled $N_{fit} = 3$ is the result of extending the sum in (7.22) such that it truncates at 3 rather than 2 in each of the i, j, k directions. The point labelled $+\log(M_{\eta_h}/M_{\eta_c})^2$ represents the result of adding a $\rho_2 \log(M_{\eta_h}/M_{\eta_c})^2$ term in the first set of brackets in (7.22), where ρ_2 is a new fit parameter with the same prior distribution as ρ_{\log} . The lowest point shows the result of our direct extrapolation of $f_0^s(q_{\max}^2)$ to the physical point, divided by the PDG value for $\sqrt{M_{B_c}}$ [1] and the result of our extrapolation of f_{B_c} to the physical point detailed in sec. 6.3.5. 132
- 7.7 $R_{0,+}^s(q^2) = f_{0,+}^s(q^2)/(f_{H_c}\sqrt{M_{H_c}})$ against q^2 . The grey band shows the result of the extrapolation at $a = 0$ and physical l, s, c and b masses. Sets listed in the legend follow the order of sets in table 7.1. 133
- 7.8 $f_0^s(q_{\max}^2)$ against M_{η_h} (a proxy for the heavy quark mass). The grey band shows the result of the extrapolation at $a = 0$ and physical l, s and c masses. We also include the result from a previous lattice calculation, which used the NRQCD discretisation for the b quark [101]. Sets listed in the legend follow the order of sets in table 7.1. 134
- 7.9 Results of tests of the $f_0^s(q_{\max}^2)$ extrapolation. The top three blue points show $f_0^s(q_{\max}^2)$ at continuum and physical b mass, if data from the fine, superfine or ultrafine ensembles are not used in the fit. The fourth and fifth blue points show the result if data at the highest/lowest am_{h0}^{val} value on each ensemble are removed. The point labelled $N_{fit} = 3$ is the result of extending the sum in (7.22) such that it truncates at 3 rather than 2 in each of the i, j, k directions. The point labelled $+\log(M_{\eta_h}/M_{\eta_c})^2$ represents the result of adding a $\rho_2 \log(M_{\eta_h}/M_{\eta_c})^2$ term in the first set of brackets in (7.22), where ρ_2 is a new fit parameter with the same prior distribution as ρ_{\log} . The lowest point shows the result from the extrapolation of $R_0^s(q_{\max}^2)$, multiplied by the PDG value for $\sqrt{M_{B_c}}$ [1] and the result of our extrapolation of f_{B_c} to the physical point detailed Sec. 6.3.5. 145

7.10 $f_{0,+}^s(q^2)$ against q^2 . The grey band shows the result of the extrapolation at $a = 0$ and physical l, s, c and b masses. Sets listed in the legend follow the order of sets in table 7.1.	146
7.11 Final result for $f_{0,+}^s(q^2)$ against q^2 at the physical point	147
7.12 Error budget for $f_{0,+}^s(q^2)$ against q^2	147
7.13 Results for $f_{0,+}^s(q^2)$ against q^2 at the physical point, from both the ratio method and the direct method.	148
7.14 Our final result for $f_{0,+}^s(q^2)$ against form factors calculated from a previous study using the NRQCD action for the b quark [101]	149
7.15 Decay rates for the $B_s \rightarrow D_s \mu \nu_\mu$ and $B_s \rightarrow D_s \tau \nu_\tau$ decays, derived using form factors calculated in this work.	149
7.16 Extrapolation of $h_+^s(1)$ through $M_{\eta h}$. The grey band shows the $a \rightarrow 0$ and physical charm, strange and light quarks result.	150

List of Tables

4.1 Parameters for gluon ensembles [91, 92]. a values for sets 0-3 were deduced in [93], set 4 from [94]. We thank C. McNeile for computing the a value on set 5. These a values are determined by measuring the Wilson flow parameter w_0/a on the lattice, then using the known value for w_0 to isolate a . Columns 5-7 give the masses used in the action for light, strange and charm quarks in the sea.	52
5.1 Parameters used in our calculation. am_{s0} and am_{c0} are the bare masses of the strange, charm valence quarks, tuned in [102], am_{b0} is the bare mass of the valence bottom quark, tuned in [76] u_0 is the 'tadpole improvement parameter' as used in [76]. $\{c_i\}$ are the coefficients for the kinetic and chromomagnetic terms in the NRQCD action (eq. (3.58)) [103]. $\{T\}$ is the set of temporal separations between source (B_s creation operator) and sink (D_s annihilation operator). a_{sm} are the radii of the exponential smearing function applied to the $B_{(s)}$ and $D_{(s)}$ creation operators.	69
5.2 Twists given to the charm propagator on each ensemble.	70
6.1 Parameters relevant to our calculation. Columns 3 and 4 give the s and c valence quark masses, these values were tuned in [94] to reproduce the correct η_s and η_c masses. We use a number of heavy quark masses to assist the extrapolation to physical the b mass, given in column 5. Column 6 gives the temporal separations between source and sink, T , of the 3-point correlation functions computed on each ensemble.	88
6.2 Normalization constants applied to the lattice axial vector current in (7.18). Z_A is found from (7.17) and Z_{disc} from (6.16).	96
6.3 Values extracted from correlation function fits for $h_{A_1}^s(1)$, along with quantities required for its extrapolation to the physical point. $h_{A_1}^s(1)$ values are found from eq. (7.18). f_{H_c} is the H_c decay constant derived from eq. (??).	102

6.4	Values extracted from correlation function fits for $h_{A_1}^s(1)$, along with quantities required for its extrapolation to the physical point. $h_{A_1}^s(1)$ values are found from eq. (7.18). f_{H_c} is the H_c decay constant derived from eq. (4.36).	103
6.5	Error budget for $h_{A_1}^s(1)$	103
6.6	Error budget for HQET low energy constants. Each column gives the % fractional error for the associated quantity.	109
7.1	Parameters for gluon ensembles [91,92]. a is the lattice spacing, values for sets 1 & 2 deduced in [93], set 3 from [94]. We thank C. McNeile for computing the a value on set 4. These a values are determined by measuring the Wilson flow parameter w_0/a on the lattice, then using the known value for w_0 to isolate a . N_x is the spatial extent and N_t the temporal extent of the lattice. Light, strange and charm quarks are included in the sea, their masses are given in columns 5-7.	117
7.2	Simulation details. Columns 2 and 3 give the s and c valence quark masses, which were tuned in [94]. In column 4 we give the heavy quark masses, we use a number of heavy quark masses to assist the extrapolation to physical the b mass. Column 5 gives the square of the spacial momentum given to the D_s meson, using a momentum twist, in lattice units. These values are chosen with the following rationale: When only 2 are used, these correspond to the $q^2 = 0$ and q_{\max}^2 points (except on the fine-physical ensemble, where we find the points q_{\max}^2 and $q_{\max}^2/2$). When 3 are used, the momenta correspond to $q^2 = 0$, $q^2 = q_{\max}^2/2$, and q_{\max}^2 points. When 4 are used, these are points for q_{\max}^2 , $3q_{\max}^2/4$, $q_{\max}^2/2$, $q_{\max}^2/4$, $q^2 = 0$. We used charm momentum in the $(1, 1, 1)$ direction. Column 6 gives the temporal separations between source and sink, T , of the 3-point correlation functions computed on each ensemble.	118
7.3	t_{cut} values used for each correlator on each ensemble. S and V_0 denote the 3-point correlators with the corresponding current S or V_0 . There is one exception to the values here: on the 3-point correlators on the ultrafine ensemble with $am_h = 0.8$ and $q^2 = 0$, the t_{cut} given here is replaced with 8,10 and 12 in the $T = 14, 17, 20$ cases respectively.	121
7.4	Normalization constants applied to the lattice axial vector current in (7.18). Z_V is found from (7.17) and Z_{disc} from (6.16).	126

7.5	Error budget for $R_0^s(q_{\max}^2)$	131
7.6	Error budget for $f_0^s(q_{\max}^2)$ found via the direct method	133
7.7	Numerical values for B_{jk} appearing in the unitarity bound for BCL coefficients, defined in (7.35), for the f_0^s and f_+^s cases. The rest of the elements can be obtained from these using the properties $B_{j(j+k)} = B_{0k}$ and $B_{jk} = B_{kj}$	136
7.8	Error budget for $R_{D_s} _{\text{SM}}$	138
7.9	Our results for z -coefficients in the BCL parameterization (7.38). The first row gives mean values, and the rest of the table gives the covariance matrix associated with these parameters	139
7.10	Values extracted from correlation function fits required for the extrapolation of $f_{0,+}^s(q^2)$, $R_{0,+}^s(q^2)$ to the physical point. The decay constant $a f_{D_s}$ is extracted from the fit via (??) and (??). D_s energies away from zero recoil are given in table 7.11	142
7.11	Parameters extracted from correlation function fits at varying q^2 points (from the fine and fine-physical ensembles, sets 2 and 3). $f_{0,+}^s(q^2)$ are extracted via (7.16) and (7.18), and $R_{0,+}^s(q^2)$ is defined in (7.19)	143
7.12	Parameters extracted from correlation function fits at varying q^2 points, from the superfine and ultrafine ensembles (sets 4 and 5)	144

Bibliography

- [1] M. et. al. Tanabashi. Review of particle physics. *Phys. Rev. D*, 98:030001, Aug 2018.
- [2] Y. Amhis et al. Averages of b -hadron, c -hadron, and τ -lepton properties as of summer 2016. *Eur. Phys. J.*, C77:895, 2017. updated results and plots available at <https://hflav.web.cern.ch><https://hflav.web.cern.ch>.
- [3] C. McNeile, C. T. H. Davies, E. Follana, K. Hornbostel, and G. P. Lepage. Heavy meson masses and decay constants from relativistic heavy quarks in full lattice QCD. *Phys. Rev.*, D86:074503, 2012.
- [4] Bugra Borasoy. Introduction to Chiral Perturbation Theory. *Springer Proc. Phys.*, 118:1–26, 2008.
- [5] Large m_w , m_z behaviour of the $\mathcal{O}(a)$ corrections to semileptonic processes mediated by w . *Nuclear Physics B*, 196(1):83 – 92, 1982.
- [6] *Phys. Rev.*, 171(1):83 – 92. [Erratum: *Phys. Rev.* 174, 2169 (1968)].
- [7] David Atwood and William J. Marciano. Radiative corrections and semileptonic b decays. *Phys. Rev. D*, 41:1736–1740, Mar 1990.
- [8] Judd Harrison, Christine Davies, and Matthew Wingate. Lattice QCD calculation of the $B_{(s)} \rightarrow D_{(s)}^* \ell \nu$ form factors at zero recoil and implications for $|V_{cb}|$. *Phys. Rev.*, D97(5):054502, 2018.
- [9] Ikaros I. Y. Bigi, Mikhail A. Shifman, N. Uraltsev, and Arkady I. Vainshtein. High power n of m_b in beauty widths and $n = 5 \rightarrow \infty$ limit. *Phys. Rev.*, D56:4017–4030, 1997. [,205(1996)].
- [10] Andre H. Hoang, Zoltan Ligeti, and Aneesh V. Manohar. B decays in the upsilon expansion. *Phys. Rev.*, D59:074017, 1999.
- [11] Heechang Na, Chris M. Bouchard, G. Peter Lepage, Chris Monahan, and Junko Shigemitsu. $B \rightarrow D \ell \nu$ form factors at nonzero recoil and extraction of $|V_{cb}|$. *Phys. Rev.*, D92(5):054510, 2015. [Erratum: *Phys. Rev.* D93,no.11,119906(2016)].

- [12] Jon A. Bailey et al. $B \rightarrow D\ell\nu$ form factors at nonzero recoil and $|V_{cb}|$ from 2+1-flavor lattice QCD. *Phys. Rev.*, D92(3):034506, 2015.
- [13] Jon A. Bailey et al. Update of $|V_{cb}|$ from the $\bar{B} \rightarrow D^*\ell\bar{\nu}$ form factor at zero recoil with three-flavor lattice QCD. *Phys. Rev.*, D89(11):114504, 2014.
- [14] Benjamin Grinstein and Andrew Kobach. Model-Independent Extraction of $|V_{cb}|$ from $\bar{B} \rightarrow D^*\ell\bar{\nu}$. *Phys. Lett.*, B771:359–364, 2017.
- [15] D Buskulic et. al. A measurement of $|v_{cb}|$ from $b^0 \rightarrow d^*l^-\nu_l$. *Physics Letters B*, 359(1):236 – 248, 1995.
- [16] Kazuo Abe et al. Measurement of $B(\text{anti-}B^0 \rightarrow D^+\ l^- \text{anti-}\nu_l)$ and determination of $|V(cb)|$. *Phys. Lett.*, B526:258–268, 2002.
- [17] Bernard Aubert et al. Measurements of the Semileptonic Decays $\text{anti-}B \rightarrow D\ l^- \text{anti-}\nu_l$ and $\text{anti-}B \rightarrow D^*\ l^- \text{anti-}\nu_l$ Using a Global Fit to $D \times l^- \text{anti-}\nu_l$ Final States. *Phys. Rev.*, D79:012002, 2009.
- [18] Bernard Aubert et al. Measurement of $|V(cb)|$ and the Form-Factor Slope in $B \rightarrow D\ l^- \text{anti-}\nu_l$ Decays in Events Tagged by a Fully Reconstructed B Meson. *Phys. Rev. Lett.*, 104:011802, 2010.
- [19] John E. Bartelt et al. Measurement of the $B \rightarrow D$ lepton neutrino branching fractions and form-factor. *Phys. Rev. Lett.*, 82:3746, 1999.
- [20] Dante Bigi, Paolo Gambino, and Stefan Schacht. A fresh look at the determination of $|V_{cb}|$ from $B \rightarrow D^*\ell\nu$. *Phys. Lett.*, B769:441–445, 2017.
- [21] Jon A. Bailey, Sunkyu Lee, Weonjong Lee, Jaehoon Leem, and Sungwoo Park. Updated evaluation of ϵ_K in the standard model with lattice QCD inputs. *Phys. Rev.*, D98(9):094505, 2018.
- [22] J. P. Lees et al. Evidence for an excess of $\bar{B} \rightarrow D^{(*)}\tau^-\bar{\nu}_\tau$ decays. *Phys. Rev. Lett.*, 109:101802, 2012.
- [23] J. P. Lees et al. Measurement of an Excess of $\bar{B} \rightarrow D^{(*)}\tau^-\bar{\nu}_\tau$ Decays and Implications for Charged Higgs Bosons. *Phys. Rev.*, D88(7):072012, 2013.
- [24] M. Huschle et al. Measurement of the branching ratio of $\bar{B} \rightarrow D^{(*)}\tau^-\bar{\nu}_\tau$ relative to $\bar{B} \rightarrow D^{(*)}\ell^-\bar{\nu}_\ell$ decays with hadronic tagging at Belle. *Phys. Rev.*, D92(7):072014, 2015.

- [25] Y. Sato et al. Measurement of the branching ratio of $\bar{B}^0 \rightarrow D^{*+}\tau^-\bar{\nu}_\tau$ relative to $\bar{B}^0 \rightarrow D^{*+}\ell^-\bar{\nu}_\ell$ decays with a semileptonic tagging method. *Phys. Rev.*, D94(7):072007, 2016.
- [26] S. Hirose et al. Measurement of the τ lepton polarization and $R(D^*)$ in the decay $\bar{B} \rightarrow D^*\tau^-\bar{\nu}_\tau$. *Phys. Rev. Lett.*, 118(21):211801, 2017.
- [27] S. Hirose et al. Measurement of the τ lepton polarization and $R(D^*)$ in the decay $\bar{B} \rightarrow D^*\tau^-\bar{\nu}_\tau$ with one-prong hadronic τ decays at Belle. *Phys. Rev.*, D97(1):012004, 2018.
- [28] Roel Aaij et al. Measurement of the ratio of branching fractions $\mathcal{B}(\bar{B}^0 \rightarrow D^{*+}\tau^-\bar{\nu}_\tau)/\mathcal{B}(\bar{B}^0 \rightarrow D^{*+}\mu^-\bar{\nu}_\mu)$. *Phys. Rev. Lett.*, 115(11):111803, 2015. [Erratum: *Phys. Rev. Lett.* 115, no. 15, 159901 (2015)].
- [29] R. Aaij et al. Measurement of the ratio of the $B^0 \rightarrow D^{*-}\tau^+\nu_\tau$ and $B^0 \rightarrow D^{*-}\mu^+\nu_\mu$ branching fractions using three-prong τ -lepton decays. *Phys. Rev. Lett.*, 120(17):171802, 2018.
- [30] R. Aaij et al. Test of Lepton Flavor Universality by the measurement of the $B^0 \rightarrow D^{*-}\tau^+\nu_\tau$ branching fraction using three-prong τ decays. *Phys. Rev.*, D97(7):072013, 2018.
- [31] Svjetlana Fajfer, Jernej F. Kamenik, and Ivan Nisandzic. On the $B \rightarrow D^*\tau\bar{\nu}_\tau$ Sensitivity to New Physics. *Phys. Rev.*, D85:094025, 2012.
- [32] Wolfgang Altmannshofer, Peter Stangl, and David M. Straub. Interpreting Hints for Lepton Flavor Universality Violation. *Phys. Rev.*, D96(5):055008, 2017.
- [33] Christoph Bobeth, Gudrun Hiller, and Giorgi Piranishvili. Angular distributions of $\bar{B} \rightarrow \bar{K}\ell^+\ell^-$ decays. *JHEP*, 12:040, 2007.
- [34] Chris Bouchard, G. Peter Lepage, Christopher Monahan, Heechang Na, and Junko Shigemitsu. Standard Model Predictions for $B \rightarrow K\ell^+\ell^-$ with Form Factors from Lattice QCD. *Phys. Rev. Lett.*, 111(16):162002, 2013. [Erratum: *Phys. Rev. Lett.* 112, no. 14, 149902 (2014)].
- [35] Roel Aaij et al. Test of lepton universality using $B^+ \rightarrow K^+\ell^+\ell^-$ decays. *Phys. Rev. Lett.*, 113:151601, 2014.

- [36] Marzia Bordone, Gino Isidori, and Andrea Patti. On the Standard Model predictions for R_K and R_{K^*} . *Eur. Phys. J.*, C76(8):440, 2016.
- [37] Sébastien Descotes-Genon, Lars Hofer, Joaquim Matias, and Javier Virto. Global analysis of $b \rightarrow s\ell\ell$ anomalies. *JHEP*, 06:092, 2016.
- [38] Bernat Capdevila, Sébastien Descotes-Genon, Joaquim Matias, and Javier Virto. Assessing lepton-flavour non-universality from $B \rightarrow K^*\ell\ell$ angular analyses. *JHEP*, 10:075, 2016.
- [39] Bernat Capdevila, Sébastien Descotes-Genon, Lars Hofer, and Joaquim Matias. Hadronic uncertainties in $B \rightarrow K^*\mu^+\mu^-$: a state-of-the-art analysis. *JHEP*, 04:016, 2017.
- [40] Nicola Serra, Rafael Silva Coutinho, and Danny van Dyk. Measuring the breaking of lepton flavor universality in $B \rightarrow K^*\ell^+\ell^-$. *Phys. Rev.*, D95(3):035029, 2017.
- [41] Aoife Bharucha, David M. Straub, and Roman Zwicky. $B \rightarrow V\ell^+\ell^-$ in the Standard Model from light-cone sum rules. *JHEP*, 08:098, 2016.
- [42] Wolfgang Altmannshofer, Christoph Niehoff, Peter Stangl, and David M. Straub. Status of the $B \rightarrow K^*\mu^+\mu^-$ anomaly after Moriond 2017. *Eur. Phys. J.*, C77(6):377, 2017.
- [43] Sebastian Jäger and Jorge Martin Camalich. Reassessing the discovery potential of the $B \rightarrow K^*\ell^+\ell^-$ decays in the large-recoil region: SM challenges and BSM opportunities. *Phys. Rev.*, D93(1):014028, 2016.
- [44] R. Aaij et al. Test of lepton universality with $B^0 \rightarrow K^{*0}\ell^+\ell^-$ decays. *JHEP*, 08:055, 2017.
- [45] Kazuo Abe et al. An Upper bound on the decay $\tau \rightarrow \mu \gamma$ from Belle. *Phys. Rev. Lett.*, 92:171802, 2004.
- [46] A. M. Baldini et al. Search for the lepton flavour violating decay $\mu^+ \rightarrow e^+\gamma$ with the full dataset of the MEG experiment. *Eur. Phys. J.*, C76(8):434, 2016.
- [47] Marat Freytsis, Zoltan Ligeti, and Joshua T. Ruderman. Flavor models for $\bar{B} \rightarrow D^{(*)}\tau\bar{\nu}$. *Phys. Rev.*, D92(5):054018, 2015.

- [48] Martin Bauer and Matthias Neubert. Minimal Leptoquark Explanation for the $R_{D^{(*)}}$, R_K , and $(g - 2)_g$ Anomalies. *Phys. Rev. Lett.*, 116(14):141802, 2016.
- [49] Andreas Crivellin, Giancarlo D'Ambrosio, and Julian Heeck. Explaining $h \rightarrow \mu^\pm \tau^\mp$, $B \rightarrow K^* \mu^+ \mu^-$ and $B \rightarrow K \mu^+ \mu^- / B \rightarrow K e^+ e^-$ in a two-Higgs-doublet model with gauged $L_\mu - L_\tau$. *Phys. Rev. Lett.*, 114:151801, 2015.
- [50] Matthew D. Schwartz. *Quantum Field Theory and the Standard Model*. Cambridge University Press, 2014.
- [51] I.S. Altarev, Yu.V. Borisov, N.V. Borovikova, S.N. Ivanov, E.A. Kolomensky, M.S. Lasakov, V.M. Lobashev, V.A. Nazarenko, A.N. Pirozhkov, A.P. Serebrov, Yu.V. Sobolev, E.V. Shulgina, and A.I. Yegorov. New measurement of the electric dipole moment of the neutron. *Physics Letters B*, 276(1):242 – 246, 1992.
- [52] David J. Gross and Frank Wilczek. Ultraviolet behavior of non-abelian gauge theories. *Phys. Rev. Lett.*, 30:1343–1346, Jun 1973.
- [53] Stefan Scherer. Introduction to chiral perturbation theory. *Adv. Nucl. Phys.*, 27:277, 2003. [,277(2002)].
- [54] S. Fubini and G. Furlan. Renormalization effects for partially conserved currents. *Physics Physique Fizika*, 1(4):229–247, 1965.
- [55] Richard F. Lebed and Mahiko Suzuki. Current algebra and the Ademollo-Gatto theorem in spin flavor symmetry of heavy quarks. *Phys. Rev.*, D44:829–836, 1991.
- [56] Leslie L. Foldy and Siegfried A. Wouthuysen. On the dirac theory of spin 1/2 particles and its non-relativistic limit. *Phys. Rev.*, 78:29–36, Apr 1950.
- [57] G. Peter Lepage, Lorenzo Magnea, Charles Nakhleh, Ulrika Magnea, and Kent Hornbostel. Improved nonrelativistic QCD for heavy quark physics. *Phys. Rev.*, D46:4052–4067, 1992.
- [58] Philippe de Forcrand. Simulating QCD at finite density. *PoS*, LAT2009:010, 2009.
- [59] M. Lüscher and P. Weisz. On-shell improved lattice gauge theories. *Comm. Math. Phys.*, 97(1-2):59–77, 1985.

- [60] P. Weisz. Continuum limit improved lattice action for pure yang-mills theory (i). *Nuclear Physics B*, 212(1):1 – 17, 1983.
- [61] P. Weisz and R. Wohlert. Continuum limit improved lattice action for pure yang-mills theory (ii). *Nuclear Physics B*, 236(2):397 – 422, 1984.
- [62] A. Hart, G. M. von Hippel, and R. R. Horgan. Radiative corrections to the lattice gluon action for HISQ improved staggered quarks and the effect of such corrections on the static potential. *Phys. Rev.*, D79:074008, 2009.
- [63] Kenneth G. Wilson. Confinement of Quarks. *Phys. Rev.*, D10:2445–2459, 1974. [,319(1974)].
- [64] John B. Kogut and Leonard Susskind. Hamiltonian Formulation of Wilson’s Lattice Gauge Theories. *Phys. Rev.*, D11:395–408, 1975.
- [65] E. Follana, Q. Mason, C. Davies, K. Hornbostel, G. P. Lepage, J. Shigemitsu, H. Trottier, and K. Wong. Highly improved staggered quarks on the lattice, with applications to charm physics. *Phys. Rev.*, D75:054502, 2007.
- [66] C. T. H. Davies et al. Precision charm physics, m(c) and alpha(s) from lattice QCD. *PoS*, LATTICE2008:118, 2008.
- [67] C. T. H. Davies. Precision charmonium and D physics from lattice QCD and determination of the charm quark mass. In *Proceedings, 34th International Conference on High Energy Physics (ICHEP 2008): Philadelphia, Pennsylvania, July 30-August 5, 2008*, 2008.
- [68] Jonna Koponen, Christine T. H. Davies, Gordon Donald, Eduardo Follana, G. Peter Lepage, Heechang Na, and Junko Shigemitsu. The D to K and D to pi semileptonic decay form factors from Lattice QCD. *PoS*, LATTICE2011:286, 2011.
- [69] Heechang Na, Christine T. H. Davies, Eduardo Follana, Jonna Koponen, G. Peter Lepage, and Junko Shigemitsu. $D \rightarrow \pi, l\nu$ Semileptonic Decays, $|V_{cd}|$ and 2nd Row Unitarity from Lattice QCD. *Phys. Rev.*, D84:114505, 2011.
- [70] Heechang Na, Chris Monahan, Christine Davies, Eduardo Follana, Ron Horgan, Peter Lepage, and Junko Shigemitsu. Precise Determinations of the Decay Constants of B and D mesons. *PoS*, LATTICE2012:102, 2012.

- [71] Heechang Na, Christine T. H. Davies, Eduardo Follana, G. Peter Lepage, and Junko Shigemitsu. $|V_{cd}|$ from D Meson Leptonic Decays. *Phys. Rev.*, D86:054510, 2012.
- [72] Jonna Koponen. Lattice results for D/D_s leptonic and semileptonic decays. In *Proceedings, 6th International Workshop on Charm Physics (Charm 2013): Manchester, UK, August 31-September 4, 2013*, 2013.
- [73] Andrew Lytle, Brian Colquhoun, Christine Davies, Jonna Koponen, and Craig McNeile. Semileptonic B_c decays from full lattice QCD. *PoS*, BEAUTY2016:069, 2016.
- [74] A. Gray, I. Allison, C. T. H. Davies, Emel Dalgic, G. P. Lepage, J. Shigemitsu, and M. Wingate. The Upsilon spectrum and m(b) from full lattice QCD. *Phys. Rev.*, D72:094507, 2005.
- [75] Christine T. H. Davies, Judd Harrison, Ciaran Hughes, Ronald R. Horgan, Georg M. von Hippel, and Matthew Wingate. Improving the Kinetic Couplings in Lattice Non-Relativistic QCD. 2018.
- [76] R. J. Dowdall et al. The Upsilon spectrum and the determination of the lattice spacing from lattice QCD including charm quarks in the sea. *Phys. Rev.*, D85:054509, 2012.
- [77] Michael E. Peskin and Daniel V. Schroeder. *An Introduction to quantum field theory*. 1995.
- [78] David J. E. Callaway and Aneesur Rahman. Microcanonical ensemble formulation of lattice gauge theory. *Phys. Rev. Lett.*, 49:613–616, Aug 1982.
- [79] David J. E. Callaway and Aneesur Rahman. Lattice gauge theory in the microcanonical ensemble. *Phys. Rev. D*, 28:1506–1514, Sep 1983.
- [80] Simon Duane and John B. Kogut. Hybrid stochastic differential equations applied to quantum chromodynamics. *Phys. Rev. Lett.*, 55:2774–2777, Dec 1985.
- [81] Simon Duane and John Kogut. The theory of hybrid stochastic algorithms. *Nuclear Physics B*, 275:398–420, 11 1986.

- [82] Nicholas Metropolis, Arianna W. Rosenbluth, Marshall N. Rosenbluth, Augusta H. Teller, and Edward Teller. Equation of state calculations by fast computing machines. *The Journal of Chemical Physics*, 21(6):1087–1092, 1953.
- [83] Simon Duane, A.D. Kennedy, Brian J. Pendleton, and Duncan Roweth. Hybrid monte carlo. *Physics Letters B*, 195(2):216 – 222, 1987.
- [84] Steven Gottlieb, W. Liu, D. Toussaint, R. L. Renken, and R. L. Sugar. Hybrid-molecular-dynamics algorithms for the numerical simulation of quantum chromodynamics. *Phys. Rev. D*, 35:2531–2542, Apr 1987.
- [85] K. Jansen. Actions for dynamical fermion simulations: are we ready to go? *Nuclear Physics B - Proceedings Supplements*, 129-130:3 – 16, 2004. Lattice 2003.
- [86] Michael Creutz. Chiral anomalies and rooted staggered fermions. *Physics Letters B*, 649(2):230 – 234, 2007.
- [87] Michael Creutz. Why rooting fails. *PoS*, LATTICE2007:007, 2007.
- [88] M. A. Clark and A. D. Kennedy. Accelerating dynamical fermion computations using the rational hybrid Monte Carlo (RHMC) algorithm with multiple pseudofermion fields. *Phys. Rev. Lett.*, 98:051601, 2007.
- [89] Andreas Frommer, Bertold Nockel, Stephan Gusken, Thomas Lippert, and Klaus Schilling. Many masses on one stroke: Economic computation of quark propagators. *Int. J. Mod. Phys.*, C6:627–638, 1995.
- [90] Beat Jegerlehner. Krylov space solvers for shifted linear systems. 1996.
- [91] A. Bazavov et al. Lattice QCD ensembles with four flavors of highly improved staggered quarks. *Phys. Rev.*, D87(5):054505, 2013.
- [92] A. Bazavov et al. Scaling studies of QCD with the dynamical HISQ action. *Phys. Rev.*, D82:074501, 2010.
- [93] R. J. Dowdall, C. T. H. Davies, G. P. Lepage, and C. McNeile. Vus from pi and K decay constants in full lattice QCD with physical u, d, s and c quarks. *Phys. Rev.*, D88:074504, 2013.
- [94] Bipasha Chakraborty, C. T. H. Davies, B. Galloway, P. Knecht, J. Koponen, G. C. Donald, R. J. Dowdall, G. P. Lepage, and C. McNeile. High-precision

- quark masses and QCD coupling from $n_f = 4$ lattice QCD. *Phys. Rev.*, D91(5):054508, 2015.
- [95] M. R. Hestenes and E. Stiefel. Methods of conjugate gradients for solving linear systems. *Journal of research of the National Bureau of Standards*, 49:409–436, 1952.
- [96] D. Guadagnoli, F. Mescia, and S. Simula. Lattice study of semileptonic form-factors with twisted boundary conditions. *Phys. Rev.*, D73:114504, 2006.
- [97] G.P.Lepage. Corrfitter: <https://github.com/gplepage/corrfitter>, 2012.
- [98] G. P. Lepage, B. Clark, C. T. H. Davies, K. Hornbostel, P. B. Mackenzie, C. Morningstar, and H. Trottier. Constrained curve fitting. *Nucl. Phys. Proc. Suppl.*, 106:12–20, 2002. [,12(2001)].
- [99] Colin J. Morningstar and J. Shigemitsu. Perturbative matching of lattice and continuum heavy-light currents with nrqcd heavy quarks. *Phys. Rev. D*, 59:094504, Mar 1999.
- [100] Christopher Monahan, Junko Shigemitsu, and Ron Horgan. Matching lattice and continuum axial-vector and vector currents with nonrelativistic QCD and highly improved staggered quarks. *Phys. Rev.*, D87(3):034017, 2013.
- [101] Christopher J Monahan, Heechang Na, Chris M Bouchard, G Peter Lepage, and Junko Shigemitsu. $B_s \rightarrow D_s \ell \nu$ Form Factors and the Fragmentation Fraction Ratio f_s/f_d . 2017.
- [102] Bipasha Chakraborty, C. T. H. Davies, B. Galloway, P. Knecht, J. Koponen, G. C. Donald, R. J. Dowdall, G. P. Lepage, and C. McNeile. High-precision quark masses and qcd coupling from $n_f = 4$ lattice qcd. *Phys. Rev. D*, 91:054508, Mar 2015.
- [103] T. C. Hammant, A. G. Hart, G. M. von Hippel, R. R. Horgan, and C. J. Monahan. Radiative improvement of the lattice nonrelativistic QCD action using the background field method with applications to quarkonium spectroscopy. *Phys. Rev.*, D88(1):014505, 2013. [Erratum: Phys. Rev.D92,no.11,119904(2015)].
- [104] Claude Bourrely, Laurent Lellouch, and Irinel Caprini. Model-independent description of $b \rightarrow \pi l \nu$ decays and a determination of $|V_{ub}|$. *Phys. Rev. D*, 79:013008, Jan 2009.

- [105] C. McNeile, C. T. H. Davies, E. Follana, K. Hornbostel, and G. P. Lepage. High-Precision c and b Masses, and QCD Coupling from Current-Current Correlators in Lattice and Continuum QCD. *Phys. Rev.*, D82:034512, 2010.
- [106] Brian Colquhoun, Christine Davies, Jonna Koponen, Andrew Lytle, and Craig McNeile. B_c decays from highly improved staggered quarks and NRQCD. *PoS*, LATTICE2016:281, 2016.
- [107] H. Schroder. New results on heavy quarks from ARGUS and CLEO. In *Heavy quark physics. Proceedings, 138th WE-Heraeus Seminar, Bad Honnef, Germany, December 14-16, 1994*, pages 9–22, 1994.
- [108] D. Bortoletto et al. Exclusive and inclusive decays of b mesons into d_s mesons. *Phys. Rev. Lett.*, 64:2117–2120, Apr 1990.
- [109] R. Fulton et al. Exclusive and inclusive semileptonic decays of b mesons to d mesons. *Phys. Rev. D*, 43:651–663, Feb 1991.
- [110] H. Albrecht et al. Measurement of the decay $b^0 \rightarrow d^{*0} l^- \nu$. *Physics Letters B*, 275(1):195 – 201, 1992.
- [111] B. Barish et al. Measurement of the anti-B $\rightarrow D^*$ lepton anti-neutrino branching fractions and $|V(cb)|$. *Phys. Rev.*, D51:1014–1033, 1995.
- [112] D. Buskulic et al. Strange b baryon production and lifetime in z decays. *Physics Letters B*, 384(1):449 – 460, 1996.
- [113] D. Buskulic et al. Heavy quark tagging with leptons in the ALEPH detector. *Nucl. Instrum. Meth.*, A346:461–475, 1994.
- [114] G. Abbiendi et al. Measurement of $|V(cb)|$ using anti-B0 $\rightarrow D^*+$ lepton-anti-neutrino decays. *Phys. Lett.*, B482:15–30, 2000.
- [115] P. Abreu et al. Measurement of V(cb) from the decay process anti-B0 $\rightarrow D^*+$ lepton- anti-neutrino. *Phys. Lett.*, B510:55–74, 2001.
- [116] N. E. Adam et al. Determination of the anti-B $\rightarrow D^* l$ anti-nu decay width and $|V(cb)|$. *Phys. Rev.*, D67:032001, 2003.
- [117] J. Abdallah et al. Measurement of $|V(cb)|$ using the semileptonic decay anti-B0(d) $\rightarrow D^*+ l$ - anti-nu(l). *Eur. Phys. J.*, C33:213–232, 2004.

- [118] Bernard Aubert et al. Determination of the form-factors for the decay $B^0 \rightarrow D^{*-} \ell^+ \nu_\ell$ and of the CKM matrix element $|V_{cb}|$. *Phys. Rev.*, D77:032002, 2008.
- [119] Bernard Aubert et al. Measurement of the Decay $B^- \rightarrow D^{*0} e^- \bar{\nu}(e)$. *Phys. Rev. Lett.*, 100:231803, 2008.
- [120] W. Dungel et al. Measurement of the form factors of the decay $B^0 \rightarrow D^{*-} \ell^+ \nu_\ell$ and determination of the CKM matrix element $|V_{cb}|$. *Phys. Rev.*, D82:112007, 2010.
- [121] A. Abdesselam et al. Precise determination of the CKM matrix element $|V_{cb}|$ with $\bar{B}^0 \rightarrow D^{*+} \ell^- \bar{\nu}_\ell$ decays with hadronic tagging at Belle. 2017.
- [122] A. Abdesselam et al. Measurement of CKM Matrix Element $|V_{cb}|$ from $\bar{B} \rightarrow D^{*+} \ell^- \bar{\nu}_\ell$. 2018.
- [123] Jack Laiho and Ruth S. Van de Water. $B \rightarrow D^* \ell \nu$ and $B \rightarrow D \ell \nu$ form factors in staggered chiral perturbation theory. *Phys. Rev.*, D73:054501, 2006.
- [124] Jonathan Flynn, Taku Izubuchi, Andreas Juttner, Taichi Kawanai, Christoph Lehner, Edwin Lizarazo, Amarjit Soni, Justus Tobias Tsang, and Oliver Witzel. Form factors for semi-leptonic B decays. *PoS*, LATTICE2016:296, 2016.
- [125] Jon A. Bailey, Tanmoy Bhattacharya, Rajan Gupta, Yong-Chull Jang, Weon-jong Lee, Jaehoon Leem, Sungwoo Park, and Boram Yoon. Calculation of $\bar{B} \rightarrow D^* \ell \bar{\nu}$ form factor at zero recoil using the Oktay-Kronfeld action. *EPJ Web Conf.*, 175:13012, 2018.
- [126] K. G. Wilson. Quarks and Strings on a Lattice. *New Phenomena in Subnuclear Physics*, Part A:69–143, 1977.
- [127] B. Sheikholeslami and R. Wohlert. Improved continuum limit lattice action for qcd with wilson fermions. *Nuclear Physics B*, 259(4):572 – 596, 1985.
- [128] Aida X. El-Khadra, Andreas S. Kronfeld, and Paul B. Mackenzie. Massive fermions in lattice gauge theory. *Phys. Rev.*, D55:3933–3957, 1997.
- [129] skopt: <https://github.com/scikit-optimize/scikit-optimize>.

- [130] C. McNeile, C. T. H. Davies, E. Follana, K. Hornbostel, and G. P. Lepage. High-Precision f_{B_s} and HQET from Relativistic Lattice QCD. *Phys. Rev.*, D85:031503, 2012.
- [131] G. C. Donald, C. T. H. Davies, J. Koponen, and G. P. Lepage. V_{cs} from $D_s \rightarrow \phi \ell \nu$ semileptonic decay and full lattice QCD. *Phys. Rev.*, D90(7):074506, 2014.
- [132] A. Bazavov et al. B - and D -meson leptonic decay constants from four-flavor lattice QCD. 2017.
- [133] Adam F. Falk and Matthias Neubert. Second order power corrections in the heavy quark effective theory. 1. Formalism and meson form-factors. *Phys. Rev.*, D47:2965–2981, 1993.
- [134] Thomas Mannel. Higher order 1/m corrections at zero recoil. *Phys. Rev.*, D50:428–441, 1994.
- [135] Andrzej Czarnecki. Two-loop qcd corrections to $b \rightarrow c$ transitions at zero recoil. *Phys. Rev. Lett.*, 76:4124–4127, May 1996.
- [136] J.E. Paschalis and G.J. Gounaris. Meson decays in the non-relativistic quark model. *Nuclear Physics B*, 222(3):473 – 492, 1983.
- [137] A. Bazavov et al. Up-, down-, strange-, charm-, and bottom-quark masses from four-flavor lattice QCD. *Phys. Rev.*, D98(5):054517, 2018.
- [138] A. Bazavov et al. Charmed and light pseudoscalar meson decay constants from four-flavor lattice QCD with physical light quarks. *Phys. Rev.*, D90(7):074509, 2014.
- [139] Nathan Isgur, Daryl Scora, Benjamin Grinstein, and Mark B. Wise. Semileptonic b and d decays in the quark model. *Phys. Rev. D*, 39:799–818, Feb 1989.
- [140] Eigo Shintani, Rudy Arthur, Thomas Blum, Taku Izubuchi, Chulwoo Jung, and Christoph Lehner. Covariant approximation averaging. *Phys. Rev. D*, 91:114511, Jun 2015.
- [141] D. Buskulic et al. Measurements of $|V(cb)|$, form-factors and branching fractions in the decays anti-B0 \rightarrow D*+ lepton- anti-lepton-neutrino and anti-B0 \rightarrow D+ lepton- anti-lepton-neutrino. *Phys. Lett.*, B395:373–387, 1997.

- [142] R. Glattauer et al. Measurement of the decay $B \rightarrow D\ell\nu_\ell$ in fully reconstructed events and determination of the Cabibbo-Kobayashi-Maskawa matrix element $|V_{cb}|$. *Phys. Rev.*, D93(3):032006, 2016.
- [143] Jon A. Bailey, A. Bazavov, C. Bernard, C. M. Bouchard, C. DeTar, Daping Du, A. X. El-Khadra, J. Foley, E. D. Freeland, E. Gámiz, Steven Gottlieb, U. M. Heller, Jongjeong Kim, A. S. Kronfeld, J. Laiho, L. Levkova, P. B. Mackenzie, Y. Meurice, E. Neil, M. B. Oktay, Si-Wei Qiu, J. N. Simone, R. Sugar, D. Toussaint, R. S. Van de Water, and Ran Zhou. $B_s \rightarrow D_s/b \rightarrow d$ semileptonic form-factor ratios and their application to $\text{BR}(B_s^0 \rightarrow \mu^+\mu^-)$. *Phys. Rev. D*, 85:114502, Jun 2012.
- [144] Mariam Atoui, Vincent Morénas, Damir Bećirević, and Francesco Sanfilippo. $b_s \rightarrow d_s l \nu_l$ near zero recoil in and beyond the standard model. *The European Physical Journal C*, 74(5):2861, May 2014.
- [145] Claude Bourrely, Irinel Caprini, and Laurent Lellouch. Model-independent description of $B \rightarrow \pi l \nu$ decays and a determination of $|V(ub)|$. *Phys. Rev.*, D79:013008, 2009. [Erratum: Phys. Rev.D82,099902(2010)].
- [146] R. J. Dowdall, C. T. H. Davies, T. C. Hammant, and R. R. Horgan. Precise heavy-light meson masses and hyperfine splittings from lattice QCD including charm quarks in the sea. *Phys. Rev.*, D86:094510, 2012.
- [147] Susumu Okubo. New improved bounds for K_{l3} parameters. *Phys. Rev. D*, 4:725–733, Aug 1971.
- [148] Susumu Okubo. Exact bounds for K_{l3} decay parameters. *Phys. Rev. D*, 3:2807–2813, Jun 1971.
- [149] C. Glenn Boyd, Benjamín Grinstein, and Richard F. Lebed. Model-independent determinations of $b \rightarrow d l \nu, d^* l \nu$ form factors. *Nuclear Physics B*, 461(3):493 – 511, 1996.
- [150] Thomas Becher and Richard J. Hill. Comment on form-factor shape and extraction of $|v_{ub}|$ from $b \rightarrow \pi l \nu$. *Physics Letters B*, 633(1):61 – 69, 2006.